Simulation and Analysis of Roller Chain Drive Systems

Pedersen, Sine Leergaard; Madsen, John M.; Thomsen, Jon Juel

Publication date:
2004

Document Version
Publisher's PDF, also known as Version of record

Simulation and Analysis of Roller Chain Drive Systems

by

Sine Leergaard Pedersen

DEPARTMENT OF MECHANICAL ENGINEERING

SOLID MECHANICS

TECHNICAL UNIVERSITY OF DENMARK

Preface

This thesis is made in fulfilment of my Ph.D. degree at the Department of Mechanical Engineering, Solid Mechanics at the Technical University of Denmark. I would like to thank my supervisors External Associate Professor John M. Hansen, MAN B&W Diesel A/S and Associate Professor Jon Juel Thomsen, Department of Mechanical Engineering, DTU, for the help, the support and the inspiration.

I wish to thank my family for their support, inspiration and help. I also want to thank my colleagues at the Department of Mechanical Engineering, Solid Mechanics for their help and entertainment.

During my Ph.D. work I visited the technical university Instituto Superior Técnico (IST) in Lisbon, Portugal for a period of three and a half month from September 2002 to December 2002. I would like to thank my advisor there Professor Jorge A. C. Ambrósio for the help and support. I would also like to thank Paula Jorge and my other friends and colleagues in Portugal for taking good care of me during my stay.

I also visited the technical university Instituto Superior de Engenharia de Coimbra in Coimbra, Portugal a couple of times for a few days. I wish to thank Cândida Pereira and Amilca Ramalho for the cooperation and their hospitality.

For a period of one month from February 2003 to March 2003 I visited the University of Arizona, Tucson, Arizona, USA. I would like to thank my advisor there Professor Parviz E. Nikravesh for the help, support and hospitality. The financial support from 'Civilingeniør Kristian Rasmussen og hustru Gunhild Katrine Rasmussens fond', which made my stay in Tucson possible, is highly appreciated.

Finally I wish to thank Per Rønnedal and Mikkel Preem et. al. from MAN B&W Diesel A/S for many fruitful meetings and discussions.

Kgs. Lyngby, August 2004

Sine Leergaard Pedersen

List of publications

Parts of this thesis are published in:

[P1] Ambrósio, J. A. C. and Pedersen, S. L. and Hansen, J. M. (2002), 'Roller-Sprocket Contact Models in Dynamics of Roller-Chain Drives', *New Developments on Tribology: Theoretical Analysis and Application to Industrial Processes*, Actas das 8^{as} Jornadas Porutguesas de Triboligia, Eds. J. Grácio, Q.H. Fan & N. Ali, Aveiro, Portugal, May 8-9, pp.195-202.

[P2] Pedersen, S. L. and Hansen, J. M. and Ambrósio, J. A. C. (2002), 'A Novel Roller Chain Drive Model Using Multibody Dynamics Analysis Tools', *Virtual Nonlinear Multibody Dynamic Systems, NATO Advances Study Institute*, Eds. W. Schiehlen & M. Valášek, Prague, Czech Republic, June 23 - July 3 2002, **II**, pp. 180-186.

[P3] Pedersen, S. L. (2002), 'A Roller Chain Drive Model based on Multibody Dynamics', *DCAMM International Symposium on Challenges in Applied Mechanics*, Eds. P. Pedersen & N. Olhoff, Hotel Frederiksdal, Kgs. Lyngby, Denmark, July 25 - 27 2002, pp 257 - 262.

[P4] Pedersen, S. L. and Hansen, J. M. and Ambrósio, J. A. C. (2003), 'A Roller Chain Drive Model Including Contact with Guide-bars', *ECCOMAS - Multibody Dynamics 2003,International Conference on Advances In Computational Multibody Dynamics*, Ed. J. A. C. Ambrósio, Lisbon, Portugal, July 1-4 2003, 16 pages on cd and book of abstracts.

[P5] Pedersen, S. L. and Hansen, J. M. and Ambrósio, J. A. C. (2004), 'A Roller Chain Drive Model Including Contact with Guide-bars', *Multibody System Dynamics*, **12**(3), pp. 285-301

[P6] Pedersen, S. L. (2004), 'Model of Contact between Rollers and Sprockets in Chain Drive Systems', *DCAMM Report No.* **694**, Archive of Applied Mechanics, (Accepted for publication)

[P7] Pedersen, S. L. (2004), 'Contact Problems in Roller Chain Drive Systems', *ICTAM04 - 21^{st} International Congress of Theoretical and Applied Mechanics*, Eds.

W. Gutkowski & T. A. Kowalewski, Warsaw, Poland, August 15-21 2004, 2 pages on cd and book of abstracts.

Additional results not included in the thesis are published in

[P8] Pereira C. and Pedersen, S. L. and Ramalho A. and Ambrósio, J. A. C. (2003), 'Comportamento Dinâmico de Transmissões por Corrente Estudo Numérico e Experimental', *Proceedings of the VI Congresso Ibero-Americano de Engenharia Mecânica*, Ed. A. M. Dias, Coimbra, Portugal, October 15-18, pp.1297-1302. (In portuguese)

Abstract

Simulation and analysis of roller chain drive systems

The subject of this thesis is simulation and analysis of large roller chain drive systems, such as e.g. used in marine diesel engines. The aim of developing a chain drive simulation program is to analyse dynamic phenomena of chain drive systems and investigate different design changes to the systems, in order to remove unwanted phenomena. Such a computer program can, when properly validated, be used as an alternative to or in combination with physical experiments. Prior investigations in this area have been done with a focus on smaller chains in high speed chain drives. For large low speed systems other phenomena occur and therefore, a specific model of the marine engine chain drive is of interest.

The research objective of the work presented in this thesis is to contribute with a novel theoretical basis for the analysis of chain drive systems, by posing and validating different mathematical models, and compare to the prior done research. Even though the model is developed at first for the use of analysing chain drive systems in marine engines, the methods can with small changes be used in general, as for e.g. chain drives in industrial machines, car engines and motorbikes.

A novel formulation for the simulation of the dynamics of roller chain drives using a continuous contact force method is developed in this work. The model of the contact surface between the rollers and sprocket has shown to be an important issue regarding the numerical stability of the simulation program and a model with a real tooth profile proves superior to other applied models. With this model it is possible to perform a dynamic simulation of large marine engine chain drives. Through the application of this method, it is shown that the interrelated dynamics of the elements in the chain drive system is captured and the contact problem is characterized. The chain drive model is compared with simplified analytical results, while the necessary experimental validation is left for future studies.

Abstrakt (In Danish)

Simulering og analyse af kædetræksystemer

Denne afhandling omhandler simulering og analyse af kædetræk, som f.eks. anvendes i dieselmotorer, primært til fremdrift af skibe. Målet med at udvikle et kædetræksimuleringsprogram, er at analysere kædetræks dynamiske fænomener og undersøge forskellige designændringer af systemet, med det formål at fjerne uønskede fænomener. Et sådan computerprogram kan, når det er passende vurderet, blive brugt som et alternativ til eller i kombination med fysiske forsøg. Tidligere forskning indenfor dette område er udført med fokus på mindre kæder og højhastigheds kædetræk. For store lavhastigheds kædetræk opstår der anderledes fænomener, og derfor er der interesse for en specifik model for kædetræk i skibsmotorer.

Det videnskabelige mål med arbejdet præsenteret i denne afhandling, er at bidrage med en ny teoretisk basis for analyse af kædesystemer, ved at foreslå og validere forskellige matematiske modeller, og sammenligne med tidligere udført forskning. Selvom modellen udvikles med kædetræk til skibsmotorer for øje, vil den udviklede metode kunne anvendes til kædetræksimuleringer generelt, som for eksempel kædetræk i industrimaskiner, bilmotorer og motorcykler.

I dette arbejde er til simulering af kædetrækdynamik udviklet en ny formulering, som anvender en kontinuert kontaktkraftmetode. Modellen for kontaktfladen mellem ruller og kædehjul har vist sig at være en vigtig faktor med henblik på numerisk stabilitet af simuleringsprogrammet, og en model med et virkeligt tandprofil er at foretrække frem for andre anvendte modeller. Med denne model er det muligt at udføre dynamisk simulering af store skibsmotorkædetræk. Ved anvendelse af denne metode er det vist, at den indbyrdes dynamik for kædesystemets dele er beskrevet og kontaktproblemet er karakteriseret. Modellen af kædetræk er sammenlignet med simplificerede analytiske resultater, medens den nødvendige eksperimentelle validering er overladt til fremtidige studier.

Contents

Nomenclature

Matrices

$\mathbf{A}$	Transformation matrix
$\mathbf{A}_g$	Transformation matrix
$\mathbf{A}_s$	Transformation matrix
$\mathbf{A}_t$	Transformation matrix
$\mathbf{I}$	Identity matrix
$\mathbf{J}^*$	Matrix of mass moments of inertia
$\mathbf{K}$	Stiffness matrix
$\mathbf{M}$	Mass matrix
$\mathbf{M}_s$	Mass matrix, for sprocket s
$\mathbf{M}_b$	Mass matrix, for a number of bodies
$\mathbf{\Phi}$	Jacobian matrix
$\mathbf{\Phi}_b$	Jacobian matrix
$\mathbf{\Phi}_i$	Part of Jacobian matrix related to roller i
$\mathbf{\Phi}_s$	Jacobian matri
$\mathbf{\Phi}_{s,i}$	Jacobian matrix related to sprocket s and roller i

Vectors

$\mathbf{a}$	Arbitrary vector
$\mathbf{b}$	Arbitrary vector
$\mathbf{d}$	Vector from tooth center to roller center
$\mathbf{d}_1$	Vector between roller center and tooth contact area 1
$\mathbf{d}_2$	Vector between roller center and tooth contact area 2
$\mathbf{d}_3$	Vector between roller center and tooth contact area 3
$\mathbf{d}_{g1}$	Vector between roller center and guide-bar contact area 1
$\mathbf{d}_{g2}$	Vector between roller center and guide-bar contact area 2
$\mathbf{d}_{g3}$	Vector between roller center and guide-bar contact area 3
$\mathbf{d}_{i1}$	Vector between two points
$\mathbf{d}_{i2}$	Vector between two points
$\mathbf{f}$	Force vector
$\mathbf{f}_b$	External force vector on a number of bodies
$\mathbf{f}_c$	Contact force vector
$\mathbf{f}_i$	Link force vector
$\mathbf{f}_r$	Resultant force vector on all rollers
$\mathbf{f}_r^r$	Reaction force vector on rollers in contact with a sprocket
$\mathbf{g}$	Generalized force vector
$\mathbf{g}_e$	External force vector
$\mathbf{g}_s$	External force vector on sprocket s
$\mathbf{l}_i$	Vector between roller $i-1$ and roller i
$\mathbf{l}_{i+1}$	Vector between roller i and roller $i+1$
$\mathbf{n}$	Unit normal vector
$\mathbf{n}_1$	Unit normal vector
$\mathbf{n}_2$	Unit normal vector
$\mathbf{n}_3$	Unit normal vector
$\mathbf{n}_4$	Unit normal vector
$\mathbf{n}_g$	Unit normal vector
$\mathbf{n}_{g1}$	Unit normal vector
$\mathbf{n}_{g3}$	Unit normal vector
$\mathbf{n}_\beta$	Unit normal vector
$\mathbf{q}$	Position vector
$\mathbf{q}_b$	The position and angle of a number of bodies
$\mathbf{q}_i$	Position vector
$\mathbf{q}_s$	The position and angle of sprocket s
$\mathbf{q}_{s,i}$	The position and angle of sprocket s and position of roller i
$\mathbf{q}_r$	Vector containing all roller positions
$\mathbf{r}$	Vector to origin of body fixed reference frame on a body
$\mathbf{r}_b$	Vector to point b
$\mathbf{r}_{b^*}$	Vector to point b^*
$\mathbf{r}_c$	Vector to point c
$\mathbf{r}_{c^*}$	Vector to point c^*
$\mathbf{r}_{d^*}$	Vector to point d^*
$\mathbf{r}_{e^*}$	Vector to point e^*
$\mathbf{r}_{gc}$	Vector to middle point of a guide-bar

$\mathbf{r}_{gei}$	Vector to center point of rounded end on a guide-bar
$\mathbf{r}_{gej}$	Vector to center point of rounded end on a guide-bar
$\mathbf{r}_{gi}$	Vector to point gi on a guide-bar
$\mathbf{r}_{gj}$	Vector to point gj on a guide-bar
$\mathbf{r}_i$	Vector to origin of body fixed reference frame on body i or roller i
$\mathbf{r}_i^p$	Vector to the contact point on roller i
$\mathbf{r}_i^P$	Vector to point P on body i
$\mathbf{r}_i^Q$	Vector to point Q on body i
$\mathbf{r}_i^R$	Vector to point R on body i
$\mathbf{r}_j$	Vector to origin of body fixed reference frame on body j or roller j
$\mathbf{r}_j^P$	Vector to point P on body j
$\mathbf{r}_s$	Vector to origin of body fixed reference frame on sprocket s
$\mathbf{r}_s^p$	Vector to the contact point on sprocket s
$\mathbf{r}_t$	Vector to a tooth center
$\mathbf{s}$	Vector on a body given relative to the body fixed reference frame
$\mathbf{s}_b$	Vector to point b given relative to the local tooth reference frame
$\mathbf{s}_{b^*}$	Vector to point b^* given relative to the local tooth reference frame
$\mathbf{s}_{bf^*}$	Vector from point b^* to point f^* given relative to the local tooth reference frame
$\mathbf{s}_c$	Vector to point c given relative to the local tooth reference frame
$\mathbf{s}_{c^*}$	Vector to point c^* given relative to the local tooth reference frame
$\mathbf{s}_{f^*}$	Vector to point f^* given relative to the local tooth reference frame
$\mathbf{s}_i$	Position vector of a point in a body given relative to the body fixed reference frame
$\mathbf{s}_j$	Position vector of a point in a body given relative to the body fixed reference frame
$\mathbf{s}_s^p$	Vector to a contact point given relative to the fixed reference frame of the sprocket
$\mathbf{s}_t$	Vector to the tooth center given relative to the fixed reference frame of the sprocket
$\mathbf{t}$	Unit tangential vector
$\mathbf{t}_2$	Unit tangential vector
$\mathbf{t}_g$	Unit tangential vector
$\mathbf{t}_\beta$	Unit tangential vector
$\mathbf{u}_i$	Unit vector
$\mathbf{u}_{i+1}$	Unit vector
$\mathbf{u}_r$	Unit vector in radial direction of a sprocket
$\mathbf{u}_t$	Unit vector in tangential direction to a sprocket
$\mathbf{v}_n$	Relative velocity in normal direction
$\mathbf{v}_t$	Relative velocity in tangential direction
$\mathbf{y}_{t=0}$	Initial values of the position and velocity of the rollers and sprockets
$\boldsymbol{\gamma}$	Vector of right hand sides of the acceleration equation
$\boldsymbol{\gamma}_{s,i}$	Vector of right hand side of the acceleration equation
$\boldsymbol{\gamma}_t$	Vector of right hand sides of the acceleration equation
$\boldsymbol{\rho}$	Vector from the origin of the body fixed reference frame to the body center of mass
$\boldsymbol{\phi}^r$	Constraint equations for revolute joints
$\boldsymbol{\phi}_{s,i}$	Constraint equations between sprocket s and roller i
$\boldsymbol{\phi}^t$	Constraint equations for translational joints

Scalars

A	Angle
A_1	Amplitude
a_1	Amplitude
A_2	Amplitude
a_2	Amplitude
B	Angle
C	Angle
C_d	Damping coefficient for rotational link damping
C_j	Cosine of the angle related to tooth j, times the sprocket pitch radius
c_0	Phase velocity of a wave
Δc_0	Phase velocity of a wave
$\mathrm{d}N$	Differential normal force

$\mathrm{d}T$	Differential tangential force
$\mathrm{d}M$	Differential moment
D	Damping coefficient for longitudinal link damping
D_c	Damping coefficient used in the Hertzian contact force
D_{ct}	Coefficient of damping
D_n	Equivalent damping coefficient for longitudinal link damping
D_r	Roller diameter
D_t	Tooth diameter
E	Young's modulus
e	Restitution coefficient
E_k	Young's Modulus for body k
E_{kin}	Kinetic energy
$E_{kin}^{(-)}$	Kinetic energy at impact
$E_{kin}^{(+)}$	Kinetic energy after impact
ΔE_{kin}	Loss in kinetic energy
F	Pre-tension force
F_{cf}	Centrifugal force
f_c	Magnitude of the contact force
f_f	Friction force
F_n	Normal force
f_n	Cyclic natural frequency
F_s	Static tension force
ΔF_s	Amplitude of torsional vibration force
f_{x_i}	Force on roller i in x direction
f_{y_i}	Force on roller i in y direction
f_{x_s}	External force on sprocket s in x direction
f_{y_s}	External force on sprocket s in y direction
f_ω	Cyclic frequency
f_Ω	Driving cyclic frequency
g	Gravitational acceleration
H	Length measure used for the real tooth profile
h	Material property
h_k	Material property of body k, $h_k = \frac{1-\nu_k^2}{\pi E_k}$
i	Index
J	Moment of inertia
j	Index
J_k	Moment of inertia of body k, $k = 1, 2, \cdots$
J_s	Moment of inertia of sprocket s
J_w	Mass moment of inertia of the weight-arm
K	Stiffness coefficient
k	Order number
K_n	Equivalent stiffness coefficient
K_g	Generalized stiffness coefficient
K_t	Stiffness coefficient of spring in tightener system
l	Length of chain string
L_0	Undeformed length of spring in tightener system
L_g	Length of flat part of guide-bar
L_{ge}	Length of rounded end of guide-bar
l_i	Distance between roller i and roller $i-1$
l_{i+1}	Distance between roller i and roller $i+1$
l_t	Length of chain string
l_z	Length of roller cylinder
M	Moment
m	Exponent used in force/indentation relation for cylindrical contact
m_e	Equivalent mass
m_k	Mass of body k, $k = i, j$
m_l	Mass of chain string per unit length
m_r	Roller mass
m_s	Sprocket mass
m_t	Total mass of chain string
m_w	Mass of the weight-arm
N	Normal force
n	Exponent used in Hertzian contact force
n_b	Number of bedded rollers
n_l	Number of chain links in the system
n_t	Number of teeth on a sprocket
P	Chain pitch distance
P_b	Chain break load
P_{cd}	Dissipated power due to damping in contact with sprockets or guide-bars
P_{driver}	Applied power
P_i	Point on body i
P_j	Point on body j
P_{ld}	Dissipated power due to longitudinal damping

P_{rd}	Dissipated power due to rotational damping
P_f	Dissipated power due to friction
P_T	Total dissipated power
Q_i	Point on body i
q_a	Tension in a chain segment
q_b	Tension in a chain segment
q_c	Centrifugal force
r_k	Radius of body k, $k = i, j$
R_E	Radius used for the real tooth profile
R_F	Radius used for the real tooth profile
R_{ge}	Radius of rounded end of guide-bar
R_i	Pitch radius of sprocket $i = 1, 2, \cdots$
R_s	Pitch radius of sprocket s
R_r	Roller radius
R_t	Tooth radius
R_{tg}	Distance form grounded point to sprocket center
ΔR	Difference between tooth radius and roller radius
s_{bf^*x}	x coordinate of vector $\mathbf{s}_{bf^*}$
s_{bf^*y}	y coordinate of vector $\mathbf{s}_{bf^*}$
S	Length measure used for the real tooth profile
S_j	Sine of the angle related to tooth j, times the sprocket pitch radius
T	Tangential force
t	Time
t_c	Time limit
t_e	Time instant where contact ends
t_r	Revolution time of the driving sprocket
t_s	Time instant where contact begins
V	Chain string velocity
v_{rpm}	Driver velocity given in rpm
v	Relative speed
v_r	Relative speed in radial direction
v_t	Relative speed in tangential direction
v_n	Relative speed in normal direction
v_t	Relative speed in tangential direction
v_t^*	Speed limit
v	Relative speed
v_{in}	Projection of relative velocity of body i in the $\mathbf{n}$ direction
v_{jn}	Projection of relative velocity of body j in the $\mathbf{n}$ direction
v_β	Relative speed in the direction of the tooth profile
$v^{(+)}$	Relative speed after impact
$v^{(-)}$	Relative speed at impact
W_1	Length measure used for the real tooth profile
W_2	Length measure used for the real tooth profile
W_3	Length measure used for the real tooth profile
W_4	Length measure used for the real tooth profile
x	Abscissa axis of global reference frame
x_{G1}	x coordinate of grounded point
x_{G2}	x coordinate of grounded point
x_i	x coordinate of the position vector for roller i
x_s	x coordinate of the position vector for sprocket s
x_{w1}	x coordinate of the center of mass position of the weight-arm
x_{w2}	x coordinate of point on the weight-arm
y	Ordinate axis of global reference frame
y_{G1}	y coordinate of grounded point
y_{G2}	y coordinate of grounded point
y_i	y coordinate of the position vector for roller i
y_s	y coordinate of the position vector for sprocket s
y_{w1}	y coordinate of the center of mass position of the weight-arm
y_{w2}	y coordinate of point on the weight-arm
z	Ordinate axis of global reference frame
α	Pitch angle
β	Angle of the semi real tooth profile
δ	Magnitude of indentation
δ_1	Indentation in tooth contact area 1
δ_2	Indentation in tooth contact area 2
δ_3	Indentation in tooth contact area 3
δ_4	Indentation in tooth contact area 4
δ_g	Initial indentation of a guide-bar pressed into the chain
δ_{g1}	Indentation in guide-bar contact area 1
δ_{g2}	Indentation in guide-bar contact area 2

δ_{g3}	Indentation in guide-bar contact area 3
δ_r	Indentation in radial direction at the position of a roller on a sprocket
δ_t	Indentation in tangential direction at the position of a roller on a sprocket
δ_β	Indentation in the tooth
δ_{max}	Maximum indentation
ϵ	Approximation constant
ζ	The pressure angle
ζ_i	Ordinate axis of local body fixed reference frame
ζ_s	Ordinate axis of local sprocket fixed reference frame
η	Relaxation factor
η_c	Hysteresis damping factor
η_g	Ordinate axis of local guide-bar fixed reference frame
η_i	Ordinate axis of local body fixed reference frame
η_s	Ordinate axis of local sprocket fixed reference frame
η_t	Ordinate axis of local tooth fixed reference frame
θ	Angle of rotation
θ_i	Angle of rotation of body i
θ_j	Angle of rotation of body j
θ_s	Rotation angle of sprocket s
θ_t	Rotation angle of a tooth
λ_i	Lagrange multiplier component
τ	External moment
τ_s	External moment on sprocket s
τ_l	Rotational damping moment
μ	Frequency
μ_c	Dynamic correction factor
μ_d	Dynamic friction coefficient
μ_s	Static friction coefficient
ν	Poisson's ration
ν_k	Poisson's ration for body k, $k = i, j$
ξ_g	Abscissa axis of local guide-bar fixed reference frame
ξ_i	Abscissa axis of local body fixed reference frame
ξ_s	Abscissa axis of local sprocket fixed reference frame
ξ_t	Abscissa axis of local tooth fixed reference frame
ϕ	Phase angle
ϕ_1	Phase angle
ϕ_2	Phase angle
ϕ_p	Phase angle
$\phi_1^{(t)}$	Constraint equation for translational joint
$\phi_2^{(t)}$	Constraint equation for translational joint
ϕ_{tg}	Rotation angle of weight-arm
φ_g	Rotation angle of guide-bar
φ_i	Relative angle between two adjacent links
φ_t	Initial rotation angle of guide-bar
φ_τ	Angle
ψ_{1a}	Angle used to define real shaped tooth profile
ψ_{2a}	Angle used to define real shaped tooth profile
ψ_{1b}	Angle used to define real shaped tooth profile
ψ_{1b^*}	Angle used to define real shaped tooth profile
ψ_{2b}	Angle used to define real shaped tooth profile
ψ_{2b^*}	Angle used to define real shaped tooth profile
ψ_{1c}	Angle used to define real shaped tooth profile
ψ_{2c}	Angle used to define real shaped tooth profile
ψ_{1c^*}	Angle used to define real shaped tooth profile
ψ_{2c^*}	Angle used to define real shaped tooth profile
ψ_1	Angle used to define real shaped tooth profile
ψ_{10}	Angle used to define real shaped tooth profile
ψ_2	Angle used to define real shaped tooth profile
ψ_{20}	Angle used to define real shaped tooth profile
ψ_3	Angle used to define real shaped tooth profile
ψ_{30}	Angle used to define real shaped tooth profile

ψ_4	Angle used to define real shaped tooth profile
ψ_{40}	Angle used to define real shaped tooth profile
ω	Radial frequency
ω_n	Radial natural frequency
ω_p	Radial frequency of tooth engagement
ω_s	Angular velocity of sprocket s
ω_t	Radial frequency of torsional vibration
$\varpi(z)$	A periodic excitation function

Chapter 1
Introduction

1.1 Background

The background for this thesis is some observations that the company MAN B&W Diesel A/S has made from roller chain drives in some of their marine diesel engines. The company MAN B&W Diesel A/S manufactures large marine diesel engines and these engines has for many years used roller chain drives to drive the camshaft by a chain connection from the crankshaft to the camshaft see Figures 1.1 and 1.2. Other methods as e.g. hydraulic lifting of the valves are presently, and the development is towards electronically controlled engines, but chain driven camshaft engines will still be produced and maintained for many years.

The roller chains on these engines are very large, some has more than 100 links and each link may have a mass of a couple of kilos. The chain drive is standard in marine engines with between 4 and 12 cylinders for a power range of 1760 to 78000 kW. The roller chain is somewhat similar to a bicycle chain in the way it looks, but far from the same size.

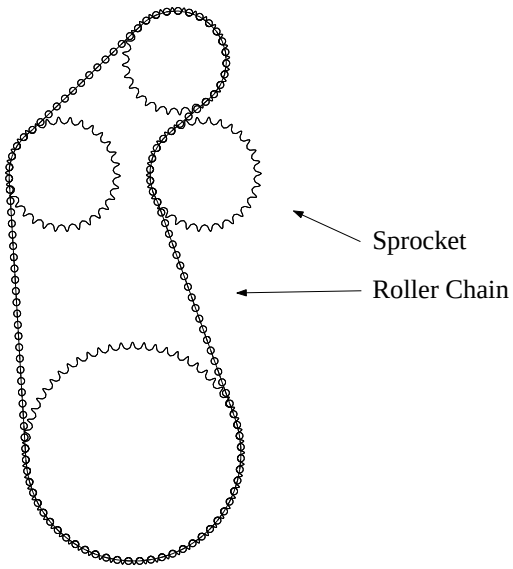

Figure 1.1: A roller chain drive system with 4 sprockets

While the engine is running the roller chain wears and because of this it extends. The chain therefore has to be tightened, frequently as it gradually extends, in order for the chain to be functional. To avoid the manual tightening of the chain, automatic chain tighteners are introduced on some of the engines. In some occasions this has caused vibration patterns of the chain and chain tightener and these vibrations were not immediately explicable. One could fear that it would cause fatigue, wear or damage in the chain and lead to a break of the chain.

Several researchers have studied the roller chain problem using various approaches e.g. Wang and Liu (1991a), Kim and Johnson (1993), Pfeiffer (1995), Pfeiffer et al. (1997), Veikos and Freudenstein (1992*a*), Veikos and Freudenstein (1992*b*), Mahalingam (1958), Bouillon and Tordion (1965), Choi and Johnson (1993*a*), Conwell and Johnson (1995), Fritz and Pfeiffer (1995), Troedson and Vedmar (1999) and Troedson and Vedmar (2001). In these studies it is pointed out that several phenomena occur in a roller chain drive. One of these phenomena is the so called polygonal effect, which occurs due to the fact that links engage and disengage on sprockets, and then the length of the coupling segment between two sprockets changes. This effect together with the impact of rollers with the sprockets is responsible for the noise and vibration of the roller chain.

The scientific basis for analysis of the large chain drive systems used in the marine engines is however not deep enough, since the prior investigations has been done with a focus on smaller chains in high speed chain drives, such as used in some car engines. The size of the chain makes the system more stiff than the smaller chain drive systems and the computation has to be made with a focus on minimizing the simulation time. The tightener systems and guide-bars in the chain drive system used in the marine diesel engine are also somewhat different from those used in e.g. some car engines. Therefore, a specific model of the marine engine chain drive is of interest.

Examination of the dynamic phenomena in these very large roller chain drives is not only of the interest for the company MAN B&W Diesel A/S. Because roller chain drives also are used in a variety of other machines, roller chain drive dynamics in general is an important area. When these dynamic phenomena are analysed it is important to investigate modifications to the system in order to remove the unwanted phenomena. These modifications are much less expensive (money and time wise) to investigate using a properly

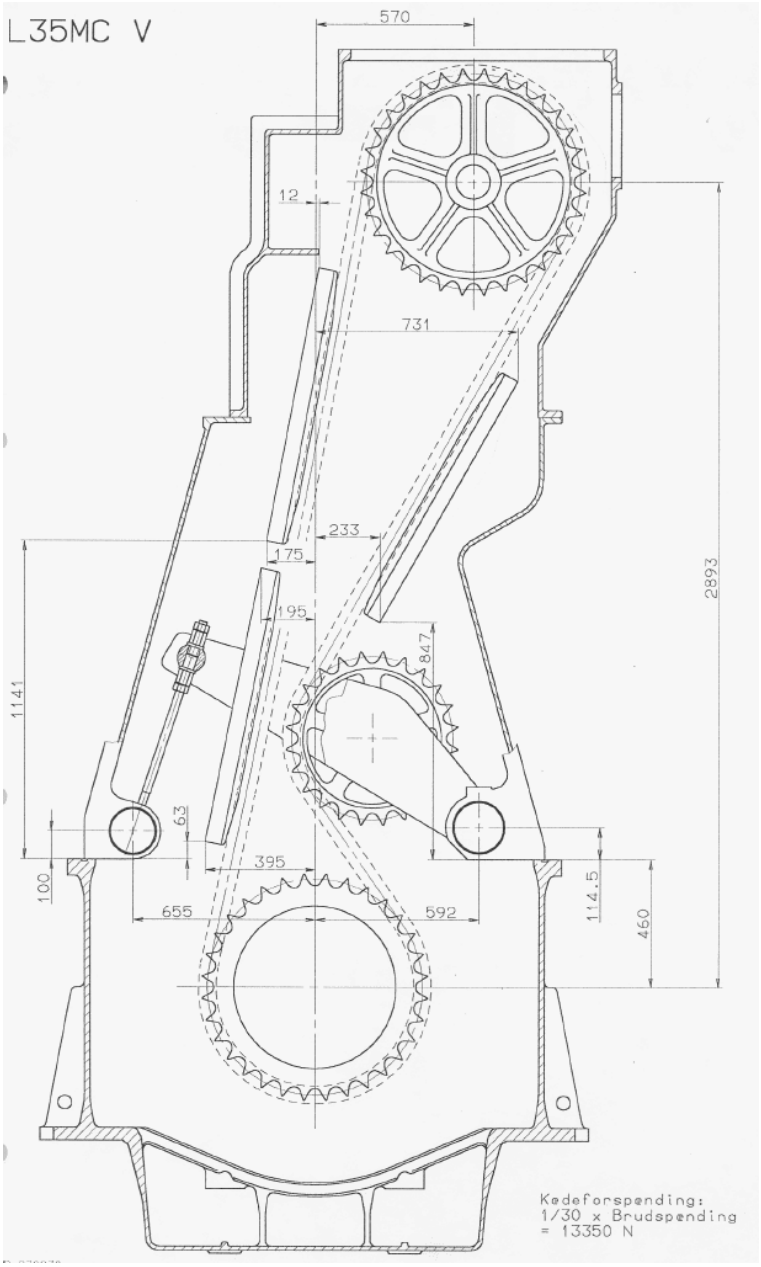

Figure 1.2: Blueprint of a L35MC Engine (from MAN B&W Diesel A/S)

validated computer program, than performing physical experiments.

To analyse the dynamic behaviour the roller chain drives a simulation program is developed. The simulation program is developed from fundamental mechanics and calculates the position, velocity and acceleration of the rollers. The reaction forces on the rollers

due to e.g. the rollers being seated on the sprockets are also calculated.

1.2 Roller Chain Drive Systems

Roller chain drives are used for many different purposes and the size of the chains and sprockets vary, from e.g. being used on bicycles to e.g. being used in large marine diesel engines, see Figure 1.3.

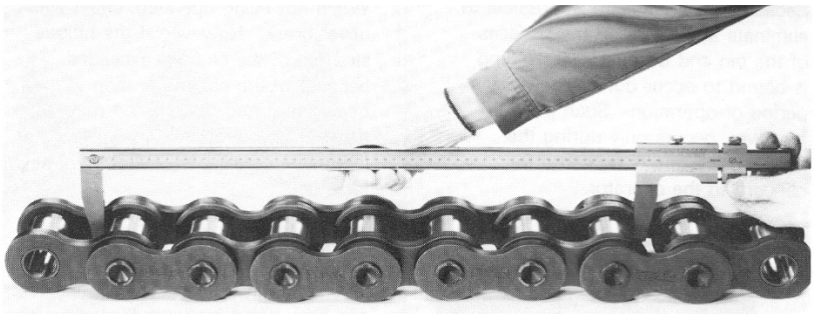

Figure 1.3: The size of the roller chain used in marine engines.

The dynamics of the roller chain drives is characterized by a complex behaviour with impacts between the chain links and sprockets and by discontinuities in the system components velocities giving rise to transversal and longitudinal vibrations on the spans of the chain. These events are the responsible factors for part of the noise presented by mechanical devices that use roller chains and ultimately by the wear of the roller chain drives. Though roller chains have been used for a long time as a reliable mechanical component to transmit power and to handle materials mechanically, only in the last decades their dynamical behaviour is studied, see e.g. Wang and Liu (1991a). The main reason for this situation is that their dynamics is very complex, making it impossible to find general analytical procedures able to describe thoroughly the problem.

With the development of fast computers some recent efforts have been put forward in order to better understand different aspects of these mechanical components, see e.g. Veikos and Freudenstein (1992*a*). In a review of the state-of-art Wang and Liu (1991a) summarized many of the investigations that have been carried out and state that integrated models describing the full dynamics of the system are necessary, in order to accurately describe

the interrelation between the different elements in the chain drive system.

The major difficulties in the study of the roller chain drives are related with the way that the roller chain wraps around the sprockets, forming a polygon. This effect, called the polygonal action, together with the impact between rollers and sprockets participates in the creation of the noise and vibration on the roller chain drive. The influence on the system dynamics of the impulsive forces that act on the rollers and sprockets at the moment of their engagement, and which results in a discontinuity of the roller velocity, has been the subject of different investigations by Turnbull and Fawcett (1972), and Chew (1985).

The combined action of the polygonal effect and the roller impact leads to the development of longitudinal and transverse vibrations on the chain strands in which the flexibility of the links plays an important role. Veikos and Freudenstein (1992*a*) proposed a discrete model, which takes into account the polygonal action. The driving span of the chain is modelled by lumped masses connected by linear springs and considers the coupling between the longitudinal and transversal vibrations and the moving boundary conditions. However, the effect of chain guides in the drive and the angular speed fluctuation of the driving sprocket are not considered.

Fritz and Pfeiffer (1995) present a methodology where the roller-sprocket and the guide-chain contacts are treated as unilateral constraints. In this study an integrated model describing the complex dynamics of the roller chain drive including chain guides and moving sprockets is proposed. Of the most resent work can be mentioned Troedson and Vedmar (1999) and Troedson and Vedmar (2001), that present a model using an iteratively force equilibrium method including the standard geometry of the sprockets.

In the present study different models of contact between the rollers and sprockets are proposed and two of them are compared with analytical results, for simplified models, see Binder (1956). The roller chain drive model has one driving sprocket and one or more driven sprockets. The complete chain is modelled by lumped masses connected by spring-damper uniaxial elements. The methodology proposed for the roller-sprocket contacts is penalty forces, which use the continuous force model proposed by Lankarani and Nikravesh (1994). Through the application of this, it is shown that the roller-chain drive interrelated dynamics of the elements in the chain drive system is captured and the contact problem is fully characterized. The model includes different parts, such as e.g. the chain tightener systems, out of balance wheels and guide-bars, from the marine

engine and can be used for different analysis of the system e.g. resonance investigations on the chain drive system with external excitations. However the necessary experimental validation is left for future studies.

1.3 Research Objective

The aim of the work presented in this thesis is to contribute with a novel theoretical basis for the analysis of chain drive systems, by posing and validating different mathematical models, and compare to prior research. Even though the model is developed at first for the use of analysing chain drive systems in marine engines, the methods can with small changes be used in general, as for e.g. chain drives in industrial machines, car engines and motorbikes. In the model several different parts that appear in the chain drive systems in the marine engines are included.

A numerical stable method is necessary in order for the simulation program to be used as a general purpose program, for roller chain calculations of different chain drive systems large as well as small. It is aimed to use as simple a model as possible that satisfies this demand. It is also important that the simulation time is minimized, because the method will often be used in design iterations. Next the model should be compared to experimental results in order to validate the method. Experimental results are not directly in hand and therefore the results are discussed with MAN B&W Diesel A/S and comparisons are made between different mathematical models.

The objective is to be able to analyse several dynamic phenomena of the chain drives system using the simulation program. These dynamic phenomena are e.g. the contact forces between the roller chain and the sprockets, the contact forces between the roller chain and the guide-bars, the vibration pattern of the free chain strands between the sprockets, the vibration pattern of the tightener system and resonances with the external excitation of the driving sprocket. If possible it should be explained why the hydraulic tightener system and chain in some occasions vibrates in patterns which has not earlier been immediately explicable. The force with which the chain affects the guide-bars is also of interest, due to the fact that if the rubber of the guide-bars breaks it will cause damage on the sprockets as well. In the future perspective the objective is to be able to suggest design changes of the chain drive system, based on the simulation results.

1.4 Multibody Dynamics

The modelling of the chain drive system is based on the use of Multibody Dynamics analysis tools. Multibody Dynamics is the field of computer-aided analysis of mechanical systems and is well presented in several books e.g. Nikravesh (1988), Hansen and Nikravesh (1998), García de Jalón and Bayo (1994) and Haug (1989). In Schiehlen (1997) a review on the roots and perspectives of Multibody Dynamics is presented and the large amount of different applications to mechanical systems is described.

In this thesis the Lagrangian formulation of the equations of motion using 2D Cartesian coordinates are used, see e.g. Nikravesh (1988). Several other methods exist, but this method is chosen because it is simple to develop a general-purpose program, and it is aimed that the chain drive program developed is general in the sense of being used on different chain drive systems. The derivation of the equations of motion is simple with this formulation and the order of non-linearity is low. The method has the disadvantage of introducing a larger amount of coordinates, compared to other formulations, however an advantage is the implementation of the forces which is straight forward and computational efficient.

1.5 Contact and Friction

When two bodies collide, impact forces and a sudden change in the velocities occur. Collision between bodies appears in many different multibody systems, e.g. bodies connected with clearance joints and bodies that experience hard stops. The applications of contact models to practical problems are wide, e.g. vibration conveyors, chimney dampers and chains, Pfeiffer (1999), in machines with clearance joints, Dubowsky and Freudenstein (1971*a*), Dubowsky and Freudenstein (1971*b*) and in train crash worthiness Milho et al. (2002). Contact between bodies may change its state from attached to detached, from sliding to stiction, and vice versa. These different states may be described in various ways, see e.g. Pfeiffer and Glocker (1996).

One way to describe the connection between the bodies is by applying or deleting kinematic constraints when the bodies respectively attach or detach. When impact occur it is assumed that the impact force acts over an infinitesimal period of time and the jump discontinuity in velocities is possible to compute. Using this method and including friction, the friction force is, for the case of sliding, iteratively calculated and applied to the system equations of motion. When the contact state changes to stiction an extra constraint is

applied to the system equations of motion, which locks the given motion. This constraint is removed when the state changes again from stiction to sliding, see García de Jalón and Bayo (1994).

A different way of describing contact with bodies is to treat the local deformations and contact forces as continuous and in contrast to the discontinuous method the velocities are here continuous. When two bodies gets in contact a continuous contact force is applied perpendicular to the contact surface and this contact force is included in the system equations of motion during the contact period, see Lankarani and Nikravesh (1994), Ambrósio and Hansen (1995), Ravn (1998), Ambrósio (2003). The contact force is known during the whole period of contact and is easy to mix with rigid body analysis methods. The method requires a more flexible numerical integration scheme than the rigid body system and very small time steps are necessary.

In this thesis the modelling of contact between the chain links and the sprockets or the guide-bars is done using the continuous contact force formulation based on a Hertzian contact force formulation, see Goldsmith (1960), Hunt and Crossley (1975), Dubowsky and Freudenstein (1971*a*), Dubowsky and Freudenstein (1971*b*). The contact model is extended to include a damping term as proposed in Lankarani and Nikravesh (1990) and Lankarani and Nikravesh (1994), whereby energy dissipation is accounted for.

The roller chain drive system is at all times lubricated, which reduces the friction, but friction will always be present. This friction is modelled by a Coulomb, or dry modelling of friction, which is included in the continuous contact force model, see e.g. García de Jalón and Bayo (1994), Haug et al. (1986), Bagci (1975). The model of Coulomb friction is used to describe friction between non-lubricated contact surfaces. The friction force dependency on the relative velocity is modified from the standard dependency in order to avoid the discontinuity at zero, see Threlfall (1978), Rooney and Deravi (1982), Ambrósio (2003), Flores et al. (2003). This modification is done by introducing a continuous dependency. By including friction an additional energy dissipative effect is accounted for.

1.6 Contents of this Thesis

In chapter 2 some general mathematical tools and definitions are given. The chapter is a presentation of some tools of multibody systems dynamics in 2D. The general equations of motion for rigid bodies and the Multibody Dynamics analysis tools in 2D including the

Lagrange Multiplier Method are given.

In chapter 3 the chain drive system is modelled and the governing equations of motion for the system are presented. The polygonal action is described and rotational damping in the link joints is included and described. Various investigated contacts models are described and discussed. A kinematic constraint method is shortly described, whereas a continuous contact forces method based on Hertz contact force is described more thoroughly. Related to the continuous contact force method different models of the shape of contact surfaces of the sprocket teeth are presented. How the different parts in the marine diesel engine are modelled and a friction model is presented at the end of the chapter.

Chapter 4 is on the numerical simulation procedure, the simulation conditions and assumptions. Some simplified analytical results for the link forces and contact forces taken from Binder (1956), analytical results for eigenfrequency analysis of the chain strands between the sprocket taken from Mahalingam (1957) and Naguleswaran and Williams (1968) and analytical results for the eigenfrequencies of the chain drive system are given.

Based on the different models and methods described in chapter 3 and chapter 4 a simulation program is developed. Two of the different ways of modelling the contact between the rollers and sprockets are compared with analytical results in chapter 5. The influence of inclusion of friction and inclusion of rotational damping on the links is presented in chapter 5. The methodologies are applied to the simulation of different chain drive systems used in marine diesel engines, and inclusion of the different parts are analysed. A resonance analysis is presented and compared with analytical results of the eigenfrequencies of the chain segments. In the last part of the chapter some experimental ways of validating the computer program, which will be done by MAN B&W Diesel A/S in the near future, are listed.

Chapter 2
General Tools and Definitions used in this Thesis

2.1 Introduction

In this chapter some general tools and definitions are given. Throughout this thesis the mathematical formulation is done in 2D and the mathematical tools and notation presented are therefore concentrated on 2D.

The general equations of motion for rigid bodies are given with the formulation for multi-body systems. The basic concepts needed to simulate a mechanical system of rigid bodies connected by joints are shown and the Lagrange Multiplier Method is presented.

2.2 Mathematical Tools

2.2.1 The Notation used in this Thesis

All matrices are written in capital with boldface, e.g. matrix $\mathbf{A}$. All vectors are written in small letters with boldface, e.g. vector $\mathbf{a}$. A vector with ' as superscript on the right side indicates that the vector is given in a local coordinate system, e.g. local vector $\mathbf{a}'$. The derivative of a quantity a with respect to time is denoted $\dot{a}$ and the second derivative of a quantity a with respect to time is denoted $\ddot{a}$ yielding

$$\dot{a} := \frac{da}{dt}, \quad \ddot{a} := \frac{d^2a}{dt^2} \tag{2.1}$$

2.2.2 Vector Notations

From a 2D vector $\mathbf{a}$ we can construct a vector $\hat{\mathbf{a}}$ called the hat vector of $\mathbf{a}$, and vector $\hat{\mathbf{a}}$ is perpendicular to vector $\mathbf{a}$ in the counter clockwise direction. If vector $\mathbf{a}$ is given by

$$\mathbf{a} = \left\{ \begin{array}{c} a_1 \\ a_2 \end{array} \right\} \tag{2.2}$$

then vector $\hat{\mathbf{a}}$ is given by

$$\hat{\mathbf{a}} = \begin{Bmatrix} -a_2 \\ a_1 \end{Bmatrix} \tag{2.3}$$

The first derivative of vector $\mathbf{a}$ with respect to time is written $\dot{\mathbf{a}}$ and the second derivative of vector $\mathbf{a}$ with respect to time is written $\ddot{\mathbf{a}}$. The transposed of a vector is denoted $\mathbf{a^T}$. The length of vector $\mathbf{a}$ (or the 2-norm) is denoted $\|\mathbf{a}\|$ and is given by

$$\|\mathbf{a}\| = (\mathbf{a}^T\mathbf{a})^{1/2} = \sqrt{a_1^2 + a_2^2} \tag{2.4}$$

2.2.3 Transformation Matrix

In 2D the transformation matrix $\mathbf{A}$ is given by the angle of rotation θ

$$\mathbf{A} = \begin{bmatrix} \cos\theta & -\sin\theta \\ \sin\theta & \cos\theta \end{bmatrix} \tag{2.5}$$

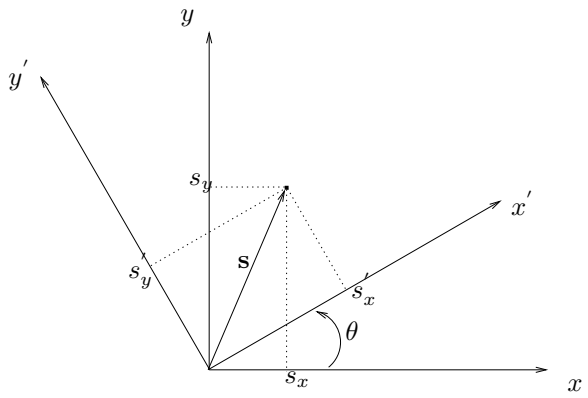

Figure 2.1: Reference frames (x, y) and $(x^{'}, y^{'})$.

The vector $\mathbf{s}$ is in the $(x^{'}, y^{'})$-coordinate system given by vector $\mathbf{s} = \{s_x^{'}, s_y^{'}\}^{'T}$, where the prime indicates local coordinate system as used in Nikravesh (1988) and in the (x, y)-coordinate system given by vector $\mathbf{s} = \{s_x, s_y\}^T$. The transformation of the vector $\mathbf{s}^{'}$ to the vector $\mathbf{s}$ is given by

$$\mathbf{s} = \mathbf{A}\mathbf{s}^{'} \tag{2.6}$$

For the transformation matrix we have $\mathbf{A}^{-1} = \mathbf{A}^T$ due to orthogonality. (In 3D the rotation of a body can be described using Euler angles, Bryant angles or Rodriges parameters. The most common used method is the Euler angles, see e.g. Nikravesh (1988).)

2.3 General Equations of Motion for Rigid Bodies

In Figure 2.2 is shown a body in 2D with the mass m_i and the mass moment of inertia to the ζ_i-axis J. The body is exposed to an external force $\mathbf{f}$ and an external moment τ. The (ξ_i, η_i)-coordinate system is the body-fixed/local coordinate system. The local coordinate system is placed at the centre of mass of the body. The (x, y)-coordinate system is the inertial/global coordinate system.

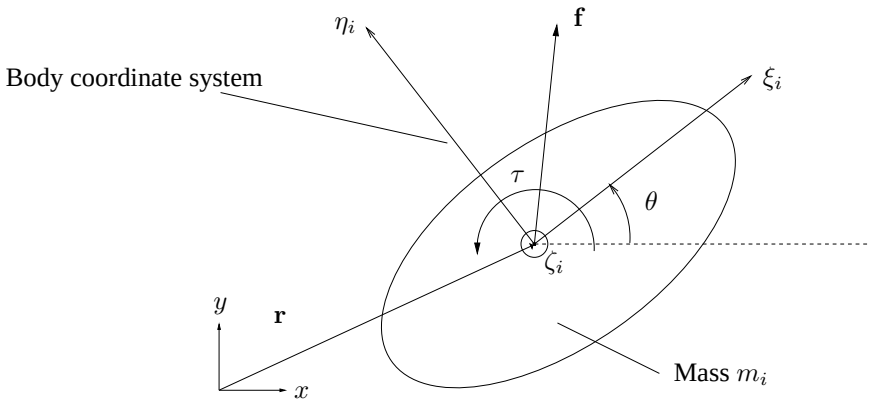

Figure 2.2: A rigid body in 2D exposed to an external force $\mathbf{f}$ and an external moment τ, with the body-fixed coordinate system placed at the centre of mass.

The equation of motion is for the case of the body-fixed coordinate system placed at the centre of mass given by

$$\begin{bmatrix} m_i\mathbf{I} & \mathbf{0} \\ \mathbf{0} & J \end{bmatrix} \begin{Bmatrix} \ddot{\mathbf{r}} \\ \dot{\omega} \end{Bmatrix} = \begin{Bmatrix} \mathbf{f} \\ \tau \end{Bmatrix} \tag{2.7}$$

where $\mathbf{I}$ is the identity matrix of order two and $\mathbf{r}$ is the vector from the inertial coordinate system to the centre of mass. The angular velocity is $\omega = \dot{\theta}$ and the angular acceleration is $\dot{\omega} = \ddot{\theta}$. The equation of motion for the case of the body-fixed coordinate system not placed at the centre of mass as shown in Figure 2.3 is given by

$$\begin{bmatrix} m\mathbf{I} & m\hat{\boldsymbol{\rho}} \\ m\hat{\boldsymbol{\rho}}^T & J + m \parallel \boldsymbol{\rho} \parallel^2 \end{bmatrix} \begin{Bmatrix} \ddot{\mathbf{r}} \\ \dot{\omega} \end{Bmatrix} = \begin{Bmatrix} \mathbf{f} + \omega^2 m\boldsymbol{\rho} \\ \tau \end{Bmatrix} \tag{2.8}$$

where $\boldsymbol{\rho}$ is the vector from the origin of the body-fixed coordinate system to the centre of mass, vector $\hat{\boldsymbol{\rho}}$ is the hat vector of $\boldsymbol{\rho}$ and $\parallel \boldsymbol{\rho} \parallel$ is the length of the vector. The vector $\mathbf{r}$ is the vector from the inertial coordinate system to the origin of the body-fixed coordinate system. The force $\mathbf{f}$ and moment τ are described with respect to the body-fixed coordinate

system. The mass moment of inertia $J + m \parallel \boldsymbol{\rho} \parallel^2$ about the origin of the body-fixed coordinate system is calculated using Steiner's theorem.

Writing (2.8) in a compact form, we use a generalised mass matrix $\mathbf{M}$ that includes both the mass and the mass moment of inertia we have

$$\mathbf{M}\ddot{\mathbf{q}} = \mathbf{g} \tag{2.9}$$

where $\mathbf{q} = \{\mathbf{r}^T, \theta\}^T = \{x, y, \theta\}^T$ is the position vector and $\mathbf{g} = \{\mathbf{f}^T, \tau\}^T = \{f_x, f_y, \tau\}^T$ is the generalised force vector.

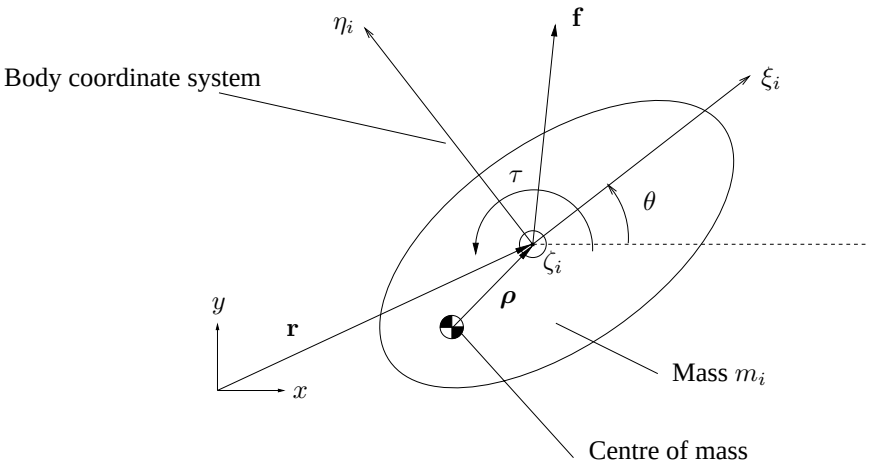

Figure 2.3: A rigid body in 2D exposed to an external force $\mathbf{f}$ and an external moment τ, with the body-fixed coordinate system not placed at the centre of mass.

2.4 Multibody System Dynamics Analysis Tools

A multibody system is an assembly of a number of bodies connected to each other by a number of kinematic joints. A joint permits certain degrees of freedom of relative motion and restricts others. In planar/2D multibody system kinematics (or dynamics), the most used joints are revolute and translational, which respectively allows one relative rotation and one relative translation. In 3D multibody system kinematics (or dynamics) e.g. cylindrical, spherical, universal joints and others are also used. For the case of a body having all degrees of freedom (position and orientation) fixed the body is a grounded body.

Kinematic constraint equations for the planar revolute joint are given by

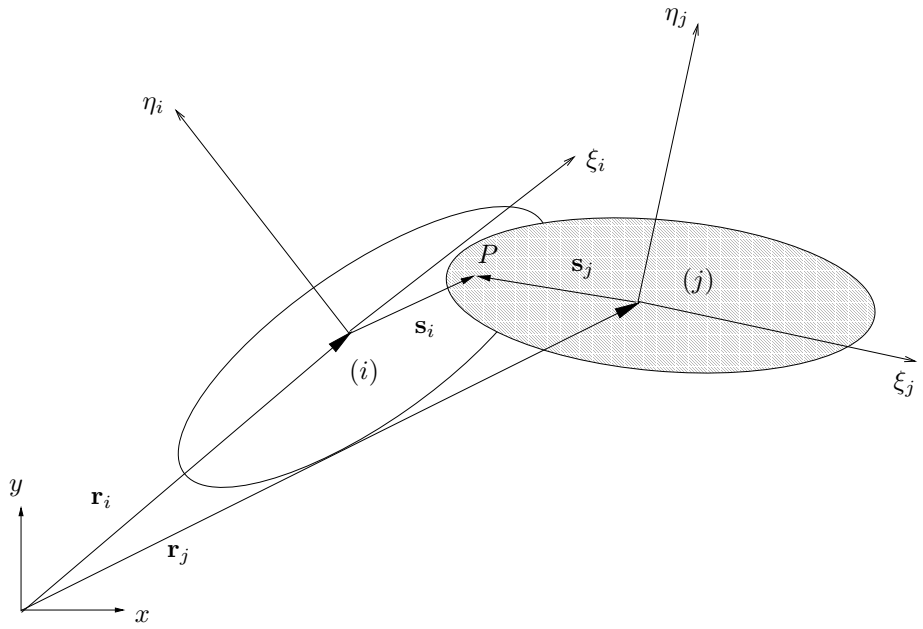

Figure 2.4: Two rigid bodies connected by a revolute joint.

$$\boldsymbol{\phi}^{(r)} = \mathbf{r}_i + \mathbf{s}_i - \mathbf{r}_j - \mathbf{s}_j = \mathbf{0} \tag{2.10}$$

where the vectors $\mathbf{r}_i$ and $\mathbf{r}_j$ are the vectors from the inertial coordinate system to the origin of the body-fixed coordinate systems of body i and body j, respectively. The vector $\mathbf{s}_i$ is the vector to point P on body i, given relative to the body fixed reference frame on body i. The vector $\mathbf{s}_j$ is the vector to point P on body j, given relative to the body fixed reference frame on body j. The two constraint equations in (2.10) forces the point P on body i two be coincident with point P on body j, see Figure 2.4.

For the planar translational joint the kinematic constraint equations $\boldsymbol{\phi}^{(t)} = \{\phi_1^{(t)}, \phi_2^{(t)}\}^T$ are given by

$$\begin{aligned} \phi_1^{(t)} &= \mathbf{d}_{i1}^T \mathbf{d}_{i2} = 0 \\ \phi_2^{(t)} &= \theta_i - \theta_j - (\theta_i^0 - \theta_j^0) = 0 \end{aligned} \tag{2.11}$$

with the vector $\mathbf{d}_{i1} = \{x_i^P - x_i^R, y_i^P - y_i^R\}^T$ and vector $\mathbf{d}_{i2} = \{x_j^P - x_i^P, y_j^P - y_i^P\}^T$. The vector from the inertial coordinate system to point P_i on body i is $\mathbf{r}_i^P = \{x_i^P, y_i^P\}^T$, to point P_j on body j it is $\mathbf{r}_j^P = \{x_j^P, y_j^P\}^T$, to point Q_i on body i it is $\mathbf{r}_i^Q = \{x_i^Q, y_i^Q\}^T$ and to point R_i on body i it is $\mathbf{r}_i^R = \{x_i^R, y_i^R\}^T$. The angles θ_i and θ_j are the rotational

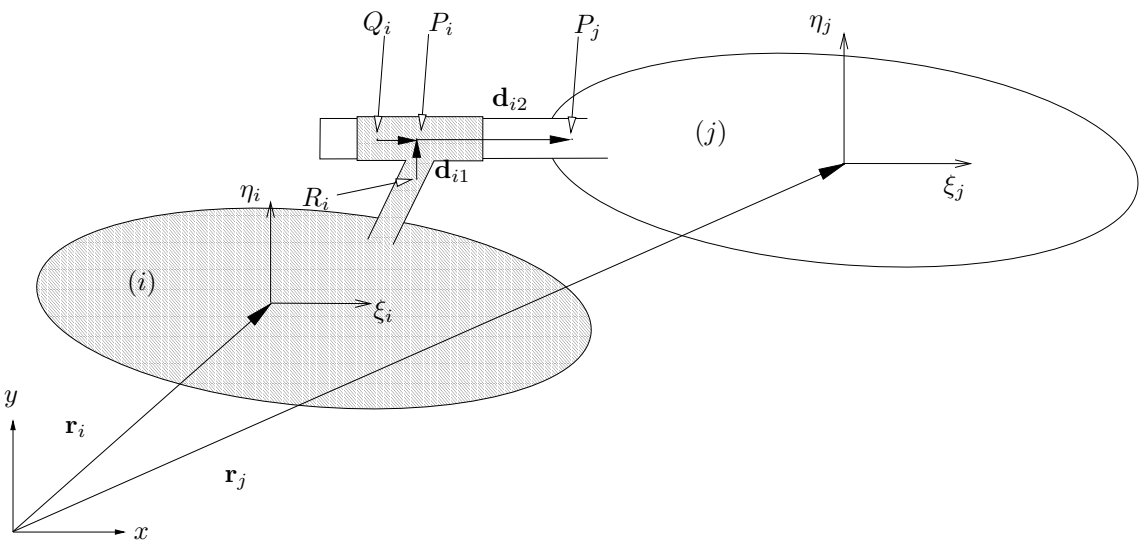

Figure 2.5: Two rigid bodies connected by a translational joint

angles of the two bodies and θ_i^0 and θ_j^0 are the initial rotational angles. The two constraints respectively forces the vector $\mathbf{d}_{i1}$ to be perpendicular to vector $\mathbf{d}_{i2}$ and forces the relative angle between the two bodies to be zero, see Figure 2.5.

For both 2D and 3D we can create our own joints depending on the mechanism we want to simulate. All the constraint equations from the joints in the multibody system are collected in on constraint vector, which during a simulation should be equal to zero. In general the constraint vector is

$$\boldsymbol{\phi}(\mathbf{q}, \dot{\mathbf{q}}, \ddot{\mathbf{q}}, t) = \mathbf{0} \tag{2.12}$$

where t is the time and $\mathbf{q}$ is a vector of the Cartesian coordinates for the multibody system given by

$$\mathbf{q}^T = (x_1, y_1, \theta_1, \ldots, x_n, y_n, \theta_n) \tag{2.13}$$

The number of bodies in the multibody system is n. The number of degrees of freedom (DOF) of the multibody system is equal to the number of coordinates minus the number of constraints. When $DOF = 0$ we have a kinematic determined system and we can simulate the system using Kinematic Analysis. When $DOF \geqq 0$ we can simulate the system using Dynamic Analysis.

Using the Lagrange Multiplier Method, see e.g. Nikravesh (1988), Hansen and Nikravesh

(1998) and Haug (1989), we have the equations of motion of the system using Cartesian coordinates given by

$$\mathbf{M}\ddot{\mathbf{q}} + \mathbf{\Phi}\boldsymbol{\lambda} = \mathbf{g_e} \tag{2.14}$$

where $\mathbf{\Phi}$ is the Jacobian matrix, $\frac{\partial \phi}{\partial \mathbf{q}}$, $\boldsymbol{\lambda}$ is the vector of Lagrange Multipliers, $\mathbf{g_e}$ is the generalised external forces. The vector of generalised forces is $\mathbf{g}$ and it is given by

$$\mathbf{g} = \mathbf{g_e} - \mathbf{\Phi}\boldsymbol{\lambda} \tag{2.15}$$

The equations of motion (2.14) and the constraint equations (2.12) together is a system of differential algebraic equations (DAE), as

$$\begin{aligned} \mathbf{M}\ddot{\mathbf{q}} + \mathbf{\Phi}\boldsymbol{\lambda} &= \mathbf{g_e} \\ \boldsymbol{\phi} &= \mathbf{0} \end{aligned} \tag{2.16}$$

Equation (2.16) can be solved using numerical integration methods for DAE's, such as Implicit Runge-Kutta and Backwards Difference Formulae, see e.g. García de Jalón and Bayo (1994).

If the constraint equations do not depend on the velocities and accelerations, the second derivative of constraint i with respect to time becomes

$$\phi_i^T \ddot{\mathbf{q}} = \boldsymbol{\gamma}_i \tag{2.17}$$

If the constraint depends on the velocity the constraint is only differentiated once and if it also depends on the acceleration the constraint is not differentiated. The right hand side $\boldsymbol{\gamma}_i$ consists of all the elements not dependent on the accelerations. In Equation (2.17) we have the second derivative of one constraint with respect to time, collecting the second derivatives of all the constraints we get

$$\mathbf{\Phi}^T \ddot{\mathbf{q}} = \boldsymbol{\gamma} \tag{2.18}$$

where $\mathbf{\Phi}$ is the Jacobian matrix. The set of equations in (2.18) and the equations of motion (2.14) is a system of ordinary differential equations (ODE), put together as

$$\begin{bmatrix} \mathbf{M} & \mathbf{\Phi}^T \\ \mathbf{\Phi} & \mathbf{0} \end{bmatrix} \begin{Bmatrix} \ddot{\mathbf{q}} \\ \boldsymbol{\lambda} \end{Bmatrix} = \begin{Bmatrix} \mathbf{g_e} \\ \boldsymbol{\gamma} \end{Bmatrix} \tag{2.19}$$

The set of equations (2.19) can be solved with numerical integration methods for ODE's such as Runge-Kutta, Gear-Method and others, see e.g. Iserles (1996) and Shampine and Gordon (1975).

When the ODE's in (2.19) are solved constraint violation may occur, because Equation (2.18) only represent the acceleration constraints. Due to numerical errors the solution can drift away from the constraint equations. The constraint violation may be avoided using stabilization methods, such as Baumgarte stabilization, see e.g. Nikravesh (1988) and García de Jalón and Bayo (1994). Another way of avoiding constraint violation is to use other formulations of the equations of motion. This could e.g. be using generalized coordinates where the constraint equations vanish, because only the differential equations of the independent coordinates are solved. A different method to be mentioned is the joint coordinate method, see Nikravesh (2001). This method has a low number of constraint equations or none at all. In García de Jalón and Bayo (1994) the natural coordinates formulation is introduced, which has a low number of coordinates.

Chapter 3
Model, Contact Formulations and Friction

3.1 Introduction

The first part of this section describes how the roller chain and sprockets are modelled in 2D and what the governing equations are. The contact between the roller chain and the sprockets can be modelled in different ways and some of these have been investigated. Starting out with a kinematic constraint method and ending with what has shown to be the most useful method, i.e., the continuous contact force method.

The numerical integration is sensitive to how the shape of the contact area is modelled in the continuous contact force method, here five different shapes of the tooth profile is described. A short discussion of other related models are given.

The models for the different parts that exist in the roller chain drive system in the marine diesel engine are described in section 3.8. In the contact between the rollers and sprockets a friction model has been included as described in section 3.9.

3.2 The Model

The roller-chain drive is modelled in 2D; that is the out-of-plane motion of the chain system is not considered. To model the roller-chain drive the various components are modelled as follows: the rollers as lumped masses, the links as springs and dampers and the sprockets as rigid bodies, as shown in Figure 3.1 and Figure 3.2. The roller-chain drive has one driving sprocket and one or more driven sprockets. The springs and dampers between the rollers are modelled with constant stiffness and damping coefficients.

In Figure 1.3 the actual links are shown, with alternating inner and outer links. The inner and outer links are assembled in pivots by bearing pins and bushes, see Figure 3.1(a).

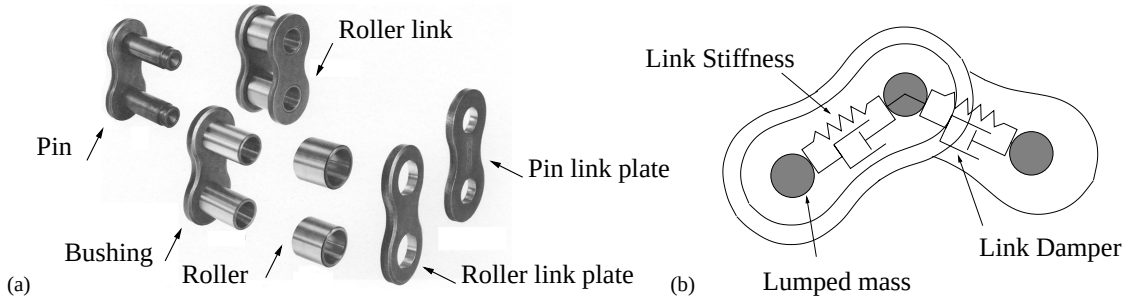

Figure 3.1: The roller links in (a) the reality (figure from Tsubaki (1991)) and (b) the simplified model.

3.2.1 Assumptions and Initializations

In the model clearances between the pin and bushing are neglected, as well as torsion and out-of-plane motion. The rotational inertia of the rollers about their center of gravity is neglected.

The initial positioning of the rollers is found by first calculating the points where the tangent lines between the sprockets touch the sprockets. These points however are not the points where the chain engages with the sprockets. The rollers are placed by assuming that roller number one is seated in one of these tangential points and then the rest of the rollers are placed from this position one by one with the given distance between the rollers. The sprockets are allowed to rotate both clockwise and counter clockwise, but the numbering of the sprockets and segments follows the rotational direction of the driver

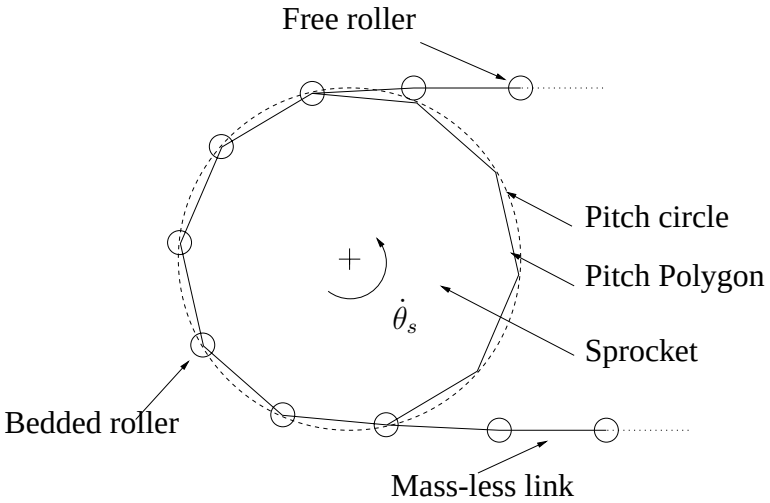

Figure 3.2: Chain engagement with sprocket in the simplified model

sprocket.

3.2.2 Equations of Motion

The rollers that are not seated on a sprocket are free particles in the plane and for each segment of free rollers the equations of motion are given by:

$$\begin{bmatrix} m_r & & & & \\ & m_r & & & \\ & & \ddots & & \\ & & & m_r & \\ & & & & m_r \end{bmatrix} \begin{Bmatrix} \ddot{x}_1 \\ \ddot{y}_1 \\ \vdots \\ \ddot{x}_{n_l} \\ \ddot{y}_{n_l} \end{Bmatrix} = \begin{Bmatrix} f_{x_1} \\ f_{y_1} - m_r g \\ \vdots \\ f_{x_{n_l}} \\ f_{y_{n_l}} - m_r g \end{Bmatrix} \tag{3.1}$$

where n_l is the number of links in the chain and m_r is the lumped mass, which is equal to the roller mass. Equation (3.1) written in compact form is with $\mathbf{I}$ as the identity matrix

$$m_r \mathbf{I} \ddot{\mathbf{q}}_r = \mathbf{f}_r \tag{3.2}$$

from which the definition of $\mathbf{f}_r$ and $\ddot{\mathbf{q}}_r$ follows. The global vector to the center of a roller r is denoted $\mathbf{r}_r$ and is given by $\mathbf{r}_r = \{x_r, y_r\}^T$. The coordinate system is chosen such that gravity acts on the roller chain in the negative y direction. The right hand side contains the forces between a roller and the two rollers next to it. The force f_{x_i} is the resultant force on roller i in the x direction. The force f_{y_i} is the resultant force on roller i in the y direction. The vectors between roller i and the two adjacent rollers are given by

$$\mathbf{l}_i = \mathbf{r}_i - \mathbf{r}_{i-1} \qquad \mathbf{l}_{i+1} = \mathbf{r}_{i+1} - \mathbf{r}_i \tag{3.3}$$

where $\mathbf{r}_i$, $\mathbf{r}_{i-1}$ and $\mathbf{r}_{i+1}$ are the global vectors to the three rollers, that is e.g. $\mathbf{r}_i^T = (x_i, y_i)$, see Figure 3.3. The length of the vectors are $l_i = \|\mathbf{l}_i\|$ and $l_{i+1} = \|\mathbf{l}_{i+1}\|$, also written as

$$\begin{aligned} l_i &= (\mathbf{l}_i^T \mathbf{l}_i)^{1/2} \\ l_{i+1} &= (\mathbf{l}_{i+1}^T \mathbf{l}_{i+1})^{1/2} \end{aligned} \tag{3.4}$$

The time rate change of the two vectors between roller i and the two adjacent rollers are denoted $\dot{\mathbf{l}}_i$ and $\dot{\mathbf{l}}_{i+1}$ and are given by

$$\dot{\mathbf{l}}_i = \dot{\mathbf{r}}_i - \dot{\mathbf{r}}_{i-1} \qquad \dot{\mathbf{l}}_{i+1} = \dot{\mathbf{r}}_{i+1} - \dot{\mathbf{r}}_i \tag{3.5}$$

The length of the vectors in (3.5) are given by

$$\begin{aligned} \dot{l}_i &= \frac{\mathbf{l}_i^T \dot{\mathbf{l}}_i}{l_i} \\ \dot{l}_{i+1} &= \frac{\mathbf{l}_{i+1}^T \dot{\mathbf{l}}_{i+1}}{l_{i+1}} \end{aligned} \tag{3.6}$$

The forces due to the flexibility of the links is on roller i, see Figure 3.3, $\mathbf{f}_i^T = (f_{x_i}, f_{x_i})$ given by

$$\begin{aligned} \mathbf{f}_i &= f_{i+1}\mathbf{u}_{i+1} - f_i\mathbf{u}_i \\ &= (K(l_{i+1} - P) + D\dot{l}_{i+1})\mathbf{u}_{i+1} - (K(l_i - P) + D\dot{l}_i)\mathbf{u}_i \end{aligned} \tag{3.7}$$

where K is the stiffness coefficient, D is the damping coefficient and P is the chain pitch i.e., the undeformed length between the centres of two adjacent rollers. The unit vectors $\mathbf{u}_i$ and $\mathbf{u}_{i+1}$ are given by $\mathbf{u}_i = \mathbf{l}_i/l_i$ and $\mathbf{u}_{i+1} = \mathbf{l}_{i+1}/l_{i+1}$.

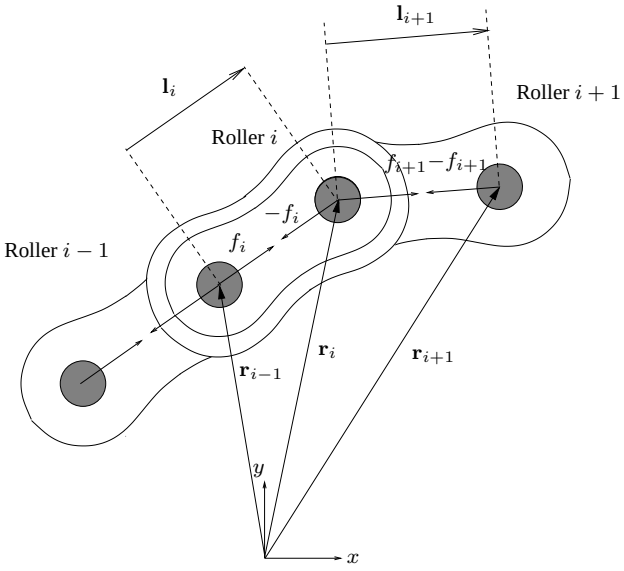

Figure 3.3: The link force between two adjacent rollers.

The equation of motion for each sprocket is given by

$$\begin{bmatrix} m_s & & \\ & m_s & \\ & & J_s \end{bmatrix} \begin{Bmatrix} \ddot{x}_s \\ \ddot{y}_s \\ \ddot{\theta}_s \end{Bmatrix} = \begin{Bmatrix} f_{x_s} \\ f_{y_s} \\ \tau_s \end{Bmatrix} \tag{3.8}$$

where J_s is the moment of inertia of the sprocket, m_s is the mass of the sprocket, $\ddot{\theta}_s$ is the angular acceleration of the sprocket and τ_s is an external applied torque. In compact form Equation (3.8) is written as

$$\mathbf{M}_s \ddot{\mathbf{q}}_s = \mathbf{g}_s \tag{3.9}$$

from which the definition of $\mathbf{M}_s$, $\ddot{\mathbf{q}}_s$ and $\mathbf{g}_s$ follows.

Each sprocket has an individual number of teeth n_t, radius R_s and pitch angle $\alpha = \frac{360^\circ}{n_t}$, see Figure 3.4. The local coordinate system (ξ_s, η_s) is placed in the center of the sprocket, with the ξ_s axis going through the lowest part of a tooth and it follows the sprocket when it rotates, i.e. it is a local coordinate system. The angle θ_s is the angle between the global x axis and the local ξ_s axis.

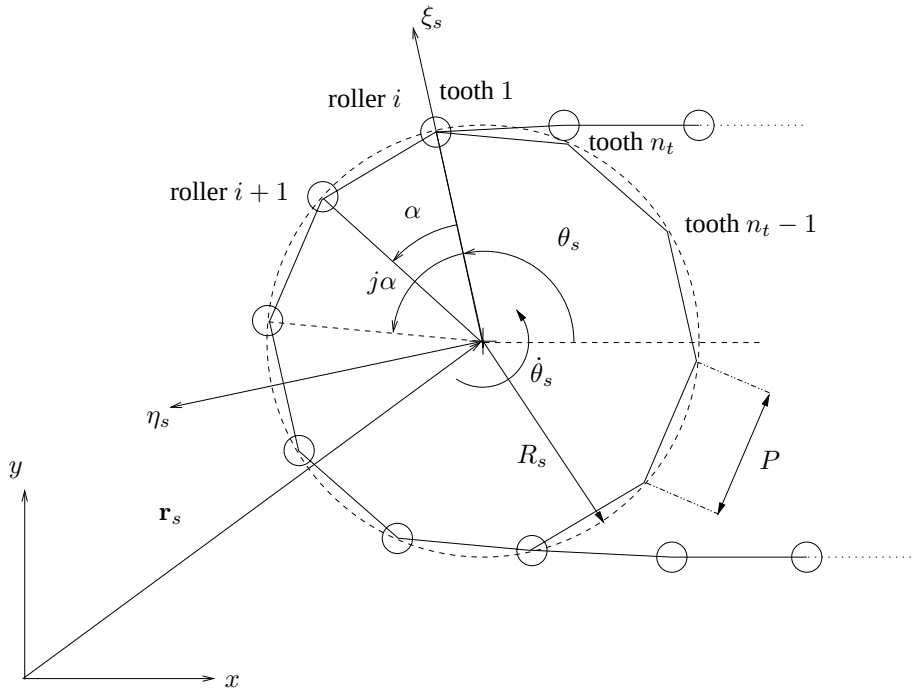

Figure 3.4: The model of a sprocket and its parameters.

In Figure 3.4 $\mathbf{r}_s = \{\ x_s,\ y_s\ \}$ is the coordinates of the center of the sprocket. The position and angle of the sprocket with respect to the global coordinate system is given by the vector $\mathbf{q}_s = \{\ x_s,\ y_s,\ \theta_s\ \}$. The angle index j is the sprocket tooth number minus one, see Figure 3.4. The index $j = 0, 1, \ldots, n_t - 1$ and the numbering of the teeth starts at the ξ_s axis and follows the direction of the rotation, see Figure 3.4.

3.3 Rotational Damping in the Link Joints

Rotational damping in the joints between the links is included in the model by adding forces to the rollers adjacent to the roller where the damping moment in the joint is to be applied. That is the rotational damping moment is replaced by two non-collinear force vectors of equal magnitude, also known as a couple, as proposed by Nikravesh (1988).

The vectors shown in Figure 3.5 are given in (3.3). The hatted vectors $\hat{\mathbf{l}}_i$ and $\hat{\mathbf{l}}_{i+1}$, are defined as the vectors perpendicular to respectively $\mathbf{l}_i$ and $\mathbf{l}_{i+1}$, rotated counter clockwise. The angle φ_i between two adjacent links is given by the relation

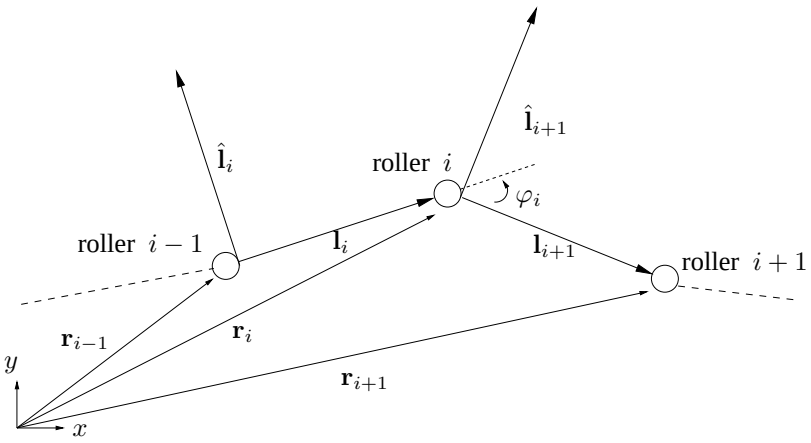

Figure 3.5: The vectors between three adjacent rollers and the relative angle between the links.

$$\mathbf{l}_i^T \mathbf{l}_{i+1} = l_i l_{i+1} \cos(\varphi_i) \tag{3.10}$$

where l_i is the length of the link between roller i and roller $i-1$ and l_{i+1} is the length of the link between roller i and roller $i+1$, given by (3.4). The time rate of the vectors between the rollers and their length are given in (3.5) and (3.6). Differentiating both sides of (3.10) with respect to time yields

$$\mathbf{l}_{i+1}^T \dot{\mathbf{l}}_i + \mathbf{l}_i^T \dot{\mathbf{l}}_{i+1} = -l_i l_{i+1} \sin(\varphi_i)\dot{\varphi}_i + (\dot{l}_i l_{i+1} + l_i \dot{l}_{i+1}) \cos(\varphi_i) \tag{3.11}$$

The derivative of the angle $\dot{\varphi}_i$ can be found by (3.11). This however, may give numerical problems as φ_i and thus $sin(\varphi_i)$ approach zero. The derivative of the angle $\dot{\varphi}_i$ can also be found by differentiating the relation given by

$$\hat{\mathbf{l}}_i^T \mathbf{l}_{i+1} = l_i l_{i+1} \cos(\frac{\pi}{2} + \varphi_i) = -l_i l_{i+1} \sin(\varphi_i) \tag{3.12}$$

Differentiating (3.12) with respect to time yields

$$\mathbf{l}_{i+1}^T\dot{\hat{\mathbf{l}}}_i + \hat{\mathbf{l}}_i^T\dot{\mathbf{l}}_{i+1} = -l_i l_{i+1}\cos(\varphi_i)\dot{\varphi}_i - (\dot{l}_i l_{i+1} + l_i\dot{l}_{i+1})\sin(\varphi_i) \tag{3.13}$$

If φ_i is close to zero Equation (3.13) should be used to compute $\dot{\varphi}_i$ and if φ_i is close to π Equation (3.11) should be used to compute $\dot{\varphi}_i$. By inserting (3.10) in (3.13), the equation for $\dot{\varphi}_i$ becomes

$$\dot{\varphi}_i = \frac{-1}{\mathbf{l}_i^T\mathbf{l}}_{i+1}(\mathbf{l}_{i+1}^T\dot{\hat{\mathbf{l}}}_i + \hat{\mathbf{l}}_i^T\dot{\mathbf{l}}_{i+1} - (\dot{l}_i l_{i+1} + l_i\dot{l}_{i+1})\sin(\varphi_i)) \tag{3.14}$$

where the angle φ_i between two adjacent links is found by

$$\tan(\varphi_i) = \frac{-\hat{\mathbf{l}}_i^T\mathbf{l}_{i+1}}{\mathbf{l}_i^T\mathbf{l}_{i+1}} \tag{3.15}$$

The rotational damping moment τ_l is given by

$$\tau_l = C_d\dot{\varphi}_i \tag{3.16}$$

where C_d is the coefficient of damping.

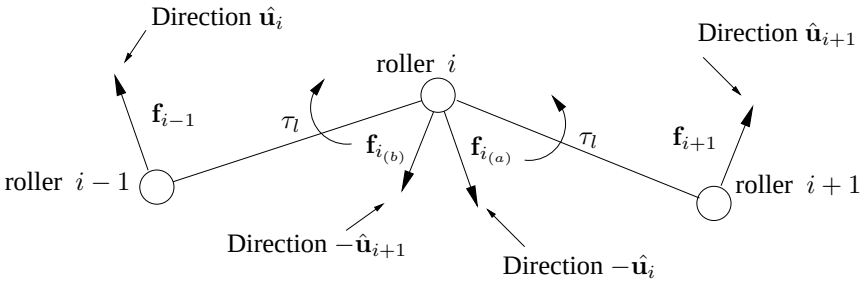

Figure 3.6: Rotational damping moment described by force couples.

The hatted unit vectors $\hat{\mathbf{u}}_i$ and $\hat{\mathbf{u}}_{i+1}$ in Figure 3.6, are defined as the vectors perpendicular to respectively $\mathbf{u}_i$ and $\mathbf{u}_{i+1}$, rotated in the counter clockwise direction. When $\dot{\varphi}_i > 0$, the moment of the damper acts on the link between roller i and roller $i+1$ in the positive rotational direction and on the link between roller i and roller $i-1$ in the negative rotational direction. When $\dot{\varphi}_i < 0$ the reverse situation occurs. The force couples of these two moments implies four forces, two with the magnitude τ_l/l_i and two with the magnitude τ_l/l_{i+1} and the directions as shown in Figure 3.6. The force vectors are given by

$$\begin{aligned} \mathbf{f}_{i_{(a)}} &= -\frac{C_d\dot{\varphi}_i}{l_i^2}\hat{\mathbf{l}}_i, & \mathbf{f}_{i_{(b)}} &= -\frac{C_d\dot{\varphi}_i}{l_{i+1}^2}\hat{\mathbf{l}}_{i+1} \\ \mathbf{f}_{i-1} &= \frac{C_d\dot{\varphi}_i}{l_i^2}\hat{\mathbf{l}}_i, & \mathbf{f}_{i+1} &= \frac{C_d\dot{\varphi}_i}{l_{i+1}^2}\hat{\mathbf{l}}_{i+1} \end{aligned} \tag{3.17}$$

3.4 Constraint Method

In the beginning of this project the first idea was to use a constraint method to model the contact between the rollers and sprockets. Even though this turned out not to be a useful model it is here shortly described, because it influenced the work done afterwards.

In the constraint method it is assumed that when the rollers are captured on the sprocket then the chain pitch is equal to the pitch of the sprocket. So chain wear and elongation during engagement is neglected i.e. it is assumed that the rollers that are seated on the sprocket forms a part of a polygon, see Figure 3.2. The tooth flexibility of the sprocket is neglected in the constraint method. In the continuous force method elongation during engagement is not neglected and the tooth flexibility is included.

When a roller is seated on sprocket s the kinematic constraints ensures that the roller is fixed to the pitch circle of the sprocket. The position coordinates of roller i are given by the vector $\mathbf{r}_i = \{\, x_i,\ y_i \,\}$, and then the constraint equations become (see Figure 3.4)

$$\phi_{s,i} = \left\{ \begin{array}{l} x_i - x_s - R_s\cos(\theta_s \pm j\alpha) \\ y_i - y_s - R_s\sin(\theta_s \pm j\alpha) \end{array} \right\} = \left\{ \begin{array}{l} 0 \\ 0 \end{array} \right\} \tag{3.18}$$

where the $\pm$ depends on the direction of rotation, $+$ when the sprocket rotates counter clockwise and $-$ when the sprocket rotates clockwise. By differentiating (3.18) once with respect to time we obtain

$$\mathbf{\Phi}_{s,i}\dot{\mathbf{q}}_{s,i} = 0 \tag{3.19}$$

By differentiating (3.18) twice with respect to time we obtain

$$\mathbf{\Phi}_{s,i}\ddot{\mathbf{q}}_{s,i} = \boldsymbol{\gamma}_{s,i} \tag{3.20}$$

The matrix $\mathbf{\Phi}_{s,i}$ is the Jacobian matrix related to the roller i and the sprocket s. The vectors $\dot{\mathbf{q}}_{s,i}$ and $\ddot{\mathbf{q}}_{s,i}$ are the velocity and acceleration respectively and $\boldsymbol{\gamma}_{s,i}$ is the right

hand side of the acceleration equation. The Jacobian matrix relating sprocket number s and roller number i is given by

$$\mathbf{\Phi}_{s,i} = \begin{bmatrix} 1 & 0 & -1 & 0 & R_s \sin(\theta_s \pm j\alpha) \\ 0 & 1 & 0 & -1 & -R_s \cos(\theta_s \pm j\alpha) \end{bmatrix} \tag{3.21}$$

this is a part of the total Jacobian matrix relating all the seated rollers on a sprocket. The part of the Jacobian matrix which is only related to roller i is denoted $\mathbf{\Phi}_i$ and is equal to the identity matrix $\mathbf{I}$ (first two columns in (3.21)). The position $\mathbf{q}_{s,i}$ vector is defined as

$$\mathbf{q}_{s,i} = \{ \quad x_i \quad y_i \quad x_s \quad y_s \quad \theta_s \}^T \tag{3.22}$$

The velocity vector is denoted $\dot{\mathbf{q}}_{s,i}$ and the acceleration vector is is denoted $\ddot{\mathbf{q}}_{s,i}$. They are given by differentiation of (3.22). The right hand side in (3.20) is given by

$$\boldsymbol{\gamma}_{s,i} = -R_s \begin{Bmatrix} \cos(\theta_s \pm j\alpha) \\ \sin(\theta_s \pm j\alpha) \end{Bmatrix} (\dot{\theta}_s)^2 = \begin{Bmatrix} C_j \\ -S_j \end{Bmatrix} (\dot{\theta}_s)^2 \tag{3.23}$$

where $C_j = -R_s \cos(\theta_s \pm j\alpha)$ and $S_j = R_s \sin(\theta_s \pm j\alpha)$. The reaction forces can be expressed as the negative transpose of the Jacobian matrix times a vector of Lagrangian Multipliers $\boldsymbol{\lambda}$ given by $\boldsymbol{\lambda} = \{ \lambda_1 \ \lambda_2 \ \ldots \ \lambda_{2 \cdot n_b} \}^T$, where n_b is the number of bedded rollers on the sprocket. Introducing the Lagrange Multiplier technique the equations of motion for a constrained sprocket and the rollers in contact with it is written in compact form given by

$$\begin{bmatrix} \mathbf{M}_s & \mathbf{0} & \mathbf{S}^T \\ \mathbf{0} & m_r\mathbf{I} & \mathbf{I} \\ \mathbf{S} & \mathbf{I} & \mathbf{0} \end{bmatrix} \begin{Bmatrix} \ddot{\mathbf{q}}_s \\ \ddot{\mathbf{q}}_r \\ \boldsymbol{\lambda} \end{Bmatrix} = \begin{Bmatrix} \mathbf{g}_s \\ \mathbf{f}_r \\ \boldsymbol{\gamma}_\mathbf{s} \end{Bmatrix} \tag{3.24}$$

where $\mathbf{I}$ is the identity matrix, $\mathbf{M}_s$ is the mass matrix consisting of the sprocket masses and mass moments of inertia in the diagonal. The matrix $\mathbf{S}$ is the part of the total Jacobian matrix related to the sprockets.

This formulation makes it possible to calculate the reaction forces on the rollers that are seated on the sprocket. The reaction force on the rollers in contact with the sprocket is given by

$$\mathbf{f}_r^r = -\mathbf{\Phi}_i \boldsymbol{\lambda} = -\mathbf{I}\boldsymbol{\lambda} = -\boldsymbol{\lambda} \tag{3.25}$$

When a roller position is detected to be inside the pitch circle of a sprocket the roller is captured and the kinematic constraint is applied. When the Lagrange multiplier coefficients have been calculated it is possible to calculate the reaction force of the sprocket on a bedded roller. This reaction force is equal to the resultant of the centrifugal force and the forces of the links acting on the roller. Whether a roller will leave the sprocket or not depends on the direction of the reaction force. When the direction of the reaction force is not contained inside a sector defined by two adjacent sides of the pitch polygon next to the candidate roller, then the roller will leave the sprocket. When a roller leaves a sprocket the corresponding kinematic constraint is removed from the equation of motion system. When the position of a roller is detected to be inside the pitch circle the roller is captured and the velocity of the roller is changed to be the tangential velocity of the sprocket.

In the constraint method it is for each reporting time step checked if a new roller is bedded to a sprocket or a roller is released from a sprocket. Only the first and the last bedded roller are allowed to be released from the sprocket and only the two rollers respectively before and after these two rollers are allowed to be bedded to a sprocket. When a new roller is either captured on or released from a sprocket the integration is restarted in order to prevent the time step size to decrease to a point where the computational cost of the simulation is too high.

Even though the velocities of the captured rollers are fitted to match the velocity of the sprocket the numerical integrator tries to adjust the time step size to this discontinuity and its size will in some cases decrease to a point where the computational cost of the simulation is very high. Furthermore the release and capture conditions used are not sufficient, because the results show a negative radial contact force, which implies that the roller should have been released earlier. The investigation of this kinematic constraint method can be found in Pedersen (2001).

3.5 Continuous Contact Force Method

As an alternative to the constraint method a continuous contact force method is proposed. In the continuous force method the contact between roller and sprocket is modelled by applying forces due to a pseudo penetration of the roller into the sprocket. All the rollers are free particles in the plane and their equations of motion given by (3.2), with the contact forces included on the right hand side in the force vector. In the continuous contact force method the bedded rollers will not be seated exactly on the pitch circle as in the constraint

method, because the model includes chain elongation during engagement.

In order to calculate the contact force due to the indentation there are different models suggested in the literature. In this project those suggested in Ambrósio and Hansen (1995), Ravn (1998), Dubowsky and Freudenstein (1971*a*) and Lankarani and Nikravesh (1990) are used.

The Kelvin-Voigt visco-elastic model is a simple contact force model. The relation between the indentation and the contact force is assumed linear. When the two bodies are separating from each other the energy loss is included in the contact force. This is done by multiplying the rebound force with a coefficient of restitution e. The coefficient of restitution is a constant $0 \leq e \leq 1$, where e = 0 relates to a fully plastic contact and e = 1 relates to a fully elastic contact.

The contact force vector $\mathbf{f}_c$ has the magnitude f_c calculated by

$$f_c = \begin{cases} K_g\delta & v > 0 \\ eK_g\delta & v < 0 \end{cases} \tag{3.26}$$

where K_g is a stiffness coefficient and v is the relative speed between the two bodies. The relative speed is positive when the two bodies are approaching each other and negative when they separate from each other. Figure 3.7 shows the energy loss as the hatched area.

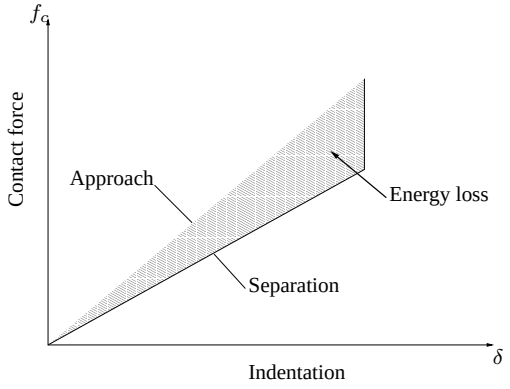

Figure 3.7: The energy loss in the linear model

The non-linear contact law known as the Hertz force-displacement law takes the material properties into account and is derived for impact between two spheres of isotropic material based on the theory of elasticity. The force is given by

$$f_c = K_g \delta^n \tag{3.27}$$

where the exponent n is set to 1.5 for metallic surfaces, but for other materials it can be either higher or lower. The generalized stiffness coefficient K_g is dependent on the material properties. For two spheres in contact the generalized stiffness coefficient is dependent on the radii of the two spheres, here denoted body i and body j, and the material properties, see e.g. Goldsmith (1960) and Lankarani and Nikravesh (1990), and is given by

$$K_g = \frac{4}{3\pi(h_i + h_j)} \left[\frac{r_i r_j}{r_i + r_j} \right]^{1/2} \tag{3.28}$$

where r_k is the radii of the two spheres and h_k is the material properties given by

$$h_k = \frac{1 - \nu_k^2}{\pi E_k} \qquad k = i, j \tag{3.29}$$

where ν_k is Poisson's ratio for body k and E_k is the modulus of elasticity for body k. For contact between a sphere denoted body *i* and a plane surface denoted body *j* ($r_j \rightarrow \infty$) the generalized stiffness coefficient depend on the radius of the sphere and the material properties as follows

$$K_g = \frac{4}{3\pi(h_i + h_j)} \sqrt{r_i} \tag{3.30}$$

In the case of internal contact (negative value of r_j) between two cylindrical bodies, body i and body j the indentation δ as a function of the force f_c is by Dubowsky and Freudenstein (1971*a*) suggested to be

$$\delta = \frac{f_c(h_i + h_j)}{l_z} \left[\ln \left(\frac{l_z^m (r_i + r_j)}{f_c(h_i + h_j) r_i r_j} \right) + 1 \right] \tag{3.31}$$

where h_k is given by (3.29), l_z is the length of the cylinder and the exponent $m = 3$. Goldsmith (1960) presented a similar expression as in (3.31), but with the exponent $m = 1$. However, this value of the exponent gives a problem with the units of (3.31), whereas the suggested exponent $m = 3$ by Dubowsky and Freudenstein (1971*a*) gives agreement with the units. The generalized stiffness coefficient can be calculated from equation (3.31) by calculating the average slope by $K = \frac{f_c}{\delta}$ or by a numerical iterative technique e.g. Newton-Raphson iteration.

The generalized stiffness coefficient for the case of a cylinder denoted body i and a plane surface denoted body j is found in the same way as for the case of two cylinders in contact,

by taking the limiting value for the radius $r_j \to \infty$. The relation between the indentation and the force thereby becomes

$$\delta = \frac{f_c(h_i + h_j)}{l_z}\left[\ln(\frac{l_z^m}{f_c(h_i + h_j)r_i}) + 1\right] \tag{3.32}$$

The definition of the coefficient of restitution is in simple one dimensional impact between two rigid bodies in pure translation, the ratio of their relative speed after impact and at the beginning of impact in the direction of impact, see e.g. Hunt and Crossley (1975) and Lankarani and Nikravesh (1990), so

$$v^{(+)} = -ev^{(-)} \tag{3.33}$$

where $v^{(+)}$ is the relative speed after impact and $v^{(-)}$ is the relative approach speed, $(-)$ indicates that it is the value just as impact begins and $(+)$ indicates that it is the value just as impact ends. The relative speeds are calculated normal to the plane of contact. The difference between the kinetic energy $E_{kin}^{(+)}$ at the beginning of impact and the kinetic energy $E_{kin}^{(-)}$ after impact is the loss in kinetic energy ΔE_{kin}, and is given by

$$\Delta E_{kin} = \frac{1}{2}m_e(v^{(-)^2} - v^{(+)^2}) \tag{3.34}$$

where m_e is the system equivalent mass and it is given by

$$m_e = \frac{m_i m_j}{m_i + m_j} \tag{3.35}$$

m_i and m_j are the masses of the two bodies in contact. Equation (3.34) is derived by assuming that the linear momentum of the system in the direction of impact is conserved, since the contact force becomes internal to the system, see Lankarani and Nikravesh (1990). By inserting 3.33) in (3.34) the energy loss can be written as

$$\Delta E_{kin} = \frac{1}{2}m_e v^{(-)^2}(1 - e^2) \tag{3.36}$$

By the assumption that the energy loss only is due to internal damping, which is only valid for low impact speeds, the contact force is extended to include the energy dissipation, by adding a damping term, see Lankarani and Nikravesh (1994)

$$f_c = K_g\delta^n + D_c v \tag{3.37}$$

where D_c is the damping coefficient, which by Hunt and Crossley (1975) was proposed to be in a hysteresis form as

$$D_c = \eta_c \delta^n \tag{3.38}$$

where η_c is the hysteresis damping factor and the exponent n is the same as in (3.27). In order to determine the hysteresis damping factor the energy loss may also be expressed by the integral of contact force around the contact force hysteresis loop, see Figure 3.8, written as

$$\Delta E_{kin} = \oint D_c v \mathrm{d}\delta \backsimeq 2 \int_0^{\delta_{max}} \eta_c \delta^n v \mathrm{d}\delta \tag{3.39}$$

where $\oint$ refers to the curve integration around a hysteresis loop. The energy loss is assumed to be small and the velocity changes sign when it changes from approaching to separating, therefore the cyclic integral can be written as two times the integral from no indentation until the maximum indentation δ_{max} as done in (3.39).

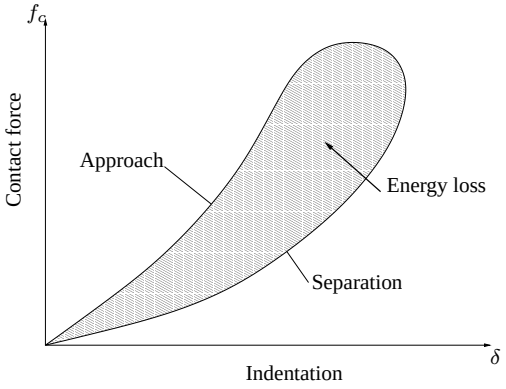

Figure 3.8: The energy loss in the non-linear model

In order to perform the integration it is necessary to have the speed written in terms of the indentation. Having the kinetic energy just as impact begins equal to $\frac{1}{2} m_e v^{(-)^2}$ then the kinetic energy in a intermediate position $0 < \delta < \delta_{max}$ is given by

$$\frac{1}{2} m_e v^2 = \frac{1}{2} m_e v^{(-)^2} - \int_0^{\delta} f_c \mathrm{d}\delta \tag{3.40}$$

the speed just as impact begins can by integration of the contact force in (3.27) be written in terms of the indentation as Hunt and Crossley (1975)

$$v^{(-)} = \sqrt{\frac{2K_g}{m_e(n+1)} \delta_{max}^{(n+1)}} \tag{3.41}$$

by inserting (3.41) in (3.40) and doing the integration the speed in an intermediate position can be rewritten as

$$v = \sqrt{\frac{2K_g}{m_e(n+1)}}\sqrt{\delta_{max}^{(n+1)} - \delta^{(n+1)}} \tag{3.42}$$

The energy loss in (3.39) can now be calculated by inserting (3.42) and do the integration by substitution, which gives

$$\begin{aligned}\Delta E_{kin} &\backsimeq 2\eta_c\sqrt{\frac{2K_g}{m_e(n+1)}}\int_0^{\delta_{max}} \delta^n\sqrt{\delta_{max}^{(n+1)} - \delta^{(n+1)}}\mathrm{d}\delta \\ &= 2\eta_c\sqrt{\frac{2K_g}{m_e(n+1)}}\frac{2}{3}\frac{1}{(n+1)}\left(\delta_{max}^{(n+1)}\right)^{\frac{3}{2}}\end{aligned} \tag{3.43}$$

Equation (3.43) can by inserting (3.41) be rewritten as

$$\Delta E_{kin} \backsimeq \frac{2}{3}\frac{\eta_c}{K_g}m_e v^{(-)^3} \tag{3.44}$$

The hysteresis damping factor η_c is determined by comparison of (3.36) and (3.44) and becomes

$$\eta_c = \frac{3K_g(1-e^2)}{4v^{(-)}} \tag{3.45}$$

yielding the damping coefficient

$$D_c = \frac{3K_g(1-e^2)}{4v^{(-)}}\delta^n \tag{3.46}$$

Substitution of the damping coefficient given by (3.46) into (3.37), gives the contact force between to metallic surfaces in contact assuming no permanent indentation written as

$$f_c = K_g\delta^n\left[1 + \frac{3(1-e^2)v}{4v^{(-)}}\right] \tag{3.47}$$

The contact force is applied to the approaching body in the normal direction of the contact surface, yielding the contact force vector

$$\mathbf{f}_c = f_c\mathbf{n} \tag{3.48}$$

where $\mathbf{n}$ is the normal unit vector out of the contact surface on the other contacting body, see Figure 3.9. The relative velocity at impact is $v^{(-)} = v_{in}^{(-)} - v_{jn}^{(-)}$, see Figure 3.9, where

$v_{in}^{(-)} = (\mathbf{v}_i^{(-)})^T(-\mathbf{n})$ and $v_{jn}^{(-)} = (\mathbf{v}_j^{(-)})^T(-\mathbf{n})$, with $\mathbf{v}_i^{(-)}$ being the impact velocity vector of body i and $\mathbf{v}_j^{(-)}$ being the impact velocity vector of body j. The approach direction is $-\mathbf{n}$ and the separation direction is $\mathbf{n}$.

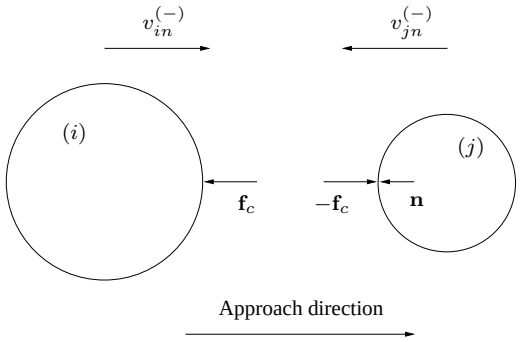

Figure 3.9: An impact between two spherical bodies.

The contact models given by (3.27) and (3.47) are only valid for colliding spheres. For internal contact between two cylinders a literature search has failed to yield an implicit force-displacement relationship. The indentation as a function of the contact force given in (3.31) suggested by Dubowsky and Freudenstein (1971*a*) is for a shaft inside a cylinder. However with a known indentation it is necessary to iteratively solve the equation to obtain the contact force. Due to the simplicity of (3.47) it is largely used for colliding cylinders using an equivalent stiffness obtained by (3.31), see e.g. Ravn (1998) and Flores et al. (2003).

3.5.1 The Shape of the Contact Surface between Rollers and Sprockets

The initial idea was to make the contact between the rollers and the sprockets as simple as one point where a contact force was applied in either tangential or normal direction. This was done in order to make the continuous contact force method similar to the way the constraint method models the contact. However this approach has shown not to be useful, why several other tooth profiles has been tested. Figure 3.10 shows the steps in the evolution of the contact shape model (the tooth profiles).

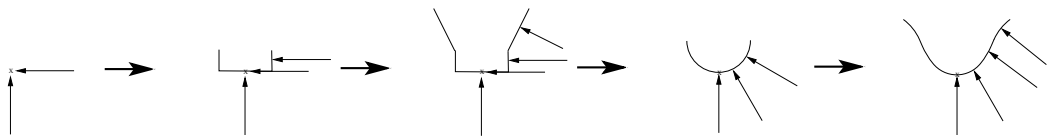

Figure 3.10: Steps in the evolution of the tooth shape model.

The five different shapes of the contact surface are respectively denoted single point contact, rectangular tooth profile, semi real tooth profile, circular tooth profile and real tooth profile, see Figure 3.10. Of the five different tooth profiles the last two, the circular tooth profile and the real tooth profile, turned out to be the most useful ones. The rectangular tooth profile and the semi real tooth profile, are able to solve some problems, but too sensitive numerically to the values of the different parameters used in the continuous contact force. The circular tooth profile and the real tooth profile are numerically more stable than the first three tooth profiles and less dependent on the values of the different parameters used in the continuous contact force.

In the following sections the first three tooth profile models will shortly be described and the last two tooth profile models will be described more thoroughly.

3.5.2 Single Point Contact

The contact force between a roller and a sprocket, when the roller is captured on the pitch circle, is split into two contact planes, a radial and a tangential, and becomes

$$\mathbf{f}_c = (K_g \delta_r^n + D_c v_r)\mathbf{u}_r + (K_g \delta_t^n + D_c v_t)\mathbf{u}_t \tag{3.49}$$

where δ_r and δ_t are the projections of the indentation vector $\boldsymbol{\delta}$ in the direction of the unit vectors $\mathbf{u}_r$ and $\mathbf{u}_t$, respectively, see Figure 3.11. The projections of the relative velocity vector $\mathbf{v}$ in the direction of the unit vectors $\mathbf{u}_r$ and $\mathbf{u}_t$ is respectively v_r and v_t. The generalized stiffness coefficient K_g is for the roller-sprocket contact, which is two cylindrical surfaces, to be found by (3.31) and the damping coefficient is given by (3.46). The unit vectors $\mathbf{u}_r$ and $\mathbf{u}_t$ are given by

$$\mathbf{u}_r = \left\{ \begin{array}{c} \cos(\theta_s \pm j\alpha) \\ \sin(\theta_s \pm j\alpha) \end{array} \right\}, \quad \mathbf{u}_t = \left\{ \begin{array}{c} -\sin(\theta_s \pm j\alpha) \\ \cos(\theta_s \pm j\alpha) \end{array} \right\} \tag{3.50}$$

where the $\pm$ dependents on whether the sprocket rotates counter clockwise $(+)$ or clockwise $(-)$, see Figure 3.4 and Figure 3.11. A roller is checked for contact with a sprocket when the roller is inside the pitch circle and released when outside the pitch circle.

3.5.3 Rectangular Tooth Profile

The rectangular tooth profile is an extension to the single point contact. For the rectangular tooth profile a rectangular area outside the pitch circle is checked for tangential contact. In this gap a relatively small indentation is allowed. This assumption is made to

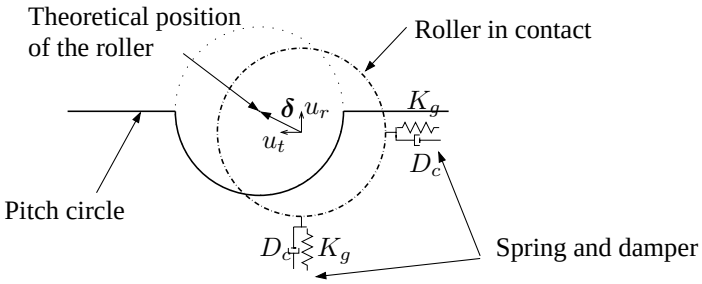

Figure 3.11: The contact between roller and sprocket

prevent the roller from oscillating too much tangentially. This tangential contact force is given by

$$\mathbf{f}_c = (K_g \delta_t^n + D_c v_t)\mathbf{u}_t \tag{3.51}$$

A roller is checked for contact with a sprocket when the roller is inside the enlarged pitch circle and released when outside the enlarged pitch circle. The radius of the enlarged pitch circle is set to be the pitch radius plus the height of the rectangular area.

3.5.4 The Semi Real Tooth Profile

The semi real tooth profile is an extension to the rectangular tooth profile and includes the tooth flexibility. The tooth flange is represented by straight lines with an angle β with respect to the rectangular area, see Figure 3.12. There is the possibility that the roller is in contact with tooth number j, when the tangential indentation δ_t is negative and in contact with tooth number $j-1$, when the tangential indentation δ_t is positive. The tangential indentation δ_t is the projection of the indentation on the unit vector $\mathbf{u}_t$.

When the roller is inside the pitch circle (see Figure 3.12), the contact between the roller and sprocket is as for the single point contact. When the center of a roller is in the area between the pitch circle and the enlarged pitch circle (see Figure 3.12), the contact between the roller and sprocket is as for the rectangular tooth profile. When the roller is in the area between the enlarged pitch circle and the outside circle there is a possibility for the roller to be in contact with one of the teeth. If the roller is in contact with a tooth a force is applied in the direction of the normal $\mathbf{n}_\beta$ to the tooth profile plane, see Figure 3.12.

The tangential vector $\mathbf{t}_\beta$ to the tooth profile, is found by rotating the unit vector $\mathbf{u}_r$, with

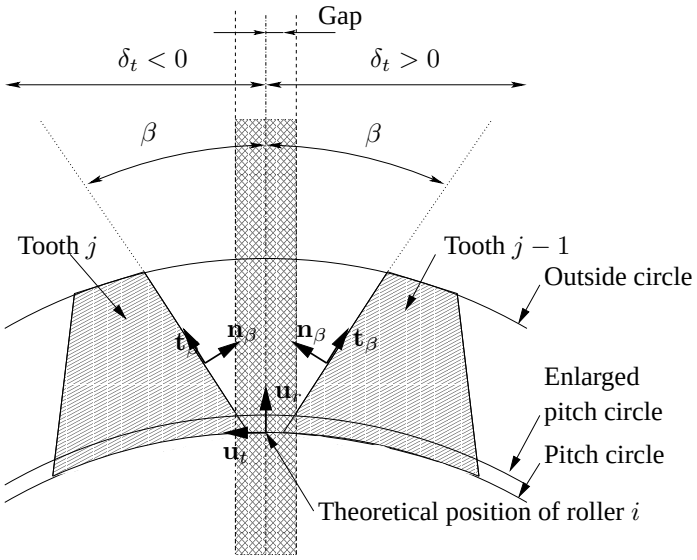

Figure 3.12: The semi real tooth profile

the angle β, see Figure 3.12. The tangential vector $\mathbf{t}_\beta$ to the tooth profile surface is given by

$$\mathbf{t}_\beta = \mathbf{A}_t \mathbf{u}_r \tag{3.52}$$

where $\mathbf{u}_r$ is the normal vector given in equation (3.50) and the transformation matrix $\mathbf{A}_t$ is given by equation 2.5, with $\theta = \pm\beta$, where the sign depends on sign of δ_t. The normal vector to the contact surface is given by

$$\mathbf{n}_\beta = \begin{cases} -\hat{\mathbf{t}}_\beta, & \delta_t < 0 \\ \hat{\mathbf{t}}_\beta, & \delta_t > 0 \end{cases} \tag{3.53}$$

where the hat ($\hat{}$) indicates that the vector is perpendicular to $\mathbf{t}_\beta$, rotated in the counter clockwise direction. The indentation in the tooth δ_β is the projection of the indentation in the direction of $\mathbf{n}_\beta$.

3.5.5 Circular Tooth Profile

In Figure 3.13 is shown the model where only the circular lower part of the tooth profile is included, this model is referred to as the circular tooth profile model. The radius of the circular tooth profile is R_t and the roller radius is R_r, yielding a clearance of $\Delta R = R_t - R_r$. The centre of the circular tooth profile is placed $R_s + \Delta R$ from the centre of the

sprocket. This is done in order to prevent all the rollers in contact with a sprocket from disengaging at the same time. The unit vectors $\mathbf{u}_r$ and $\mathbf{u}_t$ are given by Equation (3.50).

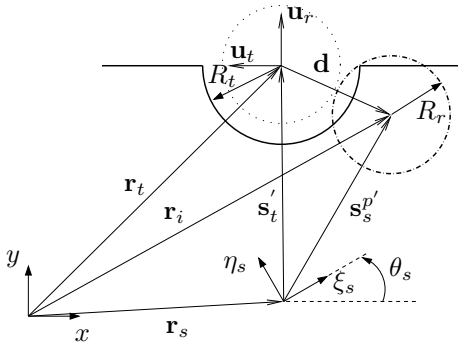

Figure 3.13: The circular tooth profile

The vector from the sprocket centre to the roller centre is in the local coordinate system (ξ_s, η_s) given by $\mathbf{s}_r{}'$. The position of the sprocket centre is in the global coordinate system (x, y) given by the vector $\mathbf{r}_s$ and the centre of the tooth profile is in the local coordinate system given by vector $\mathbf{s}_t{}'$. The roller position is in global coordinate system (x, y) given by the vector $\mathbf{r}_i$. The centre of the tooth profile is therefore in the global coordinate system given by

$$\mathbf{r}_t = \mathbf{r}_s + \mathbf{A}_s \mathbf{s}_t^{'} \tag{3.54}$$

where the transformation matrix $\mathbf{A}_s$ is given by (2.5), with the angle $\theta = \theta_s$ and the local vector $\mathbf{s}_t^{'}$ is given by

$$\mathbf{s}_t^{'} = (R_s + \Delta R) \left\{ \begin{array}{c} \cos(\pm j\alpha) \\ \sin(\pm j\alpha) \end{array} \right\} \tag{3.55}$$

The vector $\mathbf{s}_t$ becomes

$$\mathbf{s}_t = \quad \mathbf{A}_s \mathbf{s}_t^{'} = (R_s + \Delta R)\mathbf{u}_r \tag{3.56}$$

and vector $\mathbf{r}_t$ becomes

$$\mathbf{r}_t = \mathbf{r}_s + (R_s + \Delta R)\mathbf{u}_r \tag{3.57}$$

The vector $\mathbf{d}$ from the centre of the tooth profile to the roller centre is given by

$$\mathbf{d} = \mathbf{r}_i - \mathbf{r}_t \tag{3.58}$$

The pseudo penetration in the tooth is given by

$$\delta = \|\mathbf{d}\| - \Delta R \tag{3.59}$$

where $\|\mathbf{d}\|$ is the two norm of vector $\mathbf{d}$. The normal unit vector $\mathbf{n}$ to the contact surface is then given by

$$\mathbf{n} = -\frac{\mathbf{d}}{\|\mathbf{d}\|} \tag{3.60}$$

The point of application of the contact force on the roller is the centre of the roller. The vector from the sprocket centre to the point of application of the contact force on the sprocket, is in global coordinates given by

$$\mathbf{s}_s^p = \mathbf{r}_i - \mathbf{r}_s \tag{3.61}$$

and in the local sprocket coordinates (3.61) can be written as

$$\mathbf{s}_s^{p'} = \mathbf{A}_s^T \mathbf{s}_s^p \tag{3.62}$$

The velocity of the contact point on the roller is

$$\dot{\mathbf{r}}_i^p = \dot{\mathbf{r}}_i \tag{3.63}$$

and the velocity of the contact point on the sprocket is

$$\dot{\mathbf{r}}_s^p = \frac{d(\mathbf{r}_s + \mathbf{A}_s \mathbf{s}_s^{p'})}{dt} = \dot{\mathbf{r}}_s + \omega_s \mathbf{B}_s \mathbf{s}_s^{p'} \tag{3.64}$$

where $\omega_s = \dot{\theta}_s$ and the matrix $\mathbf{B}_s$ is given by

$$\mathbf{B}_s = \begin{bmatrix} -\sin(\theta_s) & -\cos(\theta_s) \\ \cos(\theta_s) & -\sin(\theta_s) \end{bmatrix} \tag{3.65}$$

The relative velocity in the normal direction v_n at the contact point is positive in the approach direction which is the direction of $-\mathbf{n}$, yielding

$$v_n = (\dot{\mathbf{r}}_i^p - \dot{\mathbf{r}}_s^p)^T (-\mathbf{n}) \tag{3.66}$$

and the relative velocity in the tangential direction v_t at the contact point is given by

$$v_t = (\dot{\mathbf{r}}_i^p - \dot{\mathbf{r}}_s^p)^T \mathbf{t} \tag{3.67}$$

where $\mathbf{t}$ is the tangential unit vector given by $\mathbf{t} = \hat{\mathbf{n}}$,where the hat ($\hat{}$) indicates that the vector is perpendicular to $\mathbf{n}$, rotated in the counter clockwise direction. The contact force of the roller can now be found using (3.47), the normal vector $\mathbf{n}$ in equations given in (3.60), the indentation δ in (3.59) and the relative velocity v in (3.66). The moment on the centre of the sprocket caused by the contact force is given by

$$\tau_s = -\hat{\mathbf{s}}_s^p \cdot f_c \tag{3.68}$$

where the hat ($\hat{}$) indicates that the vector is perpendicular to $\mathbf{s}_s^p$, rotated in the counter clockwise direction.

3.5.6 Real Tooth Profile

The standard tooth form (Type II per ASA B29.1-1950) is shown in the Figure C.1, taken from Binder (1956), see appendix C. The tooth-profile is separated into 7 areas where the roller-sprocket contact can occur, see Figure 3.14.

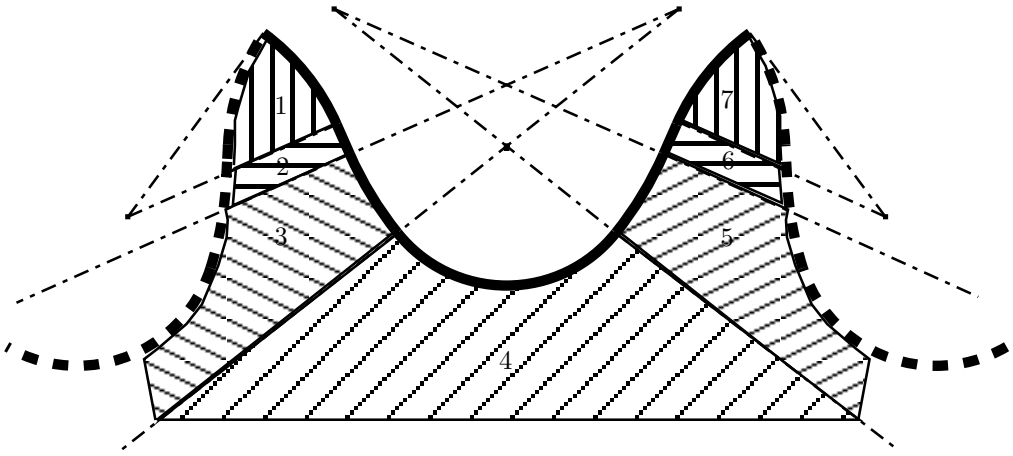

Figure 3.14: The real tooth profile separated in 7 contact areas.

The contact areas can be defined by local vectors given in the local coordinate system (ξ_t, η_t). The local vectors and angles that define the tooth profile are given in appendix C. When the roller gets in contact with the sprocket the contact area has to be found. First of all it is checked if the roller is in contact with area 4 or in contact with the left or the right side of the tooth center line.

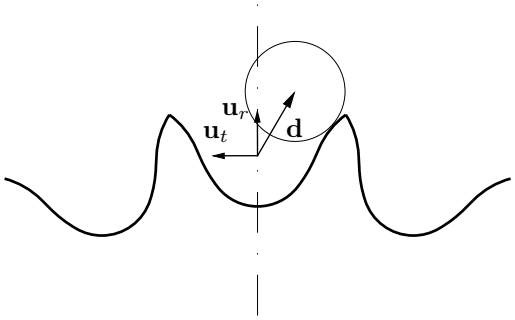

Figure 3.15: The position of the roller with respect to the tooth centre line.

The condition for the roller being either on the left side or the right side of the tooth center line is

$$\mathbf{d}^T\mathbf{u}_t = \begin{cases} < 0 : \text{right} \\ > 0 : \text{left} \end{cases} \tag{3.69}$$

where the unit vector $\mathbf{u}_t$ is given by (3.50) and vector $\mathbf{d}$ is given by

$$\mathbf{d} = \mathbf{r}_i - \mathbf{r}_t \tag{3.70}$$

Contact with the seating curve

Area 4 is referred to as the seating curve and contact with this area is analysed independently on whether the roller is on the right or the left side of the tooth center line, see Figure 3.16.

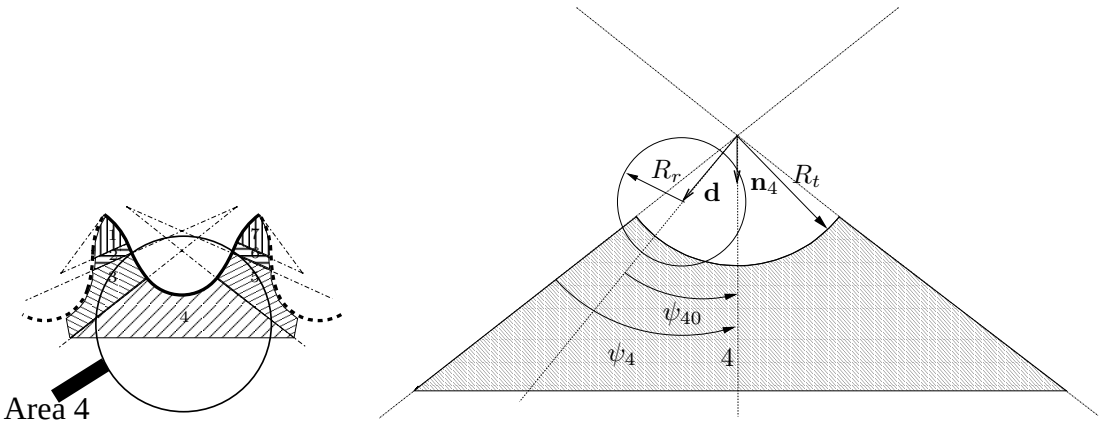

Figure 3.16: The seating curve, contact area 4.

The vector $\mathbf{n}_4$, see Figure 3.16, is given by

$$\mathbf{n}_4 = \quad -\mathbf{u}_r \tag{3.71}$$

and $\mathbf{d}$ is given in (3.70). The pseudo penetration is calculated by

$$\delta_4 = \|\mathbf{d}\| - (R_t - R_r) \tag{3.72}$$

The conditions that has to be fulfilled in order for contact to occur with area 4 are

$$\text{Contact conditions for area 4:} \begin{cases} \delta_4 > 0 \\ 0 \leq |\psi_{40}| \leq |\psi_4| \end{cases} \tag{3.73}$$

where $\psi_4 = \frac{\psi_{2a} - \psi_{1a}}{2} = \frac{\pi}{2} - A$, see appendix C, and ψ_{40} is given by

$$\cos(\psi_{40}) = \frac{\mathbf{d}^T \mathbf{n}_4}{\|\mathbf{d}\|} \tag{3.74}$$

Contact with the topping curve

Area 1 and area 7 are referred to as the topping curves. The contact with area 1 is similar to the contact with area 7, therefore only contact with area 1 is described here, see Figure 3.17. The vectors shown in Figure 3.17 are given by

$$\begin{aligned} \mathbf{n}_1 &= \quad \mathbf{A}_t \mathbf{n}_1^{'} \\ \mathbf{d}_1 &= \quad \mathbf{r}_i - \mathbf{r}_{b^*} \end{aligned} \tag{3.75}$$

where the local vector $\mathbf{n}_1^{'} = \{\cos(\psi_{1b^*} + \psi_1), \sin(\psi_{1b^*} + \psi_1)\}^T$, with $\psi_1 = \frac{\psi_{2b^*} - \psi_{1b^*}}{2}$, see appendix C. The pseudo penetration is given by

$$\delta_1 = (R_F + R_r) - \|\mathbf{d}_1\| \tag{3.76}$$

where the radius R_F is given in (C.2), see appendix C. The conditions that has to be fulfilled in order for contact to occur with area 1 are

$$\text{Contact conditions for area 1:} \begin{cases} \delta_1 > 0 \\ 0 \leq |\psi_{10}| \leq |\psi_1| \end{cases} \tag{3.77}$$

where ψ_{10} is given by

$$\cos(\psi_{10}) = \frac{\mathbf{d}_1^T \mathbf{n}_1}{\|\mathbf{d}_1\|} \tag{3.78}$$

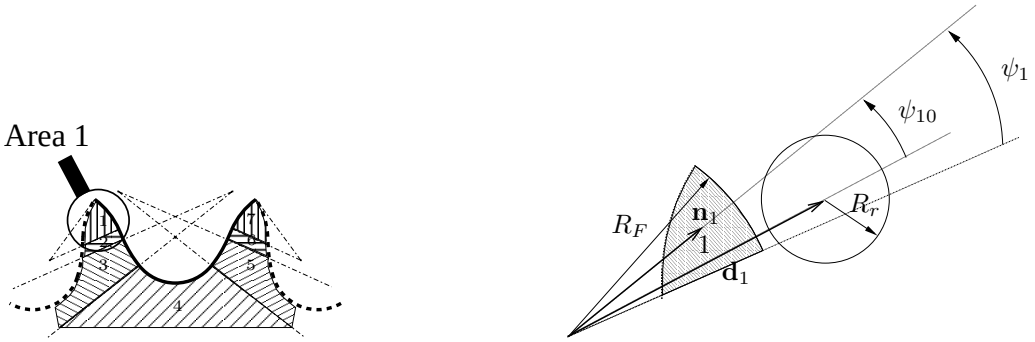

Figure 3.17: The topping curves, contact areas 1 and 7.

Contact with the working curve

Area 3 and area 5 are referred to as the working curves. The contact with area 3 is similar to the contact with area 5, therefore only contact with area 3 is described here, see Figure 3.18. The vectors shown in Figure 3.18 are given by

$$\begin{aligned} \mathbf{n}_3 &= \mathbf{A}_t \mathbf{n}_3^{'} \\ \mathbf{d}_3 &= \mathbf{r}_i - \mathbf{r}_{c^*} \end{aligned} \tag{3.79}$$

where the local vector $\mathbf{n}_3^{'} = \{\cos(\psi_{1c^*}+\psi_3), \sin(\psi_{1c^*}+\psi_3)\}^T$, with $\psi_3 = \frac{B}{2}$, see appendix C. The pseudo penetration is given by

$$\delta_3 = \|\mathbf{d}_3\| + R_r - R_E \tag{3.80}$$

where the radius R_E is given in (C.2), see appendix C. The conditions that has to be fulfilled in order for contact to occur with area 3 are

$$\text{Contact conditions for area 3:} \begin{cases} \delta_3 > 0 \\ 0 \leq |\psi_{30}| \leq |\psi_3| \end{cases} \tag{3.81}$$

where ψ_{30} is given by

$$\cos(\psi_{30}) = \frac{\mathbf{d}_3^T \mathbf{n}_3}{\|\mathbf{d}_3\|} \tag{3.82}$$

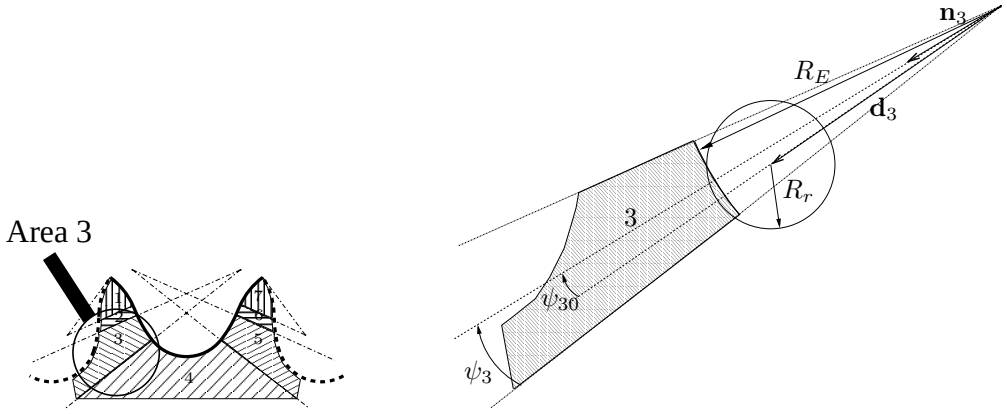

Figure 3.18: The working curves, contact areas 3 and 5.

Contact with the straight portion

Area 2 and area 6 are referred to as the straight portions. The contact with area 2 is similar to the contact with area 6, therefore only contact with area 2 is described here, see Figure 3.19. The vectors shown in Figure 3.19 are given by

$$\begin{aligned} \mathbf{t}_2 &= \frac{1}{\|\mathbf{r}_{e^*} - \mathbf{r}_{d^*}\|}(\mathbf{r}_{e^*} - \mathbf{r}_{d^*}) \\ \mathbf{n}_2 &= -\hat{\mathbf{t}}_2 \\ \mathbf{d}_2 &= \mathbf{r}_i - \mathbf{r}_{d^*} \end{aligned} \tag{3.83}$$

where the vectors $\mathbf{r}_{e^*}$ and $\mathbf{r}_{d^*}$ are the global vectors to the points e^* and d^*, see appendix C. The pseudo penetration is calculated by

$$\delta_2 = \mathbf{d}_2^T \mathbf{n}_2 - R_r \tag{3.84}$$

The conditions that has to be fulfilled in order for contact to occur with area 2 are

$$\text{Contact conditions for area 2:} \begin{cases} \delta_2 > 0 \\ \mathbf{d}_2^T \mathbf{t}_2 > 0 \\ \mathbf{d}_2^T \mathbf{t}_2 < \|\mathbf{r}_{e^*} - \mathbf{r}_{d^*}\| \end{cases}$$

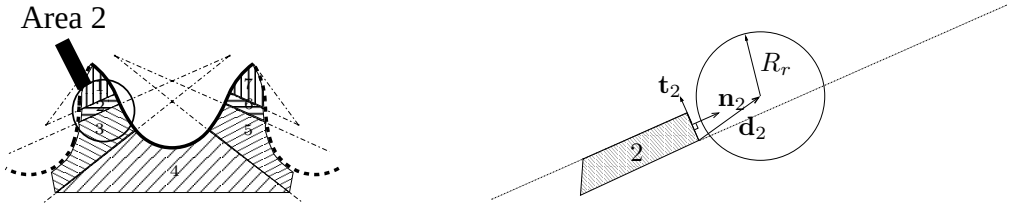

Figure 3.19: The straight portions, contact areas 2 and 6.

The contact force on the rollers is given by (3.47), with the normal vector $\mathbf{n}$ for the different contact areas being

$$\begin{aligned} \text{Area 1 (or 7)}: \quad \mathbf{n} &= \mathbf{d}_1/\|\mathbf{d}_1\| \\ \text{Area 2 (or 6)}: \quad \mathbf{n} &= \mathbf{n}_2 \\ \text{Area 3 (or 5)}: \quad \mathbf{n} &= -\mathbf{d}_3/\|\mathbf{d}_3\| \\ \text{Area 4}: \quad \mathbf{n} &= -\mathbf{d}/\|\mathbf{d}\| \end{aligned} \tag{3.85}$$

The indentation δ in (3.47) is given by δ_i, where index $i = 1, \ldots, 7$ refers to the area. The relative velocity is calculated by (3.66), with the normal vector $\mathbf{n}$ given by equation (3.85). The moment applied to the sprocket is calculated in a similar way as in equation (3.68).

3.6 The Polygonal Action

The major difficulties in the study of the roller chain drives are related to the roller chain forming a polygon while wrapped around the sprockets. When the chain is lying on a sprocket it forms polygons instead of circles, see Figure 3.4, which causes a periodic fluctuation of linear velocity together with periodic transverse displacements of both ends of the chain. The instantaneous pitch diameter alternates between that of the inscribed and circumscribed circles of the pitch polygon, see Figure 3.4 (only circumscribed circle shown). This is known as the polygonal action or polygonal effect, see e.g. Bouillon and Tordion (1965). Due to the polygonal effect the velocities of the driven sprockets will fluctuate even if the velocity of the driving sprocket is constant. The polygonal effect is thus responsible for the transverse and longitudinal vibrations that develop in the chain, see e.g. Mahalingam (1958). The excitation resulting from the impact of the roller when it seats on the sprocket and the polygonal effect participates in the creation of the noise and vibration of the roller-chain drive. In order to have a useful model of the vibration

behaviour of the chain and the tension fluctuation special attention must be paid to a correct engagement and disengagement description.

3.7 Examples of Other Possible Methods

Some other methods of describing the system have been investigated and many alternative ideas have come in mind during the work. Here three methods are mentioned the Hybrid Method, the Rigid Body Links Method and the Minimum Link Method, respectively.

3.7.1 Hybrid Method

A combination of the continuous contact force method and the constraint method has been applied. When a roller gets in contact with a sprocket the continuous force method is used at the beginning. When the relative velocity between the sprocket and the roller is close to zero within a numerical tolerance, the used contact model is switched to the constraint method. This method has been tested with some of the contact profiles described in the previous section, but the system appeared to be too stiff numerically to be solved. It is possible that a hybrid method between the continuous contact force method, where the real shaped tooth profile is used and a constraint method, where the contact is modelled by a point follower constraint could work. In this way both of the methods include chain elongation during contact and are more comparable. However the implementation of this method is left for future investigations.

3.7.2 Rigid Body Links Method

Treating the links as rigid bodies demands a formulation including clearance joints between the links. In all the previous described contact models the links has been modelled as massless links and the rotational inertia is neglected. Formulating the system using Cartesian coordinates will make the system larger, because the angles of each link also are included as coordinates. Using other coordinate methods such as the joint coordinate method, would be preferable in this case, see e.g. Nikravesh (2001). The methodology has not been investigated further.

3.7.3 Minimum Link Method

In this method the rollers that are not in contact with the sprockets are treated as free rollers in the plane as in the continuous contact force method. The rollers in contact with

the sprockets are treated as part of the sprocket wheel and contribute to the mass moment of inertia of the sprocket. Capture and release conditions are similar to the once used in the constraint method and therefore this method has similar problems as the constraint method. Because of the discontinuities with this method the numerical integration gives problems.

3.8 Including Parts, specific for the Marine Engine

In the chain drive system of the marine diesel engine different important parts are included, important with respect to the vibration pattern of the engine and ship hull. These parts are different tightener systems, guide-bars and balancing wheels.

In most cases of the numerical simulations it is assumed that the centre of all the sprockets are fixed in the plane, except the sprockets placed in the tightener system. The possibility of allowing the sprockets to move translationally is however present.

3.8.1 Tightener System

While the engine is running the roller chain wears and consequently extends. Therefore, the chain has to be tightened frequently as it gradually extends, in order to keep its functionality. To this purpose one of the driven sprockets is located in a chain tightener system. This sprocket centre can move from its initial position and then tighten the chain. To avoid the manual tightenings of the chain automatic chain tighteners have been introduced on some engines. This has caused undesirable vibration patterns of the chain and chain tightener which were not immediately explicable.

The tightener systems used in the chain drive for the marine diesel engine usually consists of a weight-arm connect to the sprocket, to the hydraulic damper and to a fixed point on the engine which is at the grounded body. The joints between the weight-arm, the sprocket and ground are either revolute joints, translational joints or spring-damper connections.

The sprocket that is in the chain tightener system translates and its movement depends on the movement of the other elements in the chain tightener system. The chain tightener system has been included in the force model. The inclusion of the tightener system is done by introducing kinematic constraints between the sprocket and the other bodies (e.g. weight-arm) in the tightener system and for the chain tightener with a hydraulic damper this is modelled as a spring-damper, see Figure (3.20). In the figure the model of the chain

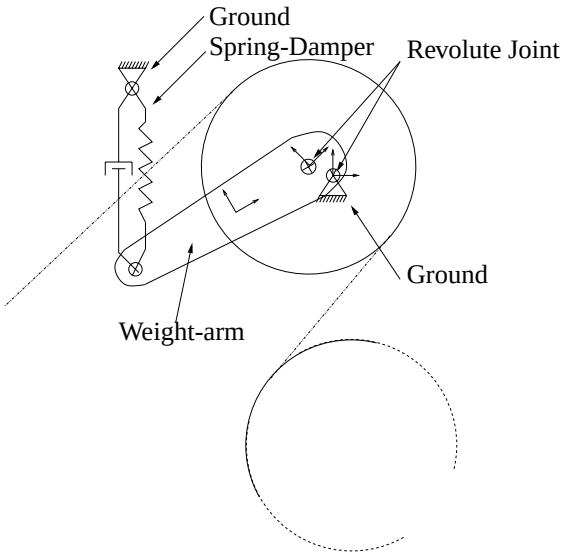

Figure 3.20: The tightener system as part of the chain drive system.

drive system consist of a sprocket connected with a weight-arm with a revolute joint. The weight-arm is connected with a grounded body with a revolute joint and a spring/damper connection. This tightener system allows for the centre of the sprocket to move along a circular path while the engine is running.

The constraint equations are set up for the chain tightener system including revolute joint constraint and translational joint constraints, see e.g. section 2.4. These constraint equations are differentiated twice with respect to time, and using the Lagrange multiplier technique as described in section 2.4 the total set of equations for the chain tightener system is written as

$$\begin{bmatrix} \mathbf{M}_s & \mathbf{0} & \mathbf{\Phi_s}^T \\ \mathbf{0} & \mathbf{M}_b & \mathbf{\Phi_b^T} \\ \mathbf{\Phi_s} & \mathbf{\Phi_b} & \mathbf{0} \end{bmatrix} \begin{Bmatrix} \ddot{\mathbf{q}}_s \\ \ddot{\mathbf{q}}_b \\ \boldsymbol{\lambda} \end{Bmatrix} = \begin{Bmatrix} \mathbf{g}_s \\ \mathbf{f}_b \\ \boldsymbol{\gamma_t} \end{Bmatrix} \tag{3.86}$$

where $\mathbf{M}_b$ is the mass and inertia of the other bodies in the chain tightener system, $\ddot{\mathbf{q}}_b$ is the accelerations of the bodies, $\mathbf{f}_b$ is the forces on the bodies, $\boldsymbol{\gamma_t}$ is the right hand side from the acceleration of the constraint equations and $[\mathbf{\Phi_s \Phi_b}]$ is the Jacobian matrix. The mass and inertia of the sprocket in the tightener system are given in the mass matrix $\mathbf{M}_s$, the vector $\ddot{\mathbf{q}}_s$ is the accelerations of the sprocket and the vector $\mathbf{g}_s$ is the forces on the sprocket. In the tightener system shown in Figure (3.20), the number of bodies is two, which are the weight-arm and a grounded body.

3.8.2 Guide-bars

Figure 3.21 shows an example of the placement of three guide-bars in a chain drive system.

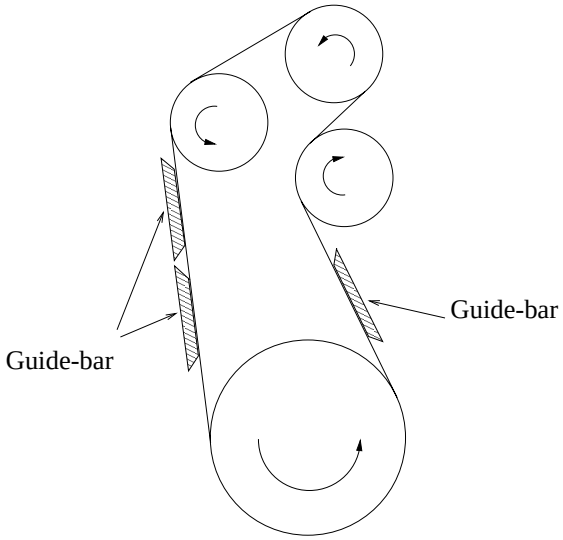

Figure 3.21: Guide-bars in a 6S90MC-C fore end chain drive system.

The contact between the roller chain strands and the guide-bars is modelled with the continuous contact force model. The global coordinates of the end points of the flat part of the guide-bars are $\mathbf{r}_{gi}$ and $\mathbf{r}_{gj}$, the radius of the rounded ends is R_{ge}, the length of the rounded end is L_{ge} and the length of the flat part is L_g, see Figure 3.22.

The detection of contact is split into three parts, i.e., the two rounded end parts (area 1 and 3) and the flat part (area 2). In order for contact to appear between a roller and the flat part of the guide-bar the necessary conditions are

$$\text{Contact condition for area 2:} \begin{cases} \mathbf{d}_{g2}^T \mathbf{t}_g > 0 \\ \mathbf{d}_{g2}^T \mathbf{t}_g < L_g \\ \delta_{g2} > 0 \end{cases} \tag{3.87}$$

where δ_{g2} is the pseudo penetration given by

$$\delta_{g2} = -\mathbf{d}_{g2}^T \mathbf{n}_g \tag{3.88}$$

and the normal vector to the contact surface is $\mathbf{n}_g$ is given by (D.2), see appendix D. In appendix D is given a detailed description of the vectors used for detection of contact with

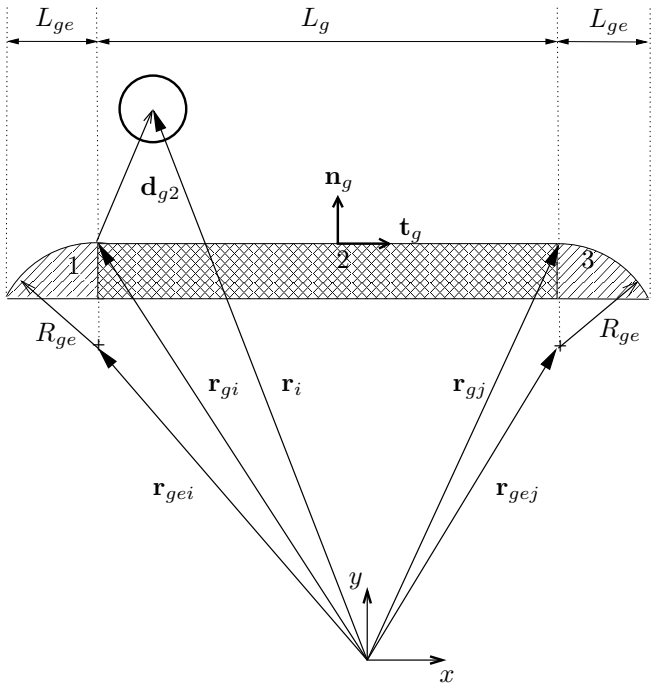

Figure 3.22: Contact with the guide-bar area 2 (flat part)

the rounded ends, see Figure D.3 and Figure D.4 in the appendix. The following three conditions have to be fulfilled for the contact to appear with the rounded end, area 1

$$\text{Contact condition for area 1:} \begin{cases} \mathbf{d}_{g2}^T \mathbf{t}_g < 0 \\ \mathbf{d}_{g2}^T \mathbf{t}_g > -L_{ge} \\ \delta_{g1} > 0 \end{cases} \tag{3.89}$$

where δ_{g1} is the pseudo penetration given by

$$\delta_{g1} = R_{ge} - \|\mathbf{d}_{g1}\| \tag{3.90}$$

and the normal vector to the contact surface for area 1 is given by

$$\mathbf{n}_{g1} = \frac{\mathbf{d}_{g1}}{\|\mathbf{d}_{g1}\|} \tag{3.91}$$

The following three conditions have to be fulfilled for the contact to appear with the rounded end, area 3

$$\text{Contact condition for area 3:} \begin{cases} \mathbf{d}_{g2}^T \mathbf{t}_g < L_g + L_{ge} \\ \mathbf{d}_{g2}^T \mathbf{t}_g > L_g \\ \delta_{g3} > 0 \end{cases} \tag{3.92}$$

where δ_{g3} is the pseudo penetration given by

$$\delta_{g3} = R_{ge} - \|\mathbf{d}_{g3}\| \tag{3.93}$$

and the normal vector to the contact surface for area 3 is given by

$$\mathbf{n}_{g3} = \frac{\mathbf{d}_{g3}}{\|\mathbf{d}_{g3}\|} \tag{3.94}$$

The contact force on the rollers is given by (3.47), with the normal vector $\mathbf{n}$ for the different contact areas calculated by (D.2) (see appendix D), (3.91) or (3.94). The relative velocity is equal to the velocity of the roller, because the guide-bar position is fixed. The indentation δ in equation (3.47) is for the different contact areas calculated by (3.88), (3.90) or (3.93). The stiffness coefficient calculated from (3.30) using material data for the guide-bar and roller; the same value is used for all guide-bar contact areas.

Indentation of Guide-bar and Rotated Guide-bar

If the end points of the guide-bar are placed on the tangent line between the sprockets, then the initial indentation of the guide-bar into the chain is zero. In order to investigate the effect of other values of the indentation the end points is translated along the $\mathbf{n}_g$ vector, see Figure D.5 in appendix D. Having the new guide-bar end points coordinates for the rotated guide-bar the contact detection follows as described prior in this section.

At the present the guide-bars in the marine diesel engines are fixed parallel to the tangent line between the sprockets. However it might be desirable to investigate whether a small rotation of the guide-bar with respect to the tangent line could reduce the contact forces on the guide-bar. In the model the rotation of the guide-bar is chosen to be around the middle point of the guide-bar, see Figure D.6 in appendix D. The angle of rotation of the guide-bar is used to find the new global vectors to the rotated guide-bar end points. Having the new guide-bar end point coordinates for the rotated guide-bar the contact detection follows as described prior in this section. For further details see appendix D.

3.8.3 Balancing Wheels

In order to avoid excessive excitation when the frequency of excitation coincides with the natural frequency of the ship hull vibrations it is relevant to consider outbalancing, see MAN B&W (1995). Dependent on the engine type, some of the sprockets in the chain drive system are fitted with counterweights which can reduce the vertical moment.

In some engine types resonance can occur with a frequency corresponding to twice the engine speed, this is when the 2nd order moment acts, which only acts in the vertical direction. Figure 3.23 shows how the 2nd order moment compensators are located on the aft end and fore end of the engine.

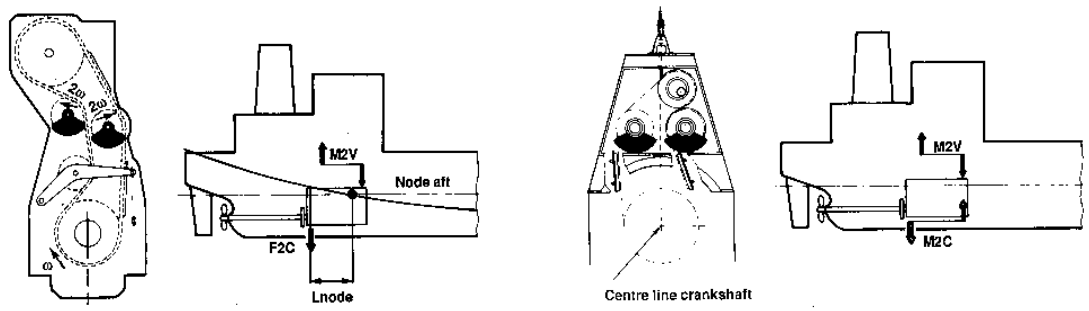

Figure 3.23: The location of the 2nd order compensators on the aft end and the fore end (from MAN B&W (1995))

In the 2D simulation program the influence of the 2nd order moment compensators are included in the moment of inertia of the sprocket as in equation (2.8), by using Steiner's theorem.

3.9 Friction

The roller chain drive system is at all times lubricated, which reduces the friction, but friction will always be present. Friction has, therefore, been included in the continuous contact force method between the rollers and the sprockets. From a numerical point of view this is advantageous, since the inclusion of friction will damp out some of the high force peaks in the beginning of the contact. The Coulomb modelling of friction, is used with a modification of the standard formulation, see e.g. Bagci (1975), Threlfall (1978), Rooney and Deravi (1982), Haug et al. (1986) García de Jalón and Bayo (1994).

In Figure 3.24 v is the relative velocity between the block and the ground. The standard friction force f_f is given by

$$\begin{array}{ll} \text{Slip (dynamic)} & f_f = \mu_d F_n \\ \text{Stick (static)} & f_f \leq \mu_s F_n \end{array}$$

where F_n is the normal force ($F_n > 0$) to the contact surface, μ_d is the dynamic friction coefficient and μ_s is the static friction coefficient, with $\mu_s > \mu_d$. The state conditions are

Stick to slip:	$f_f > \mu_s F_n$
Slip to stick:	Change in sign of $\dot{x}$

where $\dot{x}$ is the relative velocity. In a continuous analysis method the detection of stiction is performed during the contact. When the relative tangential velocity of the impacting bodies approaches zero stiction occurs. Sliding occurs when the normal force is not large enough to separate the two bodies in contact.

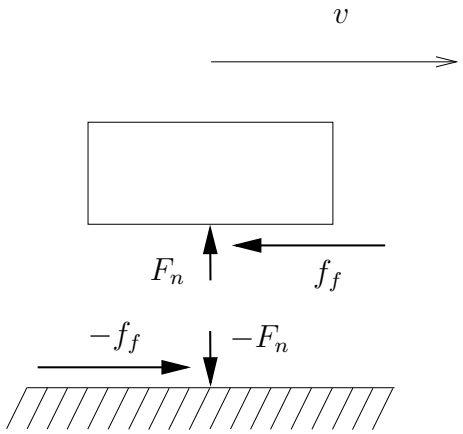

Figure 3.24: The friction force between a block and ground.

The friction force dependency of the relative velocity is modified by introducing a dynamic correction factor that prevents the friction force from changing direction for almost zero values of the tangential velocity, see Figure 3.25. This direction change of the friction force is perceived by the integration algorithm as a dynamic response with high frequency contents, which results in a reduction of the time step size. The different modifications of the friction force shown in Figure 3.25 are a linear modification (solid line), a polynomial modification (dashed-dotted line), a super elliptic modification (dotted line), a Bézier curve modification (dashed-dotted line), three different Heaviside modifications (dashed lines) and the standard friction model (solid line), see appendix G.

Including the modification the friction force vector is given by

$$\mathbf{f}_f = -\mu_d \mu_c F_n \frac{\mathbf{v}_t}{\|\mathbf{v}_t\|} \tag{3.95}$$

where μ_d is the dynamic friction coefficient, μ_c is the dynamic correction factor, $\mathbf{v}_t$ is the relative tangential velocity vector and $\|\mathbf{v}_t\|$ is the 2-norm of the relative tangential velocity vector. The relative tangential velocity is given by (3.67). Figure 3.25 shows friction force $f_f(v_t)$ normalized with respect to the normal force F_n. Since the friction force work in the opposite direction of velocity $f_f(v_t)$ is given by

$$f_f(v_t) = -\mathrm{sgn}(v_t)\mu_d\mu_c F_n \tag{3.96}$$

where $\mathrm{sgn}(v_t)$ is the signum function of the relative tangential velocity. The friction force in Equation (3.96) is applied to the roller while the friction force applied on the sprocket is $-f_f(v_t)$. The friction model represented by Equation (3.96) does not account for stiction between the contacting surfaces, but only represents the presence of sliding.

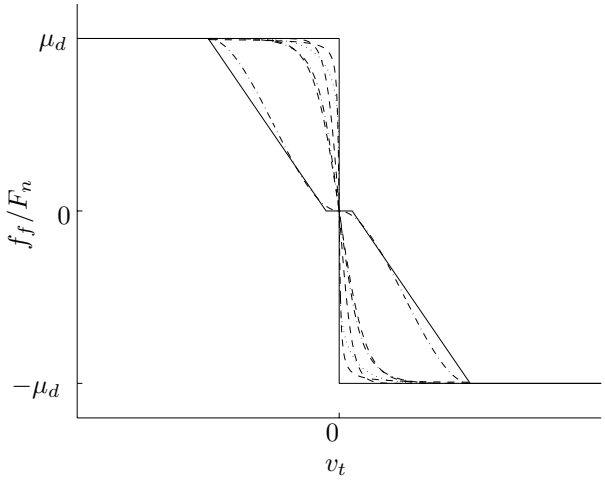

Figure 3.25: Different modifications of the friction force f_f normalized with respect to the normal force F_n as a function of the relative tangential velocity v_t.

Ambrósio (2003) suggested a linear dynamic correction factor as shown in Figure 3.26 (dotted line), which initiated the use of a polynomial correction factor in order to avoid the discontinuities, (dashed line in Figure 3.26). Several other methods exist as discussed in appendix G. In Figure 3.26 a Heaviside approximation (dashed-dotted line) is shown as an example.

Using the polynomial approximation the dynamic correction factor is given by

$$\mu_c(|v_t|) = \begin{cases} \frac{1}{(v_t^*)^3}|v_t|^2(3v_t^* - 2|v_t|), & 0 \leq |v_t| < v_t^* \\ 1, & |v_t| > v_t^* \end{cases} \tag{3.97}$$

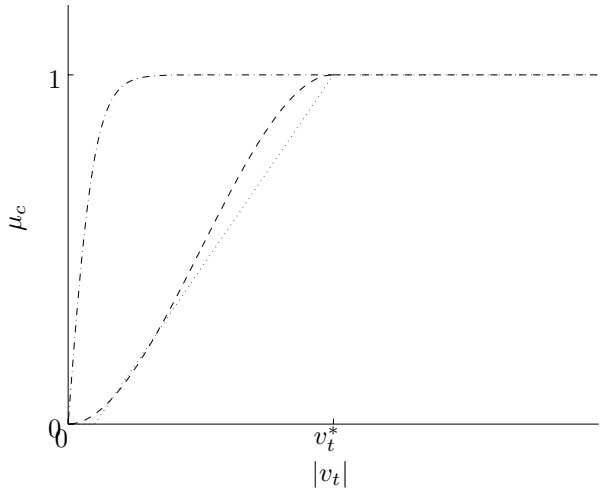

Figure 3.26: The dynamic correction factor μ_c as a function of the absolute value of the relative tangential velocity v_t.

where v_t^* is a chosen velocity that defines the area in which the dynamic correction factor is used, see Figure 3.26. Using the Heaviside approximation $H_1(x)$ the dynamic correction factor is given by

$$\mu_c(|v_t|) = \begin{cases} \tanh\left(\frac{|v_t|}{v_t^*\epsilon}\right), & 0 \leq |v_t| < v_t^* \\ 1, & |v_t| > v_t^* \end{cases} \tag{3.98}$$

where in Figure 3.26 the Heaviside approximation for $\epsilon = 0.01$ is shown. While small values of v_t^* makes the approximation closer to the idealised model it will result in slowing down the integration method. For small values of v_t^*, small relative to the velocity v_t, the difference between the use of the different correction factors is minimal.

3.10 Summary

In this chapter a mathematical model of a roller chain drive system is presented. Different contact models between the roller chain and the sprockets has been presented and discussed. Mathematical models of how different parts in the chain drive system, such as guide-bars, tightener systems and out balancing wheels can be included is presented and a friction model is presented.

Chapter 4
Numerical Simulation and Analytical Results

4.1 Introduction

The numerical integration of the equations of motion for the chain drive system modelled, as described in chapter 3, is carried out using an ordinary differential equation solver, which is described in the first part of this chapter. The needed simulation conditions and assumptions are described.

The transient period of the numerical results are shortened by first finding the static equilibrium of the system and by comparing the applied power with the dissipated power in order to find steady state.

In part of the chapter analytical results are presented, i.e., analytical results for the eigenfrequencies of the chain strands between the sprockets, eigenfrequencies of the system, simplified analytical results for the link forces and contact forces between the rollers and sprockets and calculation of the critical damping of the numerical applied longitudinal damping in the chain links.

The analytical results are in the next chapter compared with results from numerical simulations. The analytical results for the contact forces are compared with those obtained numerically and the eigenfrequencies of the chain drive system are used to identify the frequency peaks obtained in the numerical simulations.

4.2 Ordinary Differential Equation Solver

In the simulation procedure a numerical integration routine called ODE is used. This routine is a predictor-corrector variable step/order algorithm from Shampine and Gordon (1975). The accelerations of the rollers and sprockets are integrated using ODE. The vector $\mathbf{y}^{(i)}$ consist of the positions and velocities of the rollers and sprockets and is given by

$$\mathbf{y}^{(i)} = \left\{ \begin{array}{c} \mathbf{q}^{(i)} \\ \dot{\mathbf{q}}^{(i)} \end{array} \right\} \tag{4.1}$$

then the velocities and accelerations of the rollers and sprockets are given in the vector $\dot{\mathbf{y}}^{(i)}$ as

$$\dot{\mathbf{y}}^{(i)} = \left\{ \begin{array}{c} \dot{\mathbf{q}}^{(i)} \\ \ddot{\mathbf{q}}^{(i)} \end{array} \right\} \tag{4.2}$$

The vector $\mathbf{y}^{(i)}$ contains the positions and velocities at time $t = t^i$ and vector $\dot{\mathbf{y}}^{(i)}$ contains the velocities and accelerations at time $t = t^i$. By numerical integration of the vector $\dot{\mathbf{y}}^{(i)}$ the positions and velocities $\mathbf{y}^{(i+1)}$ at time $t^{i+1} = t^i + \Delta t$ is obtained. The initial conditions at $i = 0$ on $\mathbf{q}$ and $\dot{\mathbf{q}}$ are required to start the numerical integration process. The accelerations $\ddot{\mathbf{q}}$ are, at any time step, calculated by solving the equations of motion for the system.

The integrator ODE adjusts the step size and the interpolation order to control the error. When higher frequency content is detected in the dynamic response of the roller-chain drive the time step is decreased. In the case where a roller is captured on a sprocket or a guide-bar the integrator detects this as a discontinuity and the time step size is decreased.

In the simulation procedure it is necessary that the initial positions of the rollers are close to the equilibrium positions. The rollers are initially placed approximately on the tangent lines between the sprockets, see appendix A, such that the distance between each roller equal to the pitch plus pre-tension length. In the last segment this may (dependent on the given data) lead to a small gap. Therefore, in the last chain segment the distance between each roller is fit in order to eliminate the gap. The velocities are initially set to zero or alternatively the positions and velocities can be given in an input file.

Since the roller positioning depends on an approximate pre-tension which is given as input, the initial positions of the rollers are close to the equilibrium positions, but it is desirable to start the numerical simulations from static equilibrium, so that a steady state of the numerical simulation is reached faster.

The link force on a roller is calculated by (3.7) and the contact force on a roller by (3.48). If friction and rotational damping on the links are included these are calculated respectively by (3.95) and (3.17). All forces on a roller are added and put in the force vector on the right hand side of (3.2). The accelerations for all the rollers are calculated at the

same time by solving (3.2), since all the rollers are treated as free rollers in the plane. The accelerations of the driven sprockets are calculated by (3.9), where as the acceleration of the driver sprocket is given as a function of time. This function may or may not be constant. If a tightener system is included the acceleration of the tightener sprocket and the bodies in the tightener system are calculated by solving (3.86) When all accelerations of the rollers for a given time step j are calculated the auxiliary vector $\dot{\mathbf{y}}_{t=t_0+j\Delta t}$ is formed with the velocities and accelerations of all the sprockets and all the rollers. By integrating the auxiliary vector the positions and velocities for the system in the next time step are obtained.

For each step the integration routine takes it is checked which rollers are in contact with a sprocket or a guide-bar. However, a new contact is only allowed when the integration routine is updating and not during prediction and this is controlled by an implemented flag in the integration routine. Only the two first and the two last bedded rollers are checked for release from a sprocket or a guide-bar and only the two rollers respectively before and after these two rollers are checked for contact with the sprocket.

4.3 Simulation Conditions

The large roller chain drive systems are stiff systems for the numerical integration routine to solve, so the simulation time is large. The system is stiff due to the fact that the system consists of fast and slow components, so the eigenvalues are widely spread, see e.g. Nikravesh (1988). The use of the nonlinear contact force model combined with the overall motion of the roller chain drive system leads to rapid changes in the velocities and accelerations, which explain why the system is stiff. In order to prevent that the numerical errors of the results increases, a small time step must be applied.

A very small time step is also required in order for the contact forces to be applied close to the instant when contact occurs. The numerical integration routine ODE reduces the time step size, when a dynamic response with high frequencies is detected and the number of time steps needed may exceed to an amount which is undesirable, and the conditions for the numerical procedure must be controlled.

A short simulation time is desirable and discontinuities are avoided as far as possible. In order to minimize the simulation time several approaches are implemented for the upstart of the integration to be smooth. Special attention is brought to the acceleration of the

driver sprocket, both when it is running at constant angular velocity or at an oscillating angular velocity and a smooth transition is applied. Before running a simulation static equilibrium is found and the results are analysed when a steady state is reached.

The inclusion of the tightener system, implies that the equations of motion are described by a coupled set of differential and algebraic equations and the error response of such systems are sensitive to constraint violation. Stabilization techniques, such as Baumgarte Stabilization see e.g. García de Jalón and Bayo (1994), can be applied in order to keep the constraint violation under control. In the chain drive simulation program, this has not been included.

4.3.1 Acceleration of Driven Sprocket

Constant Angular Velocity

In order not to enforce a discontinuity, the driving sprocket is slowly accelerated during the first 2 seconds of the simulation and after these 2 seconds the sprocket rotates with constant speed. That is if no initial velocities are given for the system. These 2 seconds is in the following equations denoted t_c. The polynomial acceleration for an engine with the driver velocity v_{rpm}, given in rounds per minute, is given by

$$\ddot{\theta}_s = \begin{cases} \frac{v_{rpm}}{60} 2\pi \frac{6}{t_c^3} t(t_c - t) & 0 < t \leq t_c \\ 0 & t > t_c \end{cases} \tag{4.3}$$

this gives the velocity

$$\dot{\theta}_s = \begin{cases} \frac{v_{rpm}}{60} 2\pi \frac{6}{t_c^3} t^2 (\frac{t_c}{2} - \frac{1}{3}t) & 0 < t \leq t_c \\ \frac{v_{rpm}}{60} 2\pi & t > t_c \end{cases} \tag{4.4}$$

the acceleration function and velocity function are shown respectively in Figure 4.1 and Figure 4.2, for the case of $v_{rpm} = 76\text{rpm} = 7.96$ rad/s. Though the angular speed of the driving sprocket is constant after 2 seconds the angular speeds of the driven sprockets will vary with time, this is due to the polygonal action.

Oscillating Angular Velocity

Due to the fact that the engine ignition takes place in a special order and the cylinders ignite at different times, the angular velocity of the crankshaft (driver sprocket) will not be constant. The angular velocity and angular acceleration are as an example shown in Figure

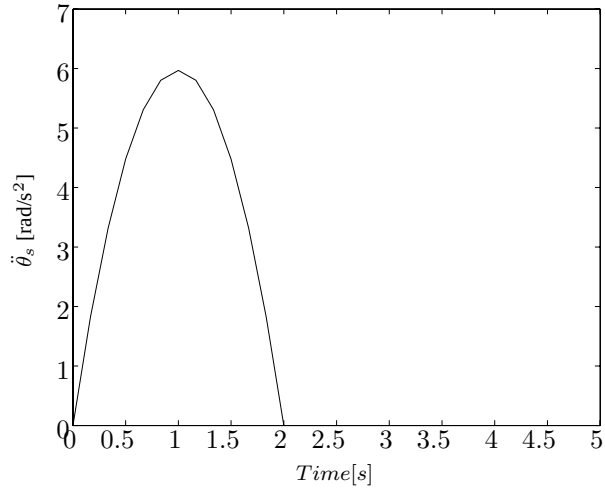

Figure 4.1: Acceleration curve

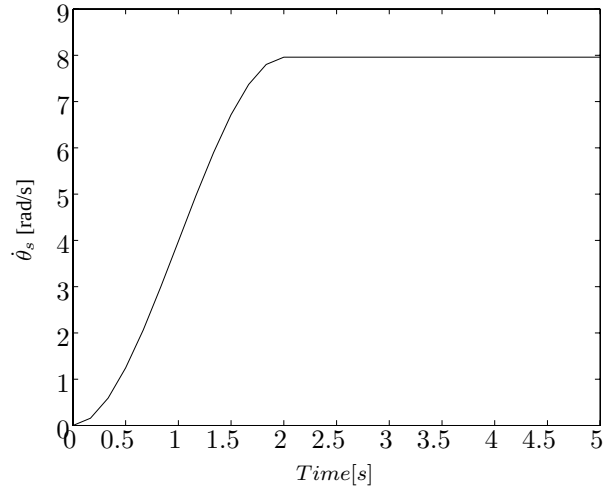

Figure 4.2: Velocity curve

4.5 and Figure 4.3 respectively, where the mean driver velocity is $v_{rpm} = 76$rpm $= 7.96$ rad/s, yielding the driving cyclic frequency $f_\Omega = 76/60 = 1.27$ Hz.

The order of the cyclic frequency content of the angular acceleration is $k = f_\omega / f_\Omega$, where f_Ω is the driving cyclic frequency and f_ω is the cyclic frequency content, see Figure 4.4. The variation of the angular acceleration has been included in the program, by including a file with the angular acceleration as a function of the angular rotation of the sprocket. A cubic spline function is used in order to find the acceleration for any given angle at a given time step. To get a good approximation, with the cubic spline function, of the angular acceleration the input file must included angles in an interval larger than $[0°; 360°]$, e.g. $[-10°; 370°]$. This is due to the fact that the periodicity of the driving sprocket is $360°$. In

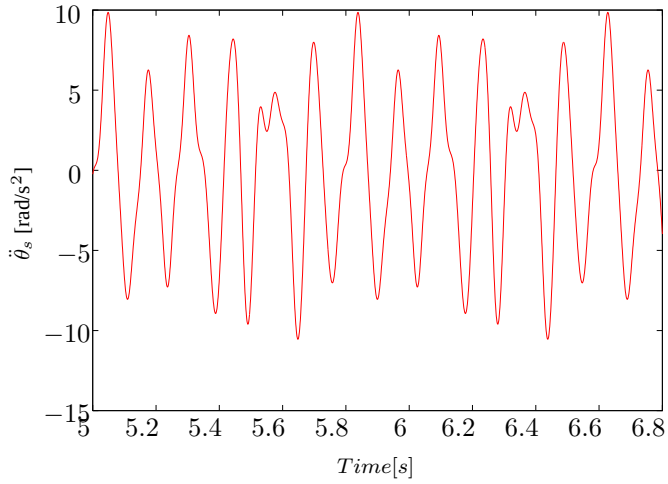

Figure 4.3: The angular acceleration of a 6S90MC engine

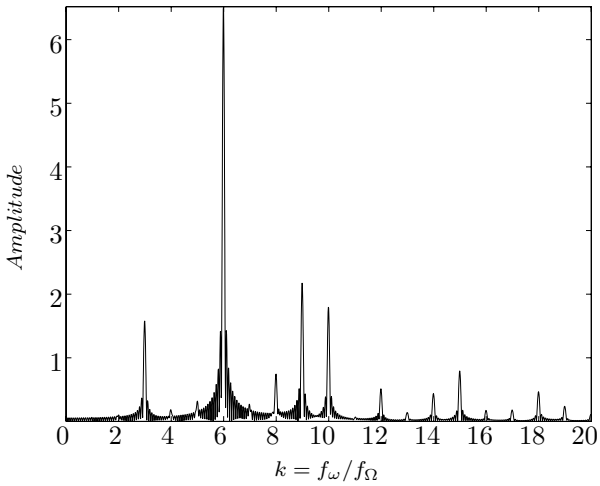

Figure 4.4: The relative frequency (order) content of the angular acceleration of an 6S90MC engine, $f_\Omega = 1.27Hz$

order to make a smooth transition from a constant angular acceleration to an oscillating angular acceleration, a linear scaling is used in a time interval of e.g. 1 second. In Figure 4.6 is shown the angular acceleration as a function of time, with the parabolic upstart ($t \in [0s; 2s]$), the oscillating angular acceleration with a linear scaling ($t \in [2s; 3s]$), and the oscillating angular acceleration ($t \in [3s; 4.5s]$). Figure 4.7 shows the angular velocity resulting from the angular acceleration shown in Figure 4.6.

Other excitations has been applied, such as a single sinus excitation given by

$$\ddot{\theta}_s = A \sin k\varphi_\tau, \quad \varphi_\tau \in [0; 2\pi] \tag{4.5}$$

where A is the amplitude and k is the excitation order. The relation between the angle φ_τ and time t is given by

$$\varphi_\tau = \frac{2\pi}{t_r} t \tag{4.6}$$

where the revolution time of the driving sprocket $t_r = \frac{60}{v_{rpm}}$.

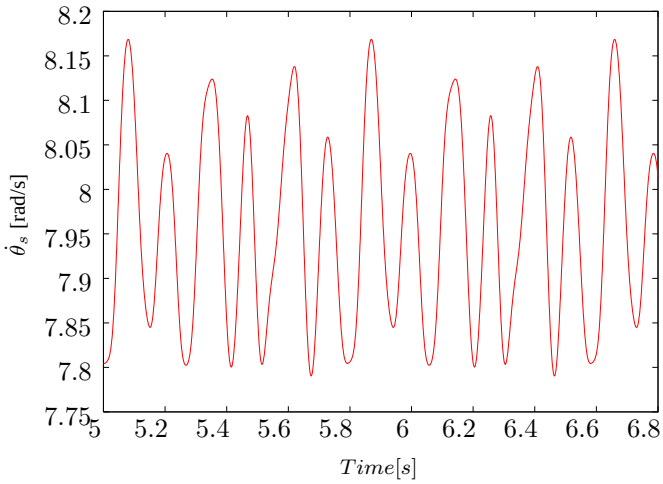

Figure 4.5: The angular velocity of a 6S90MC engine

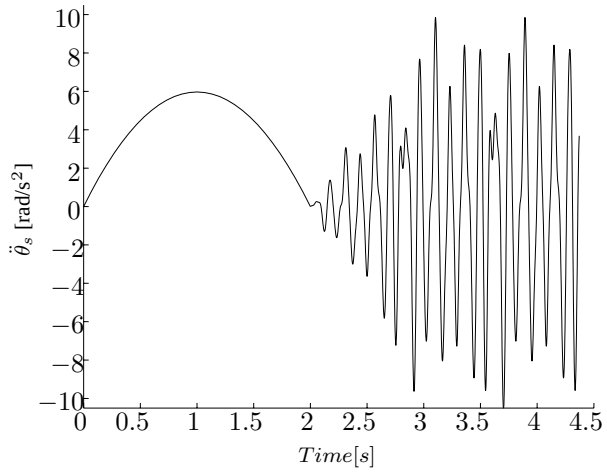

Figure 4.6: The angular acceleration of a 6S90MC engine

4.3.2 Assumptions

The nonlinear contact force in (3.47) depends on the relative velocity at impact and the relative velocity. Initially it is assumed that ratio between the relative velocity at impact and the relative velocity is

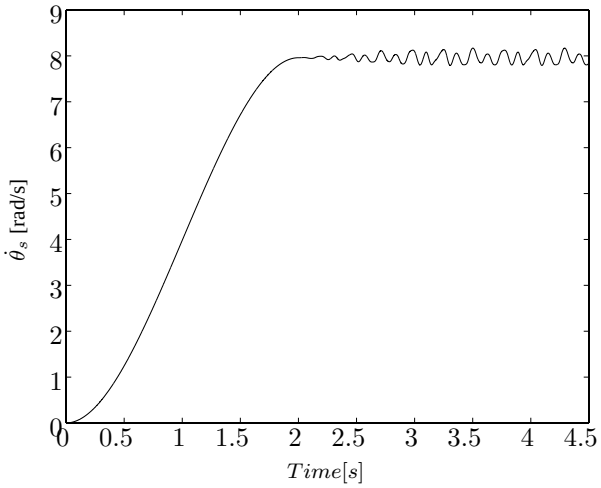

Figure 4.7: The angular velocity of a 6S90MC engine

$$\frac{v}{v^{(-)}} = 1.0 \tag{4.7}$$

This is because the speeds in the beginning of a simulation are equal to zero. Since there at all times will be rollers seated on the sprockets, this would cause a problem.

The rollers are not allowed to leave the sprocket until the roller has followed the sprocket by an angle equal to a quarter of the pitch angle. This is done in order to prevent all of the rollers in contact with a sprocket to get out of contact at the same time, which is unrealistic. Since a quarter of the pitch angle is small compared to the angle of contact on a sprocket and the fact that the contact force is zero when there is no indentation, this is assumed to have no influence on the rollers in contact.

4.3.3 Impact Detection Problem

With the single point contact model and the rectangular tooth profile applied, the tangential contact forces increased to an extent where the numerical integration routine was not able to solve the problem. With the semi real tooth profile applied, it only worked when the generalized stiffness coefficient in the contact force was modelled to increase with the indentation size, which means that a small indentation was allowed. Different values of the data used for the chain drive system made the system too stiff for the integrations to continue, so that this method was not useful in practice.

With the circular tooth profile applied it turned out to have a positive effect on the simulation due to the smooth contact surface. However the model still had numerical problems

with, on some occasions, being too stiff for the numerical integration routine to solve. A flag was implemented in order to check if the indentation at impact was larger than a prescribed tolerance. If this was the case the integration routine used was forced to reject the time step and a new time step smaller than the previous was tested. If the prescribed tolerance of the impact indentation was set to be too small, the numerical simulation still could become unstable. As an alternative to the described method an iterative procedure, such as Newton-Raphson, could also have been applied in order to find the moment in time where the instant of contact occurs.

With the real shaped tooth profile applied none of the above mentioned approaches regarding the impact was necessary, due to the smooth contact surface.

4.3.4 Static Equilibrium

The static equilibrium is found by integrating the equations of motion until $\dot{\mathbf{q}} = \ddot{\mathbf{q}} = \mathbf{0}$ to within a numerical tolerance. Artificial damping is applied to the system in order to accelerate the convergence to an equilibrium configuration. This method is easy to implement, but requires substantial computing time. The initial conditions for the system are chosen close to the equilibrium configuration that actually occurs. This is a necessary condition, because a dissipative nonconservative system may have many equilibrium configurations. This approach is also known as the dynamic settling approach, see e.g. Haug (1989). Other methods exist such as for an example the Minimum Total Potential Energy approach, but in this work the dynamic settling approach has been used.

4.3.5 Steady State

In order to analyse the numerical results a steady state must be reached. We want to remove transient behaviour resulting from the modelling of the simulation start up. Steady state in the numerical model is reached when the applied power is equal to the dissipated power. The applied power is the power needed to drive the driver sprocket with the angular velocity ω_s and is given by

$$P_{driver} = -\tau_s \omega_s \tag{4.8}$$

where τ_s is the moment calculated by the contact forces given by Equation (3.68). The power dissipated in the chain drive system is dissipated in the longitudinal damping in the links, rotational damping in the links, damping in the contact force and friction between

the rollers and sprockets. The dissipated power due to longitudinal damping in the links is given by

$$P_{ld} = \sum_{i=1}^{n_l} D\dot{l}_i^2 \tag{4.9}$$

where n_l is the number of links in the chain, D is the longitudinal damping coefficient, $\dot{l}_i$ is the time rate of change in the length of the link given by Equation (3.4). The dissipated power due to rotational link damping is given by

$$P_{rd} = \sum_{i=1}^{n_l} C_d\dot{\varphi}_i^2 \tag{4.10}$$

where C_d is the rotational damping coefficient and $\dot{\varphi}_i$ is the angle velocity given by Equation (3.15). The dissipated power due to damping in the contact between the rollers and the sprockets or guide-bars is given by

$$P_{cd} = \sum_{i=1}^{n_c} D_c(v_n)_i^2 \tag{4.11}$$

where n_c is the number of rollers in contact with either a sprocket or a guide-bar, D_c is the contact damping coefficient given by Equation (3.46) and $(v_n)_i$ is the relative velocity in the normal direction for roller i. The dissipated power due to the friction between the roller and sprockets in contact is given by

$$P_f = \sum_{i=1}^{n_c} \mu_d\mu_c F_n|(v_t)_i| \tag{4.12}$$

where μ_d is the dynamic friction coefficient, μ_c is the dynamic correction factor, F_n is the normal force on a roller and $|(v_t)_i|$ is absolute value of the relative velocity in the tangential direction for roller i. The total dissipated power is given by

$$P_T = P_{ld} + P_{rd} + P_{cd} + P_f \tag{4.13}$$

When $P_T = P_{driver}$ integrated over a period corresponding to one turn of the driver sprocket, steady state of the numerical simulation is reached.

4.4 Analytical Results

Several researchers have worked with analytical results for chain drives, see e.g. Binder (1956), Mahalingam (1957) and Naguleswaran and Williams (1968). The analytical

results presented in this section are mainly taken from Mahalingam (1957) and Naguleswaran and Williams (1968) and the analytical results for contact forces between rollers and sprockets are taken from Binder (1956).

4.4.1 Natural Frequencies of a Pre-tensioned String

The natural frequencies of the chain segments between the sprockets can be analysed by looking at transversal vibrations of a pre-tensioned string. The pre-tension force is F, the length of the string is l and m_l is the mass per unit length, see Figure 4.8 and 4.9.

Figure 4.8: A pre-tensioned string.

The system configuration and the forces acting on an infinitesimal piece of the chain string is shown in Figure 4.9 and 4.10.

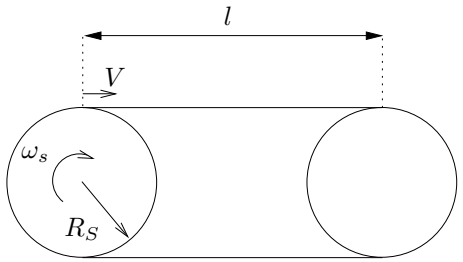

Figure 4.9: The chain string between two sprockets.

The chain string velocity V is $\omega_s R_s$, where ω_s is the angular velocity of the sprocket and R_s is the radius of the sprocket.

Force and moment equilibrium of the infinitesimal piece of string shown in Figure 4.10, assuming no gravity, gives

$$\uparrow: (T + \mathrm{d}T) - T = m_l \frac{D^2 y}{Dt^2} \mathrm{d}x \Rightarrow \qquad T' = m_l \frac{D^2 y}{Dt^2} \tag{4.14}$$

$$\rightarrow: (N + \mathrm{d}N) - N = 0 \Rightarrow \qquad N' = 0 \tag{4.15}$$

$$\curvearrowleft: (M + \mathrm{d}M) - M + T\mathrm{d}x - N\mathrm{d}y = 0 \Rightarrow \qquad M' + T - Ny' = 0 \tag{4.16}$$

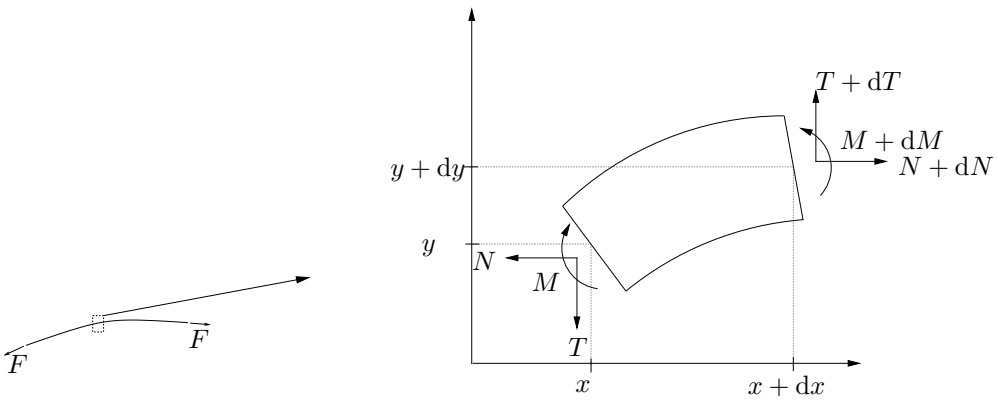

Figure 4.10: The pre-tensioned moving chain string and an infinitesimal cutout of the it.

where N' is defined as $\frac{\partial N}{\partial x}$, T' is defined as $\frac{\partial T}{\partial x}$, and so forth. The prefix ∂ is used for partial derivative, the prefix d for differential derivative and the prefix D for the total derivative of a function of more than one variable. Differentiating (4.16) with respect to x yields

$$M'' + T' - (Ny')' = 0 \tag{4.17}$$

Since it is assumed that the chain has no bending stiffness $EI = 0$, where E is Young's Modulus and I is the cross-sectional moment of inertia, HookeŠs law $M = EIy''$ implies that $M = 0$. Inserting (4.14) into (4.17) gives

$$(Ny')' = m_l \frac{D^2 y}{Dt^2} \tag{4.18}$$

Equation (4.15) implies that $N(x,t)$, with the boundary conditions $N(0,t) = F$ and $N(l,t) = F$, is constant $N(x,t) = F$. Since $y = y(x,t)$ and $x = x(t)$ the derivatives of y with respect to time becomes

$$\frac{Dy}{Dt} = \frac{\partial y}{\partial t} + \frac{\partial y}{\partial x}\frac{\mathrm{d}x}{\mathrm{d}t} \tag{4.19}$$

$$\frac{D^2 y}{Dt^2} = \frac{\partial^2 y}{\partial t^2} + 2\frac{\partial^2 y}{\partial t \partial x}\frac{\mathrm{d}x}{\mathrm{d}t} + \frac{\partial^2 y}{\partial x^2}(\frac{\mathrm{d}x}{\mathrm{d}t})^2 + \frac{\partial y}{\partial x}\frac{\mathrm{d}^2 x}{\mathrm{d}t^2} \tag{4.20}$$

Assuming that the chain string velocity is constant, $\frac{\mathrm{d}x}{\mathrm{d}t} = V$ and $\frac{\mathrm{d}^2 x}{\mathrm{d}t^2} = 0$. Inserting (4.20) into (4.18) gives

$$Fy'' = \underbrace{2m_l V \dot{y}'}_{Coriolis force} + \underbrace{m_l V^2 y''}_{Centrifugal force} + \underbrace{m_l \ddot{y}}_{Inertia force} \tag{4.21}$$

where $\dot{y}$ is defined as $\frac{\mathrm{d}y}{\mathrm{d}t}$ and $\ddot{y}$ is defined as $\frac{\partial^2 y}{\partial t^2}$. Equation (4.21) can be rewritten

$$c_0^2 y'' = 2V\dot{y}' + V^2 y'' + \ddot{y} \tag{4.22}$$

where the phase velocity of the wave c_0 is given by (see e.g. Graff (1991))

$$c_0 = \sqrt{\frac{F}{m_l}} \tag{4.23}$$

For the case of a non moving chain the radial natural frequencies for a finite string are found by setting $V = 0$ in (4.22) yielding

$$\omega_n = \frac{n\pi c_0}{l} = \frac{n\pi}{l}\sqrt{\frac{F}{m_l}} \tag{4.24}$$

and the cyclic natural frequencies $f_n = \frac{\omega_n}{2\pi}$ are given by

$$f_n = \frac{n}{2l}\sqrt{\frac{F}{m_l}} \tag{4.25}$$

For the case of a moving string $V \neq 0$ the general solution to (4.22), see e.g. Mahalingam (1957), is given by

$$y = A_1 \sin\left(\omega t + \omega x/(c_0 - V) + \phi_1\right) + A_2 \cos\left(\omega t - \omega x/(c_0 + V) + \phi_2\right) \tag{4.26}$$

where ω is the radial frequency, ϕ_1 and ϕ_2 are phase angles and A_1 and A_2 are amplitudes. Substituting the boundary conditions $y = 0$ at $x = 0$ and at $x = l$ in (4.26) gives the natural frequencies

$$\omega_n = \frac{n\pi}{l}\frac{c_0^2 - V^2}{c_0}, \quad n = 1, 2, 3 \cdots \tag{4.27}$$

and the mode of vibration is given by

$$y = \sin\left(\frac{n\pi x}{l}\right) \sin\left(\omega_n t + \frac{n\pi x}{l}\frac{V}{c_0} + \phi\right) \tag{4.28}$$

where ϕ is an arbitrary phase angle. Equation (4.27) implies that the natural frequency decreases as the string velocity V approaches the phase velocity c_0, see e.g. Mahalingam (1957) and Naguleswaran and Williams (1968). Figure 4.11 shows the cyclic natural frequency f_n as a function of the speed of the string.

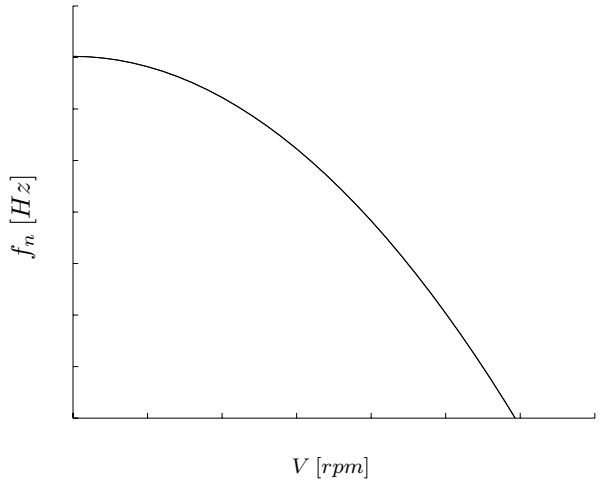

Figure 4.11: The natural frequency of the moving string as a function of the speed of the string.

4.4.2 Tension due to Centrifugal Force

When the chain is wrapped around the sprockets as shown in Figure 4.9 the tension in the moving chain string is greater than the static chain tension due to the centrifugal force, Mahalingam (1957) and Naguleswaran and Williams (1968). In Figure 4.12 is shown the effect of a chain being wrapped around the sprockets with a contact angle of π rad, see also Figure 4.9.

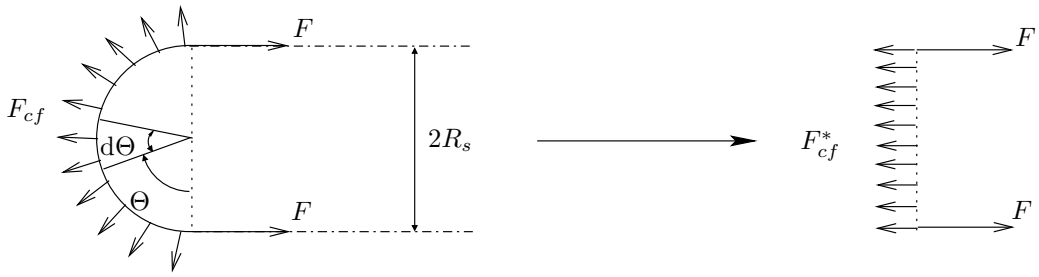

Figure 4.12: The tension due to centrifugal force.

The centrifugal force per unit length is $F_{cf} = m_l \frac{V^2}{R_s}$, with $V = \omega_s R_s$. The projection of the centrifugal force of a small element in the horizontal direction is $\mathrm{d}F^*_{cf} = F_{cf} R_s \mathrm{d}\Theta sin(\Theta)$. Assuming that the chain is in contact with the sprocket for $\Theta \in [0, \pi]$, the total projection of the centrifugal force in the horizontal direction is given by

$$F^*_{cf} = \int_0^{\pi} F_{cf} R_s \sin(\Theta) \mathrm{d}\Theta = 2R_s F_{cf} = 2m_l V^2 \tag{4.29}$$

When the contact angle between the chain and the sprocket is π rad, the tension force becomes

$$F = F_s + m_l V^2 \tag{4.30}$$

where F_s is the static tension force. For chain drive systems however the contact angle varies, depend on the placement of the sprockets relative to each other. Naguleswaran and Williams (1968) proposed that the extra tension due to the centrifugal force is given by

$$F = F_s + \eta m_l V^2, \quad \eta \in [0, 1] \tag{4.31}$$

where η describes the relaxation of the structure. Figure 4.13 shows the cyclic natural frequency f_n as a function of the speed of the string, for different values of η. In Figure 4.13 the solid line is for $\eta = 0$, the dashed line is for $\eta = 1$, the dotted line is for $\eta = 0.2$ and the dashed-dotted line is for $\eta = 0.5$.

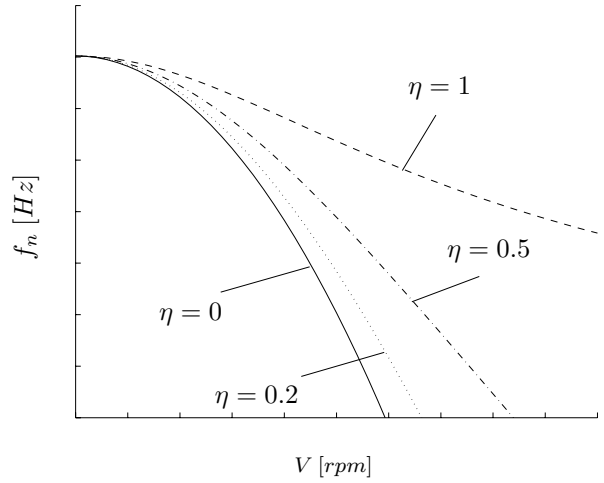

Figure 4.13: The natural frequency of the moving string as a function of the speed of the string, for different values of η. ($\eta = 0$, $\eta = 0.2$, $\eta = 0.5$ and $\eta = 1$)

4.4.3 Polygonal Action

The polygonal action, as described in section 3.6, is responsible for periodic transverse displacements at the end of the chain strings, due to engagement and disengagement. These forced vibrations due to transverse excitation are described in Mahalingam (1958) and Mahalingam (1957), where also the boundary conditions for (4.26) are given as

$$\begin{aligned} x = 0, \qquad & y = a_1 \cos(\omega_p t) \\ x = l, \qquad & y = a_2 \cos(\omega_p t + \phi_p) \end{aligned} \tag{4.32}$$

where ϕ_p is the phase difference between the two ends of the chain corresponding to the fractional pitch in the tangent length of the chain. The radial frequency ω_p is the frequency of the tooth engagement given by

$$\omega_p = \frac{2\pi V}{P} \tag{4.33}$$

where P is the pitch of the chain. Forced vibrations due to the polygonal action may reach resonance when the frequency of the tooth engagement is equal to the natural frequency of the moving chain string. In Mahalingam (1957) it was pointed out that the fluctuating tension, which arises mainly from the polygonal action of the sprockets is an important vibration effect of the system.

4.4.4 Vibrations due to Longitudinal Excitation

For the case of one of the sprockets in the system being subjected to torsional vibrations, Mahalingam (1957) indicated that the stability of the chain would be determined by the solutions to an equation of the Mathieu type, but the work was not taken further. In Naguleswaran and Williams (1968) this work was continued and the stability of a moving band was described using a Galerkin manifold.

When a sprocket is subjected to torsional vibrations, the tension of the chain string will be

$$F = F_s + \eta m V^2 + \Delta F_s \cos(\omega_t t) \tag{4.34}$$

where ω_t is the radial frequency of the torsional vibration of the sprocket. Substituting the tension force including the extra tension from torsional vibrations into (4.22) the equation of motion becomes

$$(c_0 + \Delta c_0 \cos(\omega_t t))y'' = 2V\dot{y}' + V^2 y'' + \ddot{y} \tag{4.35}$$

where $c_0 = \sqrt{\frac{F_s + \eta m V^2}{m_l}}$ and $\Delta c_0 = \sqrt{\frac{\Delta F_s}{m_l}}$. Using $y(x,t) = e^{i\mu x} y_0(t)$ and $\omega_t t = 2z$ as proposed in Mahalingam (1957) Equation (4.35) becomes

$$\ddot{y_0} + 2i\mu V \dot{y_0} + (c_0^2 + \Delta c_0^2 \cos(2z))\mu^2 y_0 = 0 \tag{4.36}$$

Substituting $y_0 = e^{-iV\mu z}u(z)$ into (4.36) as proposed in Mahalingam (1957) the equation becomes

$$\ddot{u} + (\mu^2 c_0^2 + \mu^2 \Delta c_0^2 \cos(2z))u = 0 \tag{4.37}$$

Equation (4.37) is an equation of the Mathieu type. For the case where the torsional vibrations of the sprocket is not a single harmonic function, but a general periodic excitation function Equation (4.37) becomes

$$\ddot{u} + (\mu^2 c_0^2 + \mu^2 \Delta c_0^2 \varpi(z))u = 0 \tag{4.38}$$

where $\varpi(z)$ is a periodic excitation function. Equation (4.38) is an equation of the Hill type, see e.g. Pedersen (1985).

Naguleswaran and Williams (1968) concluded that the most violent instability of a band occurs when the excitation due to fluctuation in band tension is at twice the lateral natural frequency of the band. The authors also concluded that the value of η has a strong influence on the location of the critical running speeds.

4.4.5 Effect of Damping on the Natural Frequency

Mahalingam (1957) investigated the influence of taking damping into account, by assuming a damping force proportional to the transverse velocity. This was done by adding the term $b(Vy' + \dot{y})$ to the equation of motion 4.22), where b is the damping coefficient divided by the mass per unit length. Mahalingam (1957) concluded that the resonant amplitudes decrease for an increase in the running speed. Naguleswaran and Williams (1968) also concluded that the resonant range is sensitive to the damping of the system.

The damping force in the vibrating chain is provided by the frictional resistance between the pins and bushes during the relative link motion, the resistance of air, influence of lubrication, etc. It is difficult to determinate the damping factors accurately, however Mahalingam (1957) verified experimentally that the suggested damping force approximation was fairly good.

4.4.6 Contact Force between Rollers and Sprockets

Binder (1956) described analytical results for the contact force between the roller and sprocket. These analytical results however only include two sprockets and thereby two chain segments of which only one of them was under tension and the other was slack. In

the case of more sprockets connected and different tension occurring in the segments, the analytical results presented here are extended, so both of the segments in contact with a sprocket may be under tension.

The link forces f_l in the n_b links of rollers in contact with a sprocket are

$$(f_l)_i = q_a\Big(\frac{\sin(\zeta)}{\sin(\zeta+\alpha)}\Big)^i + q_b\Big(\frac{\sin(\zeta)}{\sin(\zeta+\alpha)}\Big)^{n_b-i+1} + q_c, \qquad i = 1,\ldots,n_b \tag{4.39}$$

where the angle ζ, referred to as the pressure angle, see Binder (1956), is defined by

$$\zeta = 35^\circ - \frac{120^o}{n_t} \tag{4.40}$$

and the contact forces f_c on the n_b bedded rollers in contact with a sprocket are

$$(f_c)_i = q_a\Big(\frac{\sin(\zeta)}{\sin(\zeta+\alpha)}\Big)^{i-1}\frac{\sin(\alpha)}{\sin(\zeta+\alpha)} + q_b\Big(\frac{\sin(\zeta)}{\sin(\zeta+\alpha)}\Big)^{n_b-i}\frac{\sin(\alpha)}{\sin(\zeta+\alpha)} + 2q_c\sin(\frac{\alpha}{2}), \quad i = 1,\ldots,n_b \tag{4.41}$$

where q_a is the tension in one segment, q_b is the tension in the other segment, α is the pitch angle, n_t is number of teeth on the sprocket and q_c is the centrifugal force given by

$$q_c = \frac{m_r V^2}{Pg}, \qquad V = \omega_s R_s \tag{4.42}$$

where m_r is the roller mass, P is the pitch, ω_s is the angular velocity of the sprocket, R_s is the radius of the sprocket and g is the gravitational acceleration.

4.4.7 Eigenfrequencies of the Chain Drive System

The equations of motion of an undamped free system are

$$\mathbf{M}\ddot{\mathbf{q}} + \mathbf{K}\mathbf{q} = \mathbf{0} \tag{4.43}$$

assuming the solution $\mathbf{q} = \mathbf{x}\cos(\omega t)$ one obtain the eigenvalue problem (EVP) for determination of ω and $\mathbf{x}$

$$(\mathbf{K} - \omega^2\mathbf{M})\mathbf{x} = \mathbf{0} \tag{4.44}$$

where ω^2 is an eigenvalue and $\mathbf{x}$ is an eigenvector. For nontrivial solutions $\mathbf{x} \neq \mathbf{0}$ to exist the determinant of the coefficient matrix must vanish

$$| \mathbf{K} - \omega^2 \mathbf{M} | = 0 \tag{4.45}$$

Solving (4.45) one obtain the n set of eigenfrequencies $\omega_i^2, i = 1, \ldots, n$.

The total stiffness matrix of the chain drive system is put together of a number of sub-matrices, where the sub-stiffness-matrix from each of the segments are

$$\mathbf{K}^* = \begin{bmatrix} 2K & -K & & & \\ -K & 2K & -K & & \\ & \ddots & \ddots & \ddots & \\ & & -K & 2K & -K \\ & & & -K & 2K \end{bmatrix} \tag{4.46}$$

The number of rows and columns in the sub-stiffness-matrix is equal to the number of free rollers in the segment. The sub-stiffness-matrix from the sprockets is, as shown below, given by

$$\mathbf{K}^* = \begin{bmatrix} 2KR_1^2 & & & & \\ & 2KR_2^2 & & & \\ & & \ddots & & \\ & & & 2KR_{n-1}^2 & \\ & & & & 2KR_n^2 \end{bmatrix} \tag{4.47}$$

The number of elements is equal to the total number of sprockets in the chain drive system minus one, because the driver sprocket is fixed rotationally. Hence the row and column associated with it is removed. The 2 by 1 matrices resulting from the contact between the two segment and a sprocket i are given by

$$\mathbf{K} = [-KR_i \quad -KR_i] \tag{4.48}$$

An example is shown in Figure 4.14 and 4.15.

The stiffness coefficient of the springs between the rollers are denoted k, the rotational angle of sprocket number 2 is θ_2, the radius is R_2 and the mass moment of inertia is J_2. Sprocket number 1 is fixed rotationally. The forces shown in Figure 4.15 are in the coordinate directions shown in Figure 4.14 given by

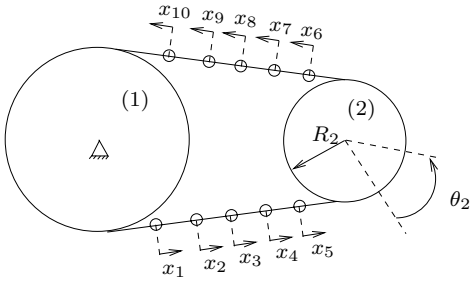

Figure 4.14: Chain drive system consisting of two sprockets.

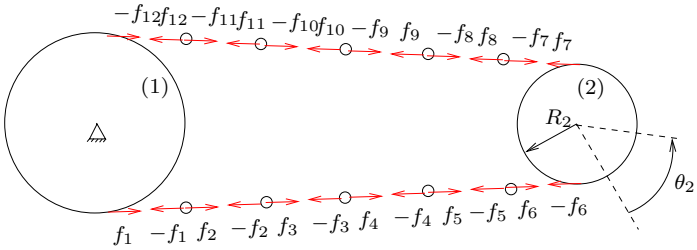

Figure 4.15: The forces in a chain drive system consisting of two sprockets.

$$
\begin{aligned}
f_1 &= Kx_1 \\
f_2 &= K(x_2 - x_1) \\
&\vdots \\
f_5 &= K(x_5 - x_4) \\
f_6 &= K(\theta_2 R_2 - x_5) \\
f_7 &= K(x_6 - \theta_2 R_2) \\
f_8 &= K(x_7 - x_6) \\
&\vdots \\
f_{11} &= K(x_{10} - x_9) \\
f_{12} &= Kx_{10}
\end{aligned}
\tag{4.49}
$$

From force equilibrium of each roller with mass m_r we obtain the equations of motion

$$\begin{aligned}
m_r\ddot{x}_1 = \quad & f_2 - f_1 = \quad -2Kx_1 + Kx_2 \\
m_r\ddot{x}_2 = \quad & f_3 - f_2 = \quad Kx_1 - 2Kx_2 + Kx_3 \\
& \vdots \\
m_r\ddot{x}_5 = \quad & f_6 - f_5 = \quad Kx_4 - 2Kx_5 + K\theta_2 R_2 \\
m_r\ddot{x}_6 = \quad & f_8 - f_7 = \quad Kx_7 - 2Kx_6 + K\theta_2 R_2 \\
& \vdots \\
m_r\ddot{x}_{10} = \quad & f_{12} - f_{11} = \quad -2Kx_{10} + Kx_9
\end{aligned} \tag{4.50}$$

From momentum equilibrium about the center of sprocket 2 we get the equation of motion

$$J_2\ddot{\theta}_2 = -f_6 R_2 + f_7 R_2 \tag{4.51}$$

The generalised system mass matrix $\mathbf{M}$ is given by

$$\mathbf{M} = \begin{bmatrix}
J_1 & & & & & & & & & \\
& m_r & & & & & & & & \\
& & \ddots & & & & & & & \\
& & & m_r & & & & & & \\
& & & & J_2 & & & & & \\
& & & & & m_r & & & & \\
& & & & & & \ddots & & & \\
& & & & & & & m_r & &
\end{bmatrix} \tag{4.52}$$

the system position vector is $\mathbf{q}^T = (\theta_1, x_1, \ldots, x_5, \theta_2, x_6, \ldots, x_{10})$ and $\mathbf{K}$ is the system stiffness matrix given by

$$\mathbf{K} = \begin{bmatrix}
KR_1^2 & -KR_1 & & & & & & & & -KR_1 \\
-KR_1 & 2K & -K & & & & & & & \\
& -K & 2K & -K & & & & & & \\
& & & \ddots & & & & & & \\
& & & -K & 2K & -K & & & & \\
& & & & -K & 2K & -KR_2 & & & \\
& & & & & -KR_2 & KR_2^2 & -KR_2 & & \\
& & & & & & -KR_2 & 2K & -K & \\
& & & & & & & -K & 2K & -K \\
& & & & & & & & \ddots & \\
-KR_1 & & & & & & & & -K & 2K
\end{bmatrix} \tag{4.53}$$

Applying the boundary condition that sprocket number one is fixed rotationally implies that the first row and column can be removed from both the mass matrix and the stiffness matrix and two matrices become band matrices. The stiffness matrix is in general given in appendix F. The eigenvalues of the system is found by solving (4.45), but this yields only the longitudinal natural frequencies of the chain.

4.4.8 Natural Frequencies of the Sprockets Alone

An alternative way of calculating the natural frequencies for the rotational vibrations of the sprockets is found by connecting the sprockets with springs. In Figure 4.16 is shown a chain drive system consisting of 5 sprockets connected with springs. The stiffness coefficient of the springs between the sprockets are calculated by

$$\begin{aligned} 1/K_i = \;& 1/K + 1/K + \ldots + 1/K = \;\; (n_i+1)/K \\ \Downarrow & \\ K_i = \;& \qquad\qquad K/(n_i+1) \end{aligned} \tag{4.54}$$

where n_i is the number of free rollers in segment i and K is the spring stiffness of the spring between two rollers.

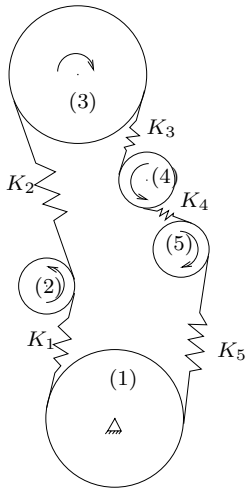

Figure 4.16: A chain drive system consisting of 5 sprockets connected with springs.

The mass moment of inertia of the sprockets including the part of the chain in connect with the sprocket is calculated using Steiner's theorem

$$J_i^* = J_i + m_i R_i^2 \tag{4.55}$$

where J_i is the mass moment of inertia of sprocket i, m_i is the mass of the rollers in contact with sprocket i and R_i is the radius of sprocket i. The equations of motion for the system shown in figure 4.16, where sprocket 1 is fixed rotationally, are

$$\begin{bmatrix} J_2^* & & & \\ & J_3^* & & \\ & & J_4^* & \\ & & & J_5^* \end{bmatrix} \begin{Bmatrix} \ddot{\theta}_2 \\ \ddot{\theta}_3 \\ \ddot{\theta}_4 \\ \ddot{\theta}_5 \end{Bmatrix} + \tag{4.56}$$

$$\begin{bmatrix} R_2^2(K_1+K_2) & -R_2R_3K_2 & & \\ -R_2R_3K_2 & R_3^2(K_2+K_3) & -R_3R_4K_3 & \\ & -R_3R_4K_3 & R_4^2(K_3+K_4) & -R_4R_5K_4 \\ & & -R_4R_5K_4 & R_5^2(K_4+K_5) \end{bmatrix} \begin{Bmatrix} \theta_2 \\ \theta_3 \\ \theta_4 \\ \theta_5 \end{Bmatrix} = \begin{Bmatrix} 0 \\ 0 \\ 0 \\ 0 \end{Bmatrix}$$

or written in compact form

$$\mathbf{J}^*\ddot{\theta} + \mathbf{K}\theta = \mathbf{0} \tag{4.57}$$

Solving (4.45) with the mass matrix and stiffness matrix from (4.57) the eigenfrequencies for the rotational vibrations of the sprockets are found.

4.4.9 Critical Damping

The critical damping coefficient in the longitudinal direction of the links are calculated by assuming that the chain is one long open string of springs connected and then approximating this with one mass and one spring connected with ground, see Figure 4.17.

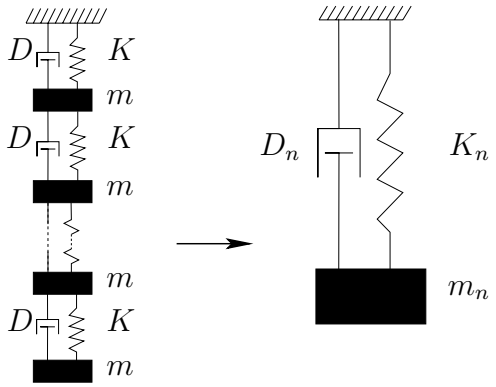

Figure 4.17: A open string of masses connected with springs approximated with a single mass connected with ground.

For the case of a series of springs connected we get the total spring stiffness

$$\begin{aligned} 1/K_n = &\quad 1/K + 1/K + \ldots + 1/K = \quad n/K \\ &\Downarrow \\ K_n = &\qquad\qquad\qquad K/n \end{aligned} \tag{4.58}$$

where K is the stiffness coefficient of each single spring and K_n is the total stiffness coefficient of n springs connected in a series. The total mass is $m_n = n \cdot m$, where m is the mass of one roller.

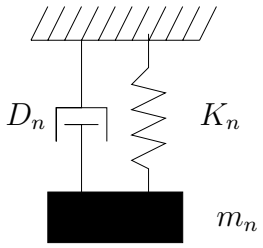

Figure 4.18: A single mass with a spring damper connection to ground.

The critical damping coefficient D_n is for a mass m_n connected with a spring with the stiffness K_n to the ground, as shown in Figure 4.18 given by

$$D_n = 2\sqrt{m_n K_n} \tag{4.59}$$

yielding

$$D_n = 2\sqrt{n \cdot mK/n} = 2\sqrt{mK} \tag{4.60}$$

So the critical damping D for each individual link given by

$$\begin{aligned} 1/D_n = &\quad 1/D + 1/D + \ldots + 1/D = n/D \\ &\Downarrow \\ D = &\qquad\qquad\qquad nD_n \end{aligned} \tag{4.61}$$

yielding

$$D = 2n\sqrt{mK} \tag{4.62}$$

The damping coefficient D is used as margin for which damping coefficient should be used.

4.5 Summary

In first part of this chapter the numerical integration routine used in the simulation program is presented and the used simulation conditions and assumptions are given. The advantage of using the real shaped tooth profile, compared with other tooth shape models from a numerical stability point of view is given. In the last part of this chapter some analytical results for the eigenfrequencies of models for the chain drive system are shown and analytical results for the contact force between rollers and sprocket are presented.

Chapter 5
Application and Validation

5.1 Introduction

The methodologies described in chapter 3 and chapter 4 are used to develop a simulation program. Simulating the behaviour of a two stroke diesel marine engine roller chain drives, the different models are compared. The drives are standard in marine engines that have between 4 and 12 cylinders for a power range of 1760 to 78000 kW. The numerical simulations are done with application to two different chain drive systems of MAN B&W diesel engines. The reason for the change of the engine type was the prospect of some experimental results, which however was not conducted by the company during the project period.

Two of the different models for the contact between the rollers and sprockets are compared, that is the circular tooth profile and the real tooth profile. The results from these numerical models are also compared with simplified analytical results. As mentioned in chapter 3 the other applied models of the contact surface have shown not to be useful, hence the results from application of these are excluded.

The influence of inclusion of friction and inclusion of rotational damping on the links is presented in this chapter. The methodologies are applied to the simulation of different chain drive systems used in marine diesel engines, and inclusion of the different parts, such as the guide-bars and the tightener system are analysed.

In section 5.9 a resonance analysis is presented and compared with analytical results of the eigenfrequencies of the chain segments. In the last part of the chapter some experimental approaches of validating the computer program, which will be carried out by MAN B&W Diesel A/S in the near future, are listed.

5.2 Comparison of Circular and Real Tooth Profile

In this section the implementation of two different models suggested to describe the contact surface between rollers and sprockets, in a simulation program are described and

compared. The models are the circular tooth profile and the real tooth profile. For both methods the equations of motion of the roller chain drive system are given by (3.2) and (3.9). Both methods use the same contact force model to describe the contact between the rollers and sprockets, given by (3.47). However, the calculation of the indentation, relative velocity and normal vector used in equation (3.47) are calculated differently. For both models the link force between two adjacent rollers is the spring/damper force between the two lumped masses.

The results from the numerical simulation are compared with results from a simplified analytical model. The contact forces between the rollers and sprockets are in the analytical simplified model given by (4.41) and the link forces are given by (4.39).

5.2.1 Application to a Chain Drive of a MAN B&W Diesel Engine

The methodologies for the two methods are applied to simulation of the fore end chain drive of a MAN B&W 6L60MC marine diesel engine. The roller chain drive placed at the fore end of the engine 6L60MC is composed of four sprockets and a chain made of 122 links, see Figure 5.1.

The sprocket number (3) in the top of the chain drive is part of the pre-tensioning system and it is located 0.3366 m to the right of the center of the crankshaft and 3.0944 m above it during normal operating conditions, see Figure 5.1. Each link of the chain, with a pitch of 0.0889 m and a mass of 3.01 kg, is modelled as a flexible element with a stiffness of 815 MN/m, according to experimental data obtained by the manufacturer, see appendix B. The driver sprocket which is the sprocket on the crankshaft rotates in the numerical simulations with a constant angular velocity of 120 rpm, which gives a driving frequency of 120/60 = 2 Hz and the driver sprocket has 60 teeth yielding a tooth frequency of $f_t =$ 2Hz$\cdot$ 60 = 120 Hz. The time it takes for one link to move one complete revolution in the chain drive is $t_r = \frac{1}{2\ Hz}\frac{122}{60} = 1.017$ s.

The purposes of the 4 different sprockets in the chain drive are

Sprocket 1 = Crankshaft sprocket (driver)
Sprocket 2 = Counterweight sprocket
Sprocket 3 = Tightener sprocket
Sprocket 4 = Counterweight sprocket

The data for the system used in the numerical simulation are given in Table 5.1, Table 5.2,

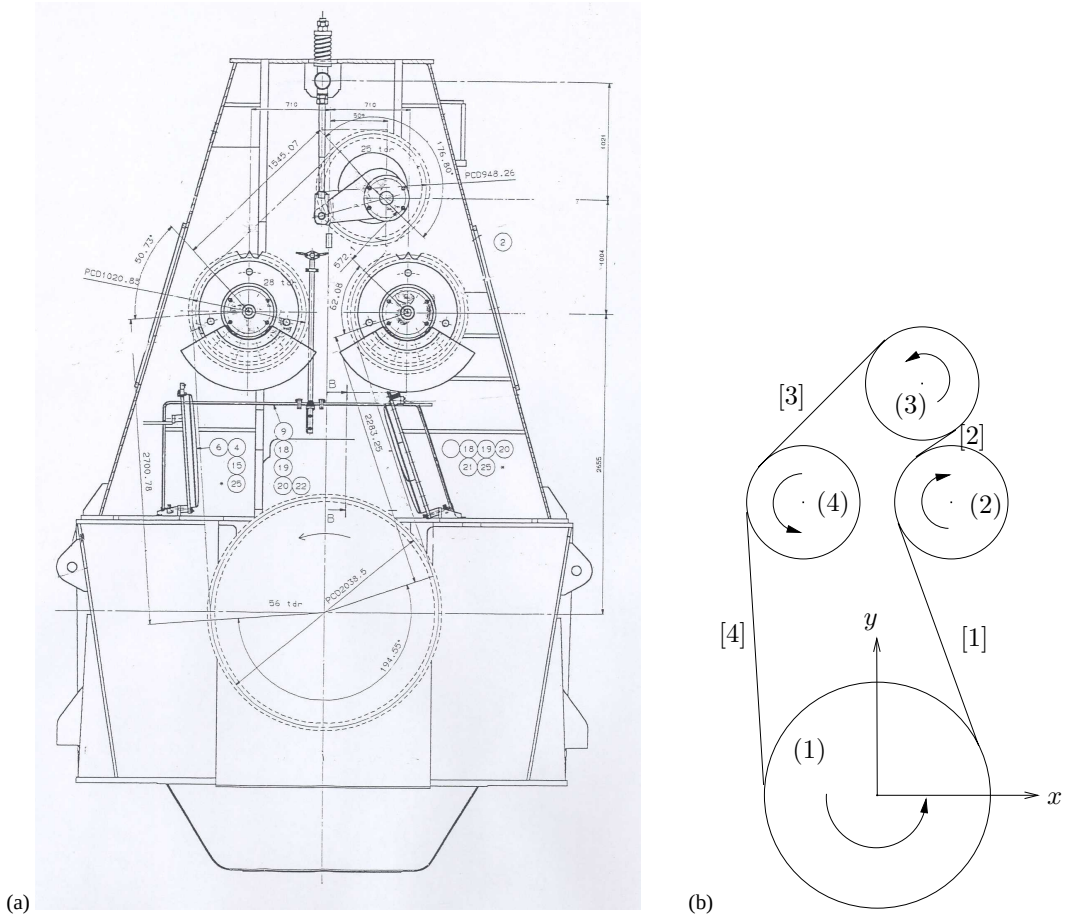

Figure 5.1: L60MC fore chain drive, (a) Blueprint of the chain drive (from MAN B&W Diesel A/S) and (b) the numbering of the sprockets [] and the chain segments ().

Table 5.3 and Table 5.4.

	Units	Sprocket 1	Sprocket 2	Sprocket 3	Sprocket 4
Pitch circle radius, R_s	m	0.849325	0.425245	0.397000	0.425245
position, x_s	m	0.0000	0.5560	0.3366	-0.5560
position, y_s	m	0.0000	2.2020	3.0944	2.2020
number of teeth, n_t		60	30	28	30
mass, m_s	kg	850	759	183	759
mass moment of inertia, J_s	kgm^2	435	82	15	82

Table 5.1: Data for the sprockets

	Units	Value
Mass per. roller, m_r	kg	3.01
Chain pitch, P	m	0.0889
Roller length, l_z	m	0.02699
Roller radius	m	0.027
Link stiffness, K	MN/m	815
Link damping, D	kg/s	250
Pre-tension	kN	21
Number of links, n_l		122

Table 5.2: Data for the roller-chain

The critical damping calculated by assuming the chain as being a long open string of a series of masses connected with springs is for a chain with n_l number of links $D_{cr} = 2n_l\sqrt{m_r K}$, yielding for the test case $D_{cr} \approx 1.2 \cdot 10^6$ kg/s. For a single mass connected to ground with a spring the critical damping coefficient is $D^*_{cr} = 2\sqrt{m_r K}$, yielding for the test case $D^*_{cr} \approx 1.0 \cdot 10^5$ kg/s. The damping coefficient used in the simulation corresponds to 0.002% of D_{cr} and 0.25% of D^*_{cr}.

	Units	Value
Poisson's ratio, ν		0.3
Young's modulus, E	N/m^2	$2.06 \cdot 10^{11}$
exponent, m		3
material property, h	m^2/N	$1.406 \cdot 10^{-12}$

Table 5.3: Material data

From the data given in Table 5.3 and the length of the roller given in Table 5.2 an average generalized coefficient of stiffness is calculated using (3.31) and the value used in (3.47) is $K_g = 1$ GN/m. The coefficient of restitution is a constant $0 \leq e \leq 1$, where $e = 0$ relates to a fully plastic contact and $e = 1$ relates to a fully elastic contact. In order to include maximal energy dissipation in the model $e = 0$ is used. Different values of e has been applied resulting in similar conclusions as presented in this section, and is discussed further in section 5.4.

	Units	Segment 1	Segment 2	Segment 3	Segment 4
Length	m	1.8797	0.4104	1.2619	2.2312
Angle on sprocket i	rad	0.3485	2.2748	2.3337	3.2010
Angle on sprocket j	rad	3.4901	5.4164	2.3337	3.2010

Table 5.4: Segment length and contact angles

In Table 5.4 the data for the four segments in the chain drive are given, where segment 1 is the chain strand between sprocket one and sprocket two, segment 2 is the chain strand between sprocket two and sprocket three and so forth, see Figure 5.1(b).

5.2.2 Comparison of Numerical and Analytical Results

In the following the link force between two adjacent rollers, the average link force (average over all links in a segment) between the neighbouring rollers in a segment and the transversal oscillation of the middle of a segment between two sprockets are investigated. This is done by comparing the two different contact surface models, which is the circular tooth profile and the real tooth profile. Further the contact force between rollers and sprockets are investigated by comparing a simplified analytical model with the two different models used for the numerical simulations.

Friction and rotational damping are not included in these numerical simulations. The numerical simulations are carried out using initial positions and velocities from an earlier simulation, so the driver sprocket is running at the constant velocity 120 rpm during a complete simulation period of 10 seconds.

The Link Forces

The variation of the link forces and analysis of the transversal oscillations of the chain strands exemplify the type of results useful for the design of the roller chain drives.

Figure 5.2 shows a comparison between the two methods, of the link force between two adjacent rollers during one second of the simulation. The dashed line is the result obtained using the real tooth profile and the solid line is the result obtained using the circular tooth profile. The link force obtained using the real tooth profile has a noticeable variation when the link is in contact with sprocket number one in the time period [9.3 s;9.6 s] and

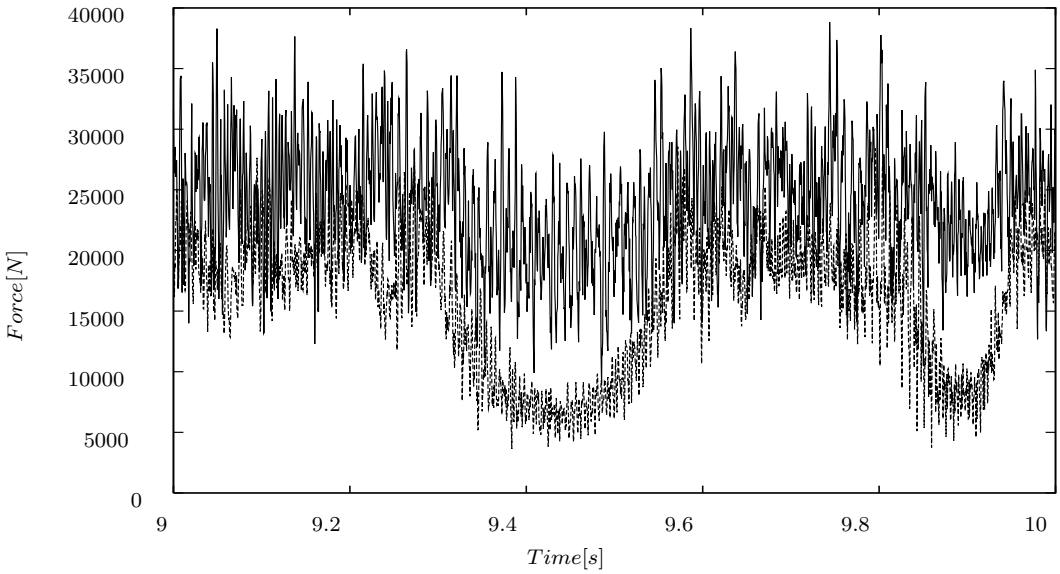

Figure 5.2: The link force between two adjacent rollers during one second. Dashed line for the real tooth profile and solid line for the circular tooth profile.

with sprocket number three in the time period [9.8 s;9.9 s], whereas for the circular tooth profile the large variations are in the time periods before and after. The amplitude for the real tooth profile is also noticeable smaller than for the circular tooth profile. We observe that in this case the use of the real tooth profile has a decreasing effect on the link force.

Figure 5.3 shows a comparison between the two methods, of the average link force (average over all links in the segment) between the neighbouring rollers in segment one during one second of the simulation, that is the free links situated in the chain strand between sprocket one and two. The dashed line is the result obtained using the real tooth profile and the solid line is the result obtained using the circular tooth profile. The mean value of the average link force is for the circular tooth profile approx. 25 kN, whereas it for the real tooth profile approx. 19 kN. The amplitude of the average link force when using the circular tooth profile is up to approx. 13 kN, whereas it for the real tooth profile is up to approx. 6 kN. We observe that in this case the use of the real tooth profile has a decreasing effect on the average link force as expected due to the decreasing effect on the link force described in relation to Figure 5.2. This is also to be expected, since the circular tooth profile is placed on a pitch circle with a radius ΔR larger than the one used for the real tooth profile. Hence the chain has more pre-tension, see section 3.5.5.

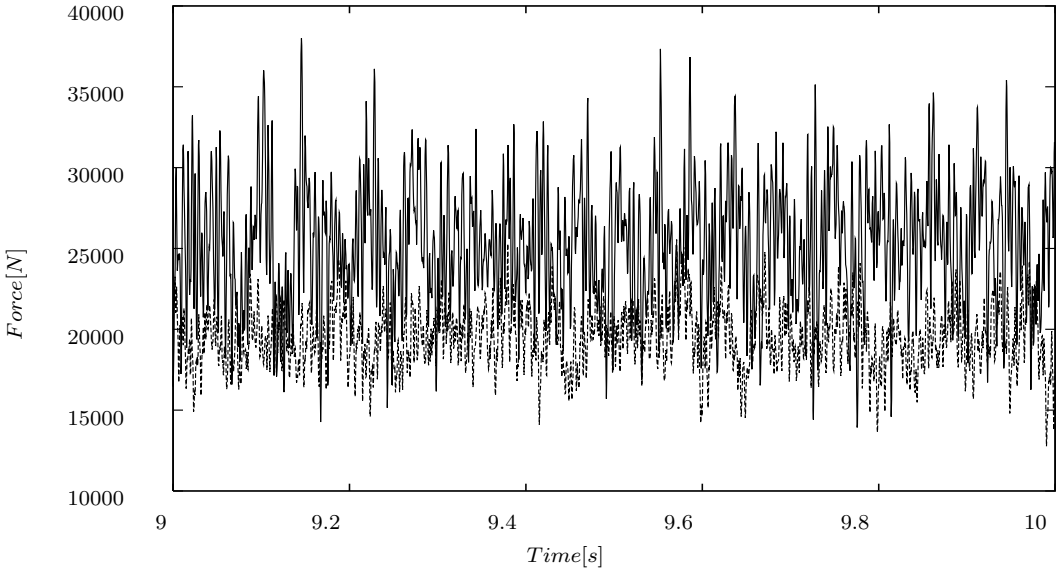

Figure 5.3: An average link force between the neighbouring rollers in segment one during one second. Dashed line for the real tooth profile and solid line for the circular tooth profile.

From Figure 5.2 and Figure 5.3 it can be seen that there is numerical noise on the results, which partly is due to the low value of the damping coefficient D compared with the critical damping coefficient. Higher values of D has been tested and they have a smoothing effect on the link forces, but increases the simulation time. For higher values of D however the same conclusion with respect to comparison of the two models are drawn.

The Oscillations of Chain Strands

For the analysis of the transversal vibrations of the chain, the perpendicular distance between the link closest to the middle of the initial chain strand line and the middle point of the initial chain strand line is calculated.

Figure 5.4 shows a comparison between the two methods for the oscillation of segment one, that is the perpendicular distance between the middle of the segment and the initial chain strand line. The dashed line is the result obtained using the real tooth profile and the solid line is the result obtained using the circular tooth profile. The figure shows that the result from the two methods are similar, the vibrations are with approximately the same major frequency. Again as for the link force we observe that the real tooth profile has a smoothing effect on the result compared to the circular tooth profile.

Figure 5.5 shows a comparison between the two methods for the oscillation of segment four, that is the perpendicular distance between the middle of the segment and the initial chain strand line. The dashed line is the result obtained using the real tooth profile and the solid line is the result obtained using the circular tooth profile. The figure shows that the results from the two methods are somewhat different in the size of the amplitudes of the vibrations. Again as for the link force we observe that the real tooth profile has a smoothing effect on the result compared to the circular tooth profile.

Figure 5.6 shows the frequency spectra from a FFT (Fast Fourier transformation) of the results shown in Figure 5.4, the left figure for the results obtained using the circular tooth profile and the right figure for the results obtained using the real tooth profile. Both the frequency spectra show a major peak around 5.5 Hz, that for the circular tooth profile the peak is at approx 6.1 Hz and for the real tooth profile the peak is at approx. 5.1 Hz. The other smaller peaks are not comparable. The main excitation frequencies are the driver frequency 2 Hz and the tooth frequency 120 Hz, but neither of these frequencies are seen in Figure 5.6.

The eigenfrequencies f_n for a free undamped pre-tensioned string is given by

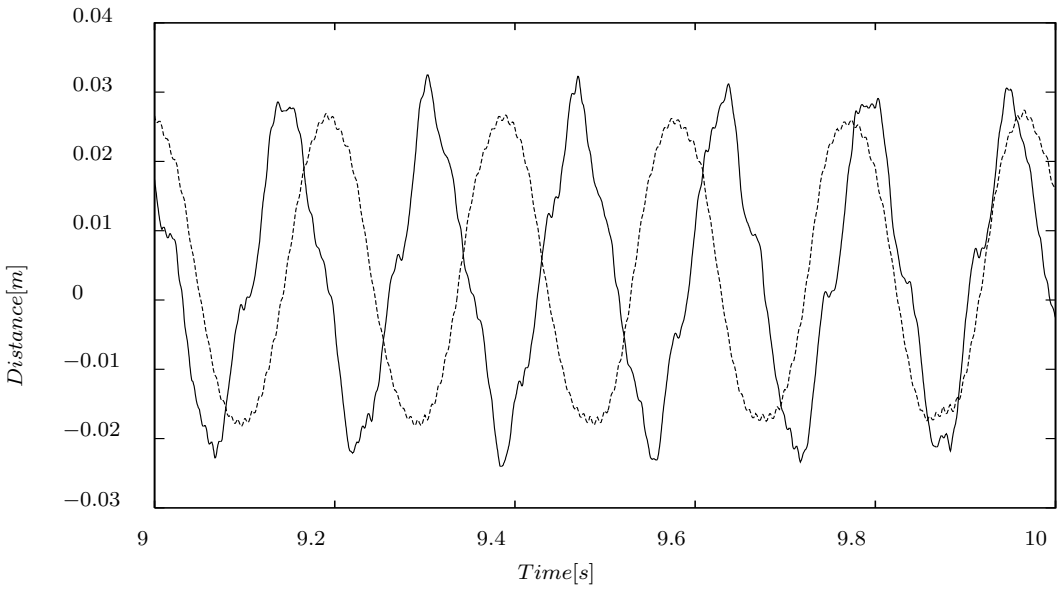

Figure 5.4: The oscillation of the middle of segment one about the initial position. Dashed line for the real tooth profile and solid line for the circular tooth profile.

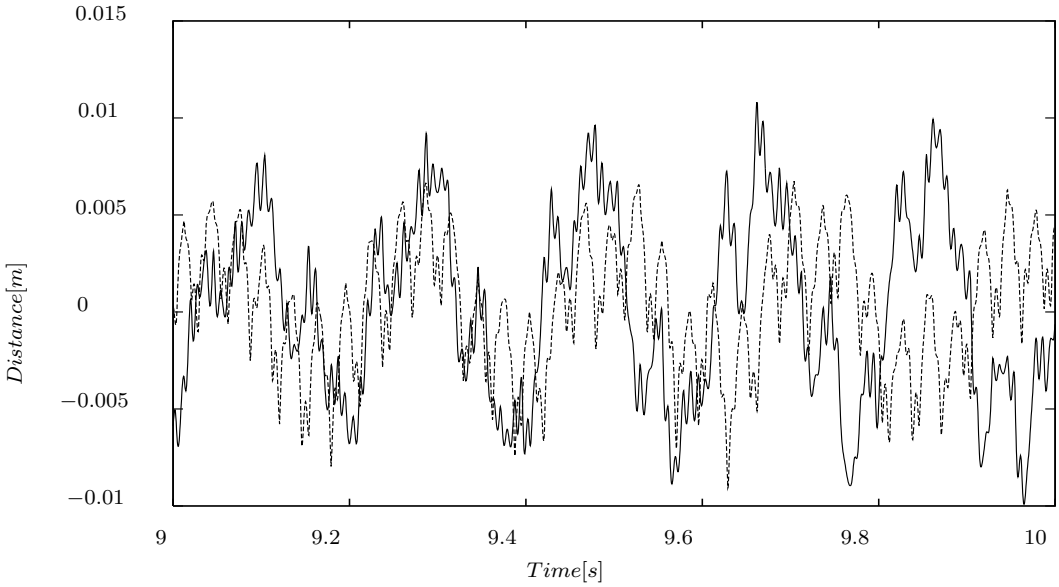

Figure 5.5: The oscillation of the middle of segment four about the initial position. Dashed line for the real tooth profile and solid line for the circular tooth profile.

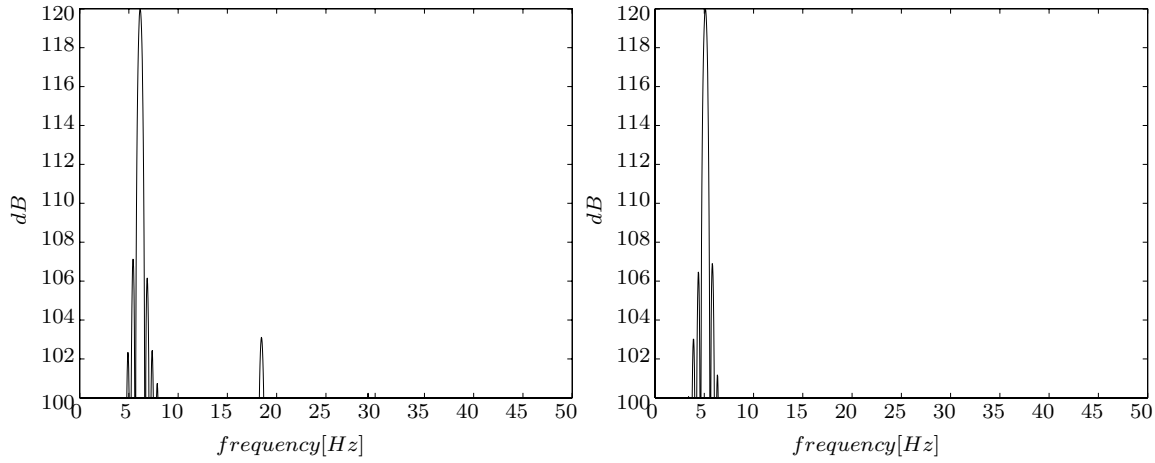

Figure 5.6: The frequency of the oscillation of the middle of segment one - For the circular tooth profile (left) and for the real profile (right).

$$f_n = n\sqrt{\frac{F}{4l_t m_t}}, \quad n = 1, 2, \ldots \tag{5.1}$$

where n is the eigenfrequency number, F is the pre-tension force, l_t is the length of the string and m_t is the mass of the string, see section 4.4.1. For segment number one the

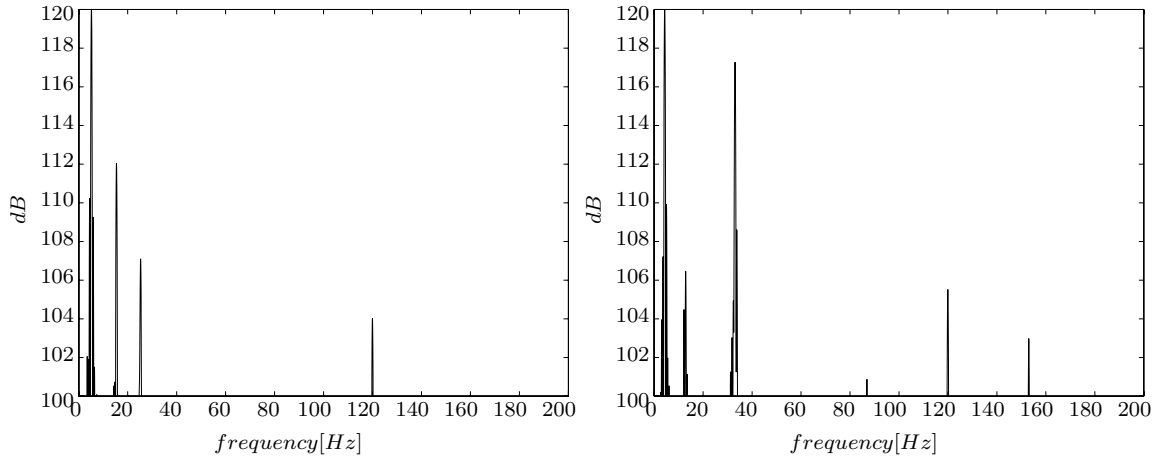

Figure 5.7: The frequency of the oscillation of the middle of segment four - For the circular tooth profile (left) and for the real profile (right).

length is $l_t \approx 1.8797$ m, corresponding to approx 21 links which yields a string mass of $m_t \approx 63.21$ kg. For the circular tooth profile we found the mean average link force to be $F \approx 25$ kN and for the real tooth profile it is $F \approx 19$ kN. Using (5.1) we obtain the first eigenfrequency for segment number one, assuming it is comparable to a pre-tensioned string, that is for the circular tooth profile $f_1^{(c)} \approx 7.3$ Hz and for the real tooth profile $f_1^{(r)} \approx 6.3$ Hz. For the numerical simulation damping is included in the longitudinal direction of the links, which lowers the eigenfrequency. As described in section 4.4.1 the velocity of the chain string has an influence on the eigenfrequency and the eigenfrequency decreases when the velocity increases, see Figure 4.11. It is therefore likely that the 6.1 Hz and 5.1 Hz corresponds to the first eigenfrequency of the chain strand in the transversal direction.

Figure 5.7 shows the frequency spectra from a FFT of the results shown in Figure 5.5, the left figure for the results obtained using the circular tooth profile and the right figure for the results obtained using the real tooth profile. Both the frequency spectra show a major peak about 5 Hz, that is for the circular tooth profile the peak is at approx. 5.2 Hz and for the real tooth profile the peak is at approx. 4.5 Hz. Both methods also have a peak at the tooth frequency 120 Hz. For the circular tooth profile the other major peaks are at approx. 15.5 Hz, 25.5 Hz, 83 Hz and 157 Hz and for the real tooth profile the peaks around the same values are approx. 13 Hz , 33 Hz, 87 Hz and 153 Hz.

For segment number four the length is $l_t \approx 2.2312$ m, corresponding to approx 25 links

which yields a string mass of $m_t \approx 75.25$ kg. For the circular tooth profile we found the mean average link force to be $F \approx 26$ kN and for the real tooth profile it is $F \approx 20$ kN. Using (5.1) we obtain the first eigenfrequency for segment number four, assuming it is comparable to a pre-tensioned string, that is for the circular tooth profile $f_1^{(c)} \approx 6.2$ Hz and for the real tooth profile $f_1^{(r)} \approx 5.5$ Hz. It is therefore likely, due to the damping, that the 5.2 Hz and 4.5 Hz corresponds to the first eigenfrequency of the chain strand in the transversal direction.

The Contact Force

The variation of the contact forces between the rollers and sprockets exemplify another type of results that can be derived from the numerical simulation program. In order to compare the analytical result with numerical result, the analytical found forces are plotted versus a time scale given by

$$(t)_i = t_s + (i-1) \cdot \frac{t_e - t_s}{n_b - 1}, \qquad i = 1, \ldots, n_b \tag{5.2}$$

where t_s is the start time when the contact begins and t_e is the end time when the contact ends. The start and end time t_s and t_e are estimated from the numerical results. The tension forces in the segments q_a and q_b are also estimated from the numerical results, by an average value of the link force in a segment.

Figure 5.8 shows the contact force on a roller during one second of the simulation in the time period [9 s;10 s]. The dashed line is the result obtained using the real tooth profile and the solid line is the result obtained using the circular tooth profile. The following figures are from the same simulation time period, but taken in the shorter time periods, where contact has occurred.

Figure 5.9 shows the contact force on a roller during contact with sprocket number one (left) and sprocket number two (right). The dashed line is the analytical result calculated by (4.41), where the average tension force is found by the real tooth profile method, the dashed-dotted line is the analytical result where the average tension force is found by the circular tooth profile method, the solid line is the numerical using the circular tooth profile and the solid-dotted line is the numerical using the real tooth profile. The start and end time of the contact period are for the analytical results estimated by the numerical results and same values are used for both analytical results.

Figure 5.10 shows the contact force on a roller during contact with sprocket number three

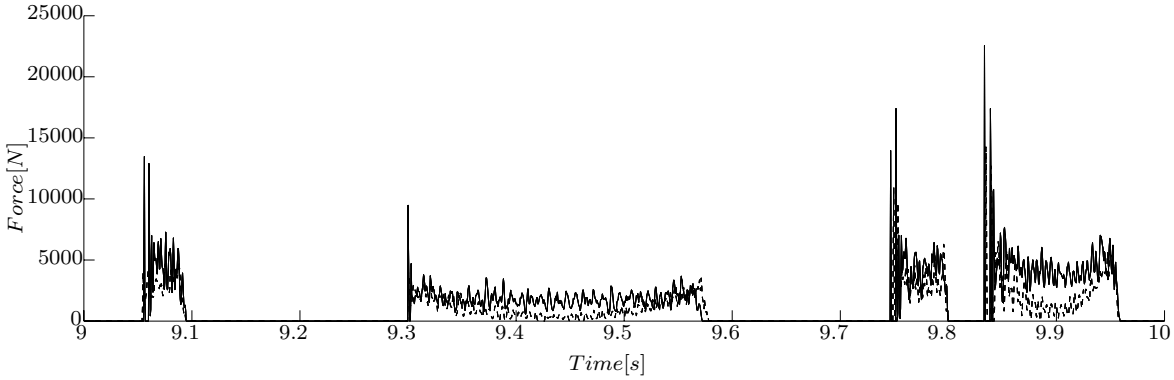

Figure 5.8: Contact force on a roller during one revolution. Dashed line for the real tooth profile and solid line for the circular tooth profile.

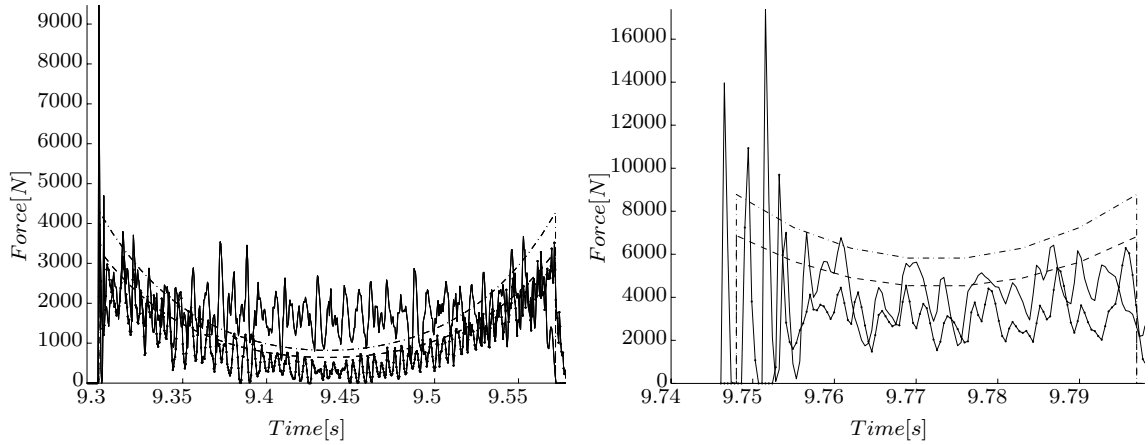

Figure 5.9: Contact forces on sprocket one (left) and sprocket two (right). The solid line (numerical) and dashed-dotted line (analytical) for the circular tooth profile. The solid-dotted line (numerical) and the dashed line (analytical) for the real tooth profile.

(left) and sprocket number four (right). The dashed line is the analytical result where the average tension force is found by the real tooth profile method, the dashed-dotted line is the analytical result where the average tension force is found by the circular tooth profile method, the solid line is the numerical using the circular tooth profile and the solid-dotted line is the numerical using the real tooth profile. The start and end time of the contact period are for the analytical results estimated by the numerical results and same values are used for both analytical results.

The contact forces between the rollers and the sprockets are in better agreement with the analytical expected results, when the real tooth profile is used. However for the two counterweight sprockets (two and four) where the contact period is short, the analytical

fig

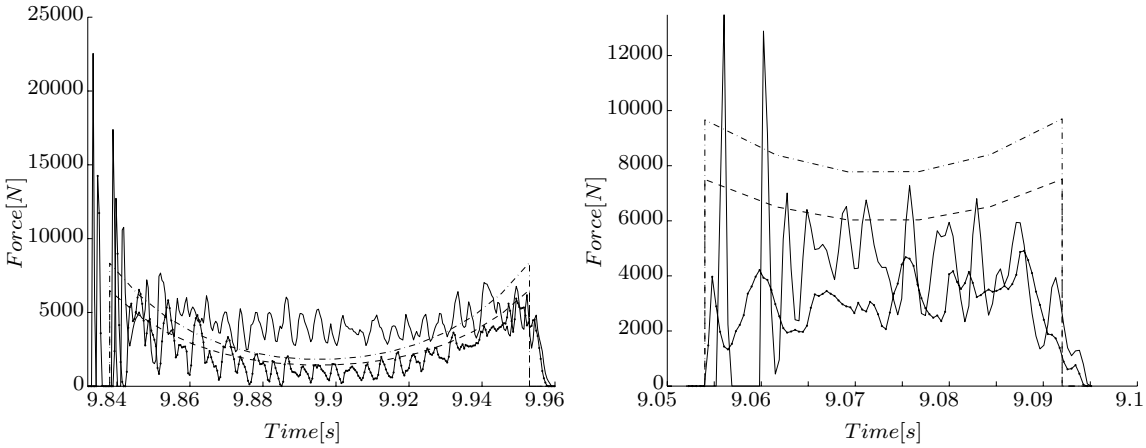

Figure 5.10: Contact force from sprocket three (left) and four (right).The solid line (numerical) and dashed-dotted line (analytical) for the circular tooth profile. The solid-dotted line (numerical) and the dashed line (analytical) for the real tooth profile.

result doesn't compare well with either of the two methods. In the analytical results it is assumed that the angular velocity is constant, which in the numerical simulation only is true for the driver sprocket one. It is also in the analytical results assumed that the angle where there is contact (the pressure angle) is constant during the whole contact period, whereas in the numerical simulations this varies. These are some of the reasons, for the difference between the results.

5.3 Inclusion of Friction in the Model

In this section the results of two numerical simulations are compared, one where friction is included and one where friction is not included. The friction force given by Equation (3.9), depends on the dynamic friction coefficient μ_d and the dynamic correction factor μ_c, see section 3.9. Rotational damping is not included in these numerical simulations.

5.3.1 Application to a Chain Drive of a MAN B&W Diesel Engine

The methodology is applied to simulation of the fore end chain drive of a MAN B&W 6S90MC-C marine diesel engine. The roller chain drive placed at the fore end of the engine 6S90MC-C is composed by four sprockets and a chain made of 144 links, see Figure 5.11.

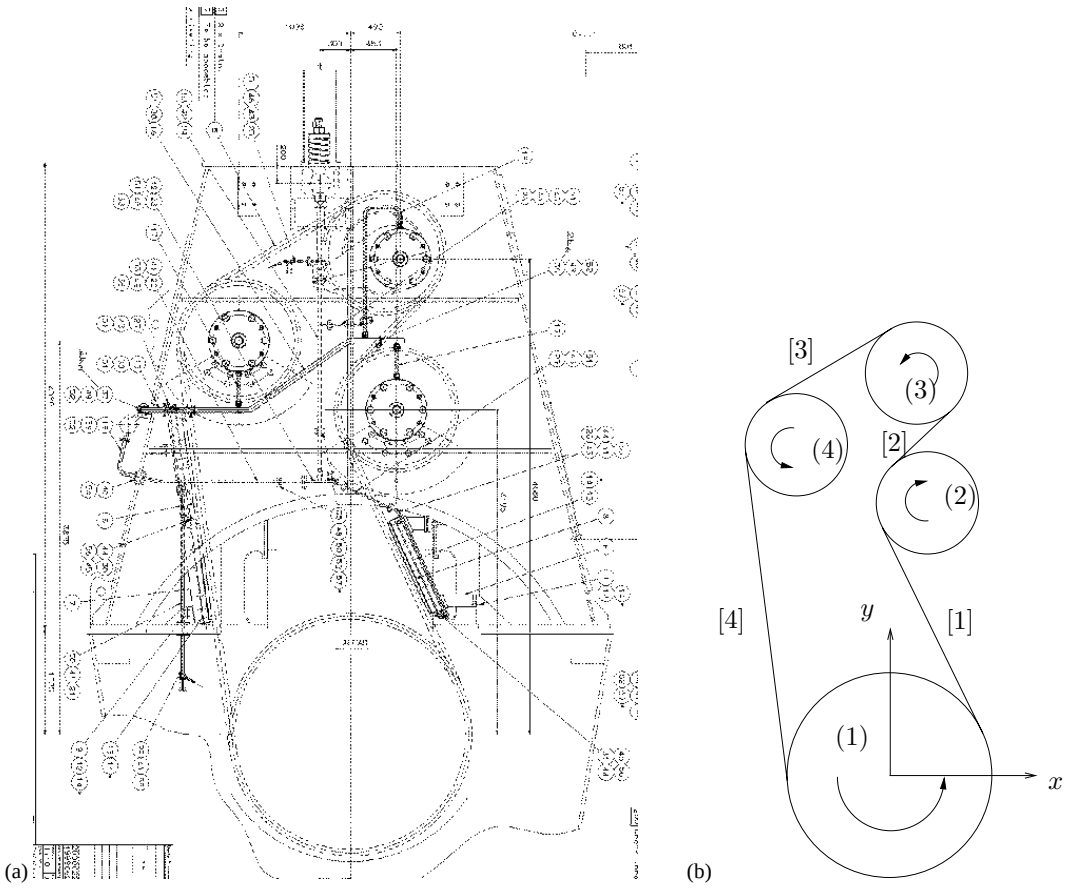

Figure 5.11: 6S90MC-C fore chain drive, (a) Blueprint of the chain drive (from MAN B&W Diesel A/S) and (b) the numbering of the sprockets [] and the chain segments ().

The sprocket number (3) in the top of the chain drive is part of the pre-tensioning system and it is located 0.333 m to the right of the crankshaft and 4.748 m above it during normal operating conditions, see Figure 5.11. Each link of the chain, with a pitch of 0.1143 m and a mass of 6.8 Kg, is modelled as a flexible element with a stiffness of 1069 MN/m, according to experimental data obtained by the manufacturer, see appendix B. The driver sprocket which is the sprocket on the crankshaft, rotates in the numerical simulations with a constant angular velocity of 76 rpm, which gives a driving cyclic frequency of 76/60 = 1.27 Hz, driving radial frequency $\omega_d = (76 \cdot 2\pi)/60 = 7.96$ rad/s and the driver sprocket has 64 teeth yielding a tooth frequency of $f_t = 1.27\text{Hz} \cdot 64 = 81.1$ Hz. The time it takes for one link to move one complete revolution in the chain drive is $t_r = \frac{1}{1.27\ Hz}\frac{144}{64} = 1.78$ s.

The fore chain drive of the engine 6S90MC-C has 4 sprockets and a double chain. These

two chains are in the simulation treated as one chain, with the double link mass and the double link stiffness. The purposes of the 4 different sprockets in the chain drive are

Sprocket 1 = Crankshaft sprocket (driver)
Sprocket 2 = Counterweight sprocket
Sprocket 3 = Tightener sprocket
Sprocket 4 = Counterweight sprocket

The data for the system used in the numerical simulation are given in Table 5.5, Table 5.6, Table 5.7 and Table 5.8.

	Units	Sprocket 1	Sprocket 2	Sprocket 3	Sprocket 4
Pitch radius, R_s	m	1.164715	0.583055	0.583055	0.583055
position, x_s	m	0.000000	0.453	0.333	-1.098
position, y_s	m	0.000000	3.195	4.748	3.875
teeth, n_t		64	32	32	32
mass, m_s	kg	1	3414	849	3414
mass moment of inertia, J_s	kg m^2	1	3712	776	3712

Table 5.5: Data for the sprockets

	Units	Value
Mass per. roller, m_r	kg	13.6
Chain pitch, P	m	0.1143
Roller length, l_z	m	0.068
Roller radius	m	0.036195
Link stiffness, K	MN/m	2137
Link damping, D	kNs/m	20
Pre-tension	kN	40
Number of links, n_l		144

Table 5.6: Data for the roller-chain

The critical damping calculated by assuming the chain as being a long open string of a series of masses connected with springs is for a chain with n_l number of links $D_{cr} =$

$2n_l\sqrt{m_rK}$, yielding for the test case $D_{cr} \approx 4.9 \cdot 10^7$ kg/s. For a single mass connected to ground with spring the critical damping coefficient is $D^*_{cr} = 2\sqrt{m_rK}$, yielding for the test case $D^*_{cr} \approx 3.4 \cdot 10^5$ kg/s. The damping coefficient used in the simulation corresponds to 0.04% of D_{cr} and 6% of D^*_{cr}.

	Units	Value
Poisson's ratio, ν		0.3
Young's modulus, E	N/m^2	$2.06 \cdot 10^{11}$
exponent, m		3
material property, h	m^2/N	$1.406 \cdot 10^{-12}$

Table 5.7: Material data

From the data given in Table 5.7 and the length of the roller given in Table 5.6 an average generalized coefficient of stiffness is calculated using (3.31) and the value used in (3.47) is $K_g = 1$ GN/m. The coefficient of restitution is a constant $0 \leq e \leq 1$, where $e = 0$ relates to a fully plastic contact and $e = 1$ relates to a fully elastic contact. In order to include maximal energy dissipation in the model $e = 0$ is used. Different values of e has been applied resulting in similar conclusions as presented in this section, and is discussed further in section 5.4.

	Units	Segment 1	Segment 2	Segment 3	Segment 4
Length	m	2.71266	1.0329	1.6765	3.98533
Angle i	rad	0.4315	2.3726	2.1186	3.2728
Angle j	rad	3.5731	5.5143	2.1186	3.2728

Table 5.8: Segment length and contact angles

In Table 5.8 the data for the four segments in the chain drive are given, where segment one is the chain strand between sprocket one and sprocket two, segment two is the chain strand between sprocket two and sprocket three and so forth, see Figure 5.11(b).

5.3.2 Comparison of the Numerical Results with and without Friction

For the numerical results presented in this section, the numerical simulations are carried out using initial positions and velocities from an earlier simulation, so the driver sprocket is running at the constant velocity 76 rpm during a complete simulation period of 10

seconds. Figure 5.12 shows the roller center path during contact with a sprocket, from a numerical simulation without friction (a) and from a numerical simulation including friction (b). The dynamic friction coefficient is set to be $\mu_d = 0.1$ and the dynamic correction factor μ_c is modelled by Equation (3.98), that is the Heaviside approximation with $H_1(x)$ (see appendix G), with $\epsilon = 0.01$ and $v_t^* = 0.1$.

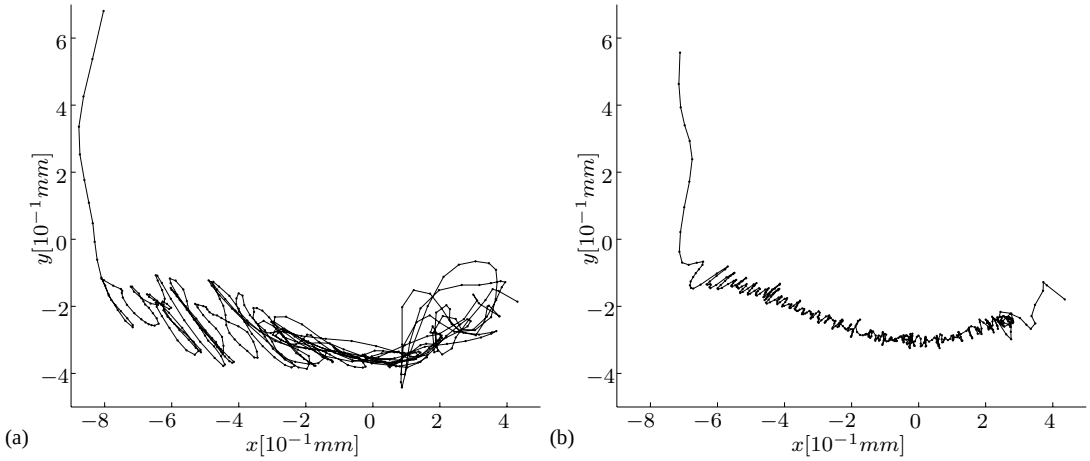

Figure 5.12: The roller center path without friction (a) and with friction $\mu_d = 0.1$ (b)

Figure 5.13 shows the tangential relative speed during a simulation period of 2 seconds and Figure 5.14 shows the friction force during a simulation period of 2 second . During the 2 seconds the roller is in contact with all four sprockets, since the revolution time of a roller in the chain drive system is approximately 1.8 s.

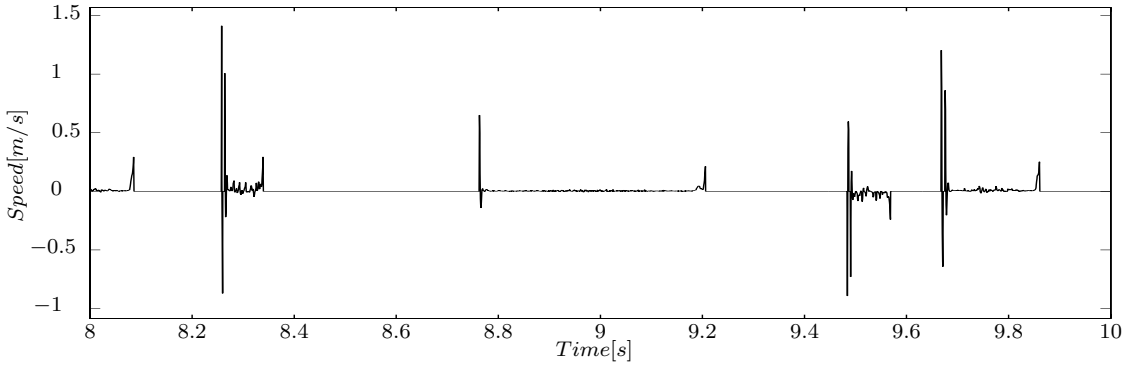

Figure 5.13: The relative tangential speed, with $\mu_d = 0.1$

In the time period $t \in [8.25s; 8.34s]$ the roller is in contact with sprocket number 4, for $t \in [8.75s; 9.2s]$ the roller is in contact with sprocket number 1, for $t \in [9.48s; 9.57s]$ the

roller is in contact with sprocket number 2 and for $t \in [9.65s; 9.85s]$ the roller is in contact with sprocket number 3, see Figure 5.11. The figures show that tangential relative speed during contact oscillates around zero over the contact period implying that the friction force also oscillates around zero.

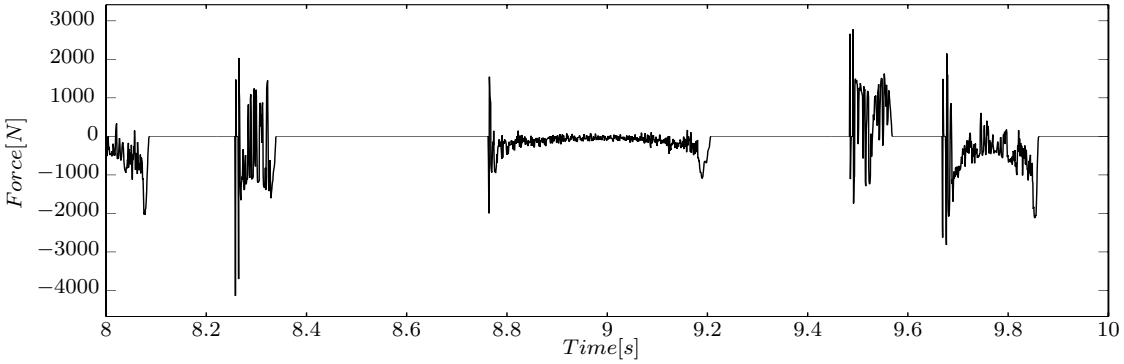

Figure 5.14: The friction force on a roller, with $\mu_d = 0.1$

Figure 5.15 shows the friction force normalised with the normal force versus the relative tangential speed. The figure shows that the use of an approximation for the signum function is important since the friction force changes direction for small values of the tangential relative speed, which will slow down the numerical integrations.

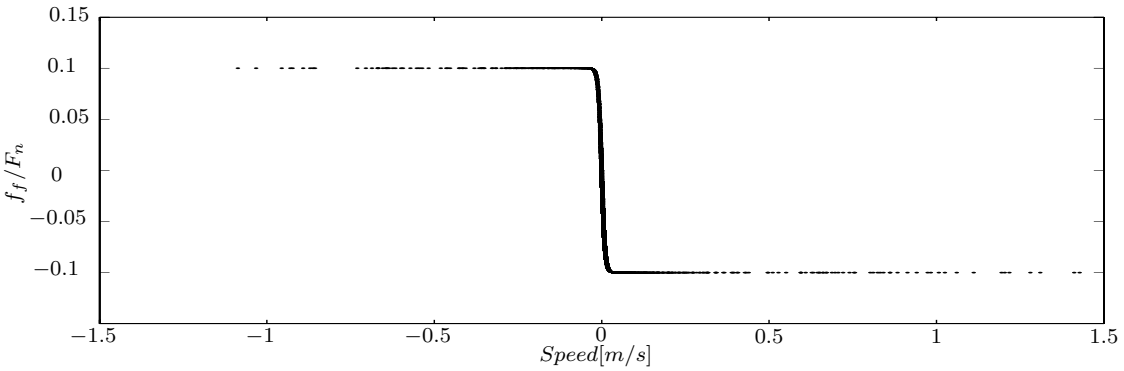

Figure 5.15: The friction force normalized with the normal force, with $\mu_d = 0.1$

Figure 5.16 shows the contact force on a roller during a simulation period of 2 seconds. The figures show contact between the roller and all four sprockets. Figure 5.16 (top) shows results from the numerical simulation without friction and Figure 5.16 (bottom) shows results from the numerical simulation where friction is included. The figures show that the inclusion of friction in the model has a smoothing effect on the contact force.

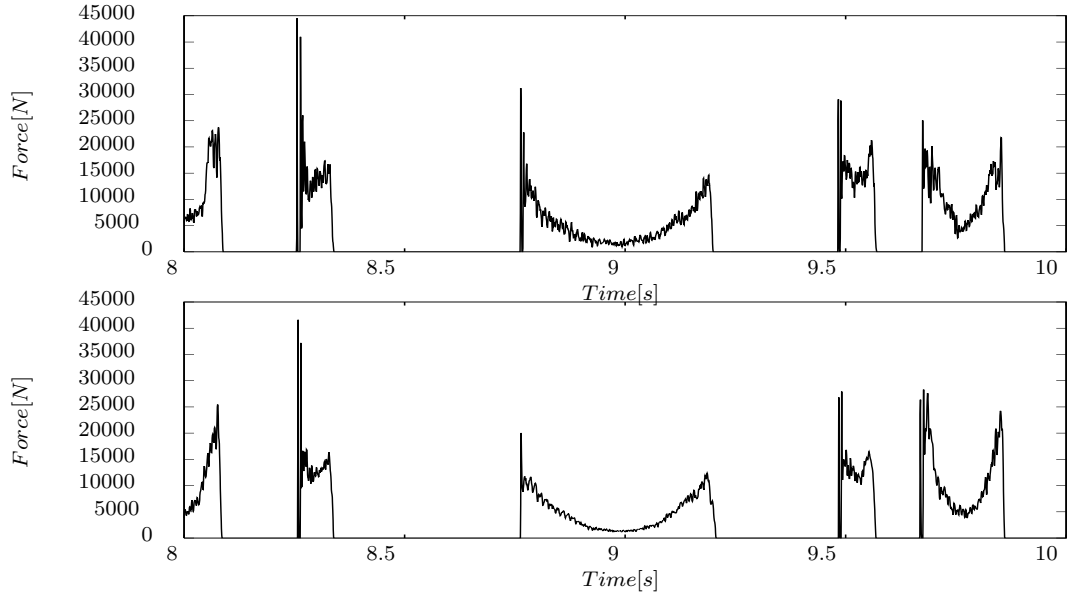

Figure 5.16: The contact force on a roller from simulation without friction (top) and with friction $\mu_d = 0.1$ (bottom).

Figure 5.17 shows the link force on a roller during a simulation period of 2 seconds. Figure 5.17(top) shows the results from the numerical simulation without friction and Figure 5.17 (bottom) shows the results from the numerical simulation with friction included. The figures show that the inclusion of friction in the model has a smoothing effect on the link force, which is to be expected since the contact force is smoother.

5.4 Influence of the Coefficient of Restitution

The contact force given by Equation (3.47), depends on the hysteresis damping factor given by (3.45) yielding the damping coefficient given by (3.46), because the damping coefficient depends on the coefficient of restitution e. The coefficient of restitution is a constant $0 \leq e \leq 1$, where $e = 0$ relates to a fully plastic contact and $e = 1$ relates to a fully elastic contact. In order to include maximal energy dissipation in the numerical model $e = 0$ is used. However this is not physical correct, with the interpretation of $e = 0$ relating to a fully plastic contact, when at the same time it is assumed that there is no permanent indentation.

Various values of e has been applied to a numerical simulation of the marine diesel engine 6S90MC-C fore end chain drive, with the chain drive data given in section 5.3.1. Figure

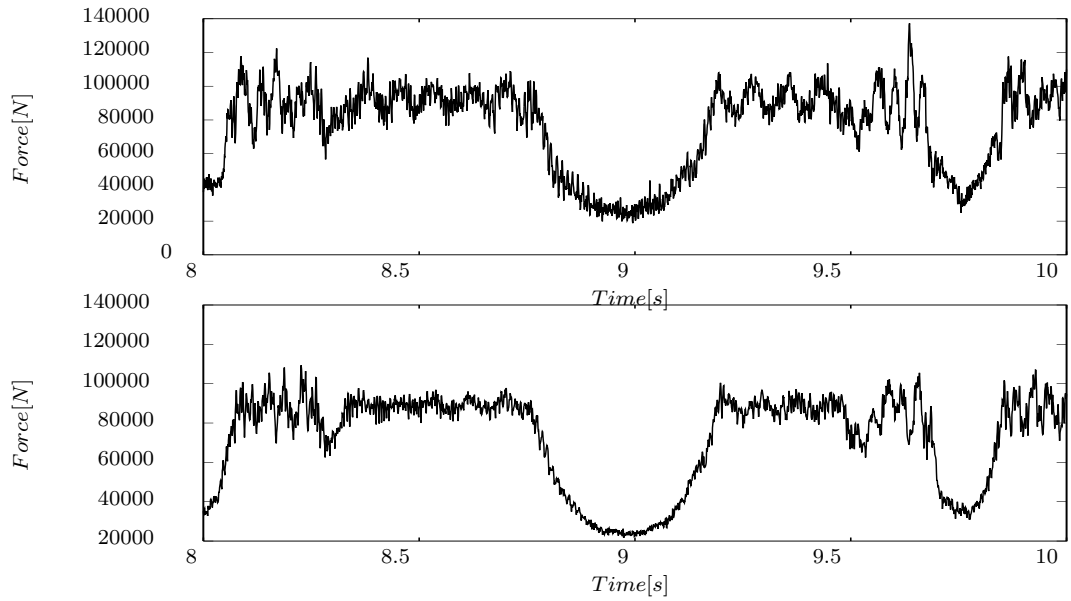

Figure 5.17: The link force in a link from simulation without friction (top) and with friction $\mu_d = 0.1$ (bottom).

5.18 shows the contact force f_c, between a roller and a sprocket, as a function of the indentation δ, for four different values of the coefficient of restitution $e = 1.0$, $e = 0.9$, $e = 0.8$ and $e = 0.0$.

In Figure 5.19 the contact force f_c, between a roller and a sprocket, as a function of time, is shown for four different values of the coefficient of restitution $e = 1.0$ (dotted line), $e = 0.9$ (solid-dotted line), $e = 0.8$ (dashed line) and $e = 0.0$ (solid line). The figure shows that the contact force for $e = 1.0$, that is no damping is included, bounces back and forth between zero contact force and up to approximately 100 kN. The figure shows that the contact force for $e = 0.9$, $e = 0.8$ and $e = 0.0$ are similar and the contact force is reduced to be around 15 kN. However for $e = 0.0$ the figure shows that the high frequency content is damped out and the roller does not get in and out of contact in the beginning of the contact.

Both figures 5.18 and 5.19, show that the difference between using a coefficient of restitution equal to $e = 0.8$ and $e = 0.0$ is minimal. The choice of using $e = 0$ is taken from a numerical point of view, due to the fact that the integrator reduces the time step size, when high frequency contents are detected. No lubrication is included in the numerical model, and such a lubrication will lower the impact force and have a damping influence

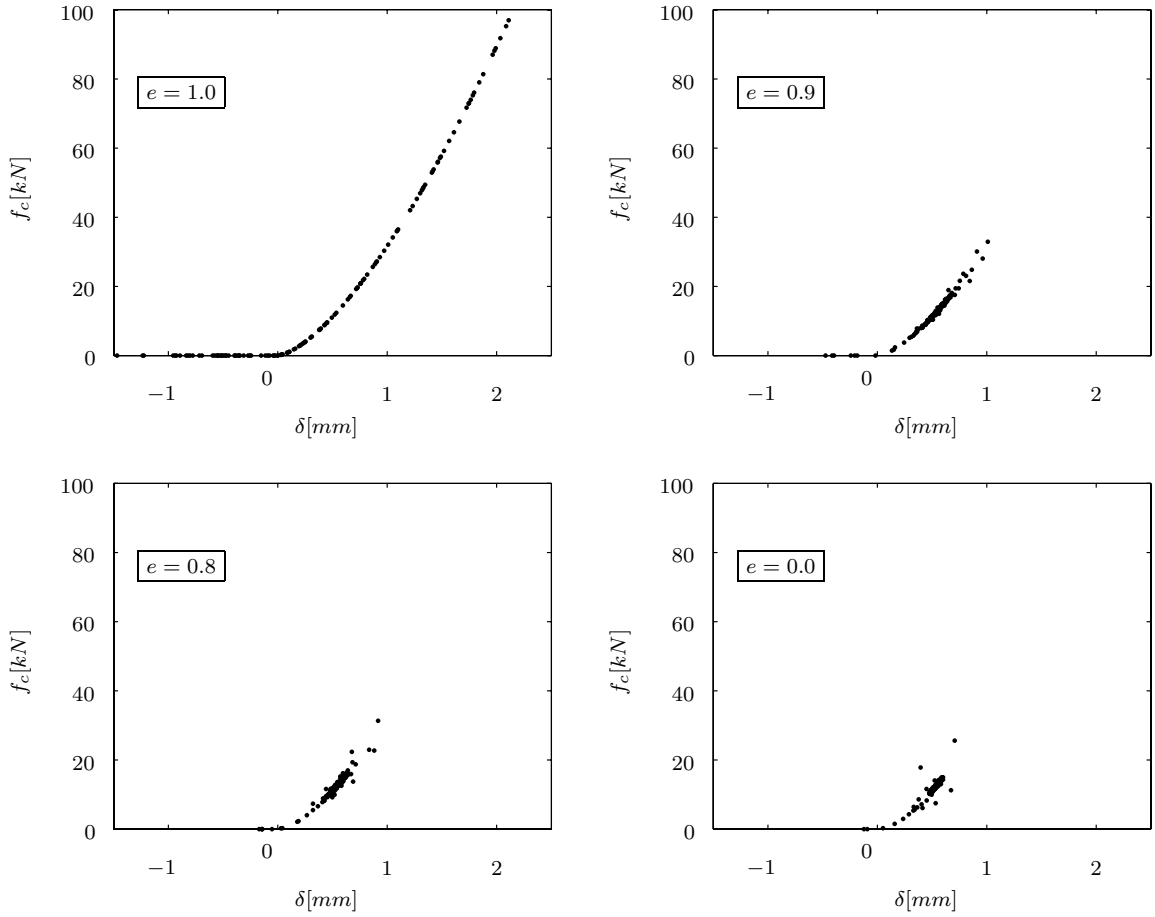

Figure 5.18: The contact force as a function of the indentation, for $e = 1.0$ (top left), $e = 0.9$ (top right), $e = 0.8$ (bottom left) and $e = 0.0$ (bottom right).

during contact. Setting the coefficient of restitution to $e = 0$ may be argued from this point of view.

5.5 Influence of Longitudinal Link Damping

The link force given by Equation (3.7), includes viscous damping in the longitudinal direction of the links. No direct experimental assessment has been done by the manufacturer to obtain the damping coefficient D, but there might be a possibility to get information from other indirect measurements. A reasonable value of D has to be chosen, that is a value below the critical damping coefficient, see section 4.4.9.

Different values of the coefficient of damping D used in the longitudinal damping, has

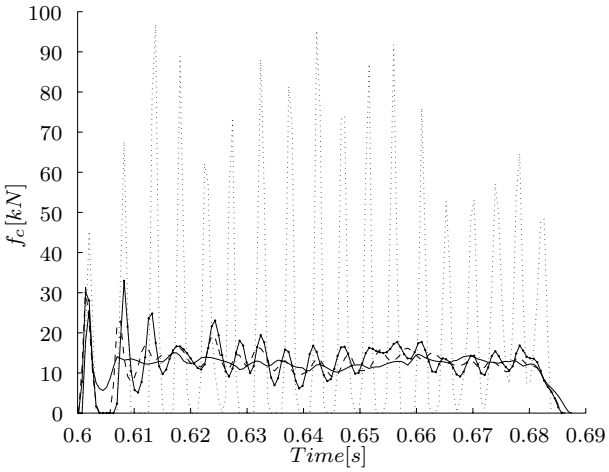

Figure 5.19: The contact force as a function of time , for $e = 1.0$ (dotted line), $e = 0.9$ (solid-dotted line), $e = 0.8$ (dashed line) and $e = 0.0$ (solid line).

been applied to a numerical simulation of the marine diesel engine 6S90MC-C fore end chain drive, with the chain drive data given in section 5.3.1. A damping coefficient was chosen to 20 kNs/m, which is within the limits of the critical damping as described in section 5.3.1. The results for different values of the longitudinal damping coefficient are similar, but when some higher values of the damping coefficient are applied, the computer time becomes prohibitive. This is not intuitively expected, but might be due to the fact that the link forces become larger and make the system more stiff.

5.6 Inclusion of Rotational Link Damping

The chain consists of rollers and link plates, see Figure 3.1. In the numerical model the chain is represented by rollers modelled as lumped masses connected by springs and dampers. In this model the rotational inertia of the link plates about their centre of gravity is neglected. The joints between the link plates consist of a pin inside a bushing, see Figure 3.1, and it is lubricated, but there is still some friction. This friction is modelled as a rotational damping moment, which in the model is applied as force couples. The forces applied on the rollers from substituting the rotational damping moment into force couples are given by Equation (3.17).

Different values of the coefficient of damping C_d in the rotational damping, has been applied to a numerical simulation of the marine diesel engine 6S90MC-C fore end chain drive, with the chain drive data given in section 5.3.1. The numerical simulations are

carried out using initial positions and velocities from an earlier simulation, and the driver sprocket is running at the constant velocity 76 rpm during a whole simulation period of 10 seconds. In the numerical simulation friction between the roller and sprocket was included, with a dynamic friction coefficient $\mu_d = 0.1$ and the dynamic correction factor μ_c is modelled by Equation (3.98), that is the Heaviside approximation with $H_1(x)$ (see appendix G), with $\epsilon = 0.01$ and $v_t^* = 0.1$.

The rotational damping in the links is a model of the friction in the joints, and the damping must be lower than the physical amount of possible friction. Figure 5.20 shows a pin with radius R_p inside a bushing, subjected to a link force F_n, a friction force f_f and a damping moment τ_l.

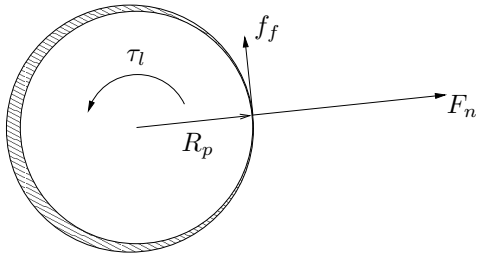

Figure 5.20: The friction between the pin and bushing.

The friction force is given by $f_f = \mu_d F_n$, where μ_d is the dynamic coefficient of friction, and the damping moment on the centre of the pin is given by $\tau_l = f_f R_p = \mu_d F_n R_p$. For a roller chain with a pre-tension force up to $F_n \approx 70$ kN, a pin radius $R_p = 0.02224$ m and a dynamic coefficient of friction $\mu_d < 0.1$ the damping moment is $\tau_l < 155Nm$.

Figure 5.21 shows the damping moment during a simulation period of 10 second, for a coefficient of damping chosen to be $C_d = 5$ Ns. The figure shows that the damping moment during the simulation always is within ± 150 Nm.

Figure 5.22 shows a comparison of the oscillation of chain segment one, see Figure 5.11. The figure shows results from a numerical simulation without rotational damping in the links (top) and from a numerical simulation with rotational damping in the links with $C_d = 5$ Ns (bottom). The oscillation of a chain segment is analysed by calculating the perpendicular distance between the link closest to the middle of the initial chain strand line and the middle point of the initial chain strand line is calculated. Both of the results are for a simulation period of 10 second. The rotational damping has a major influence

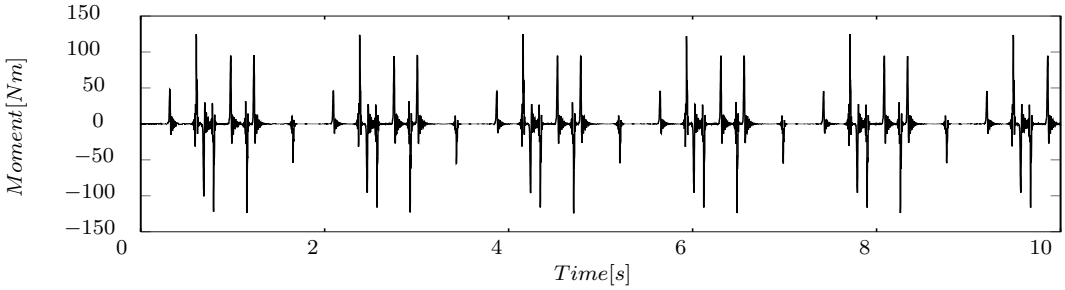

Figure 5.21: The damping moment on a roller, for $C_d = 5$, as a function of time.

on the oscillations of the middle of the chain segment, the amplitude is damped out and the oscillations are more smooth.

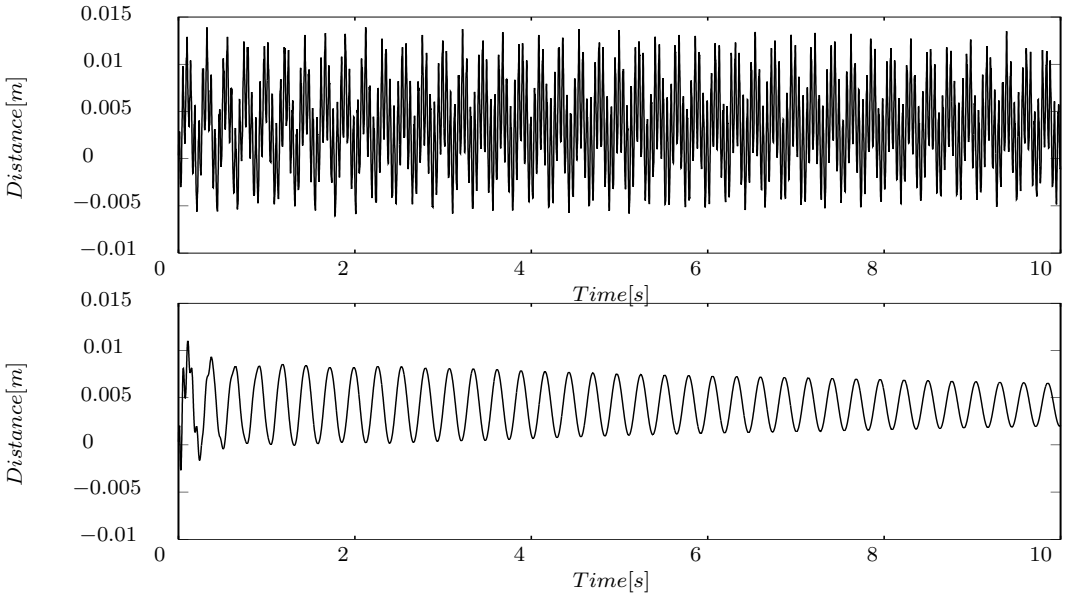

Figure 5.22: Oscillations of chain segment one, without rotational damping (top) and with rotational damping $C_d = 5$ (bottom), as a function of time.

Figure 5.23 shows the link force in a link during a numerical simulation without rotational damping in the links (top) and from a numerical simulation with rotational damping in the links with $C_d = 5$ Ns (bottom). Both of the results are for a simulation period of 10 second. The rotational damping has a smoothing effect on the link force and the average value of the link force is approximately 70 kN, instead of the approximately 90 kN when the rotational damping is not included.

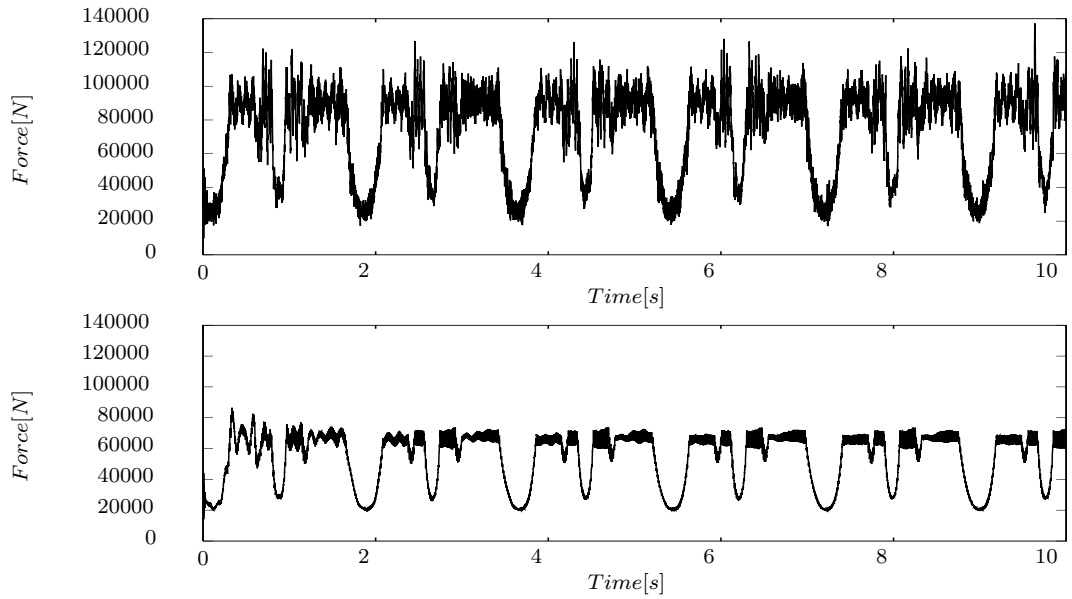

Figure 5.23: The link force in a link, without rotational damping (top) and with rotational damping $C_d = 5$ (bottom), as a function of time.

5.7 Results with Guide-bars

In this section the results from numerical simulations are compared, some where no guide-bars are included in the numerical model and some where three guide-bars are included in the numerical model. The three guide-bars are placed as shown in Figure 3.21.

The methodology is applied to a MAN B&W 6S90MC-C diesel engine fore end chain drive, and the chain drive data are given in section 5.3.1. In the numerical simulation friction between the roller and sprocket was included, with a dynamic friction coefficient $\mu_d = 0.1$ and the dynamic correction factor μ_c is modeled by Equation (3.98), that is the Heaviside approximation with $H_1(x)$ (see appendix G), using $\epsilon = 0.01$ and $v_t^* = 0.1$. Rotational damping is included with a damping coefficient chosen to be $C_d = 0.5$ Ns. The damping coefficient is chosen smaller than the one used in section 5.6, since it is assumed that the amount of friction is less than described in that section.

Results from numerical simulations with and without guide-bars are compared and results with constant angular velocity and oscillating angular velocity is compared as well. The guide-bars are positioned parallel with the tangent line between the sprockets and are pressed 0.005 m into the chain. Three guide-bars are applied, one on chain segment

number one and two on chain segment number four, which are the two longest chain segments in the chain drive system, see Figure 5.11. An average generalized coefficient of stiffness for the guide-bar contact, is calculated using (3.32) and the value used in (3.47) is $K_g = 3$ MN/m. The data used to calculate the average stiffness coefficient is given in Table 5.7 and for the guide-bars Poisson's ratio is $\nu = 0.5$ and the value of Young's modulus is set to be $E = 5$ MN/m^2.

5.7.1 Comparison of the Oscillations of the Middle of the Chain Segments

Figure 5.24 shows oscillations of the middle of chain segment number one from the numerical simulation where the guide-bars are not included (bottom curve) and from the numerical simulations where the guide-bars are included (top curve). The figure shows that the guide-bars reduce the amplitude of the oscillations. The numerical simulations are carried out with a constant angular velocity of 76 rpm.

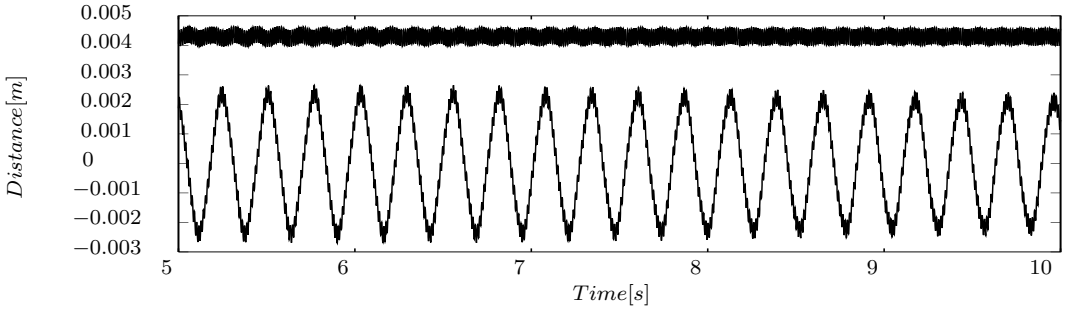

Figure 5.24: Comparison of the oscillations of the middle of chain segment 1, with guide-bars (top curve) and without guide-bars (bottom curve). A constant angular velocity is applied for the driving sprocket.

Figure 5.25 shows oscillations of the middle of chain segment number four from the numerical simulation where the guide-bars are not included (bottom curve) and from the numerical simulations where the guide-bars are included (top curve). The figure shows that the guide-bars reduce the amplitude of the oscillations. The numerical simulations are carried out with a constant angular velocity of 76 rpm.

Figure 5.26 shows the frequency content of the oscillations of the middle of chain segment number one from the numerical simulation where the guide-bars are not included (top) and from the numerical simulations where the guide-bars are included (bottom). The top figure shows that when the guide-bars are not included the dominating frequency is at approximately 3.8 Hz and we also see the tooth frequency of 81 Hz. The bottom

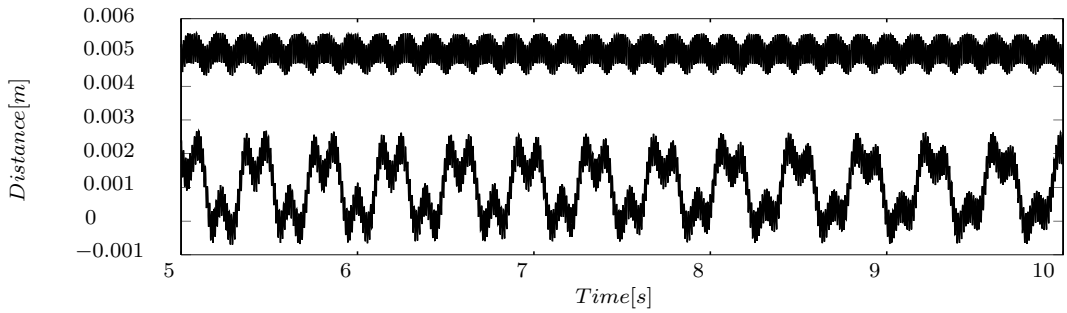

Figure 5.25: Comparison of the oscillations of the middle of chain segment 4, with guide-bars (top curve) and without guide-bars (bottom curve). A constant angular velocity is applied for the driving sprocket.

figure shows that when the guide-bars are included the dominating frequency is the tooth frequency of 81 Hz and a lower frequency at approximately 7.8 Hz. These results show that the inclusion of the guide-bars as expected changes the vibration frequency of the chain strands with guide-bars.

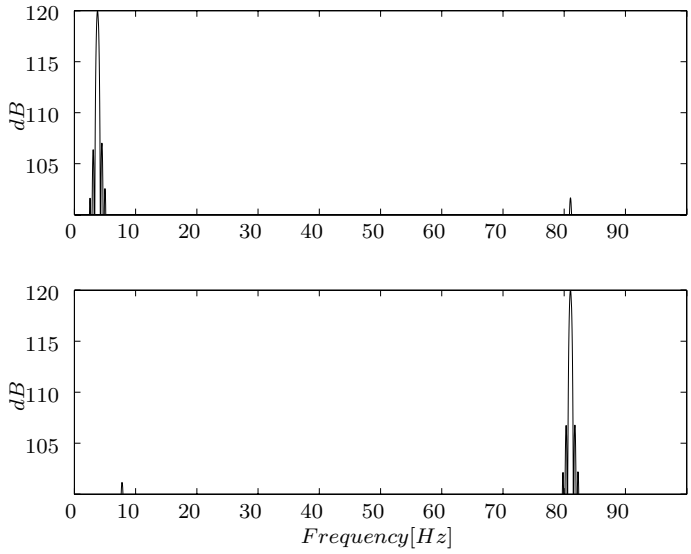

Figure 5.26: Frequency content of the oscillations of chain segment 1, without guide-bars (top) and with guide-bars (bottom). A constant angular velocity is applied for the driving sprocket.

Figure 5.27 shows the frequency content of the oscillations of the middle of chain segment number four from the numerical simulation where the guide-bars are not included (top) and from the numerical simulations where the guide-bars are included (bottom). The top figure shows that when the guide-bars are not included the dominating frequencies are at approximately 2.6 Hz, at approximately 7.8 Hz and at the tooth frequency of 81 Hz. The

bottom figure shows that when the guide-bars are included the dominating frequency is the tooth frequency at 81 Hz. The dominating lower frequencies found are at approximately 6.6 Hz and at approximately 13.2 Hz. The inclusion of the guide-bars changes the vibration frequency of the chain strands.

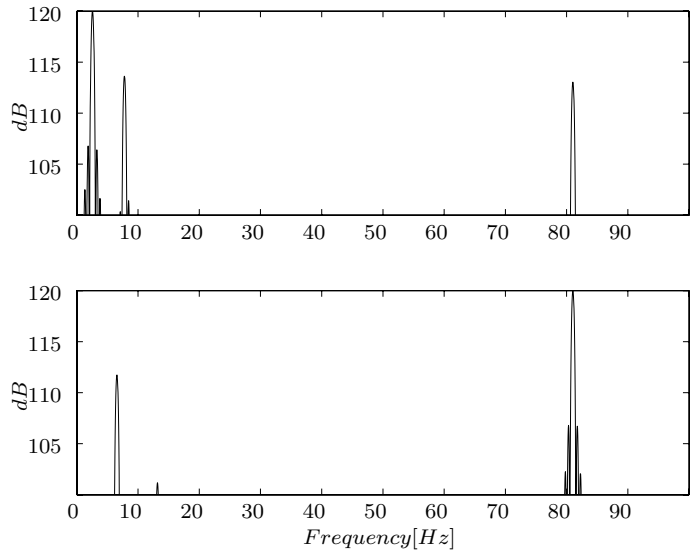

Figure 5.27: Frequency content of the oscillations of chain segment 4, without guide-bars (top) and with guide-bars (bottom). A constant angular velocity is applied for the driving sprocket.

The numerical simulations show no major difference in the vibration pattern of the two chain segment number two and three, whether there is or is not included guide-bars at the other chain strands.

Figure 5.28 shows the oscillations of the middle of chain segment number one from the numerical simulation where the guide-bars are not included (top) and from the numerical simulations where the guide-bars are included (bottom). The figure shows that the guide-bars reduce the amplitude of the oscillations. The numerical simulations are carried out with an oscillating angular velocity as shown in Figure 4.5.

In Figure 5.28 the segment seems to have no horizontal tangent when the segment vibrates from a negative displacement to a positive, however a closer look at the curves as shown in Figure 5.29, shows that this is not the case. The segment however changes faster from negative to positive displacement, even in the case where no guide-bars are included. This might be because the release direction of the roller, which is tangential to the sprocket pitch circle, is in the positive direction of the distance shown in Figure 5.28.

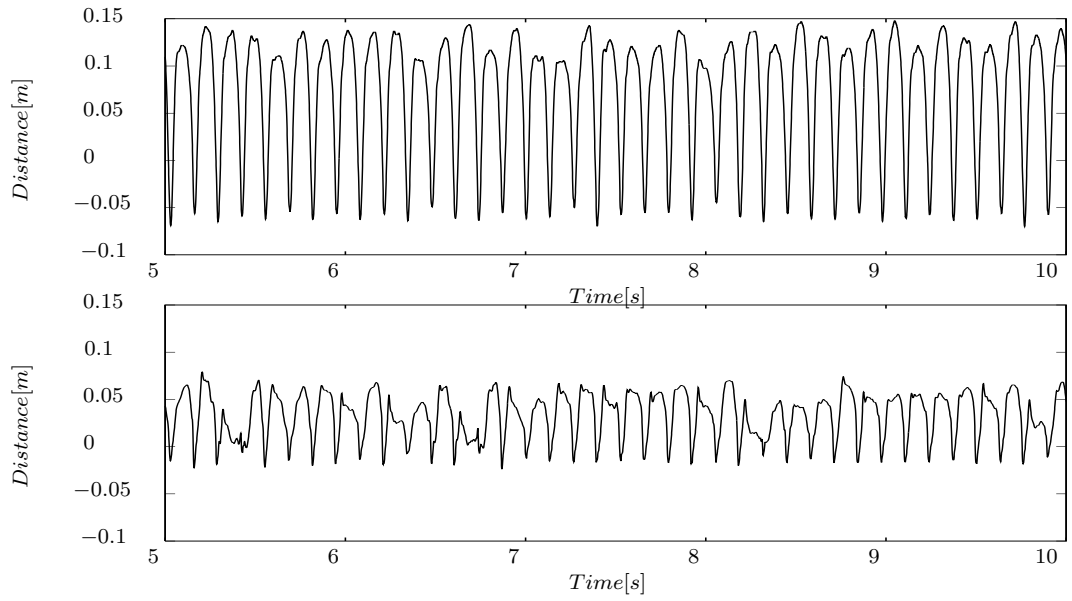

Figure 5.28: Comparison of the oscillations of the middle of chain segment 1, with guide-bars (bottom) and without guide-bars (top). An oscillating angular velocity, as shown in Figure 4.5, is applied for the driving sprocket.

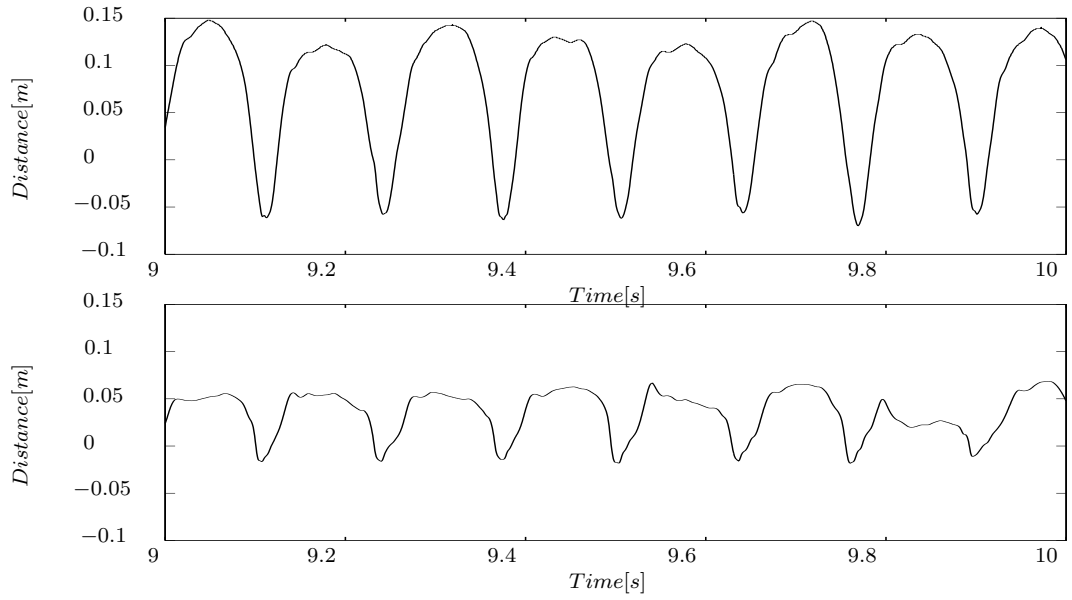

Figure 5.29: Comparison of the oscillations of the middle of chain segment 1, with guide-bars (bottom) and without guide-bars (top). An oscillating angular velocity, as shown in Figure 4.5, is applied for the driving sprocket.

Figure 5.30 shows the oscillations of the middle of chain segment number four from the numerical simulation where the guide-bars are not included (top) and from the numerical simulations where the guide-bars are included (bottom). The figure shows that when the guide-bars are included the amplitude of the oscillation is greater than when the guide-bars are not included. The numerical simulations are carried out with an oscillating angular velocity as shown in Figure 4.5. As for the oscillations of the middle of chain segment number one, a closer look at the oscillations of chain segment number four shows that there is a horizontal tangent, when the displacements changes from negative to positive.

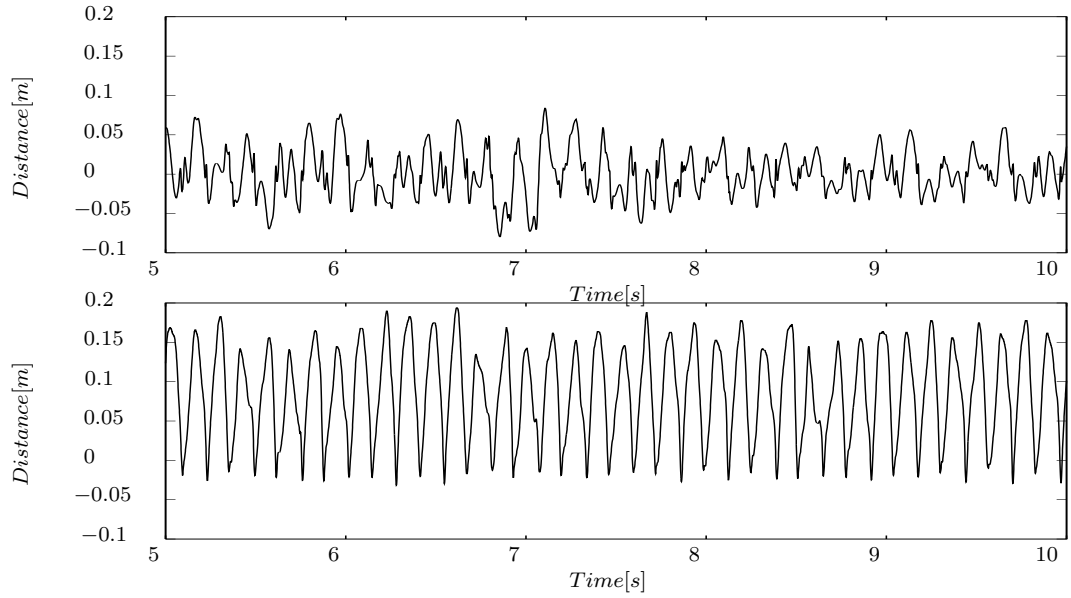

Figure 5.30: Comparison of the oscillations of the middle of chain segment 4, with guide-bars (bottom) and without guide-bars (top). An oscillating angular velocity, as shown in Figure 4.5, is applied for the driving sprocket.

Figure 5.31 shows the frequency content of the oscillations of the middle of chain segment number one from the numerical simulation where the guide-bars are not included (top) and from the numerical simulations where the guide-bars are included (bottom). The figure shows that for both the case of included guide-bars and not included guide-bars the dominating frequency is at approximately 7.6 Hz, which is the 6th order excitation frequency, see Figure 4.4. The two higher order peaks at approximately 15.2 Hz and approximately 22.9 Hz are also seen for both the case of included guide-bars and not included guide-bars. However the bottom figure shows that some lower frequencies occur,

when the guide-bars are included.

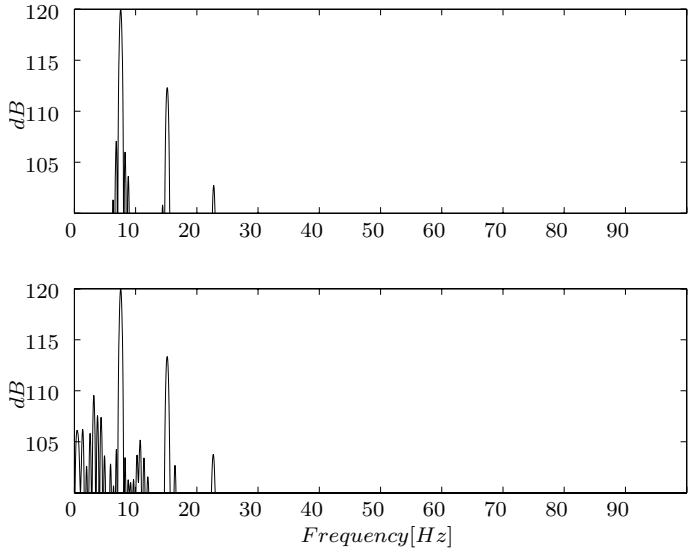

Figure 5.31: Frequency content of the oscillations of chain segment 1, without guide-bars (top) and with guide-bars (bottom). An oscillating angular velocity, as shown in Figure 4.5, is applied for the driving sprocket.

Figure 5.32 shows the frequency content of the oscillations of the middle of chain segment number four from the numerical simulation where the guide-bars are not included (top) and from the numerical simulations where the guide-bars are included (bottom). The figure shows that for the case of included guide-bars the dominating frequency is at approximately 7.6 Hz, which is the 6th order excitation frequency, see Figure 4.4. The higher order peaks are at approximately 15.2 Hz, which is the 12th order excitation frequency and a peak at approximately 19 Hz, which is the 15th order excitation frequency. The figure shows that for the case when the guide-bars are not included the dominating frequencies are at approximately 1.9 Hz, 5.6 Hz and 11.4 Hz, where none of them are directly related to the excitation frequency.

5.7.2 Comparison of the Link Forces

Figure 5.33 shows the link force in a link, for the case of no guide-bars included (top) and when guide-bars are included (bottom). The numerical results are carried out using a constant angular velocity. The figure shows that the link force is similar for both the case of inclusion of guide-bars and not. The figures also show that for the given position of the tightener sprocket the pre-tension in the chain is approximately 70 kN.

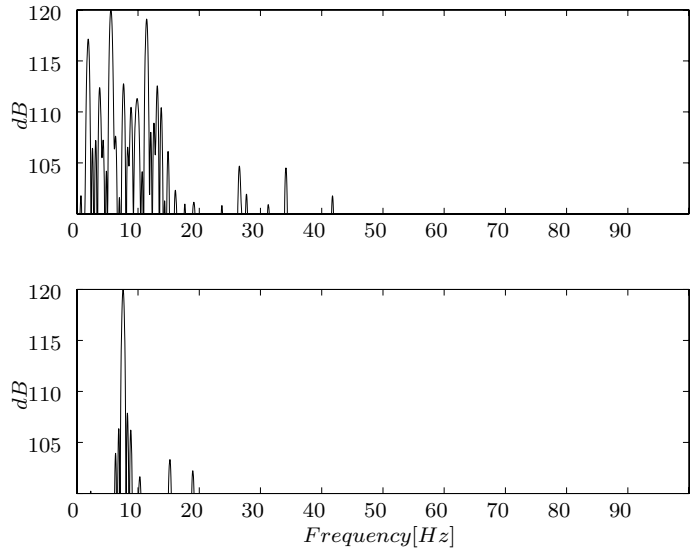

Figure 5.32: Frequency content of the oscillations of chain segment 4, without guide-bars (top) and with guide-bars (bottom). An oscillating angular velocity, as shown in Figure 4.5, is applied for the driving sprocket.

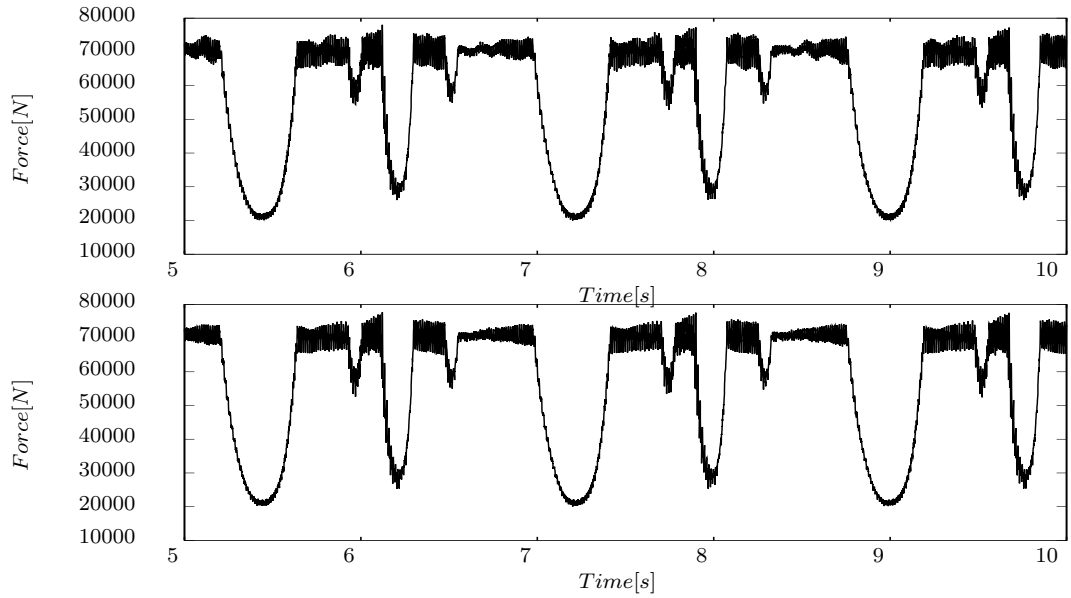

Figure 5.33: The link force in a link, when no guide-bars are included (top) and guide-bars are included (bottom). A constant angular velocity is applied for the driving sprocket.

Figure 5.34 shows the link force in a link, for the case of no guide-bars included (top) and when guide-bars are included (bottom). The numerical results are carried out using

an oscillating angular velocity as shown in Figure 4.5. The figures show that the amount of the link force changes from a maximal link force of approximately 1.8 MN when no guide-bars are included to approximately 1.2 MN when the guide-bars are included. The link force when the oscillating angular velocity is applied is approximately twice the size of the link force when the constant angular velocity is applied.

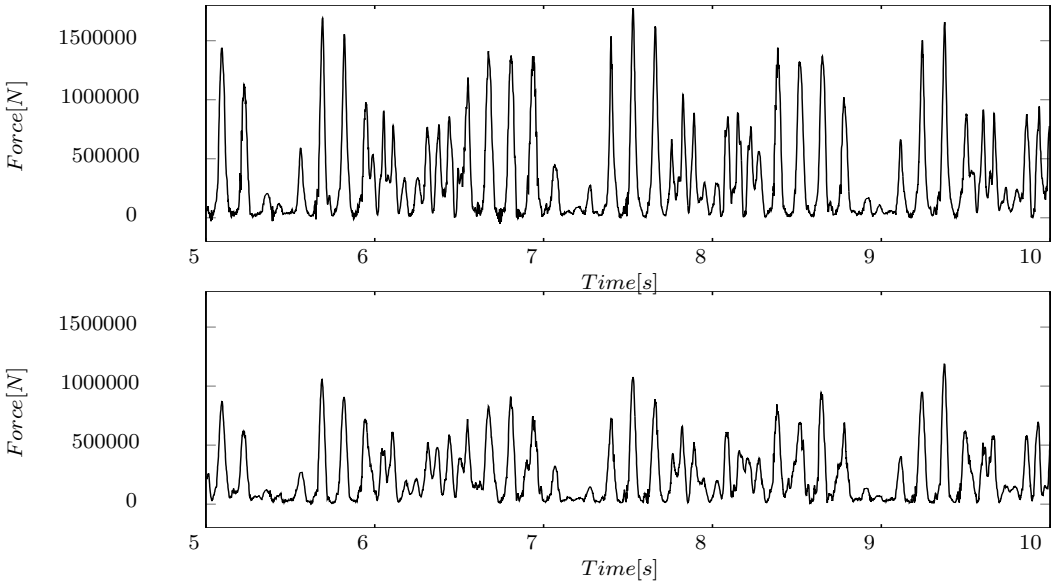

Figure 5.34: The link force in a link, when no guide-bars are included (top) and when guide-bars are included (bottom). An oscillating angular velocity, as shown in Figure 4.5, is applied for the driving sprocket.

5.7.3 Comparison of the Contact Forces

Figure 5.35 shows the contact force on a link, for the case of no guide-bars included (top) and when guide-bars are included (bottom). The numerical results are obtained with a constant angular velocity for the driving sprocket. The figure shows that the contact force is similar for both the cases. The figure also shows that the largest contact force is approximately 25 kN.

Figure 5.36 shows the contact force on a link, for the case of no guide-bars included (top) and when guide-bars are included (bottom). The numerical results are carried out using an oscillating angular velocity as shown in Figure 4.5. The figures show that the contact force changes from a maximal value of approximately 400 kN when the guide-bars are not included to a maximal value of approximately 200 kN when guide-bars are included.

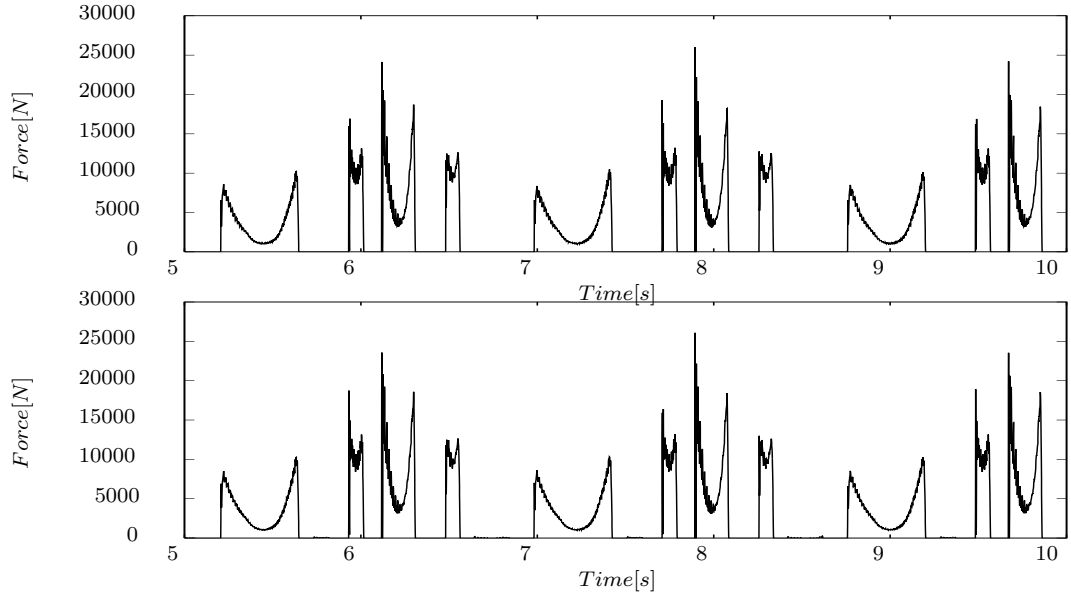

Figure 5.35: The contact force on a link, when no guide-bars are included (top) and when guide-bars are included (bottom). A constant angular velocity is applied for the driving sprocket.

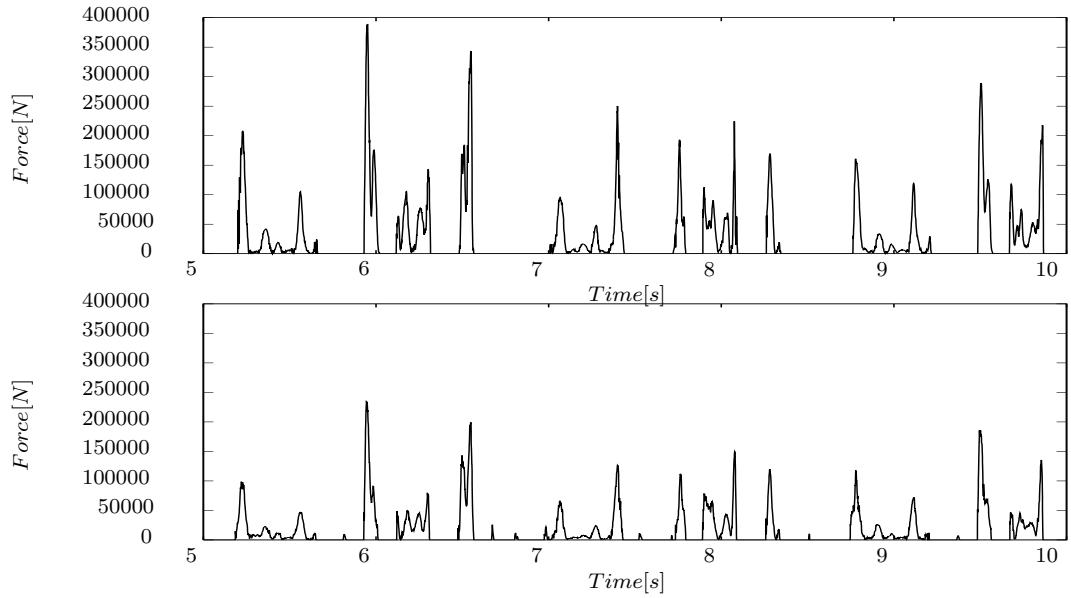

Figure 5.36: The contact force on a link, when no guide-bars are included (top) and when guide-bars are included (bottom). An oscillating angular velocity, as shown in Figure 4.5, is applied for the driving sprocket.

The contact forces from the numerical simulation using an oscillating angular velocity are more than ten to twenty times larger than the contact force from the numerical simulation

using a constant angular velocity for the driving sprocket.

5.8 Results with Tightener System

In this sections the results from numerical simulations are shown, where the tightener system is included and the tightener sprocket centre is allowed to move. The influence of including the tightener system is in this section presented with application to a MAN B&W 6S90MC-C marine diesel engine fore end chain drive. The chain drive data are given in section 5.3.1. In the numerical simulation friction between the roller and sprocket was included, with a dynamic friction coefficient $\mu_d = 0.1$ and the dynamic correction factor μ_c is modelled by Equation (3.98), that is the Heaviside approximation with $H_1(x)$ (see appendix G), using $\epsilon = 0.01$ and $v_t^* = 0.1$. Rotational damping is included with a damping coefficient chosen to be $C_d = 0.5$ Ns.

The tightener system is modelled with the centre of mass of the weight-arm at $(x_{w1}, y_{w1}) = (0.1975, 4.7328)$m, the point on the weight-arm where the spring is attached at $(x_{w2}, y_{w2}) = (-0.3, 4.425)$m, the two grounded points at $(x_{G1}, y_{G1}) = (0.490, 4.680)$m and $(x_{G2}, y_{G2}) = (-0.3, 5.625)$m, see Figure 5.37 and Figure 5.11. The initial position of the centre of sprocket number three, which is in the tightener system, is given in table 5.5. The mass and mass moment of inertia of the weight-arm are chosen to be $m_w = 300$ kg and $J_w = 10$ kgm^2 respectively. The data for the spring-damper in the tightener system are chosen such that the undeformed length of the spring is $L_0 = 1.19$ m, the stiffness coefficient is $K_t = 6$ MN/m and the damping coefficient is $D_{ct} = 0.8$ kNs/m. The bodies in the tightener system are connected as described in section 3.8.1 and shown in Figure 3.20.

The results from two different numerical simulations are compared, where both include a tightener system and guide-bars. The two simulations are carried out, respectively with a constant angular velocity and with an oscillating angular velocity, applied to the driver sprocket. The guide-bars are positioned parallel with the tangent line between the sprockets and are pressed 0.005 m into the chain. Three guide-bars are applied, one on chain segment number one and two on chain segment number four, which are the two longest chain segments in the chain drive system, see Figure 5.11. An average generalized coefficient of stiffness for the guide-bar contact, is calculated using (3.32) and the value used in (3.47) is $K_g = 3$ MN/m. The data used to calculate the average stiffness coefficient is given in Table 5.7 and for the guide-bars Poisson's ratio is $\nu = 0.5$ and the value of Young's modulus is set to be $E = 5$ MN/m^2.

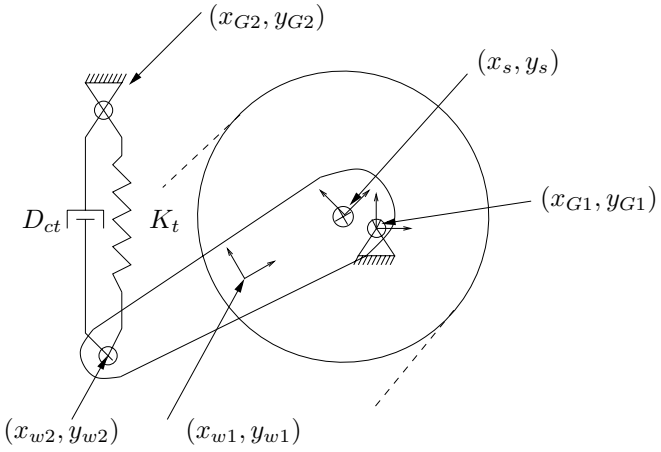

Figure 5.37: The connection points between the bodies in the model of the tightener system of the 6S90MC-C fore end chain drive system.

5.8.1 Oscillations of the weight-arm centre of mass

In section 5.7 it was shown that the oscillations of the middle of the chain segments are larger, when an oscillating angular velocity is applied to the driver sprocket, than when a constant angular velocity is applied. However the results shown in this section are not directly comparable with those shown in the previous section, because the centre position of the sprocket in the tightener system is slightly different from the position given in Table 5.5. When the static equilibrium is found the centre position of sprocket number 3 is changed to $(x_s, y_s) = (0.334, 4.749)$m, due to the chosen configuration of the tightener system.

Figure 5.38 shows the x coordinate of the centre of mass position of the weight-arm, that is x_{w1} as a function of time. The figure shows result from a 10 seconds simulation, where a constant angular velocity is applied.

Figure 5.39 shows the x coordinate of the centre of mass position of the weight-arm, that is x_{w1} as a function of time. The figure shows result from a 10 seconds simulation, where an oscillating angular velocity, as shown in Figure 4.5, is applied. For both the numerical simulation with a constant angular velocity and an oscillating angular velocity, only the oscillations of the x_{w1} coordinate is presented, since the vibration pattern of the y_{w1} coordinate is similar.

The figures show that when a constant angular velocity is applied the amplitude of the

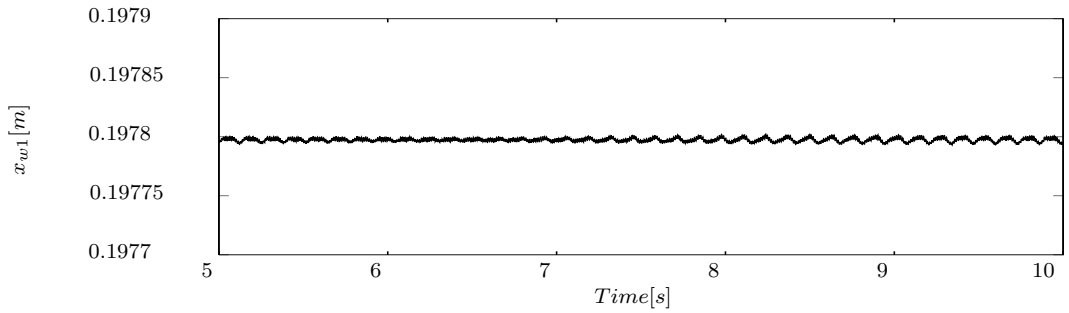

Figure 5.38: The x coordinate of the centre of mass position of the weight-arm. A constant angular velocity is applied for the driving sprocket.

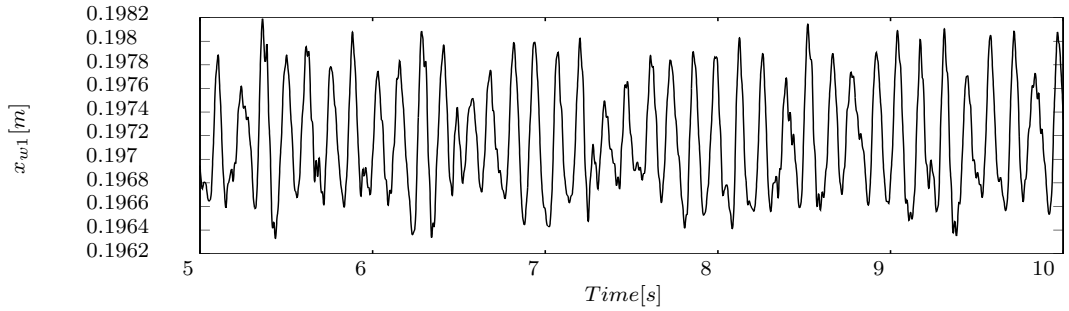

Figure 5.39: The x coordinate of the centre of mass position of the weight-arm. An oscillating angular velocity, as shown in Figure 4.5, is applied for the driving sprocket.

oscillations of the weight-arm are smaller than when an oscillating angular velocity is applied, since the chain vibrations become much larger.

Figure 5.40 shows the frequency content of the oscillations of the x coordinate of the centre of mass position of the weight-arm. For a constant angular velocity applied for the driver sprocket (top) and for an oscillating angular velocity is applied (bottom). The figure shows that the dominating frequencies are at approximately 7.6 Hz, 15.2 Hz and we also see the tooth frequency of 81 Hz, when the constant angular velocity is applied. For the case of an oscillating angular velocity applied to the driver sprocket, the dominating frequencies are again at approximately 7.6 Hz and at approximately 15.2 Hz, which also is the 6th order excitation frequency, see Figure 4.4, and twice the 6th order excitation frequency, respectively.

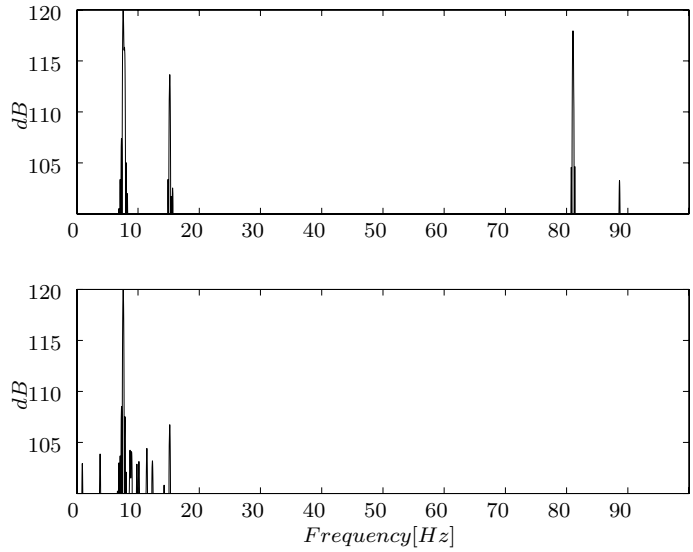

Figure 5.40: Frequency content of the oscillations of the x coordinate of the centre of mass position of the weight-arm. For a constant angular velocity applied for the driving sprocket (top) and for an oscillating angular velocity, as shown in Figure 4.5, is applied for the driving sprocket.

5.8.2 Oscillations of the Middle of the Chain Segments

Figure 5.41 shows oscillations of the middle of chain segment number one from the numerical simulation done with a constant angular velocity of 76 rpm is applied for the driver sprocket. Figure 5.42 shows oscillations of the middle of chain segment number one from the numerical simulation done with an oscillating angular velocity, as shown in Figure 4.5, applied for the driving sprocket.

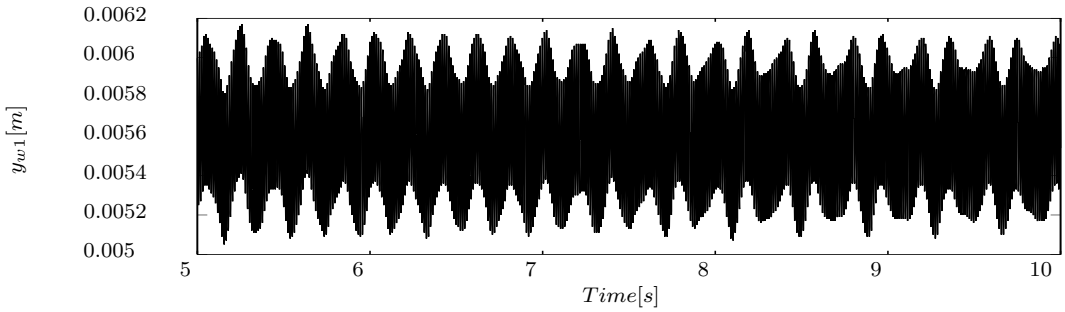

Figure 5.41: The oscillations of the middle of chain segments 1. A constant angular velocity is applied for the driving sprocket.

Figure 5.43 shows the frequency content of the oscillations of the middle of chain segment number one from the numerical simulation where a constant angular velocity is applied for

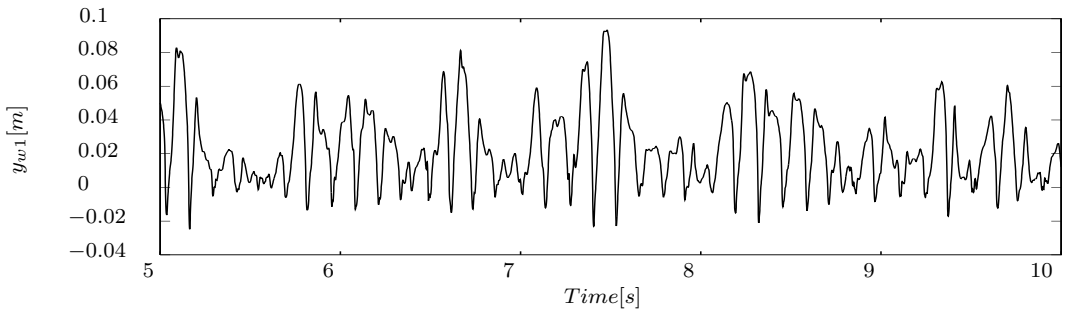

Figure 5.42: The oscillations of the middle of chain segments 1. An oscillating angular velocity, as shown in Figure 4.5, is applied for the driving sprocket.

the driver sprocket (top) and when an oscillating angular velocity is applied (bottom). The figure shows that the dominating frequencies are at approximately 5.1 Hz and we also see the tooth frequency of 81 Hz, when the constant angular velocity is applied. For the case of an oscillating angular velocity applied to the driver sprocket, the dominating frequency is at approximately 7.6 Hz, which is the 6th order excitation frequency, see Figure 4.4. The peaks at approximately 15.2 Hz is at twice the 6th order excitation frequency.

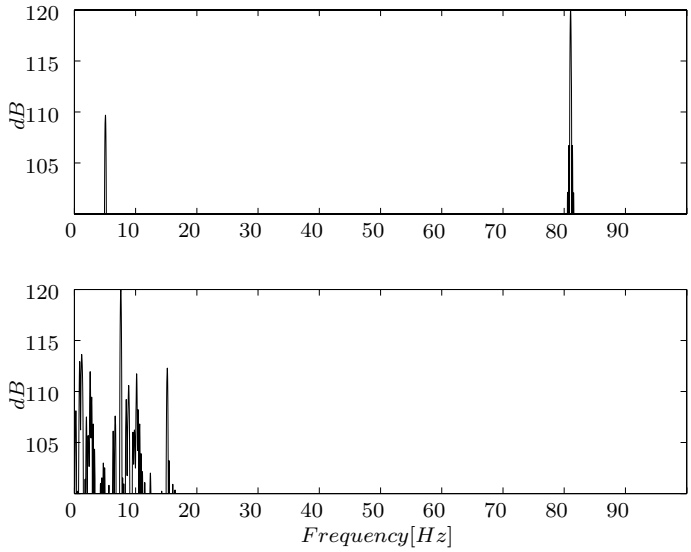

Figure 5.43: Frequency content of the oscillations of chain segment 1, a constant angular velocity applied for the driving sprocket (top) and an oscillating angular velocity, as shown in Figure 4.5, is applied for the driving sprocket.

5.8.3 Comparison of the Link Forces

Figure 5.44 shows the link force in a link, when a constant angular velocity is applied for the driving sprocket. The figure shows that the link force pattern is different from the results obtained when the tightener sprocket was fixed, see Figure 5.33. The pre-tension in the chain is also different and is, when the tightener system is applied, approximately 90 kN.

Figure 5.45 shows the link force in a link, when an oscillating angular velocity, is applied for the driving sprocket. The figure again shows that the amount and pattern of the link force changes, when compared to the results obtained with a fixed tightener sprocket, see Figure 5.34. The maximal link force is when the tightener system is included approximately 0.8 MN.

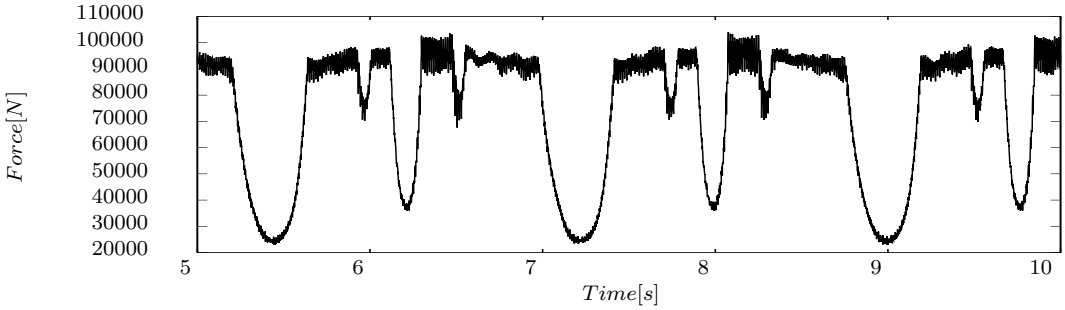

Figure 5.44: The link force in a link, when a constant angular velocity is applied for the driving sprocket.

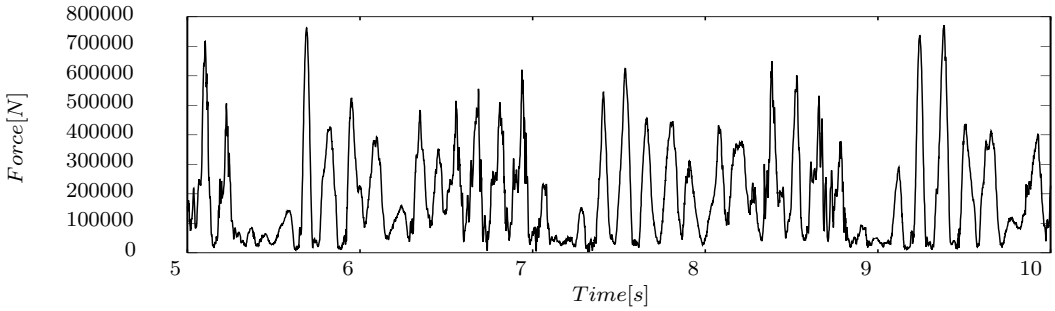

Figure 5.45: The link force in a link, when an oscillating angular velocity, as shown in Figure 4.5, is applied for the driving sprocket.

5.8.4 Comparison of the Contact Forces

Figure 5.46 shows the contact force on a link, when a constant angular velocity is applied for the driving sprocket. The figure shows the contact force is similar, to the contact forces obtained, when the tightener sprocket is fixed, see Figure 5.35. The figure also shows that the approximately larges contact force is 35 kN.

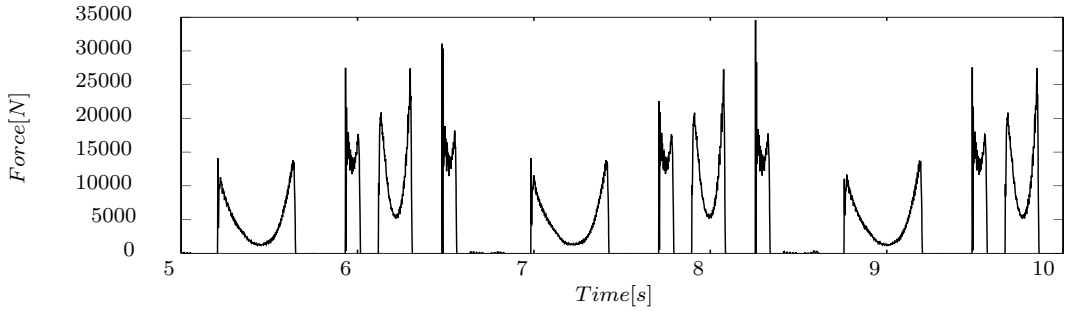

Figure 5.46: The contact force on a link, when a constant angular velocity is applied for the driving sprocket.

Figure 5.47 shows the contact force on a link, when an oscillating angular velocity, is applied for the driver sprocket. The figure shows the contact force is similar, to the contact forces obtained, when the tightener sprocket is fixed, see Figure 5.36. The figures show that the contact force has a maximum value of approximately 160 kN when guide-bars are included.

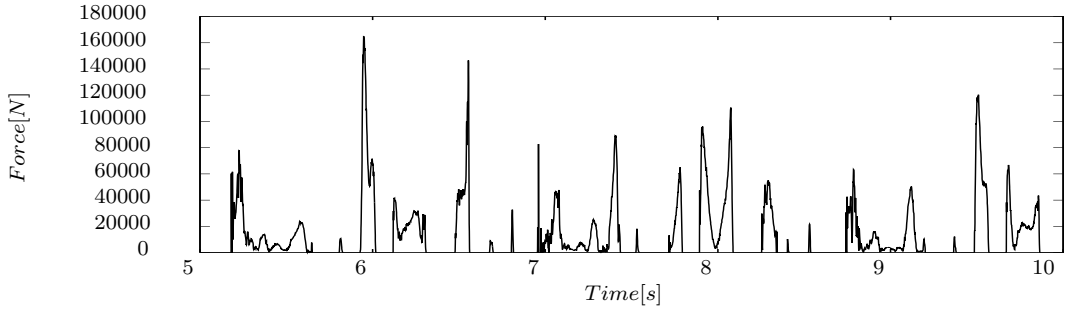

Figure 5.47: The contact force on a link, when an oscillating angular velocity, as shown in Figure 4.5, is applied for the driving sprocket.

It is observed that the contact forces looks somewhat similar to the contact forces calculated, when the tightener sprocket was fixed, see Figure 5.35 and Figure 5.36.

5.9 Analysis of Resonance

One of the purposes of a chain drive simulation program is to be able to investigate possible resonance for e.g. different values of pre-tension and driver velocity. Several simulations have been carried out with application to marine diesel engine 6S90MC-C fore end chain drive. The chain drive data are given in section 5.3.1. The results presented in this section are from numerical simulations, which were carried out before the friction and rotational damping models were developed and implemented. The number of numerical simulations that where carried out to calculate these results is large, therefore due to lack of remaining time in the project period, friction and rotational damping are not included in these presented results.

5.9.1 Natural Frequency of the Chain Segment.

Resonance can occur when the excitation frequency coincides with the natural frequencies of the chain segments between the sprockets. Figure 5.48 shows the cyclic natural frequency of chain segment one, see Figure 5.11, for different values of the pre-tension in the string as a function of the chain speed presented in percentage of Maximum Continuous Rating, MCR = 76 rpm (the driver velocity). The cyclic natural frequency is given by $f_n = \frac{\omega_n}{2\pi}$, where the radial natural frequency ω_n is given by Equation (4.27). The pre-tension in the chain, given as a fraction of the fracture load of the chain $P_b = 2002$ kN, shown in the figure are 1/5, 1/10, 1/25, 1/30, 1/35, 1/40 and 1/45. The solid lines are for the relaxation factor in (4.31) $\eta = 0$ and the dotted lines are for the relaxation factor in (4.31) $\eta = 1$. The different marks on the solid and dotted lines represent the different amount of pre-tension as follows, star (—∗—/ · ∗ ·) is for $F = 1/5P_b$, circle (—○—/ · ○· ·) is for $F = 1/10P_b$, square (—□—/ · □· ·) is for $F = 1/25P_b$, diamond (—◇—/ · ◇· ·) is for $F = 1/30P_b$, plus (—+—/ · +· ·) is for $F = 1/35P_b$, triangle (—△—/ · △· ·) is for $F = 1/40P_b$ and cross (—x—/ · x· ·) is for $F = 1/45P_b$. The dotted line that crosses the natural frequency lines is the cyclic tooth engagement frequency $f_p = \frac{\omega_p}{2\pi}$, where ω_p is given by Equation (4.33). The dashed-dotted line with a circle represents the 6th order excitation frequency and the dashed-dotted line being half the 6th order excitation frequency.

Figure 5.49 shows the cyclic natural frequency of chain segment one as in figure 5.48, but for only one pre-tension force, that is $F = 1/25P_b$. The most critical resonance value of the frequency occurs when half the excitation frequency is equal to the natural frequency of the chain string. Figure 5.49 shows that when the pre-tension is set to 1/25

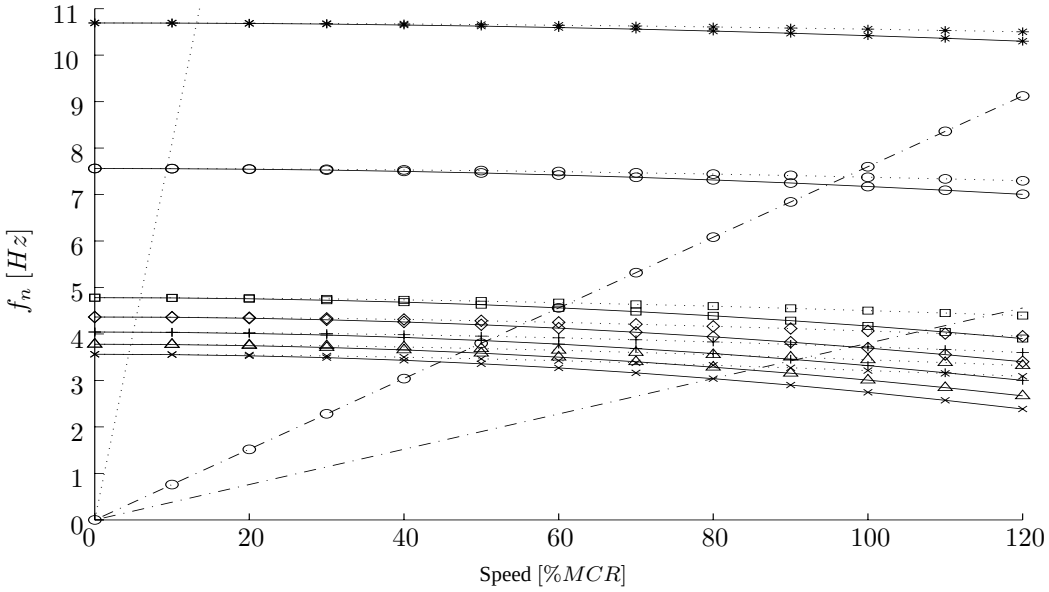

Figure 5.48: The natural cyclic frequency of chain segment 1, for different values of the pre-tension. The different marks on the solid and dotted lines represent $*$: $1/5P_b$, $\circ$: $1/10P_b$, $\square$: $1/25P_b$, $\diamond$: $1/30P_b$, $+$: $1/35P_b$, $\triangle$: $1/40P_b$ and x: $1/45P_b$ respectively. The dotted line is the cyclic tooth engagement frequency. The dashed-dotted line with a circle represents the 6th order excitation frequency and the dashed-dotted line being half the 6th order excitation frequency.

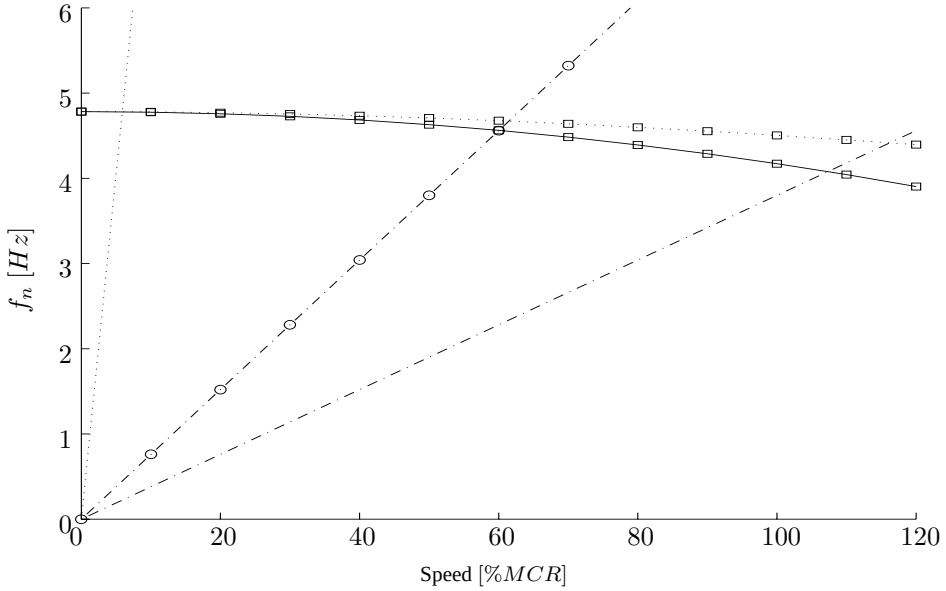

Figure 5.49: The natural frequency of chain segment (1), for the pre-tension force of 1/25 of the fracture load P_b. The dotted line is the cyclic tooth engagement frequency. The dashed-dotted line with a circle represents the 6th order excitation frequency and the dashed-dotted line being half the 6th order excitation frequency.

of the fracture load, then resonance is reached for values of the speed higher than MCR, that is at between 107 %MCR and 116 %MCR, dependent on the factor of relaxation of the structure $\eta \in [0, 1]$. Resonance with the tooth engagement frequency is reached at approximately 6 %MCR and resonance with the excitation frequency is reached at approximately 60 %MCR.

Figure 5.50 shows the cyclic natural frequency of the other three chain segments in the chain drive system, see Figure 5.48, for one pre-tension force, that is $F = 1/25P_b$. These three strings are in contact with the three small driven sprockets, which are half the size of the driver sprocket, so they run with twice the angular velocity, yielding MCR for the smaller to 152 rpm. The most critical resonance value of the frequency occurs when half the excitation frequency is equal to the natural frequency of the chain string.

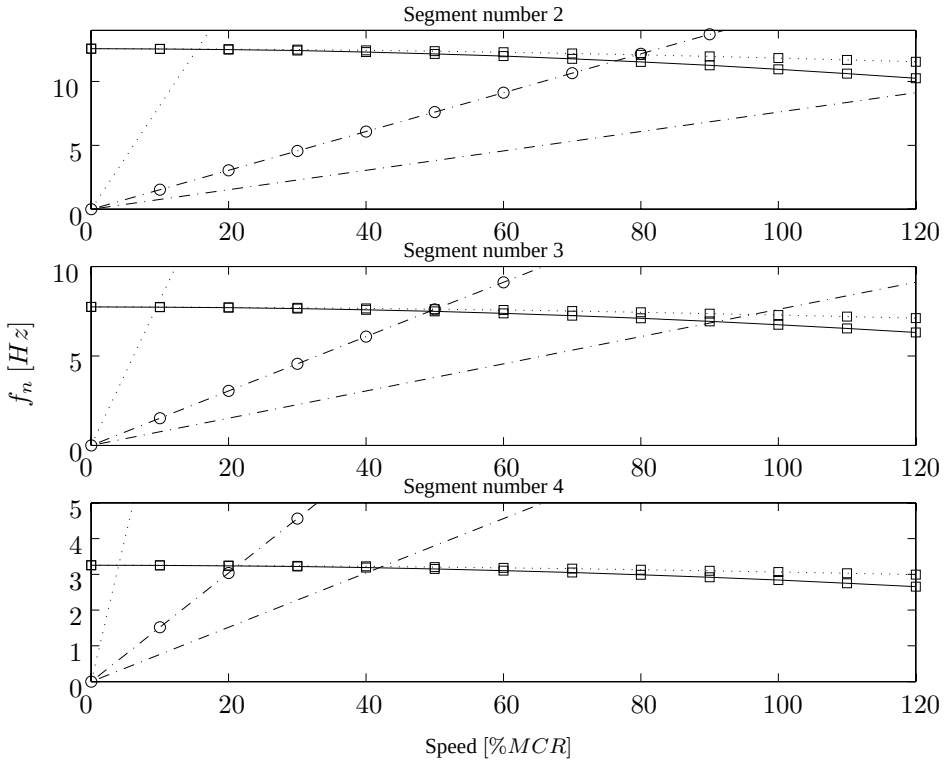

Figure 5.50: The natural frequency of chain segment 2, 3 and 4, for the pre-tension force of 1/25 of the fracture load P_b. The dotted line is the cyclic tooth engagement frequency. The dashed-dotted line with a circle represents the 6th order excitation frequency and the dashed-dotted line being half the 6th order excitation frequency.

Figure 5.50 shows that when the pre-tension is set to 1/25 of the fracture load resonance is reached for values of the speed higher than MCR for segment number 2, but for seg-

ment number 3 it is reached at approximately 93 %MCR and for segment number 4 at approximately 42 %MCR.

5.9.2 Variation of the Pre-tension in the Chain.

Knowing the coordinates of the grounded point on the weight-arm in the tightener system, the center position of the sprocket can be found for any angle ϕ_{tg}, because the distance R_{tg} is fixed. When the angle is changed the chain becomes either more tight or more slack. Figure 5.51 shows how the center of the sprocket in the tightener system is connected to the weight-arm, which is connected to ground. The distance between the tightener sprocket center and the grounded point is set to be $R_{tg} = 0.171$ m. The angle ϕ_{tg} is the angle between the global x-axis and the line between the center of the tightener sprocket and the grounded point, having the local coordinate system for the ground coincident with the global coordinate system, see Figure 5.51.

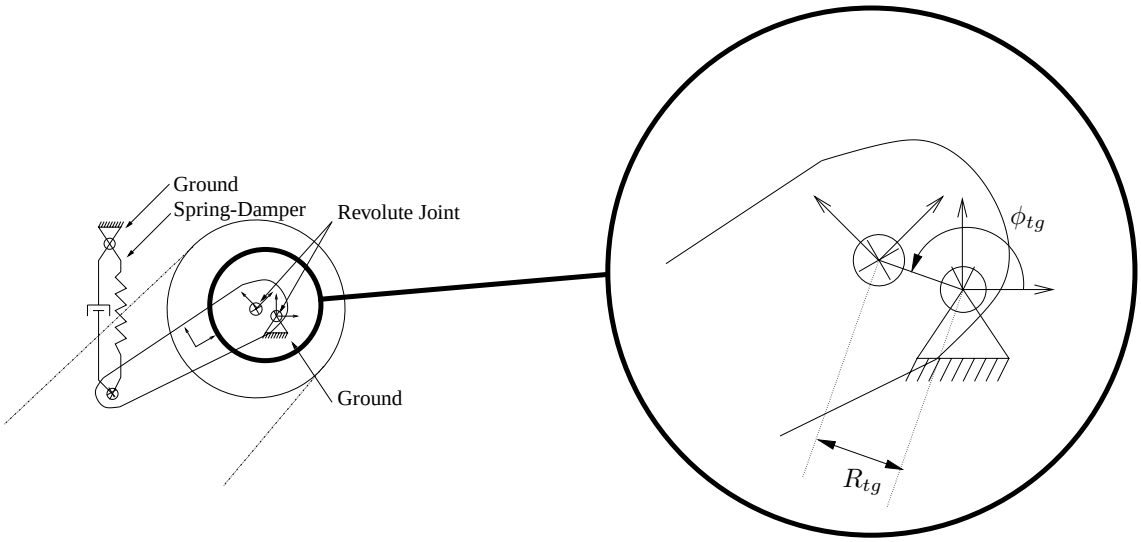

Figure 5.51: The relation between the grounded point on the weight-arm and the center of the sprocket.

Figure 5.52 shows the maximal link force in one link normalized with the fracture load of the chain $P_b = 2002$ kN. These results are obtained from numerical simulations, where the center of the tightener sprocket is fixed during the simulation, but for each simulation at a different point dependent on the angle ϕ_{tg} in the range $\phi_{tg} \in [152°; 161°]$. When the angle is increased the pre-tension in the chain is decreased.

The solid line is the results from simulations of 10 seconds, when the driving sprocket is

rotating with a constant angular velocity of 76 rpm, the three different dashed lines are results from simulations, when the driving sprocket rotates with a oscillating angular velocity as shown in Figure 4.5. The dashed line is results obtained from a simulation of 10 seconds using the end positions and velocities from the simulation with constant velocity as the initial positions and velocities. The dashed-dotted line are results obtained from a simulation of 10 seconds using the end positions and velocities from the previous simulation with the previous angle being smaller than the present angle as the initial positions and velocities. The dotted line are results obtained from a simulation of 10 seconds using the end positions and velocities from the previous simulation with the previous angle being larger than the present angle as initial positions and velocities. For all of the four simulations the maximal force in the link is calculated in the time from 5 to 10 seconds.

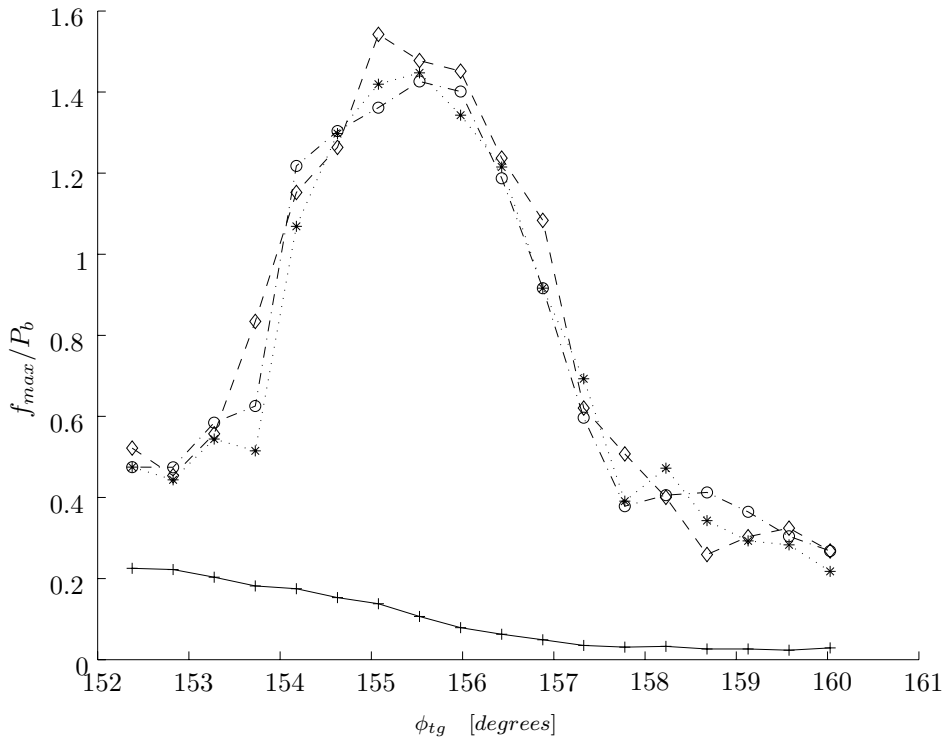

Figure 5.52: The maximal link force for constant and oscillating velocity of the driving sprocket.

In Figure 5.52 we observe that a resonance peak occur when the angle ϕ_{tg} is around 155 degrees. This indicates which angles/positions of the tightener sprocket are preferable and which are not. The numerical results presented here are given merely to give an impression of what kind of analysis can be performed with the numerical simulation tool, since friction and rotational damping was not included, which as shown in the prior sections

has a major influence on e.g. the magnitude of the link force and the oscillations of the chain segments.

5.9.3 Variation of the Angular Velocity.

In Figure 5.53 results from simulations with a fixed angle $\phi_{tg} = 156.5°$ are shown, yielding the coordinates for the center of the tightener sprocket $(x_s, y_s) = (0.333199, 4.748179)$m. The simulations are carried out for different angular velocities $\dot{\theta}_s \in [32rpm; 90rpm]$, with sweeps of 2 rpm. The solid line is from the simulation using a constant angular velocity, the dashed line is from the simulation using a oscillating angular velocity as shown in Figure 4.5 and the dotted line is from the simulation using a oscillating angular velocity with a pure sinus excitation as given in Equation (4.5), with $k = 6$.

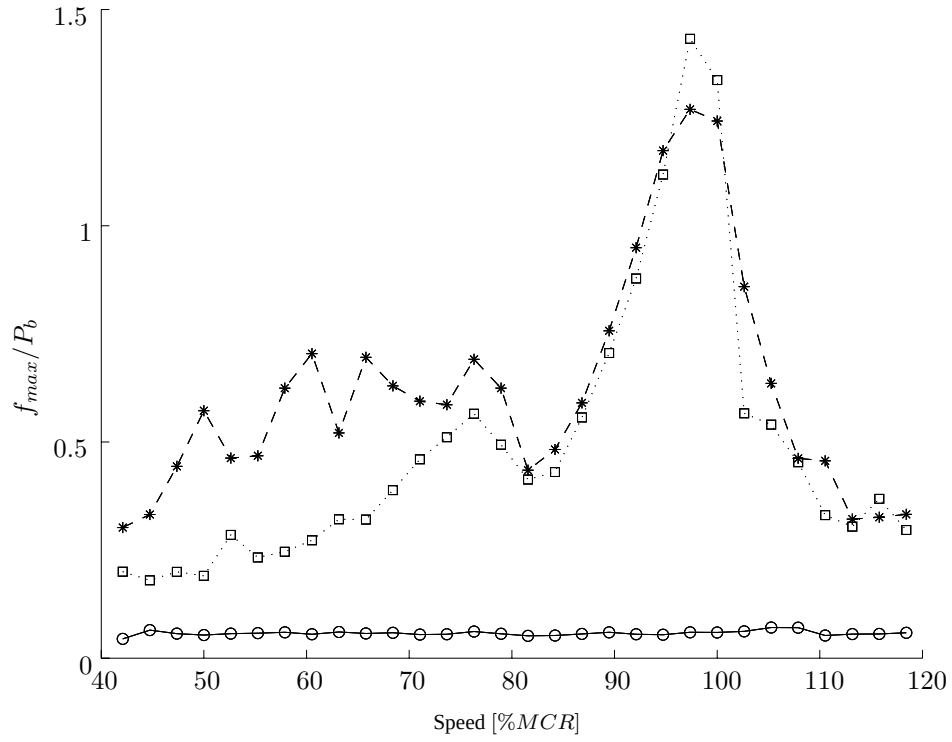

Figure 5.53: The maximal link force for constant and oscillating velocity of the driving sprocket.

Figure 5.53 shows the maximal link force in one link normalized with the fracture load of the chain $P_b = 2002$ kN as a function of the speed given in percentage of the MCR = 76 rpm. In Figure 5.53 we observe that a resonance peak occur around 98 %MCR. This indicates that the critical speed of the engine is reached before MCR for the given chain drive system configuration analysed here.

The angular acceleration provided by MAN B&W Diesel A/S is shown in Figure 4.5 and the frequency content in Figure 4.4. From the frequency content of the angular oscillation we see that the major peak is at the 6th excitation order. Therefore the pure 6th order sinus excitation was analysed separately. Comparing the two resonance peaks from the two different excitations shown in Figure 5.53, it can be concluded that the resonance peak is triggered by the 6th order excitation.

However the numerical results presented here are given merely to give an impression of what kind of analysis can be performed with the numerical simulation tool, since friction and rotational damping was not included, which as shown in the prior sections has a major influence on e.g. the magnitude of the link force and the oscillations of the chain segments.

5.10 Experimental Validation

The numerical simulation tool is yet to be validated by experimental results. The company MAN B&W Diesel A/S has earlier done some experiments on their roller chain drives, but for these results no chain drive system data is available. However MAN B&W Diesel A/S is planning to do some new experiments in the near future.

In order to validate the results obtained by the simulation program several things should be measured while the engine is running at different angular velocities. The kind of experiments that has earlier been performed included e.g. measurement of a link force, the pre-tension force, transversal vibration of the chain segments, vibration of the tightener system and angular acceleration of the sprockets. Such measurements can all be directly compared with the results obtained from the simulation program.

By placing wireless Strain Gauges on one or more links and doing measurement while the engine is running the link force in a chain link can be calculated. In order to calculate the pre-tension force in the chain, strain gauge measurements are performed on the tightener bolt in the chain tightener system. In a similar way the position of the centre of the sprocket in the tightener system can be moved and the pre-tension can be found from the simulation.

The transversal vibrations of the chain segments between the sprockets can be monitored by a light-emitting diode device developed by MAN B&W Diesel A/S. These measurements are to be compared with the transversal vibrations of the middle of the chain seg-

ments that are calculated by the simulation program, both with and without guide-bars.

It is also important to measure the angular accelerations of all the sprockets in the chain drive system, in order to verify the numerical simulation program. This can be done using a sensor that traces the sprocket teeth, from which the measurement of the change in time can represent the torsional vibrations of the sprocket axle. Due to the fact that the angular acceleration of the sprockets in numerical simulations depend on the contact forces and the position where the contact forces acts on the sprocket, these experiments can verify the usefulness of the contact force model as it is used in the simulation program.

Other experiments are also planned, such as measuring the temperature in the guide-bars, measuring the translation of the sprocket centres and measuring the loss of power in the chain drive. The most important measurements related with verification of the numerical simulation program are the link force, the angular acceleration and the transversal oscillation of the chain segments in order to validate the simulation program.

5.11 Discussion

In this chapter it was shown that the mathematical model including the real shape of the tooth profile is preferable compared with a circular tooth profile. Using the real tooth profile it was shown that some of the noise, that occurs when the circular tooth profile was used, was smoothed out. Comparing the contact force between the rollers and sprockets obtained by the two tooth shape models with a simplified analytical model also showed that the real shaped tooth profile is a better model. Furthermore the real tooth profile model has shown to be more numerically stable and able to solve some problems, where the circular tooth profile model has failed.

Including friction between the rollers and sprockets in contact has shown to have a smoothing effect on the contact force and therefore also on the link forces and chain vibrations. When the rotational damping was included the results showed that this had a major influence. For the same configuration of a chain drive system the calculated amount of pre-tension in the chain changed significantly when the rotational damping was included. When the rotational damping was included the chain vibrations had smaller amplitudes and therefore the link forces became significantly lower. The rotational damping also showed to be important in order for the numerical simulation quickly to reach steady state.

Numerical results including the simplified models of the guide-bars and tightener systems shows the kind of simulations that can be performed using the chain drive program, which are important when one wants to make comparison with a real marine engine. The last section in this chapter presents a number of different experiments that are described and related to the important validation of the numerical simulation program, which is left for future work.

In the numerical results it is observed that, when a constant angular velocity is applied to the driver sprocket, the frequency responses originate from the chain string eigenfrequencies, the tooth frequency etc. In the case of applying an oscillating angular velocity to the driver sprocket, the dominating excitation frequency is also seen in the response.

Chapter 6
Conclusion

A novel formulation for the simulation of the dynamics of roller chain drives using a continuous contact force method is developed in this work. With this model it is possible to perform a dynamic simulation of the roller-chain/sprocket system, including the polygonal effect, which appears when the individual chain links engage and disengage with the sprockets, the roller impact at engagement, the flexibility of the links and the coupling between axial and transverse vibrations. Moreover, the formulation allows for the introduction of multiple and different sized sprockets and different parts present in real marine engines.

The application to chain drives of large marine engines demonstrates the level of modelling that is possible to achieve with the proposed formulation. The variation of the link forces and analysis of the transversal oscillations of the chain strands exemplify the type of results useful for the design of the roller chain drives in terms of fatigue and wear. The continuous contact force model includes the tooth flexibility, modelled by the actual shape. The model does, however, not include for example clearance between pin and bushing or the rotational inertia of the link elements.

The continuous contact force model used throughout this thesis has earlier been compared with a kinematic constraint method and was found to be the most numerical stable method and the simulation time was found to be much lower, why the emphasis has been put on this method. Through the application of this method, it is shown that the interrelated dynamics of the elements in the chain drive system is captured and the contact problem is characterized.

A mathematical model including the actual shape of the sprocket teeth is suggested and compared with other contact models and analytical results. The numerical results obtained from the simulations with two different contact models, the circular tooth profile and the real tooth profile, are compared with each other and with analytical results for simplified models. The model with a real tooth profile proves superior to the model with a circular tooth profile. The simulation time is more or less the same for both the circular tooth profile method and the real tooth profile method. For some large examples with more

links and sprockets, the circular tooth profile method fails to solve the problem.

Using the real tooth profile it is observed that much of the noise, that occurs when the circular tooth profile is used, is damped out. The frequencies of the oscillations of the middle of the segments are somewhat similar for the two methods, but the amplitudes are different in some of the segments. The real tooth profile method is preferable to model the contact, because the model is numerically more stable, the noise on the results are damped out and the results obtained with this method are in better agreement with analytical expected results and it is closer to reality.

Including friction between the rollers and sprockets in contact has shown to have a smoothing effect on the contact force and therefore also on the link forces and chain vibrations. When the rotational damping is included the numerical results show that this also has a large influence. For the same configuration of a chain drive system the calculated amount of pre-tension in the chain change significantly, when the rotational damping is included. When the rotational damping is included the chain vibrations are smaller and therefore the link forces are significantly lower. The inclusion of friction and rotational damping is found to be important for the process of finding static equilibrium and a steady state. Including friction and rotational damping also makes the model more realistic. Even though the chain drive system at all times is lubricated, which reduces the friction, friction will always be present.

The influence of the moment applied to the sprocket due to contact forces is important to verify experimentally, because it has an influence on the angular velocity of the driven sprockets and thereby also on the vibration pattern of the chain strands oscillations both transversal and longitudinal. In the simulation program rotational damping can e.g. be applied to the sprocket centre, which can be used in order to calibrate the numerical results with experimental results.

Including simple models of the guide-bars and the tightener system shows the possible analysis, which can be done for different chain drive systems. This is important due to their influence on the vibration patterns of the whole system. With the simulation program the influence of design changes for these parts can be estimated. The analyses of the influence of the off-centre sprockets in the roller-chain drives, which are sources of extra excitations on the drive, are left for future studies.

The amount of pre-tension in the chain is an important part of the performance of the

chain drives system, because resonances between the external excitation and the eigenfrequency of the free chain strands depend on this. The effect of different values of the pre-tension can be analysed e.g. by moving one of the sprockets. The results from the numerical simulation presented in this thesis, showed that a resonance peak occurred before it is expected from the analytical results of the string eigenfrequencies. However since for instance the simulation program has not been experimentally validated, these results are presented to give an impression of what kind of analysis can be performed with the numerical simulation tool.

With the numerical model presented in the thesis it is possible to perform realistic dynamic simulation of large marine engine chain drives, within a moderate simulation time. It is therefore possible to compare the numerical results with experimental results.

6.1 Suggestions for Further Work

As shown in the numerical results presented in this thesis, the influence of the data used has a noticeable effect on the results. Therefore it is necessary to validate the simulation program experimentally, in order to more accurately evaluate the model. Using the program as an alternative to performing experiments each time a design change is suggested is only possible after such a validation has been done.

A parameter study using the simulation program is a possible extension which does not imply large programming changes. By application to the chain drive systems this can be used for suggesting design changes or even optimizing the design. Design changes are needed in order to avoid damage on the system due to vibration patterns, and this might be obtained by changing e.g. the position and angle of the guide-bars, the different length and sizes on the weight-arm in the tightener system and by the pre-tension of the chain.

Implementation of a lubrication model, such as e.g. suggested in Flores et al. (2003), is a possible extension to the program. This can be preferable in order to get a more realistic model and it would further smoothen out the contact forces between the rollers and sprockets. The inclusion of lubrication might e.g. be done by modelling a squeeze film force during free flight of the roller combined in a hybrid model also including friction force.

Regarding the chain tightener system a possible extension is e.g. to change the simplified model of the hydraulic damping system, such that a model taking the hydraulics into

account is used instead of a spring damper connection. The model of the guide-bars is also a simplified model and a possible extension to this model could e.g. be to include the characteristics of the rubber material on the surface of the guide-bar instead of the simplified model where a constant contact spring stiffness coefficient is used.

Several other methods of modelling the chain and sprockets and their contact exist as discussed earlier. Two of the models, which both could be interesting to compare with the formulation presented in this thesis, are e.g. the hybrid method between a continuous contact force method and a point follower constraint method and a rigid body model where the links are modelled as rigid bodies connected with clearance joints.

References

Ambrósio, J. A. C. (2003), 'Impact of rigid and flexible multibody systems: Deformation description and contact models', *Virtual Nonlinear Multibody Systems, NATO Science Series* **103**, 57–83.

Ambrósio, J. A. C. and Hansen, J. M. (1995), 'Dynamics of roller-chain drives theory', *Technical note, [jmh@mek.dtu.dk]*.

Bagci, C. (1975), 'Dynamic motion analysis of plane mechanism with Coulomb and viscous damping via the joint force analysis', *Journal of Engineering for Industry* pp. 551–560.

Binder, R. C. (1956), *Mechanics of the Roller Chain Drive*, Prentice Hall, Englewood Cliffs, N. J.

Bouillon, G. and Tordion, G. V. (1965), 'On polygonal action in roller chain drives', *Journal of Engineering for Industry, ASME Transactions.* **87**, 243–250.

Chew, M. (1985), 'Inertia effects of a roller-chain on impact intensity', *Journal of Mechanisms, Transmissions, and Automation in Design* **107**, 123–130.

Choi, W. (1993), *Vibration of Roller Chain Drives with and without a Tensioner*, PhD Thesis, University of Michigan.

Choi, W. and Johnson, G. E. (1993*a*), 'Transverse vibrations of roller chain drive with tensioner', *Vibrations of Mechanical Systems and the History of Mechanical Design, ASME, DE-Vol.* **63**, 19–28.

Choi, W. and Johnson, G. E. (1993*b*), 'Vibration of the roller chain drives at low , medium and high operating speeds', *Vibration of Mechanical Systems and the History of Mechanical Design,ASME, DE-Vol.* **63**, 29–40.

Conwell, J. C. and Johnson, G. E. (1995), 'Experimental investigation of link tension and the roller-sprocket impact in roller chain drives', *Mech. Mach. Theory* **31**, 533–544.

Dubowsky, S. and Freudenstein, F. (1971*a*), 'Dynamic analysis of mechanical systems with clearances, part 1: Formation of dynamic model', *Journal of Engineering for Industry, ASME* pp. 305–309.

Dubowsky, S. and Freudenstein, F. (1971*b*), 'Dynamic analysis of mechanical systems with clearances, part 2: Dynamic response', *Journal of Engineering for Industry, ASME* pp. 310–316.

Flores, P., Ambrósio, J. A. C. and Claro, J. P. (2003), Dynamic analysis for planar multibody mechanical systems with real joints, *in* J. A. C. Ambrósio, ed., 'Multibody Dynamics 2003,International Conference on Advances In Computational Multibody Dynamics', ECCOMAS, p. 26 on CD (Book of Abstracts).

Fritz, P. and Pfeiffer, F. (1995), 'Dynamics of high-speed roller-chain drives', *Design Engineering Technical Conferences* **3-Part A**, 573–584.

García de Jalón, J. and Bayo, E. (1994), *Kinematic and Dynamic Simulation of Multibody Systems*, Springer-Verlag, New York.

Goldsmith, W. (1960), *Impact, The Theory and Physical Behavior of Colliding Solids*, Edward Arnold LTD., London.

Graff, K. F. (1991), *Wave Motion in Elastic Solids*, Dover Publications, Inc., New York.

Hansen, J. M. and Nikravesh, P. E. (1998), *Planar Multibody Dynamics, analysis & design, Lecture notes*.

Haug, E. J. (1989), *Computer-Aided Kinematics and Dynamics of Mechanical Systems, Volume I: Basic Methods*, Allyn and Bacon, Needham Heights, Massachusetts.

Haug, E. J., Wu, S. C. and Yang, S. M. (1986), 'Dynamics of mechanical systems with coulomb friction, stiction, impact and constraint addition-deletion-i', *Mechanics and Machine Theory* **Vol. 21 No. 5**, 401–406.

Hunt, K. H. and Crossley, F. R. E. (1975), 'Coefficient of restitution interpreted as damping in vibroimpact', *Journal of Applied Mechanics, ASME* **7**, 440–445.

Iserles, A. (1996), *A First Course in the Numerical Analysis of Differential Equations*, Cambridge University Press, Cambridge, United Kingdom.

Kim, M. S. (1990), *Dynamic Behavior of Roller Chain Drives at Moderate and High Speeds*, PhD Thesis, University of Michigan.

Kim, M. S. and Johnson, G. E. (1993), 'A general, multibody dynamic model to predict the behavior of roller chain drives at moderate and high speeds', *Advances in Design Automation* **1**, 257–268.

Lankarani, H. M. and Nikravesh, P. E. (1990), 'A contact force model with hysteresis damping for impact analysis of multibody systems', *Journal of Mechanical Design* **112**, 369–376.

Lankarani, H. M. and Nikravesh, P. E. (1994), 'Continuous contact force models for impact analysis in multibody systems', *Nonlinear Dynamics* **5**, 193–207.

Mahalingam, S. (1957), 'Transverse vibrations of power transmission chains', *British Journal of Applied Physics* **8(4)**, 145–148.

Mahalingam, S. (1958), 'Polygonal actions on chain drives', *J.Franklin Inst.* **265(1)**, 23–28.

MAN B&W (1995), 'An introduction to vibration aspects of two-stroke diesel engines in ships', *MAN B&W Diesel A/S Report* pp. 1–11.

Milho, J. F., Ambrósio, J. A. C. and Pereira, M. F. O. S. (2002), 'A multibody methodology for the design of anti-climber devices for train crashwothiness simulation', *IJCrash* **7**, 7–19.

Naguleswaran, S. and Williams, C. J. H. (1968), 'Lateral vibrations of band-saw blades, pulleys and the like', *Int. J. Mech. Sci.* **10**, 239–250.

Nikravesh, P. E. (1988), *Computer-Aided Analysis of Mechanical Systems*, Prentice Hall, Englewood Cliffs, New Jersey.

Nikravesh, P. E. (2001), 'Joint coordinate formulation', *AME, Lecture notes, DCAMM course: Advances in Mechanical Systems* pp. 223–257.

Pedersen, N. L. (1998), 'Analysis and synthesis of complex mechanical systems', *Ph.D.-thesis, DCAMM Report No.* **S 77**, 1–119.

Pedersen, N. L. (2002), 'On optimization of bioprobes', *(To appear in Int. J. Num. Meth. Eng.), DCAMM, Report No.* **672**, 1–20.

Pedersen, N. L. (2003), 'Optimization of holes in plates for control of eigenfrequencies', *(To appear in Struct. Multidisc. Optim.), DCAMM, Report No.* **683**, 1–16.

Pedersen, P. (1985), 'On stability diagrams for damped hill equations', *Quarterly of Applied Mathematics* **42(4)**, 477–495.

Pedersen, S. L. (2001), 'Chain vibrations', *Master thesis, Department of Mechanical Engineering, Solid Mechanics, The Technical University of Denmark*.

Pfeiffer, F. (1995), 'Chain dynamics', *Design Engineering Technical Conferences* **3-Part A**, 1187–1194.

Pfeiffer, F. (1999), 'Unilateral problems of dynamics', *Archive of Applied Mechanics* **69**, 503–527.

Pfeiffer, F. and Glocker, C. (1996), *Multibody Dynamics with Unilateral Contacts*, John Wiley & Sons, Ltd., New York.

Pfeiffer, F., Fritz, P. and Srnik, J. (1997), 'Nonlinear vibrations of chains', *Journal of Vibration and Control* **3**, 397–410.

Ravn, P. (1998), 'Analysis and synthesis of planar mechanical systems including flexibility, contact and joint clearance', *Ph.D.-thesis, DCAMM Report No.* **S 78**, 1–156.

Rooney, G. T. and Deravi, P. (1982), 'Coulomb friction in mechanical sliding joints', *Mechanism and Machine Theory* **17**, 207–211.

Schiehlen, W. (1997), 'Multibody system dynamics: Roots and perspectives', *Multibody System Dynamics* **1**, 149–188.

Shampine, L. F. and Gordon, M. K. (1975), *Computer Solution of Ordinary Differential Equations : The Initial Value Problem*, W.H. Freeman, San Francisco, California.

Threlfall, D. C. (1978), 'The inclusion of coulomb friction in mechanisms programs with particular reference to dram', *Mechanism and Machine Theory* **13**, 475–483.

Troedson, I. and Vedmar, L. (1999), 'A dynamic analysis of the oscillations in a chain drive method to determine the static load distribution in a chain drive', *Transactions of the ASME* **121**, 402–408.

Troedson, I. and Vedmar, L. (2001), 'A dynamic analysis of the oscillations in a chain drive', *Journal of Mechanical Design* **123**, 395–401.

Tsubaki (1991), *Tsubaki Marine Engine Roller Chain, maintenance manual. Catalog*, Vol. 1211, Tsubaki Chain Co., Japan.

Turnbull, S. and Fawcett, J. (1972), 'Dynamic behavior of roller chain drives', *Mechanisms 1972* pp. 29–35.

Veikos, N. and Freudenstein, F. (1992*a*), 'On the dynamic analysis of roller chain drivers: Part i - theory', *Mechanical Design and Synthesis, ASME, DE-Vol.* **46**, 431–439.

Veikos, N. and Freudenstein, F. (1992*b*), 'On the dynamic analysis of roller chain drivers: Part ii - case study', *Mechanical Design and Synthesis, ASME, DE-Vol.* **46**, 441–450.

Wang, K. W. and Liu, S. P. (1991a), 'On the noise and vibration of chain drive systems', *The Shock and Vibration Digest* **23(4)**, 8–13.

Wang, K. W., Liu, S. P., Hayek, S. I. and Chen, F. H. (1991b), 'On the impact intensity of vibrating axially moving roller chains', *Machinery Dynamics and Element Vibrations* **36**, 97–104.

Appendix A
The Tangent Line Between two Circles

We wish to calculate the length of the tangent lines between two circles and the contact angles. There exist four different tangents between two circles as shown in Figure A.1, two outer tangent lines and two inner tangent lines.

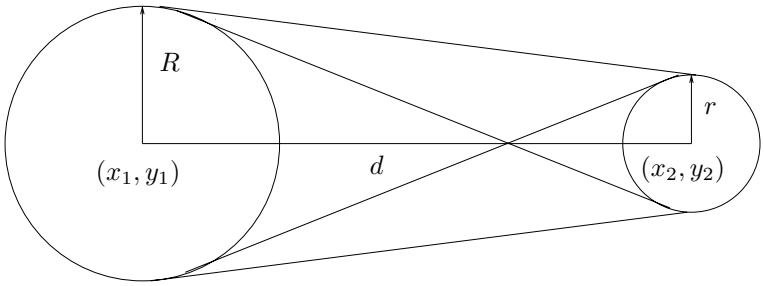

Figure A.1: Tangent lines between two circles

The center position and radii of the two circles are: left sprocket center (x_1, y_1) and radius R and right sprocket center (x_2, y_2) and radius r. The distance d between the sprocket centers are

$$d = \sqrt{(x_1 - x_2)^2 + (y_1 - y_2)^2} \tag{A.1}$$

A.1 Outer Tangent Lines

The contact angle α for an outer tangent, see Figure A.2 and A.3, is given by

$$\cos(\alpha) = \frac{R - r}{d} \tag{A.2}$$

and the angles θ_1 and θ_2 are given by

$$\theta_1 = 2\pi - 2\alpha \tag{A.3}$$

$$\theta_2 = 2\alpha \tag{A.4}$$

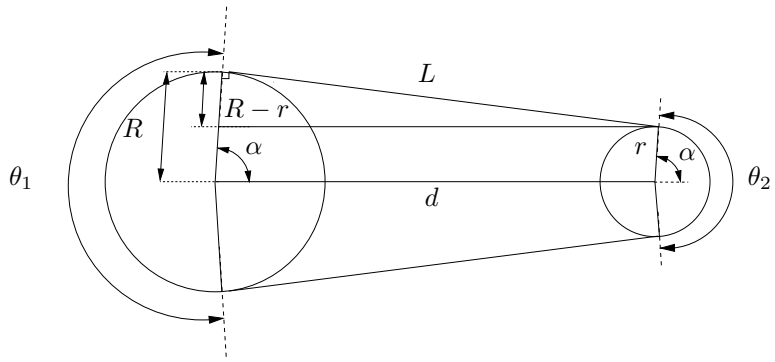

Figure A.2: The outer tangent lines between two circles

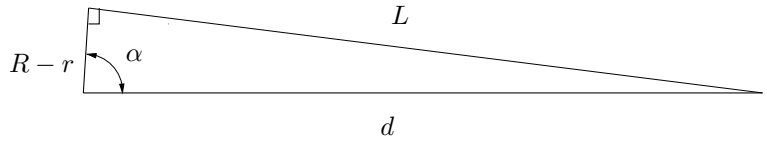

Figure A.3: The outer tangent lines between two circles

The length of the outer tangent line, see Figure A.3, is

$$L = (R - r)\tan(\alpha) \tag{A.5}$$

or directly from Pythagoras

$$L^2 = d^2 - (R - r)^2 \tag{A.6}$$

A.2 Inner Tangent Lines

The contact angle α for an inner tangent line, see Figure A.4 and A.5, is given by

$$\begin{aligned} \cos(\alpha) =& \frac{R}{d_1} \\ \cos(\alpha) =& \frac{r}{d_2} \\ \Downarrow d =& d_1 + d_2 = \frac{(R + r)}{\cos(\alpha)} \end{aligned} \tag{A.7}$$

which yields

$$\cos(\alpha) = \frac{R + r}{d} \tag{A.8}$$

and the angle $\theta = \theta_1 = \theta_2$ is given by

$$\theta = 2\pi - 2\alpha \tag{A.9}$$

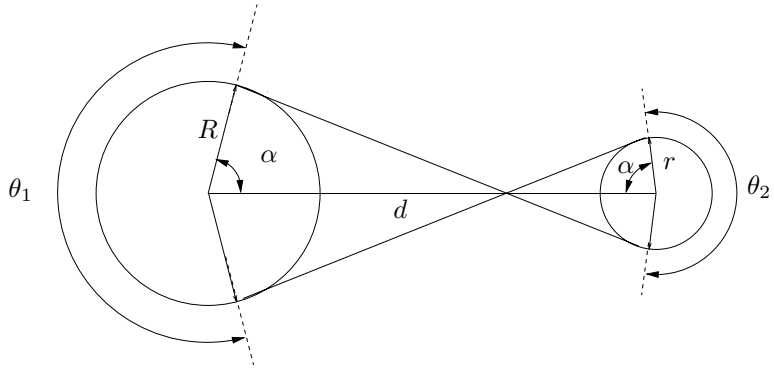

Figure A.4: The inner tangent lines between two circles

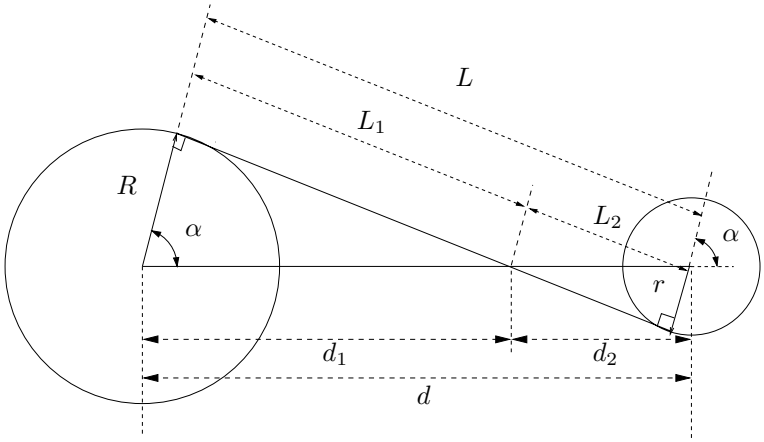

Figure A.5: The inner tangent lines between two circles

The length of the tangent line L, see Figure A.5, A.6 and A.7, is given by

$$\begin{aligned}\tan(\alpha) =& \frac{R}{L_1} \\ \tan(\alpha) =& \frac{r}{L_2} \\ \Downarrow L =& L_1 + L_2 = \frac{(R+r)}{\tan(\alpha)}\end{aligned} \tag{A.10}$$

which yields

$$\tan(\alpha) = \frac{(R+r)}{L} \tag{A.11}$$

or directly from Pythagoras

$$L^2 = d^2 - (R+r)^2 \tag{A.12}$$

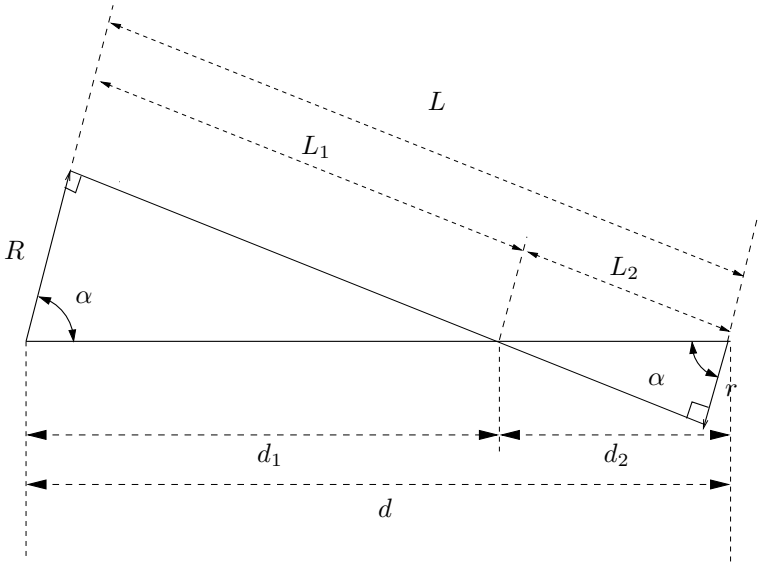

Figure A.6: The inner tangent lines between two circles

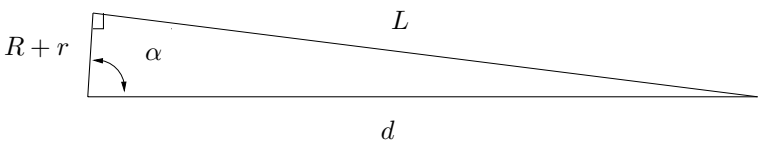

Figure A.7: The inner tangent lines between two circles

A.3 Rotated Sprockets

When the two sprockets are not horizontal aligned the rotation has to be included in the contact angle, see Figure A.8. The rotation of the sprockets are given by

$$\tan\psi = \frac{y_2 - y_1}{x_2 - x_1} \tag{A.13}$$

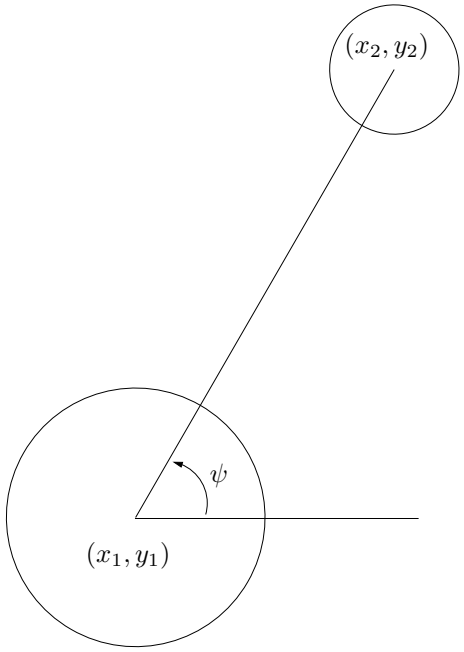

Figure A.8: The rotation of the sprockets.

A.4 Contact Angles

For the case of outer tangents the contact angles, see Figure A.9, are given by

$$\zeta_{11} = \zeta_{12} = \quad \alpha + \psi \tag{A.14}$$

$$\zeta_{21} = \zeta_{22} = \quad 2\pi - \alpha + \psi \tag{A.15}$$

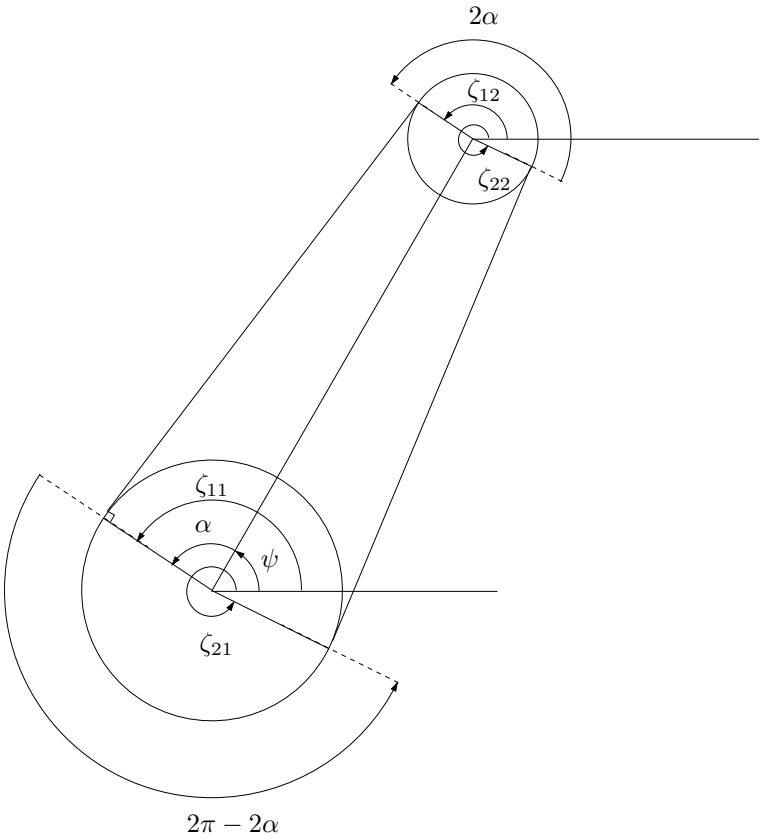

Figure A.9: The outer tangent lines between two circles

For the case of inner tangents the contact angles, see Figure A.10 are given by

$$\zeta_{11} = \alpha + \psi \tag{A.16}$$

$$\zeta_{21} = 2\pi - \alpha + \psi \tag{A.17}$$

$$\zeta_{12} = \pi + \alpha + \psi = \zeta_{21} + \pi \tag{A.18}$$

$$\zeta_{22} = \pi - \alpha + \psi = \zeta_{11} + \pi \tag{A.19}$$

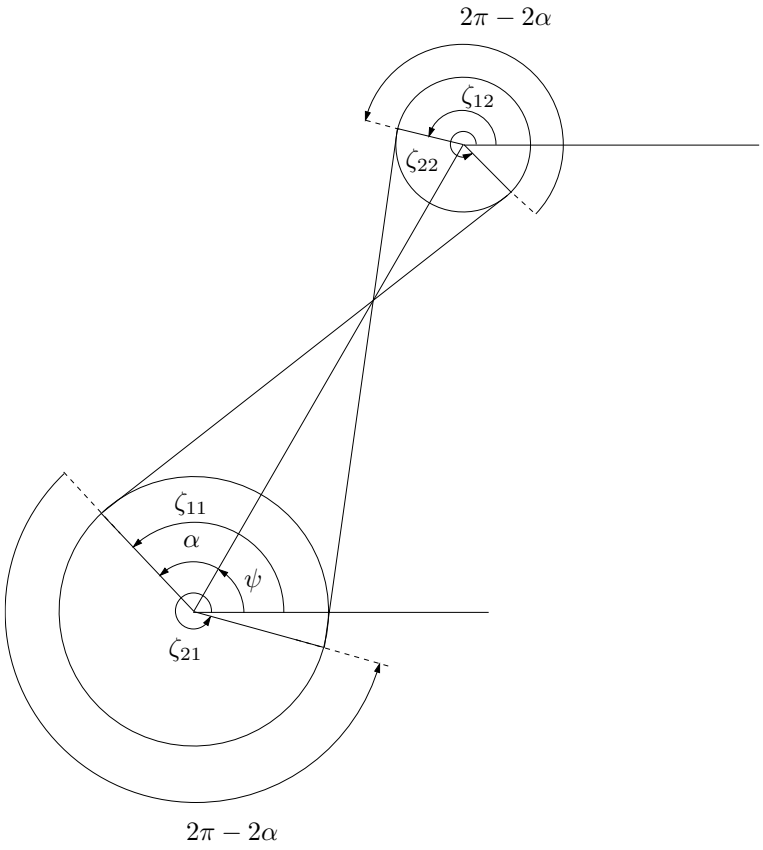

Figure A.10: The inner tangent lines between two circles

Appendix B
The Link Stiffness (Engine 6S90MC-C)

The pitch angle α is calculated by

$$\alpha = \frac{2\pi}{n_t} \tag{B.1}$$

where n_t is the number of teeth on the sprocket. The chain pitch P is calculated by

$$P = 2R_s \sin\frac{\alpha}{2} \tag{B.2}$$

where R_s is the radius of the sprocket, see Figure B.1.

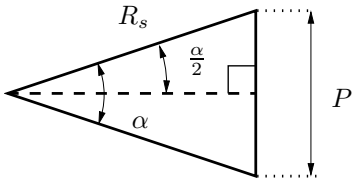

Figure B.1: Pitch angle α and chain pitch P

One of the sprockets used in the chain drive of the engine 6S90MC-C has the radius $R_s = 1.164715$ m and number of teeth $n_t = 64$, which gives a pitch angle $\alpha = 0.9817$ rad and a chain pitch $P = 0.1143$ m. The chain used in MAN B&W Diesel A/S's diesel engine 6S90MC-C is in a category of chains that has the chain constant *k* (flexibility) given as

$$k = 8.19 \cdot 10^{-9} \frac{\text{m}}{\text{m N}} \tag{B.3}$$

which is a constant from the producer of the chain. The chain constant is the elongation of an 1 m long chain, when loaded with $F = 1$ N. The elongation ΔL of one link is given by

$$\Delta L = kPF \tag{B.4}$$

yielding a stiffness coefficient *K* given by

$$K = \frac{1}{kP} = \frac{1}{8.19 \cdot 10^{-9} \frac{\text{m}}{\text{m N}} 0.1143\text{m}} = 1068 \frac{\text{MN}}{\text{m}} \tag{B.5}$$

Appendix C
The Real Shaped Tooth Profile

The standard tooth form (Type II per ASA B29.1-1950) is shown in the Figure C.1, taken from Binder (1956). According to American standards the dimensions shown in Figure C.1 are defined below (in inches). P is the chain pitch, n_t is the number of teeth, $D_r = 2R_r$ is the roller diameter, $D_t = 2R_t$ is the seating curve diameter. The angles A and B in Figure C.1 are defined by

$$A = 35^\circ + \frac{60^o}{n_t}$$
$$B = 18^\circ - \frac{35^o}{n_t} \tag{C.1}$$

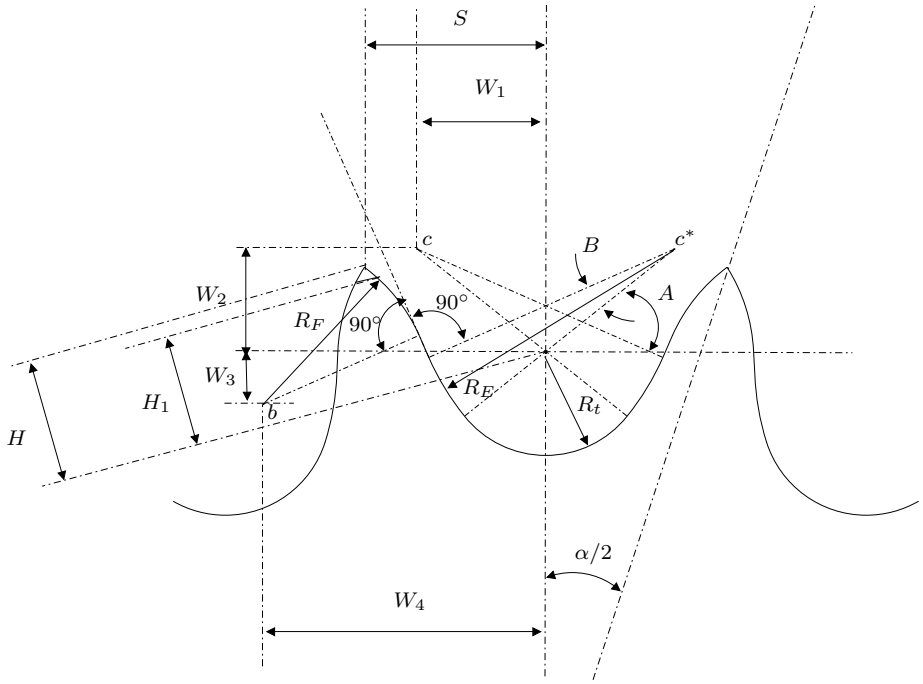

Figure C.1: The standard sprocket tooth form (Type II per ASA B29.1-1950)

The different lengths shown in Figure C.1 are defined by

$$
\begin{aligned}
&D_t = 1.005D_r + 0.003, \qquad W_1 = 0.8D_r \cos A \\
&W_2 = 0.8D_r \sin A, \qquad R_E = 1.3025D_r + 0.0015 \\
&W_3 = 1.24D_r \cos \tfrac{180^\circ}{n_t}, \qquad W_4 = 1.24D_r \sin \tfrac{180^\circ}{n_t} \\
&R_F = D_r[0.8 \cos B + 1.24 \cos C - 1.3025] - 0.0015 \\
&H = \sqrt{R_F F^2 - (1.24D_r - \tfrac{P}{2})^2}, \qquad S = \tfrac{P}{2} \cos \tfrac{180^\circ}{n_t} + H \sin \tfrac{180^\circ}{n_t}
\end{aligned}
\tag{C.2}
$$

where the angle C is given by

$$
C = 17^\circ - \frac{64^o}{n_t} \tag{C.3}
$$

Separating the tooth-profile into areas we obtain 7 areas where the roller-sprocket contact can occur, see Figure C.2.

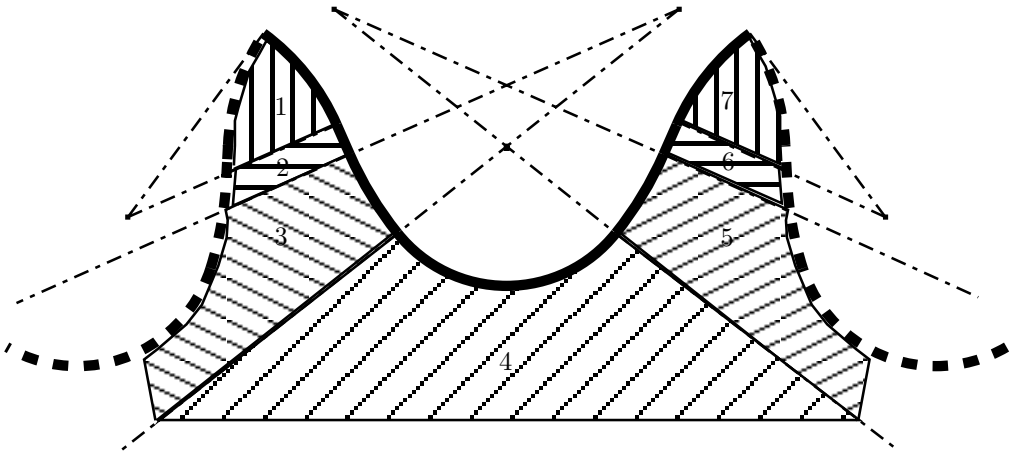

Figure C.2: The real tooth profile separated in 7 contact areas.

The contact areas can be defined by local vectors given in the local coordinate system (ξ_t, η_t), see Figure C.3 and the angles shown in figure C.5.

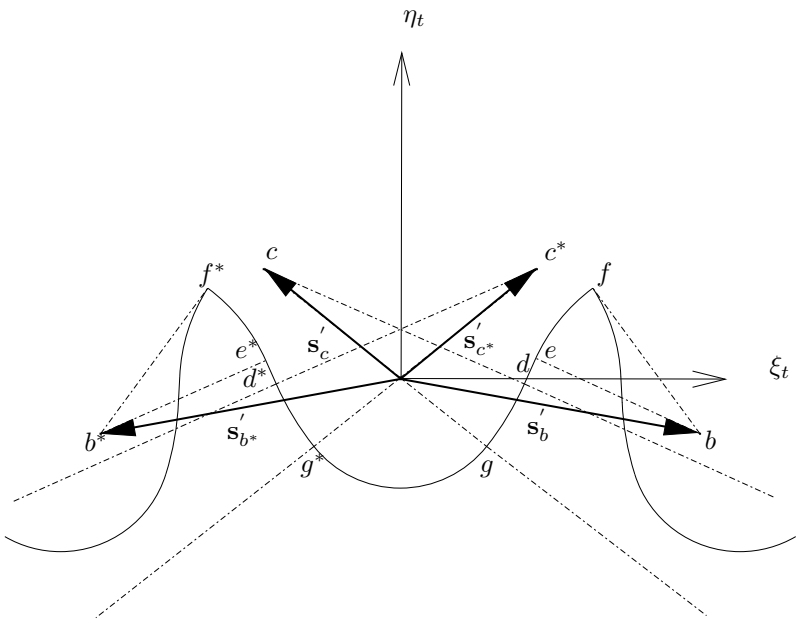

Figure C.3: The 10 reference points used to describe the shape of the tooth profile.

All the points denoted with $*$ in superscript are related to the left side of the tooth and those without relates to the right side. The vectors in Figure C.3 are given by

$$\begin{aligned} \mathbf{s}_b' &= \{W_3, W_4\}^T, \qquad \mathbf{s}_{b^*}' = \{-W_3, W_4\}^T, \\ \mathbf{s}_c' &= \{-W_1, W_2\}^T, \qquad \mathbf{s}_{c^*}' = \{W_1, W_2\}^T \end{aligned} \tag{C.4}$$

The local coordinate system placed at the center of the j'th tooth is rotated with an angle $\theta_t = \theta_s - \frac{\pi}{2} \pm j\alpha$ with respect to the global coordinate system, where again the $\pm$ depends on the rotational direction of the sprocket. The transformation matrix $\mathbf{A}_t$ going from the local tooth coordinates system to the global coordinate system, is given by (2.5), with the angle $\theta = \theta_t$. The global vectors to the 10 reference points shown in Figure C.3 are all found in the same way, e.g. the global vector $\mathbf{r}_{c^*}$ to point c^* is given by

$$\mathbf{r}_{c^*} = \mathbf{r}_t + \mathbf{A}_t \mathbf{s}_{c^*}' \tag{C.5}$$

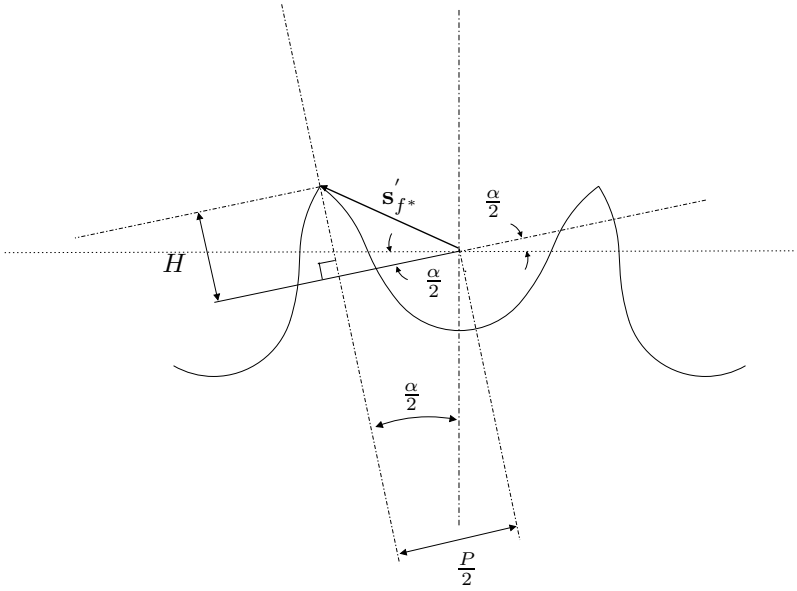

Figure C.4: The local vector $\mathbf{s}'_{f*}$ used to describe the shape of the tooth profile

The local vector $\mathbf{s}'_{f*}$ shown in Figure C.4 is given by

$$\mathbf{s}'_{f*} = \left\{ \begin{array}{c} -\frac{P}{2}\cos(\frac{\alpha}{2}) - H\sin(\frac{\alpha}{2}) \\ \\ -\frac{P}{2}\sin(\frac{\alpha}{2}) + H\cos(\frac{\alpha}{2}) \end{array} \right\} \tag{C.6}$$

The local vector from point b^* to point f^* is given by

$$\mathbf{s}'_{bf*} = \mathbf{s}'_{f*} - \mathbf{s}'_{b*} = \left\{ \begin{array}{c} s'_{bf*x} \\ s'_{bf*y} \end{array} \right\} \tag{C.7}$$

The global vector to the center of the tooth is given by

$$\mathbf{r}_t = \mathbf{r}_s + R_s\mathbf{u}_r \tag{C.8}$$

Equation (C.8) is similar to (3.57), but with a difference of ΔR, that was added for numerical reasons in the circular tooth profile.

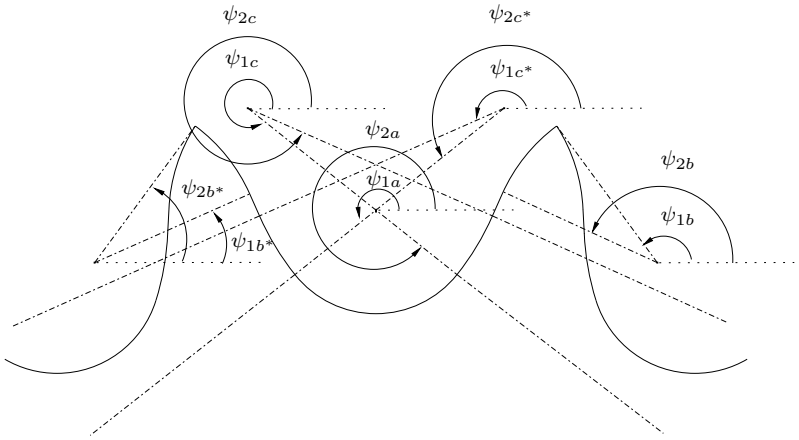

Figure C.5: Angles used to describe the shape of the tooth profile.

The angles shown in Figure C.5 are given by

$$\begin{array}{lllllllll} \psi_{1a} & = & \pi + A, & \psi_{2a} & = & 2\pi - A, & \psi_{1c} & = & 2\pi - A, \\ \psi_{2c} & = & 2\pi - A + B & \psi_{1c^*} & = & \pi + A - B, & \psi_{2c^*} & = & \pi + A, \\ \psi_{2b} & = & \pi - A + B, & \psi_{1b^*} & = & A - B & & & \end{array}$$

The angles at point b and b^* are found by

$$\begin{aligned} \tan\left(\psi_{2b^*}\right) &= \frac{s'_{bf^*y}}{s'_{bf^*x}} \\ \psi_{1b} &= 2\pi - \psi_{2b^*} \end{aligned} \tag{C.9}$$

Appendix D
The Guide-bars

In this appendix the vectors and angles used to define contact with the guide-bars are given. Figure 3.21 shows an example of the placement of three guide-bars in a chain drive system.

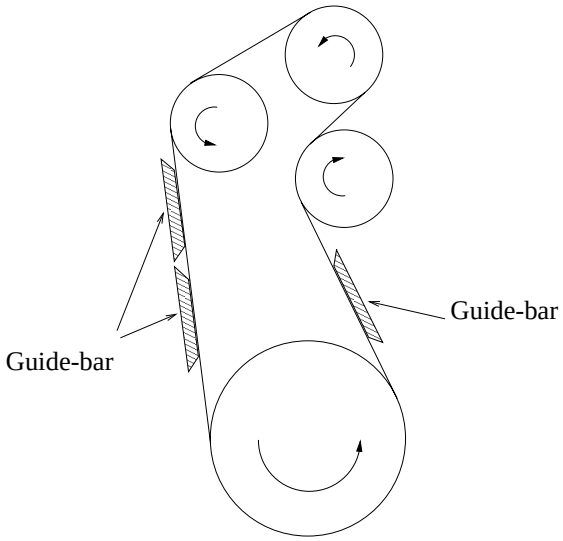

Figure D.1: Guide-bars in a 6S90MC-C fore end chain drive system.

The contact between the roller chain strands and the guide-bars is modelled with the continuous contact force model. The global coordinates of the end points of the flat part of the guide-bars are $\mathbf{r}_{gi}$ and $\mathbf{r}_{gj}$, the radius of the rounded ends is R_{ge}, the length of the rounded end is L_{ge} and the length of the flat part is L_g, see Figure 3.22. The end points of the flat part of the guide-bars are specified such that the tangential vector is given by

$$\mathbf{t}_g = \frac{\mathbf{r}_{gi} - \mathbf{r}_{gj}}{L_g} \tag{D.1}$$

and the normal vector to the contact surface is given by

$$\mathbf{n}_g = \hat{\mathbf{t}}_g \tag{D.2}$$

where the hat ($\hat{}$) indicates that the vector is perpendicular to $\mathbf{t}_g$, rotated in the counter clockwise direction.

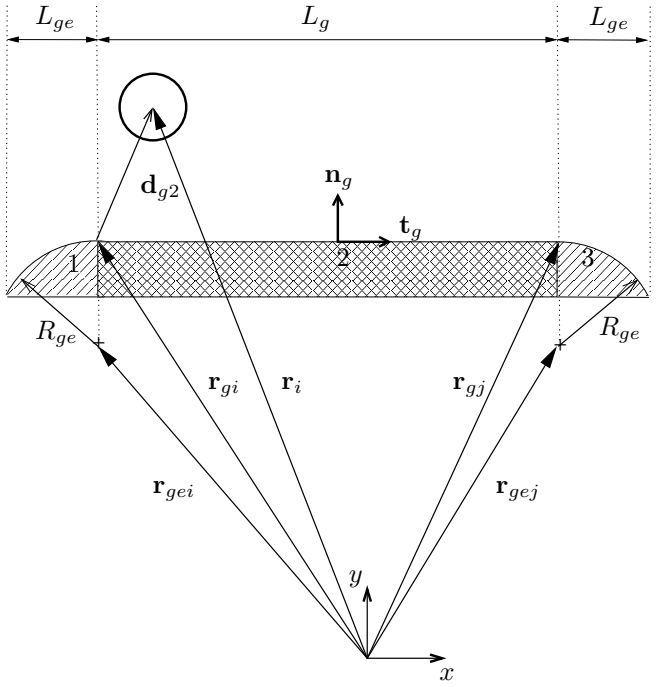

Figure D.2: Contact with the guide-bar area 2 (flat part)

The vector $\mathbf{d}_{g2}$ in Figure 3.22 is given by

$$\mathbf{d}_{g2} = \mathbf{r}_i - \mathbf{r}_{gi} \tag{D.3}$$

where $\mathbf{r}_i$ is the global coordinates of the roller. The centre of the arc of the rounded end at area 1 is in global coordinates given by (see Figure D.3)

$$\mathbf{r}_{gei} = \mathbf{r}_{gi} - R_{ge}\mathbf{n}_g \tag{D.4}$$

The vector $\mathbf{d}_{g1}$ in Figure D.3 is given by

$$\mathbf{d}_{g1} = \mathbf{r}_i - \mathbf{r}_{gei} \tag{D.5}$$

The centre of the arc of the rounded end at area 3 is in global coordinates given by (see Figure D.4)

$$\mathbf{r}_{gej} = \mathbf{r}_{gj} - R_{ge}\mathbf{n}_g \tag{D.6}$$

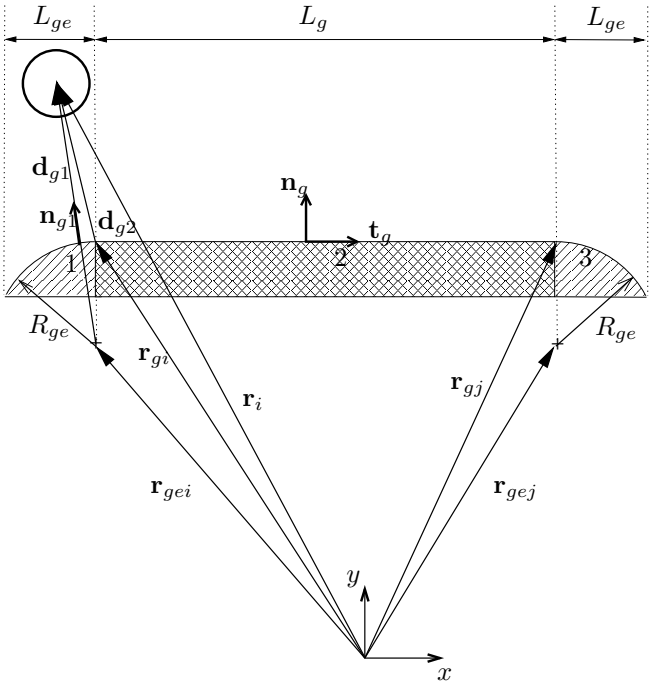

Figure D.3: Contact with guide-bar area 1 (rounded end)

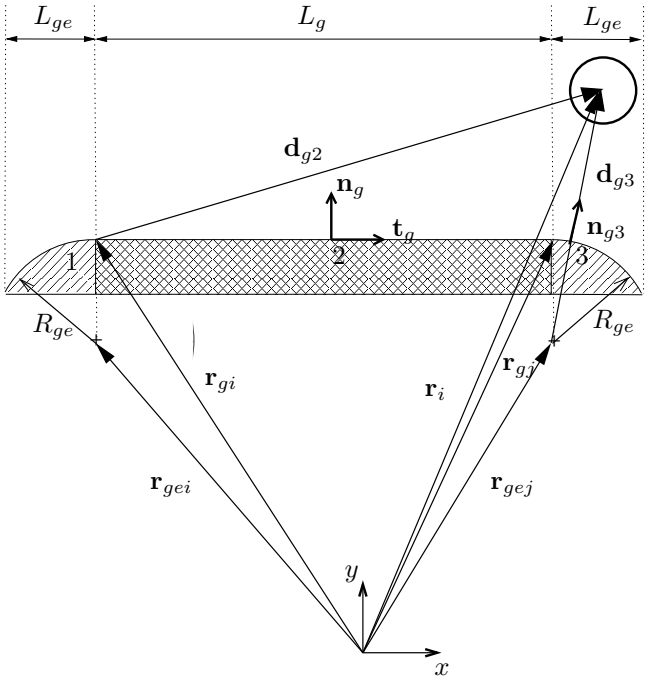

Figure D.4: Contact with guide-bar area 3 (rounded end)

The vector $\mathbf{d}_{g3}$ in Figure D.3 is given by

$$\mathbf{d}_{g3} = \mathbf{r}_i - \mathbf{r}_{gej} \tag{D.7}$$

Indentation of Guide-bar

If the end points of the guide-bar is placed on the tangent line between the sprockets, then the initial indentation of the guide-bar into the chain is zero. In order to investigate the effect of other values of the indentation the end points is translated along the $\mathbf{n}_g$ vector, see Figure D.5. The new global vectors to the guide-bar end points are denoted $\mathbf{r}^*_{gi}$ and $\mathbf{r}^*_{gj}$ and are given by

$$\begin{aligned} \mathbf{r}^*_{gi} &= \mathbf{r}_{gi} + \delta_g \mathbf{n}_g \\ \mathbf{r}^*_{gj} &= \mathbf{r}_{gj} + \delta_g \mathbf{n}_g \end{aligned} \tag{D.8}$$

where δ_g is the amount of the initial indentation, that is the amount the guide-bar is pressed into the chain initially, see Figure D.5. Having the new guide-bar end point coordinates for the rotated guide-bar the contact detection follows as described prior in this section.

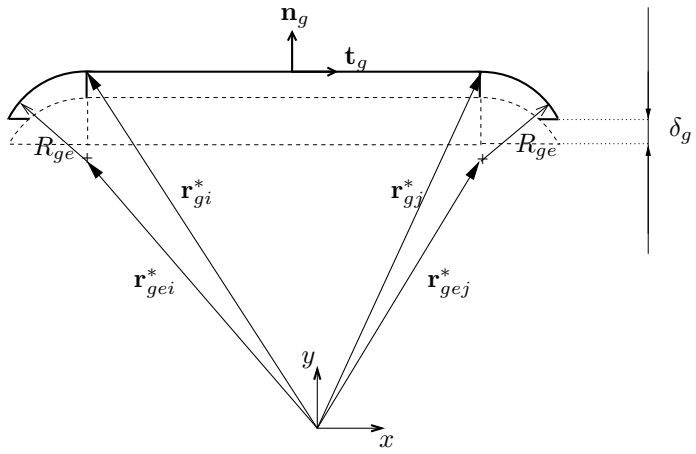

Figure D.5: The indentation of the guide-bar into the chain.

Rotated Guide-bar

At the present the guide-bars in the marine diesel engines are fixed parallel to the tangent line between the sprockets. However it might be desirable to investigate whether a small rotation of the guide-bar with respect to the tangent line could reduce the contact forces on

the guide-bar. In the model the rotation of the guide-bar is chosen to be around the middle point of the guide-bar and the global coordinates of the middle point of the guide-bar $\mathbf{r}_{gc}$ is given by

$$\mathbf{r}_{gc} = \mathbf{r}_{gi} + \frac{L_g}{2}\mathbf{t}_g \tag{D.9}$$

Figure D.6 shows the positive direction of rotation of the guide-bar relative to the tangent line. The local coordinate system (ξ_g, η_g) of the guide-bar is fixed at the middle point, with ξ_g parallel to the flat part (area 2) of the guide-bar, see Figure D.6.

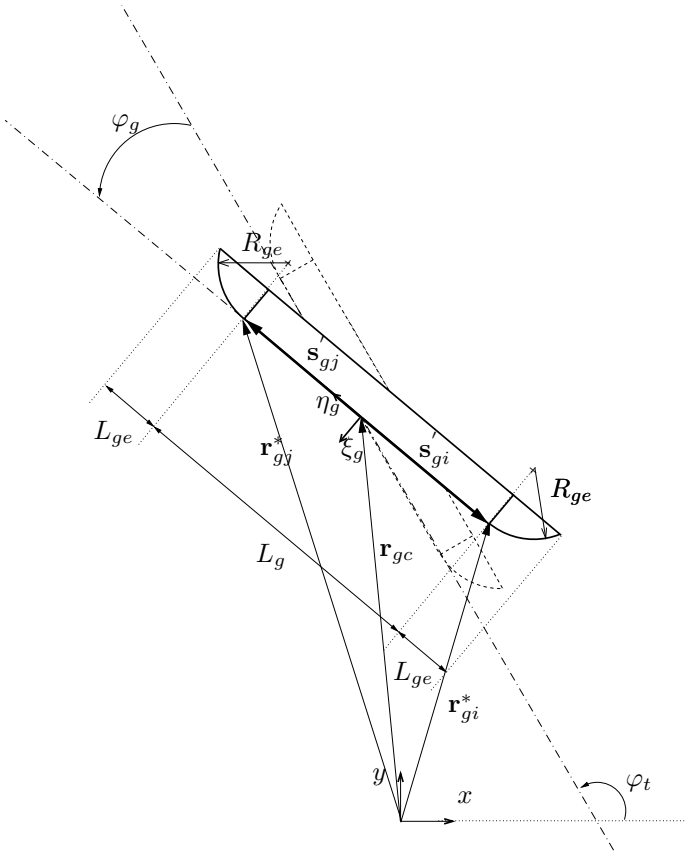

Figure D.6: Rotation of guide-bar relative to the tangent line.

The local vectors $\mathbf{s}'_{gi} = \{-\frac{L_g}{2}, 0\}^T$ and $\mathbf{s}'_{gj} = \{\frac{L_g}{2}, 0\}^T$ are given in the (ξ_g, η_g) coordinate system the vectors to the guide-bar end points. The new global vectors to the rotated guide-bar end points are denoted $\mathbf{r}^*_{gi}$ and $\mathbf{r}^*_{gj}$ and are given by

$$\begin{aligned} \mathbf{r}^{*}_{gi} &= \mathbf{r}_{gc} + \mathbf{A}_g \mathbf{s}^{'}_{gi} \\ \mathbf{r}^{*}_{gj} &= \mathbf{r}_{gc} + \mathbf{A}_g \mathbf{s}^{'}_{gj} \end{aligned} \tag{D.10}$$

where the transformation matrix $\mathbf{A}_g$ going from the local guide-bar coordinate system to the global coordinate system, is given by (2.5), with the angle $\theta = \varphi_t + \varphi_g$. The angle φ_t is the angle from the global x-axis to the tangent line and the angle φ_g is the angle of the rotated guide-bar relative to the tangent line, see Figure D.6. Having the new guide-bar end point coordinates for the rotated guide-bar the contact detection follows as described prior in this section.

Appendix E
Oscillation of the Middle of a Chain Segment

The chain segments between the sprockets are initially placed along the tangent line between two sprockets. The points on the two sprockets where the tangent line is in contact are known and the middle point (x_m, y_m) of the tangent line piece between the contact points can be found. The tangent line is denoted line l_1, and can be described by the slope α and the line constant q.

When the transversal vibrations of the chain segments are analysed, first the two rollers that are nearest to the middle point (x_m, y_m) are found. The two rollers nearest to the middle point are denoted roller i and roller j, and their positions are (x_i, y_i) and (x_j, y_j), see Figure E.1.

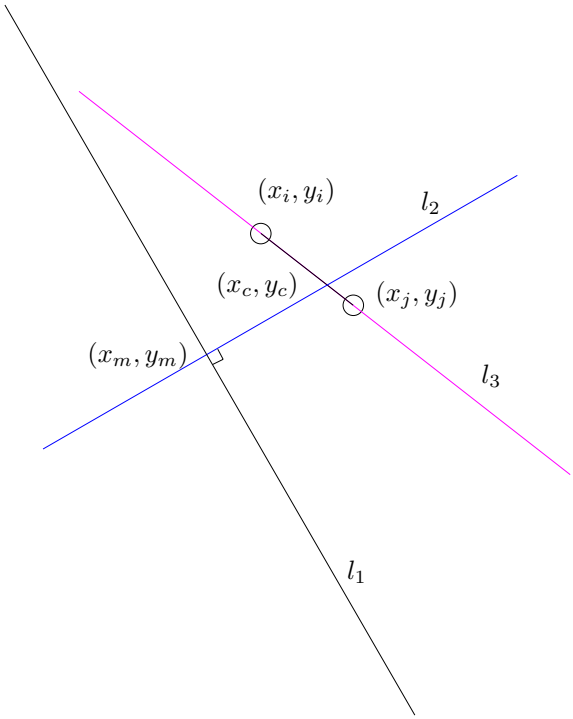

Figure E.1: The distance perpendicular to the segment line.

The three lines shown in Figure E.1 are given by the equations

$$\begin{aligned} l_1: &\quad y = \alpha x + q \\ l_2: &\quad y = \beta x + p \\ l_3: &\quad y = \xi x + r \end{aligned} \tag{E.1}$$

Line l_1 and line l_2 are perpendicular and crosses in the middle point (x_m, y_m), yielding, with line l_2 given by the slope β and line constant p

$$\beta = \frac{-1}{\alpha}, \qquad p = y_m - \beta x_m \tag{E.2}$$

The line l_3 goes through the points (x_i, y_i) and (x_j, y_j), yielding the slope ξ and line constant r for the line

$$\xi = \frac{y_j - y_i}{x_j - x_i}, \qquad r = y_i - \xi x_i \tag{E.3}$$

The lines l_2 and l_3 crosses in the point (x_c, y_c) given by

$$x_c = \frac{r - p}{\beta - \xi}, \qquad y_c = \beta x_c + p \tag{E.4}$$

The distance between (x_m, y_m) and (x_c, y_c) is used as a measure of how the middle of a chain segment oscillates. The sign of the displacement is calculated by the dot-product of a vector from (x_m, y_m) to (x_c, y_c) and a chosen unit normal vector to the initial tangent line and since these two vectors are parallel this dot-product in fact gives the wanted distance including the sign.

Appendix F
The Stiffness Matrix

The stiffness matrix in general for a chain drive system model consisting of multiple sprockets and chain links is, when K is the stiffness coefficient of the springs between the rollers and the radius of sprocket number i is R_i, given by

$$
\mathbf{K} = \begin{bmatrix}
2KR_1^2 & -KR_1 & & & & & & & & & & & & & & & & & & & & & & & & & & & & -KR_1 \\
-KR_1 & 2K & -K & & & & & & & & & & & & & & & & & & & & & & & & & & & \\
 & -K & 2K & -K & & & & & & & & & & & & & & & & & & & & & & & & & \\
 & & \ddots & \ddots & & & & & & & & & & & & & & & & & & & & & & & & & \\
 & & & -K & 2K & -K & & & & & & & & & & & & & & & & & & & & & & & \\
 & & & & -K & 2K & -KR_2 & & & & & & & & & & & & & & & & & & & & & & \\
 & & & & -KR_2 & 2KR_2^2 & -KR_2 & & & & & & & & & & & & & & & & & & & & & & \\
 & & & & & -KR_2 & 2K & -K & & & & & & & & & & & & & & & & & & & & & \\
 & & & & & & -K & 2K & -K & & & & & & & & & & & & & & & & & & & & \\
 & & & & & & & \ddots & \ddots & & & & & & & & & & & & & & & & & & & & \\
 & & & & & & & & -K & 2K & -K & & & & & & & & & & & & & & & & & & \\
 & & & & & & & & & -K & 2K & -KR_n & & & & & & & & & & & & & & & & & \\
 & & & & & & & & & & -KR_n & 2KR_n^2 & -KR_n & & & & & & & & & & & & & & & & \\
 & & & & & & & & & & & -KR_n & 2K & -K & & & & & & & & & & & & & & & \\
 & & & & & & & & & & & & -K & 2K & -K & & & & & & & & & & & & & & \\
 & & & & & & & & & & & & & \ddots & \ddots & & & & & & & & & & & & & & \\
 & & & & & & & & & & & & & & -K & 2K & -K & & & & & & & & & & & & \\
 & & & & & & & & & & & & & & & -K & 2K & & & & & & & & & & & & \\
 & & & & & & & & & & & & & & & & \ddots & \ddots & & & & & & & & & & & \\
 & & & & & & & & & & & & & & & & & -K & 2K & -K & & & & & & & & & \\
 & & & & & & & & & & & & & & & & & & -K & 2K & & & & & & & & & \\
 & & & & & & & & & & & & & & & & & & & \ddots & \ddots & & & & & & & & \\
 & & & & & & & & & & & & & & & & & & & & -K & 2K & -K & & & & & & \\
 & & & & & & & & & & & & & & & & & & & & & -K & 2K & & & & & & \\
 & & & & & & & & & & & & & & & & & & & & & & \ddots & \ddots & & & & & \\
 & & & & & & & & & & & & & & & & & & & & & & & -K & 2K & -K & & & \\
 & & & & & & & & & & & & & & & & & & & & & & & & -K & 2K & & & \\
 & & & & & & & & & & & & & & & & & & & & & & & & & \ddots & \ddots & & \\
 & & & & & & & & & & & & & & & & & & & & & & & & & & -K & 2K & -K \\
 & & & & & & & & & & & & & & & & & & & & & & & & & & & -K & 2K \\
 & & & & & & & & & & & & & & & & & & & & & & & & & & & & -KR_1
\end{bmatrix}
$$

Appendix G
Various Modifications for the Friction Force

The modification of the friction force can be done by using different approximations of the signum function $sgn(x)$. The signum function is given by

$$sgn(x) = \begin{cases} -1, & x < 0 \\ 0, & x = 0 \\ 1, & x > 0 \end{cases} \tag{G.1}$$

or

$$sgn(x) = 2H(x) - 1 \tag{G.2}$$

where $H(x)$ is the Heaviside Step Function given by

$$H(x) = \begin{cases} 0, & x < 0 \\ \frac{1}{2}, & x = 0 \\ 1, & x > 0 \end{cases} \tag{G.3}$$

The Heaviside Step Function can be approximated by the following three limits

$$\begin{aligned} H_1(x) &= \lim_{\epsilon \to 0} \frac{1}{2}(1 + \tanh(x/\epsilon)) \\ H_2(x) &= \lim_{\epsilon \to 0} (\frac{1}{2} + \frac{1}{\pi} \arctan(x/\epsilon)) \\ H_3(x) &= \lim_{\epsilon \to 0} (1 + \exp(-x/\epsilon))^{-1} \end{aligned} \tag{G.4}$$

The Heaviside approximations are shown in the three figures G.1, G.2 and G.3, the solid line for $\epsilon = 0.01$, the dashed line for $\epsilon = 0.1$ and the dashed-dotted line for $\epsilon = 0.5$, see e.q. http://mathworld.wolfram.com/HeavisideStepFunction.html.

Other approximations for the signum function can also be made by using e.g. a super elliptic approximation or a Bézier curve approximation as shown in the figures G.4(a) and G.4(b). For further information about the Bézier curve see e.q. Pedersen (2002) and about the super elliptic approximation see e.q. Pedersen (2003). With the Bézier curve approximations it is possible to control the slope at the ends of the curve and for the

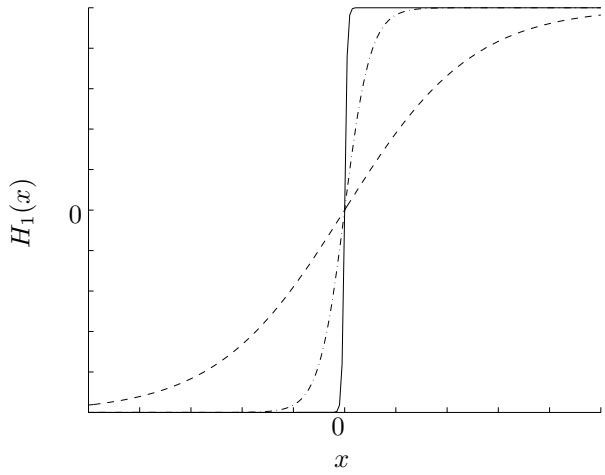

Figure G.1: Heaviside approximation $H_1(x)$ for $\epsilon = 0.5, 0.1, 0.01$

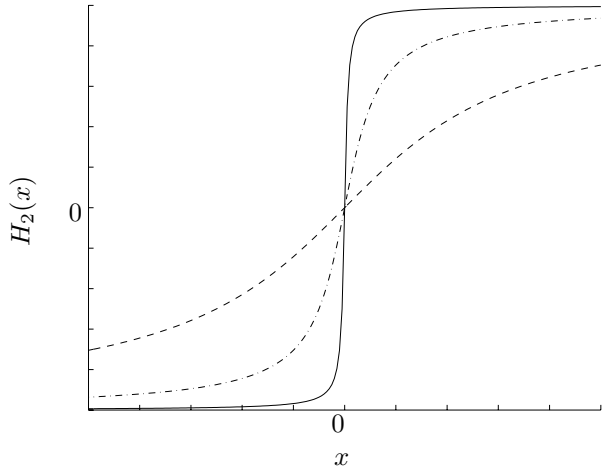

Figure G.2: Heaviside approximation $H_2(x)$ for $\epsilon = 0.5, 0.1, 0.01$

super elliptic approximation the slope at one end is vertical and at the other horizontal. Both the super elliptic approximation and the Bézier approximations shown in the figures G.4(a) and G.4(b), consist of four curve parts two in the 1 st quadrant and two in the third quadrant, calculated by either of the approximations. The approximations are given by

$$A(x) = \begin{cases} -1, & x < -x^* \\ -A^*(x), & -x^* < x \leq 0 \\ A^*(x), & 0 \leq x < x^* \\ 1, & x > x^* \end{cases} \tag{G.5}$$

For the super elliptic approximation $A^*(x)$ is given by

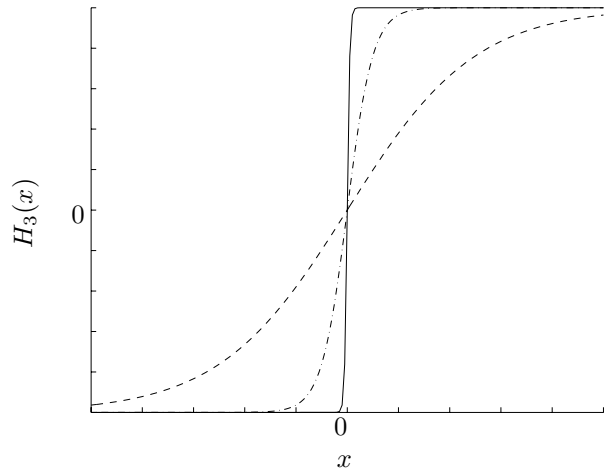

Figure G.3: Heaviside approximation $H_3(x)$ for $\epsilon = 0.5, 0.1, 0.01$

$$A^*(x) = \sin\left(\arccos\left(\frac{-x}{x^*+1}\right)^{\frac{\epsilon}{2}}\right)^{\frac{\epsilon}{2}} \tag{G.6}$$

For the Bézier approximation $A^*(x)$ is given by

$$x = \frac{1-\epsilon_2}{\epsilon_1-\epsilon_2}(3t-3t^2)+x^*t^3 \tag{G.7}$$

$$A^*(x) = \epsilon_1\frac{1-\epsilon_2}{\epsilon_1-\epsilon_2}(3t-3t^2)+t^3 \tag{G.8}$$

For values of x the third order polynomial (G.8) is solved for the corresponding t, which used in (G.8) gives the wanted value of $A^*(x)$. The Bézier approximation is $B(x) = A(x)$, using $A^*(x)$ calculated from (G.8) and the super elliptic approximation is $S(x) = A(x)$, using $A^*(x)$ calculated from (G.6).

Figure G.5(a) shows a comparison of the three Heaviside approximations with $\epsilon = 0.01$ (dashed lines), the Bézier approximation (dashed-dotted line), the super elliptic approximation (dotted) and the signum function (solid line).

Figure G.5(b) shows a polynomial modification (dashed line) compared with the signum function (solid line). The polynomial modification $P(x) = A(x)$, with $A^*(x)$ given by

$$A^*(x) = \frac{1}{(x^*)^3}x^2(3x^*-2x) \tag{G.9}$$

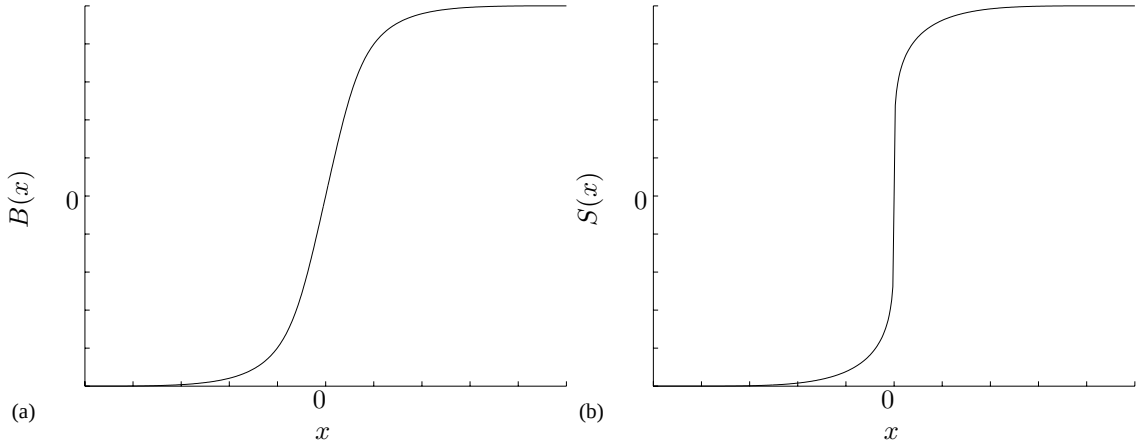

Figure G.4: (a) Bézier modification for $\epsilon_1 = 10^{15/4}, \epsilon_2 = 0$ and (b) Super elliptical modification for $\epsilon = 5$

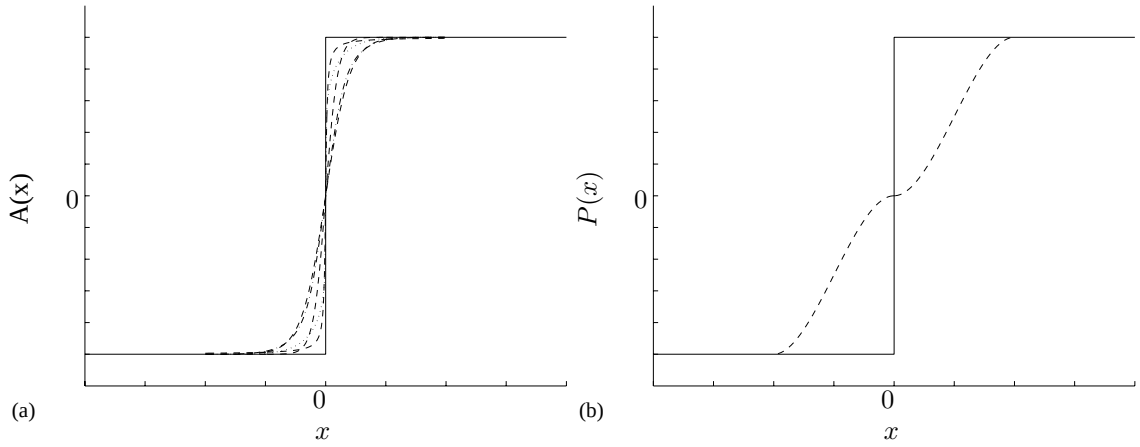

Figure G.5: (a) Comparison of the different modifications and (b)The polynomial modifications.